HU ISSN 2063-6792

MATERIALS SCIENCE AND ENGINEERING

A Publication of the University of Miskolc

Volume 45, Number 1

Miskolc University Press
2020

HU ISSN 2063-6792

CONTENTS

Materials Science and Engineering, Volume 45, No. 1 (2020), pp. 7–19.
DOI: 10.32974.mse.2020.001

FINITE ELEMENT MODELLING OF RESIDUAL STRESSES IN WELDED PIPE WELDS WITH DISSIMILAR MATERIALS

MAHMOOD ALHAFADHI[1] – GYÖRGY KRÁLLICS[2]

Abstract: Many methods might be used for investigation of the pipe weld failures. Residual stresses play a very prominent role in the growth of crack after the welding. In this study presented the finite element method simulation of residual stresses in case of pipe welding. A two-dimensional axisymmetric (2-D) finite element model is employed to calculate the residual stress. The model was validated using hardness measurement. The results were compared with experimentally measured data to evaluate the accuracy of the finite element modelling. Good agreement was found between the measurements and simulations results. The developed FE model was used to study the effects of welding heat input on welding residual stresses. It is shown that the welding heat input has a significant effect on the magnitude and distribution of residual stresses of the studied joints.

Keywords: Residual Stresses, simulation, finite element, Heat input, dissimilar pipe modelling

INTRODUCTION

Welding is one of the most common joining techniques used in many manufacturing industries, such as steel structure construction, power plant, and oil gas pipes, etc. [1]. Manual Metal Arc Welding (MMAW) is one of the earliest of the welding processes. Dissimilar pipe welds are commonly found in various industrial applications due to both technical and economic reasons [2]. Heat input is an essential factor in quality control in (MMAW) [3]. One of the significant problems in welded structures is residual stress, because of the high heat input are concentrated in the welded joint, and the residual stresses also are developed in and around the weld region due to the large temperature gradients generated among the weld fusion zone (FZ), heat-affected zone (HAZ), and base metal (BM) [4–9].

The heat input plays a significant role to increase or decrease the amount of residual stress in the welding structure. It is essential to identify and measure the welding residual stress distribution to improve the welding quality and reduce the negative effect with the prediction on it. Residual stresses may be measured by experi-

[1] Institut of Physical Metallurgy, Metalforming and Nanotechnology, University of Miskolc
H-3515 Miskolc-Egyetemváros, Hungary
femmahmood@uni-miskolc.hu
[2] Institut of Physical Metallurgy, Metalforming and Nanotechnology, University of Miskolc
H-3515 Miskolc-Egyetemváros, Hungary
femkgy@uni-miskolc.hu

mental measurement such as non-destructive techniques (e.g. X-ray and neutron diffraction, optical, magnetic or ultrasonic methods) and by destructive techniques (e.g. hole drilling, block removal, splitting and layering). Experimental measurement of the residual stress of pipe welding has some practical limitations. In destructive techniques, the measuring accuracy is generally high. Still, the sample damage is unacceptable in some cases and non-destructive techniques measurement widely used in in the laboratory due to its high accuracy, but it is expensive, the detection speed is slow and can only measure residual stress on the surface approximately 10–30 μm [10].

FEM is a perfect choice for the analysis of residual welding stresses. Numerical simulation of the problems associated with welding processes using the Finite Element Method (FEM) can help in eliminating the need for time-consuming and cost of the necessary experimental effort to optimize the welding process parameters such as heat input. For the last decades, it has been used for the solution of many types of problems. Many researchers have been inspired to conduct studied in this area, most of them only investigated heat input and welding residual stresses in the steady regions of the welded pipe by using 2D models or 3D models [11–17] Brickstad and Josefson estimated (2-D) axisymmetric models to numerically simulate multi-pass circumferential butt-welds of stainless steel pipes up to 40 mm thick in a non-linear thermo-mechanical finite element analysis (Brickstad and Josefson) [18]. Qureshi (2008) used numerical simulations to predict the residual stresses were affected by weld travel speed on in a thick-walled cylinder. The result of these simulations showed that for low welding speed, the magnitudes of residual stresses usually are higher at both the inner and outer surfaces [19]. One of the parameters that affect the control of residual stresses is the heat input (Kumar and Shahi 2011) [20]. Keehan (2004) reported that increasing heat input leads to increase the area of the weld bead, and results demonstrated that in less number of passes being required to fill up the weld completely [21].

As briefly mentioned, there is limited work to incorporate the effect of heat input and residual stresses of the welded joint for multi-pass pipe welds. In this work, finite element approach based on MARC software is developed to simulate residual stresses caused by welding in multi-pass welded pipe (2-D) model. The model was validated using hardness measurement. The P460NH_1 steel, E355K2 steel and the filler (A5.1-04: E6010) and for the second and third passes (A5.5-96: E6010 Al) were selected respectively as the material for the welding pipe.

1. MATERIALS AND METHODS

1.1. The pipe weld joint geometry and welding parameters

Dissimilar pipes with dimensions of 450 mm in length, with different thickness (11 mm and 8 mm) and outer diameter 323.9 mm were welded by MMAW process. *Figure 1* shows the finite element model with all dimensions. The base metals and filler metal chemical composition is shown in Table1 and welding parameters are shown in *Table 2*. Mechanical properties for each material are shown in *Figure 2, 3* and *4*.

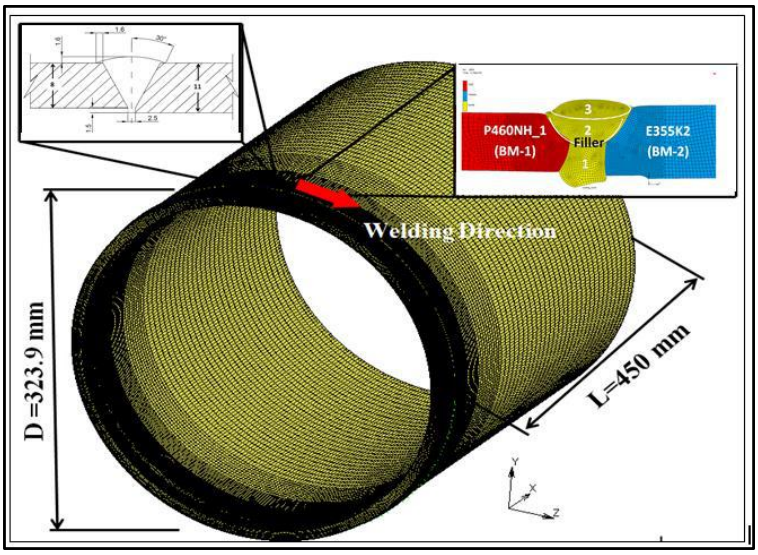

Figure 1
Finite element model of pipe with dimension (mm)

Table 1
Chemical composition (wt%)

Materials	C	S	P	Mn	Si	V	Cr	Cu
P460NH_1	0.2	0.001	0.02	1.49	0.33	0.2	0.01	0.03
E355K2	0.13	0.01	0.86	0.86	0.01	0.058	0.02	0.02
Filler	0.1	–	0.02	0.4	0.14	–	0.1	0.17

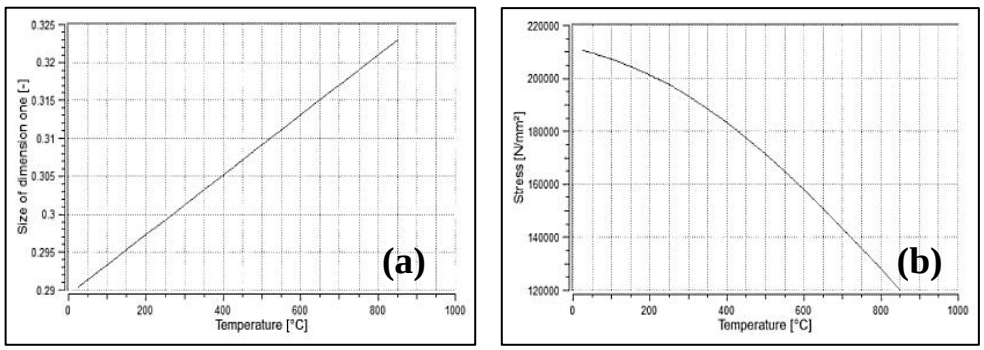

Figure 2
(a)Young's modulus and (b) Poisson's ratio for P460NH_1

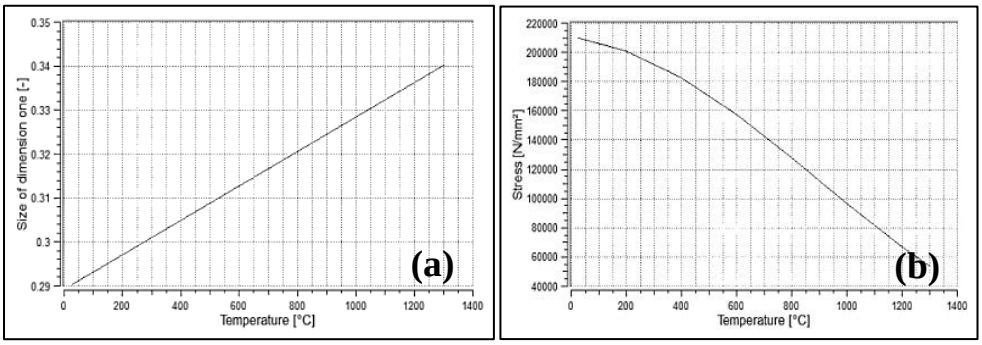

Figure 3
(a)Young's modulus and (b) Poisson's ratio for E355K2

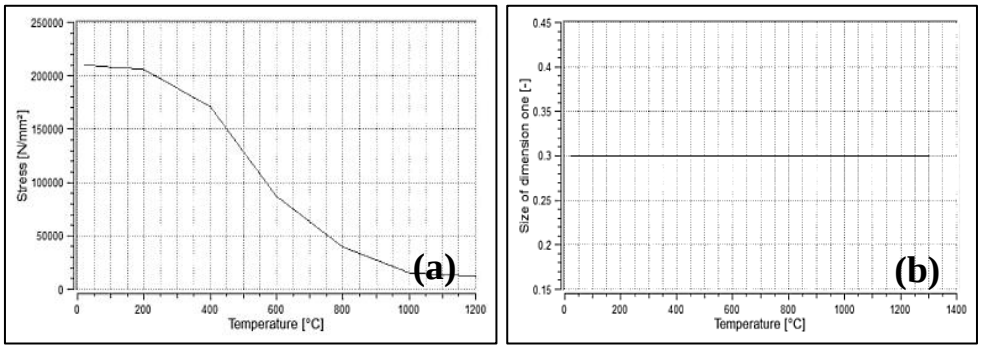

Figure 4
(a)Young's modulus and (b) Poisson's ratio for E6010

Table 2
Welding Parameters

Cases. Trial No.	**Current, I (A)**	**Voltage, U (V)**	**Welding speed v (cm/min.)**
Case A-1	100	19	12.3
Case A-2	100	22	15.21
Case B-1	150	19	12.3
Case B-2	150	22	15.21
Case C-1	175	19	12.3
Case C-2	175	22	15.21
Case D-1	200	19	12.3
Case D-2	200	22	15.21

1.2. Validation of the 2D model

In order to set up the accuracy of the numerical model, validation of the model is necessary to predict the residual stress. The cross-section welding part was polished after cutting, and the surface of the specimen was etched with HNO_3 (nitric acid) 2% solution (nitrate etching agent) to show the passes and FZ and HAZ.

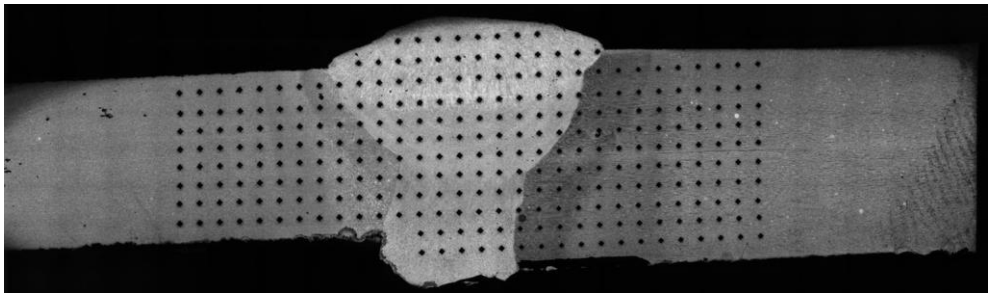

Figure 5
Vickers Hardness Testing (H_{10}) on Weld Cross-Section

The hardness measurement was carried out from top to bottom with 12 lines *(Figure 5)*. The validation of the welding simulation procedure is carried out on a multi-pass butt weld with eight tracks. The results are compared with experimental hardness test. *Figure 5* and *7* show measurements with a microscope-mounted camera showing an average of the measurement distance from the surface at a given point. The distances are in millimetre between the points of measurement, and the hardness values are in HV10. The hardness distribution from the simulation at the weld of the investigated dissimilar material with welding was calculated by using the rule of mixtures. Maynier et al. have developed a useful method to predict hardness [22]. The total hardness of steel is calculated dependent on the volume fractions of the constituents of the microstructure:

$$HV = (FP\% * HV_{F-P} + B\% * HV_B + M\% * HV_M)/100. \quad (1)$$

The hardness of the microstructures produced is given by:

$$HV_M = 127 + 949C\% + 27Si\% + 11Mn\% + 16Cr\%\ Ni\% + 21logv_R, \quad (2)$$

$$HV_B = -323 + 185C\% + 330Si\% + 153Mn\% + 144Cr\% + 191Mo\% + 65Ni\% + (logv_R)(89 + 53C\% - 55Si\% - 2Mn\% - 20Cr\% - 33Mo\% - 10Ni\%), \quad (3)$$

$$\mathrm{HV_{F-P}} = 42 + 223C\% + 53S\%i + 30Mn\% + 7Cr\% + 9Mo\% + 12.6N\%i + (logv_R)(10 - 19Si\% + 8Cr\% + 4Ni\% + 130V\%), \quad (4)$$

Where: v_R is the cooling rate in K/h; Hv is the hardness (Vickers); X_M, X_B, X_F and X_P are the volume fractions of martensite, bainite, ferrite and pearlite, respectively;

HV_M, HV_B and HV_{F+P} are the hardness of martensite, bainite and the mixture of ferrite and pearlite, respectively. For calculating of HV_M, Hv_B and HV_{F+P} were used the formula developed by Maynier et al.

Figure 6 showed the temperature profile in dissimilar welds joints was validated. The light grey region of modelled cross-section denotes fusion zone where the temperature exceeds the melting point (1,700 C), and the colour lines indicate HAZ-1 and HAZ-2 of the weld.

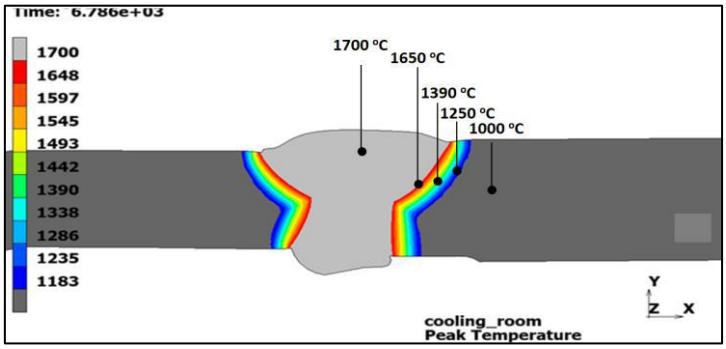

Figure 6
Temperature profile in dissimilar welds joints

Figure 7 gives information about the comparison between the predicted hardness simulation and the actual hardness measurement across weld joints at different regions from the weld centreline near the outer surface.

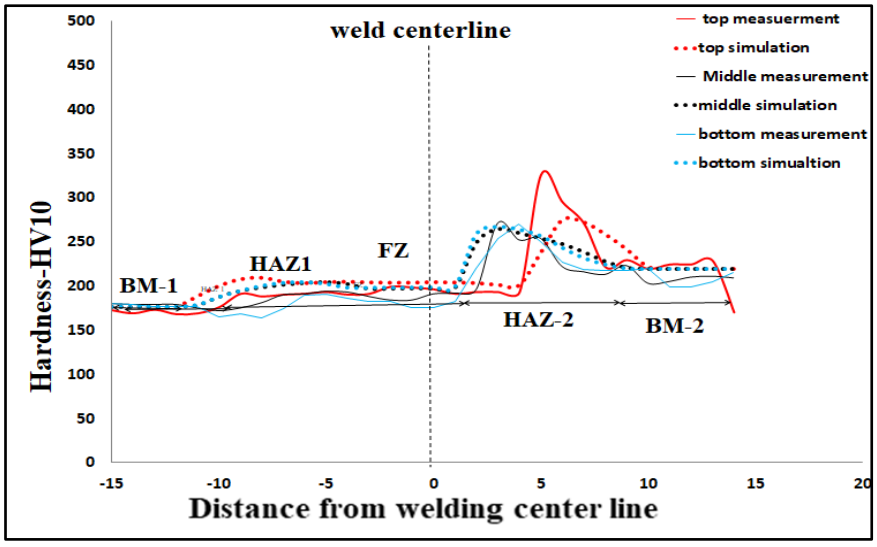

Figure 7
Comparison of the hardness measurement with simulation

The hardness test in base metal 1 (BM1) showed a steady but significant rise, which levelled out in HAZ1 and remained steady until the border of HAZ2, where a sharp peak occurs. It then falls rapidly to a level that is higher than that in HAZ2. 30 points were carried out to compare between the simulation and hardness test measurements. It shows good acceptable agreement between the simulation and the experimental results.

1.3. Finite element method

Finite element simulations of the process were performed with MSC Marc software. 2-D model with fillers was built with (birth and death) element using 8,466 elements as shown in *Figure 8*. By using appropriate mesh optimization technique, a relatively fine mesh is generated in and around the weld lines and a comparatively coarse mesh is used for areas away from weld line. In numerical simulation analysis, the accuracy of the results and required computing time are determined by the finite element size (mesh density). According to numerical analysis theory, the models with a fine mesh highly accurate results but required longer computing time. On the other hand, the model with coarse mesh (large element size) may lead to less accurate results but not much computing time.

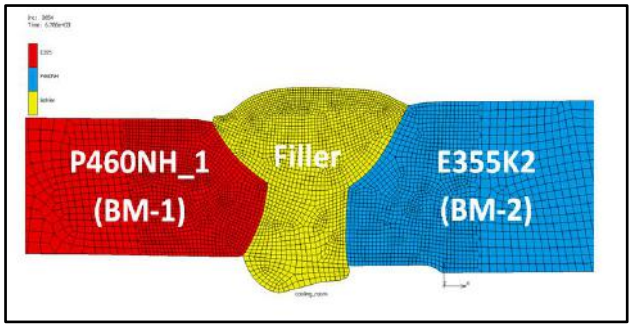

Figure 8
Finite element meshed model

The equations are used for transient heat transfer and heat source with a double ellipsoidal distribution proposed by Goldak et al. during welding is given by [23]

$$\mathrm{pc}\frac{\partial \mathrm{T}}{\partial \mathrm{t(x,y,z,t)}} = -\nabla \mathrm{q(x,y,z,t)} + \mathrm{Q(x,y,z,)} \tag{5}$$

$$\mathrm{Q(x,y,z,t)} = \frac{6\sqrt{3}\,\mathrm{f_i}\eta \mathrm{IV}}{\mathrm{abc_f}\pi\sqrt{\pi}} \mathrm{e}^{-3\left(\frac{\mathrm{x-vt}}{\mathrm{a}}\right)^2} \mathrm{e}^{-3\left(\frac{\mathrm{y}}{\mathrm{b}}\right)^2} \mathrm{e}^{-3\left(\frac{\mathrm{z}}{\mathrm{c}}\right)^2} \tag{6}$$

Where p is the density of the materials, c is the specific heat capacity, q is the heat flux vector, T is the temperature, Q is the inside heat rate, x, y and z are the coordinates in the system, t is time and ∇ is the spatial gradient operator. The various weld

parameters in a double ellipsoidal distribution proposed by Goldak et al. (see *Figure 9*).Where x, y, and z are the coordinates of the Goldak double ellipsoid model, π is the fraction of heat deposited in the weld region, the heat input rate Q = ηUI/v is calculated by welding operational parameters current (I), voltage (U) and η is the arc efficiency for the welding process, v is the speed of travel in mm/s, and t is the time in seconds. The factors f_f and f_r denote the fraction of the heat deposited in the front and rear quadrant respectively, which are set up to attain the restriction $f_f + f_r = 2$. The parameters a = 4, b = 3, $c_r = 5$ and $c_f = 8$ are related to the characteristics of the welding heat source.

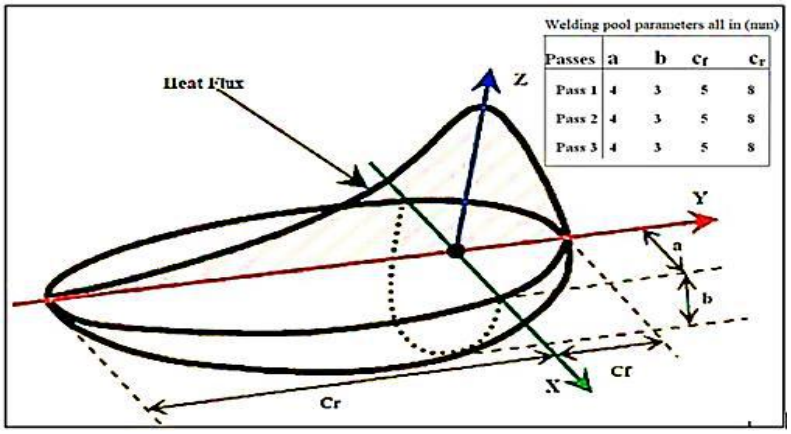

Figure 9
The Goldak double-ellipsoid heat source model

2. RESULTS AND DISCUSSION

To determine the distribution of residual stress in the welded pipe, the input of heat is the most important parameter. The results of the numerical simulation analysis were compared with eight cases of data to evaluate the residual stresses. Based on this study, 2-D modeling procedure with reasonable accuracy was investigated. From the results of residual stresses distribution, it is found that by giving the different heat inputs to the welding cases, the residual stresses increases as the heat input increased. It is found that as the heat supplied is 115.71, the value of residual stresses 182 MPa and as we increase the heat input, the residual stress reaches up to a 564 MPa as shown in *Figure 10*. *Figure 11* shows the residual stresses variations as the maximum heat input is supplied. It is shown that the residual stresses are maximum at the weld centre which is 564 MPa but as we move away from the centre of weld to the edge of the pipe, the residual stresses decrease suddenly which is 100 MPa that is known as the zone of heat-affected (HAZ-1) for base metal (P460NH_1) and (HAZ-2) for base metal E355K2 after that the stress becomes normal after a certain distance. The value of welding parameters cases and distribution of residual stresses is shown in *Table 3*.

Table 3

Welding parameters, Temperature distribution and Residual stresses

Trial Cases	Current (I) ampere	Voltage (V) volts	Welding speed *v* (cm/min.)	Heat Input (J/mm)	Residual stress (MPa)
Case A-1	100	19	12.3	123.5	221
Case A-2	100	22	15.21	115.71	182
Case B-1	150	19	12.3	185.36	385
Case B-2	150	22	15.21	173.57	232
Case C-1	175	19	12.3	216.26	411
Case C-2	175	22	15.21	202.49	313
Case D-1	200	19	12.3	247.15	564
Case D-2	200	22	15.21	231.42	421

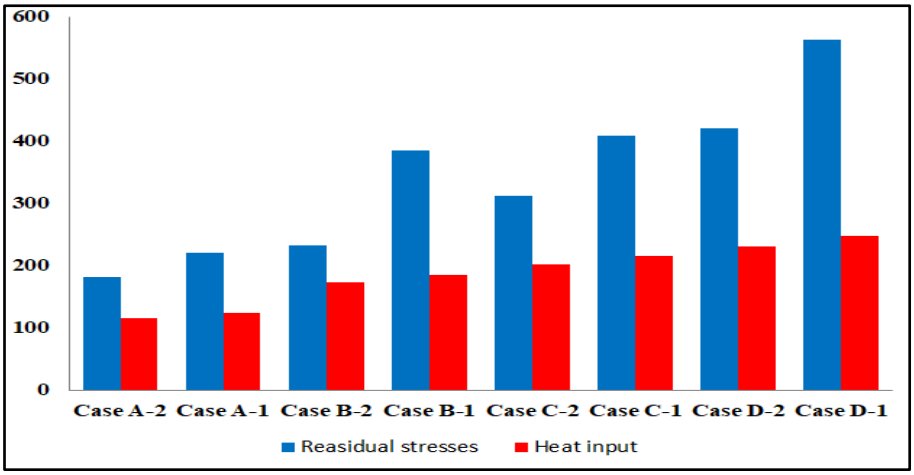

Figure 10

Effect of heat input on residual stresses

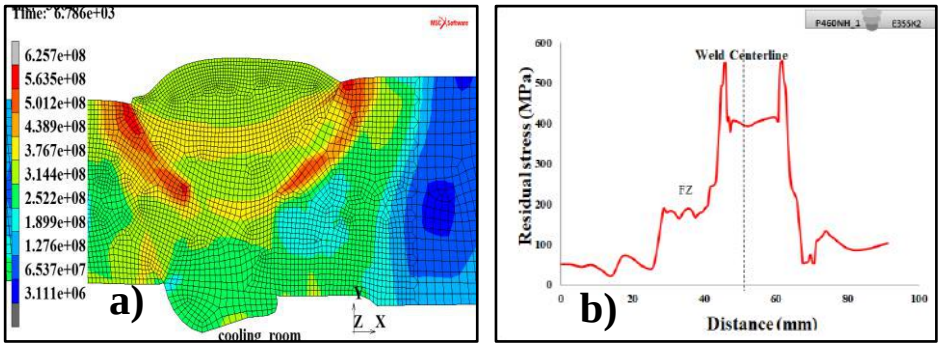

Figure 11

(a) Variation of maximum residual stress in with heat input (b) Variation of Maximum Residual stresses with distance from the weld centerline

Figure 12 represents the variation of residual stress as the minimum heat input is supplied. It is shown that the residual stresses are maximum at the weld centre which is 182 MPa, but as we move away from the weld centre to the edge of the pipe, the residual stresses decrease suddenly which is 10 MPa that is known as the (HAZ-1), (HAZ-2) and the stress become normal after a certain distance. From *Figure 9* and *10*, we can see clearly that residual stresses can be found in the middle of the model, and that is the advantage of prediction using numerical simulation.

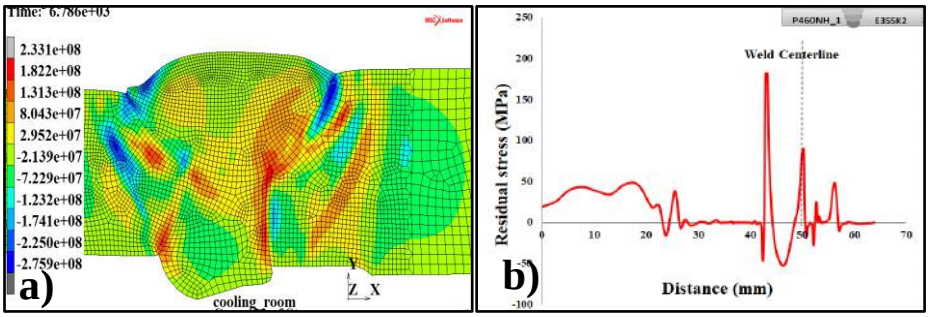

Figure 12

a) Variation of maximum residual stress in with heat input
(b) Variation of Maximum Residual stresses with distance from the weld centerline

CONCLUSION

- To conclude the results of the study, the implemented finite element simulation was able to simulate residual stresses in the welded pipe and the results showed a good approximation. Also, it shows the methodology of the simulation of welding using the finite element method.
- The study presented the mock-up that is needed to create a numerical simulation model.
- After that, the study summarizes how to build a correct finite element model in (2-D) to simulate girt welding. 2-D finite element welding simulation model was carried out by MSC Marct software with different thickness and material of the pipe. In addition, experiments were carried out so that hardness test measurements could be used to validate the 2D finite element model. The result show close agreement between simulated and experimental hardness in the weld.
- Numerical modeling based on a finite element method for simulation of dissimilar materials pipe welding has a powerful tool to predict the residual stresses in the regions further away from the weld surface.
- The welding process was simulated with eight different cases parameter. It could be concluded that by giving the different heat inputs to the welding sample the residual stresses increases as the heat input increased.

ACKNOWLEDGEMENT

The research was carried out at the University of Miskolc, within the framework of the *Thematic Excellence Program* funded by the Ministry of Innovation and Technology of Hungary. (Grant Contract reg. nr.: NKFIH-846-8/2019)

REFERENCES

[1] Kennedy, John L. (1993). *Oil and gas pipeline fundamentals*. Pennwell books.

[2] Rathod, Dinesh W. et al. (2015). Experimental analysis of dissimilar metal weld joint: Ferritic to austenitic stainless steel. *Materials Science and Engineering A*, 639, pp. 259–268.

[3] Paradowska, A. et al. (2006). The effect of heat input on residual stress distribution of steel welds measured by neutron diffraction. *Journal of Achievements in Materials and Manufacturing Engineering*, 17, 1, pp. 385–388.

[4] Žmindák, Milan et al. (2014). Finite element analysis of crack growth in pipelines. *Manufacturing Technology*, 14, 1, pp. 116–122.

[5] Alhafadhi, M. H., Krallics, G. (2019).Numerical simulation prediction and validation two dimensional model weld pipe. *Machines, Technologies, Materials*, Vol. 13, No. 10, pp. 447–450.

[6] Alhafadhi, M. H., Krallics G. (2018). The effect of heat input parameters on residual stress distribution by numerical simulation. *IOP Conference Series: Materials Science and Engineering*, Vol. 613, 5th International Conference on Competitive Materials and Technology Processes, Miskolc-Lillafüred, Hungary, pp. 1–6.

[7] Alhafadhi, M. H., Szűcs, M., Krallics, G. (2018). Finite element analysis on the formation of residual stresses during welding of oil and gas pipe. *International Journal of Metallurgical & Materials Science and Engineering*, Vol. 8, No. 3, pp. 1–10.

[8] Alhafadhi, M. H. Krallics, G. (2020). Simulation of the residual stress in a multi-pass oil and gas pipe weld joint. *Journal of Physics: Conference Series. IOP Publishing*, Vol. 1527, No.1, pp. 1–5.

[9] Alhafadhi, M. H. Krallics, G. (2020) Numerically simulated prediction of residual stresses in welding considering phase transformation effects. *Journal of Physics: Conference Series. IOP Publishing*, Vol. 1527, No. 1, pp. 1–5.

[10] Guo, Jiang et al. (2019). Recent Progress of Residual Stress Measurement Methods: A Review. *Chinese Journal of Aeronautics*,.pp. 1–25

[11] Murakawa, Hidekazu et al. (2012). Applications of inherent strain and interface element to simulation of welding deformation in thin plate structures. *Computational Materials Science*, 51, 1, pp. 43–52.

[12] Wu, Chunbiao, Jae-Woong Kim (2018). Analysis of welding residual stress formation behavior during circumferential TIG welding of a pipe. *Thin-Walled Structures*, 132, pp. 421–430.

[13] Xu, Jie, et al. (2014). Residual stress analyses in a pipe welding simulation: 3D pipe versus axi-symmetric models. *Procedia Mater Sci*., 3 pp. 511–516.

[14] Deng, Dean, Hidekazu, Murakawa (2006). Numerical simulation of temperature field and residual stress in multi-pass welds in stainless steel pipe and comparison with experimental measurements. *Computational Materials Science*, 37, 3, pp. 269–277.

[15] Duranton, P. et al. (2004). 3D modelling of multipass welding of a 316L stainless steel pipe. *Journal of Materials Processing Technology*, 153, pp. 457–463.

[16] Wang, Ying, et al. (2013). Simulation and analysis of temperature field for in-service multi-pass welding of a sleeve fillet weld. *Computational Materials Science*, 68, pp. 198–205.

[17] Wu, Chunbiao, Jae-Woong Kim (2018). Analysis of welding residual stress formation behavior during circumferential TIG welding of a pipe. *Thin-Walled Structures*, 132, pp. 421–430.

[18] Katsareas, Dimitrios Elias, Anastasius, Youtsos (2005). Residual stress prediction in dissimilar metal weld pipe joints using the finite element method. *Materials Science Forum*, Vol. 490. Trans Tech Publications Ltd.

[19] Brickstad, Björn, Josefson, B. L. (1998). A parametric study of residual stresses in multi-pass butt-welded stainless steel pipes. *International Journal of pressure Vessels and piping*, 75, 1, pp. 11–25.

[20] Obeid, Obeid, et al. (2018). Numerical simulation of thermal and residual stress fields induced by lined pipe welding. *Thermal Science and Engineering Progress*, 5 pp. 1–14.

[21] Kumar, Subodh, Shahi, A. S. (2011). Effect of heat input on the microstructure and mechanical properties of gas tungsten arc welded AISI 304 stainless steel joints. *Materials & Design*, 32, 6, pp. 3617–3623.

[22] Keehan, Enda (2004). *Effect of microstructure on mechanical properties of high strength steel weld metals*. Diss. Chalmers University of Technology and Göteborg University.

[23] Maynier, P., Jungmann, B., Dollet, J. (1978). Creusot-Loire System for the prediction of the mechanical properties of low alloy steel products.

Hardenability Concepts with Applications to Steel, The Metallurgical Society of AIME, pp. 518–545.

[24] Goldak, J., Chakravarti, A., Bibby, M. (1984). A new finite element model for welding heat sources model. *Metallurgical Transactions B*, 15, pp. 299–305.

Materials Science and Engineering, Volume 45, No. 1 (2020), pp. 20–28.
DOI: 10.32974.mse.2020.002

VEGETABLE OILS: POSSIBLE NEW PLASTICIZERS IN THE RUBBER INDUSTRY

ESZTER BORSODI[1] – KINGA TAMÁSI[2] – KÁLMÁN MAROSSY[3]

Abstract: The main goal of the research was to answer the question whether vegetable oils can be used as natural plasticizers for the rubber industry. To find out, we analyzed four types of vegetable oils (olive, rapeseed, sunflower and castor oil) by thermal analytical methods (DMA, TSDC) and compared the results with each other. Two hypotheses were set up, one is that vegetable oils will behave as a kind of macromolecule. The other hypothesis was that different fatty acid composition results in different relaxation processes and glass transition temperatures. Both of the hypotheses proved to be correct.

Keywords: vegetable oils, oil, plasticizers, thermal analytical method, DMA, TSDC

INTRODUCTION

The advantages of using vegetable oils in the plastics industry are as follows: they are renewable materials, their low price, and their environmental impact is moderate [1]. Using vegetable oils as plasticizers is not an over-researched area, there are only few studies about this topic, but oils could be important new materials, because they reduce material costs, without significant deterioration of the properties. Furthermore, there is a negative image in the consumers mind about phthalic acid esters, hence new plasticizers of natural origin could get better judgement.

1. MATERIALS AND METHODS

1.1. Materials

Oils are built of triglycerides, which consist of fatty acids and glycerin linked to each other. Fatty acids are carboxylic acids, they can be divided into two groups, depending on whether they contain a double bond, or not: saturated (do not contain double bond) and unsaturated (contain double bond) fatty acids. Notation: *Cn: k*, where *n* is the number of carbon atoms, and *k* is the number of double bonds. [2]

[1] Institute of Ceramic and Polymer Engineering, University of Miskolc
H-3515 Miskolc-Egyetemváros, Hungary
borsodies@gmail.com
[2] Institute of Ceramic and Polymer Engineering, University of Miskolc
H-3515 Miskolc-Egyetemváros, Hungary
polkinga@uni-miskolc.hu
[3] Institute of Ceramic and Polymer Engineering, University of Miskolc
H-3515 Miskolc-Egyetemváros, Hungary
polkal01@uni-miskolc.hu

The oil samples' theoretical fatty acid composition was used in the analysis. The composition of the oil samples based on data from technical literature. All mentioned studies determined the composition of the oils by gas chromatography. The data was collected from different studies (olive oil: [3, 4, 5]; rapeseed oil: [3, 5]; sunflower oil: [3, 6]; castor oil: [7], [8, 9]). Then we calculated the theoretical fatty acid values with arithmetic mean. The comparative chart shows only the most important fatty acids *(Figure 1)*. For easier comparability, we labelled the six most abundant fatty acids; the *other* ingredient contains both saturated and unsaturated fatty acids, but they occur in very small amounts in the tested oils.

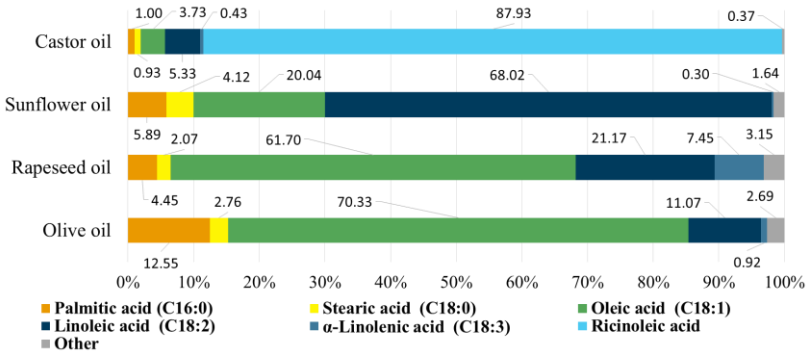

Figure 1
Theoretical fatty acid composition of the oil samples

1.2. Measuring methods

The vegetable oil samples were examined by thermal analytical methods. Thermal analytical methods are suitable for analysing transformation processes. In general, the principle of this type of methods is to measure a property (mass, modulus, etc.) as a function of temperature [10]. The methods can be used on their own, but using several methods at the same time we could get more well-grounded conclusions. In a similar study, Senatra et al. [11, 12] also examined fluids (oil-water emulsion) by thermally stimulated depolarization current, but they compared the results with the results of differential scanning calorimetry.

1.2.1. Parameters of the Dynamic Mechanical Analysis (DMA)

Because of the low viscosity, the shear (rotary) mode would be the only possible way to perform the DMA, thus a new method had to be developed due to the capabilities of the device. Ichemaguba [13] developed a method for testing plasticizers, where he measured 35 × 10 mm rectangular borosilicate glass filter paper impregnated with plasticizer, in dual cantilever mode. We followed this method, however higher capacity 150 g/m^2 non-woven fabric was used in single cantilever mode. This greatly improved the sensitivity of the method. The initial temperature was –120 °C,

and the heating rate was 2 °C/min. Measurements were made at 1 Hz frequency with ± 32 μm deformation.

1.2.2. Parameters of the Thermally Stimulated Depolarization Current (TSDC)

The oils were soaked in borosilicate "glass paper" filter with a pore size of 2.6 μm. According to the preliminary measurements, this material is two orders of magnitude less polarizable than the tested oils. The polarizing temperature was 50 °C, with –120 °C initial temperature. Both the cooling and the heating rate was 5 °C/min. The polarizing electric field strength was 500 V/mm. The evaluation was done with a special program developed by Marossy.

2. RESULTS

2.1. Results of the Dynamic Mechanical Analysis (DMA)

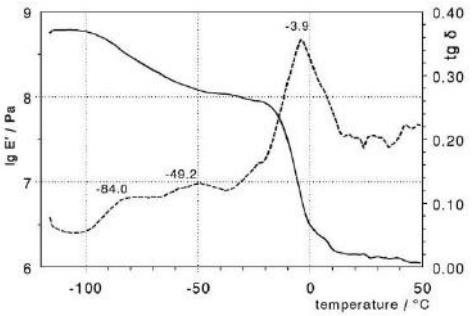

Figure 2
DMA curve of olive oil

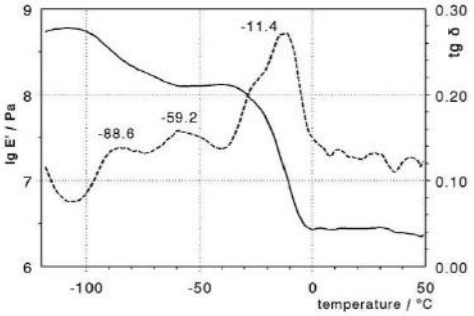

Figure 3
DMA curve of rapeseed oil

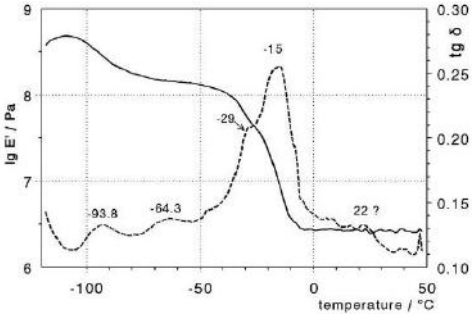

Figure 4
DMA curve of sunflower oil

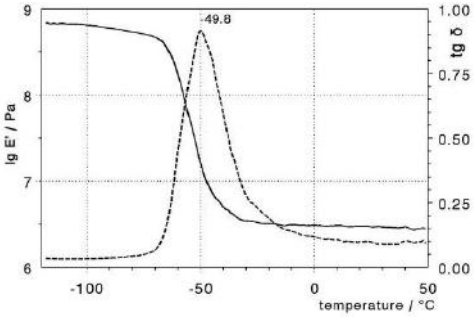

Figure 5
DMA curve of castor oil

The glass transition temperature (T_g) belongs to the highest intensity peak of the mechanical loss factor (tg δ, marked with dashed line), which is the lg E' (storage modulus, marked with a solid line) curve's inflexion point [14].

Olive oil's *(Figure 2)* and rapeseed oil's *(Figure 3)* DMA curves are very similar, they have several transitions, which is indicated by several peaks. According to the theoretical fatty acid composition, these oils have the highest oleic acid content among the four samples, and also have the highest glass transition temperature. From this, it can be deducted that the lower the oleic acid content, the lower the glass transition temperature.

The curve of sunflower oil *(Figure 4)* has the most peaks (four), this indicates four transition processes. Sunflower oil contains the largest amount of linoleic acid. The DMA curve of castor oil *(Figure 5)* is the most similar to the elastomers typical DMA curve. There is only one peak, so only one transition process, and castor oil has the lowest glass transition temperature (–49.8 °C) among the four oils tested according to DMA. This is probably due to the very high content of ricinoleic acid (~90%), which is a special unsaturated omega-9 fatty acid, having a hydroxyl functional group joined its 12nd carbon atom [15]. Thus ricinoleic acid (and castor oil itself) is more polar than most fatty acids. Probably the fatty acids' polarity affects the oils' glass transition temperature: the more polar the oil, the lower the T_g. Furthermore, it can be assumed that ricinoleic acid is a macromolecule, since castor oil shows the characteristic of polymers according to DMA.

Table 1

Glass transition temperatures according to DMA

Oils	Olive oil	Rapeseed oil	Sunflower oil	Castor oil
$\mathbf{T_g}$ [°C]	*–3.9*	*–11.4*	*–15.0*	*–49.8*

Based on the curves, it can also be stated that the olive oil with the largest saturated fatty acid content has the highest glass transition temperature, followed by in descending order – T_g and also in terms of saturated fatty acid content – rapeseed, sunflower and castor oil. It can be concluded that the lower the saturated fatty acid content, the lower the glass transition temperature.

2.2. Results of the Thermally Stimulated Depolarization Current (TSDC)

The alpha relaxation (glass transition) is determined by the main chain's segment movement, whilst the beta relaxation is associated with the side groups' movement [16]. Olive oil's TSDC curve *(Figure 6)* is very similar to DMA: it shows three peaks, so multiple transformations, which suggests that there are independent molecular motions in the material. The peak at –67.5 °C presumably indicates α relaxation, while the other two flatter peaks at –93.5 °C and –39.7 °C indicate β relaxation.

Rapeseed oil' TSDC curve *(Figure 7)* shows only one peak in the –100…–50 °C range (at –87.5 °C), unlike its DMA curve. This peak refers to α relaxation, and this oil has the lowest glass transition temperature according to the TSDC measurements.

Sunflower oil's TSDC *(Figure 8)* and DMA curves are similar. There are four peaks, several transformation processes takes place in it. The three flatter peaks (–107.0, –93.6 and –78.0 °C) may indicate β relaxation, while the peak with the highest intensity (at –23.5 °C) indicates α relaxation.

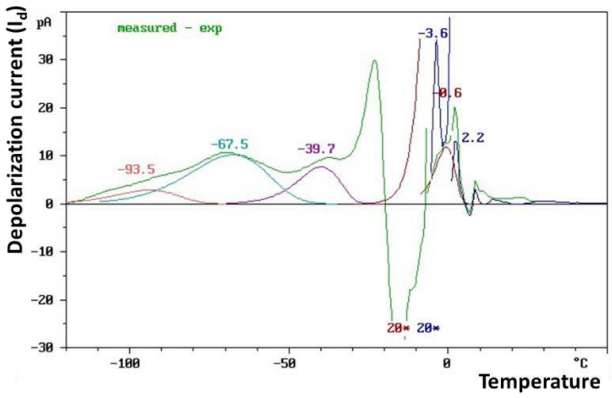

Figure 6
TSDC curve of olive oil

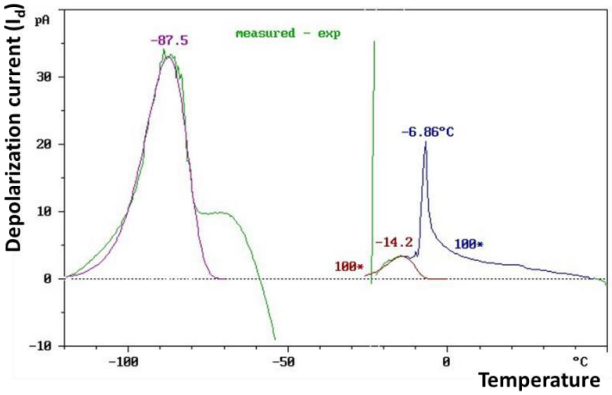

Figure 7
TSDC curve of rapeseed oil

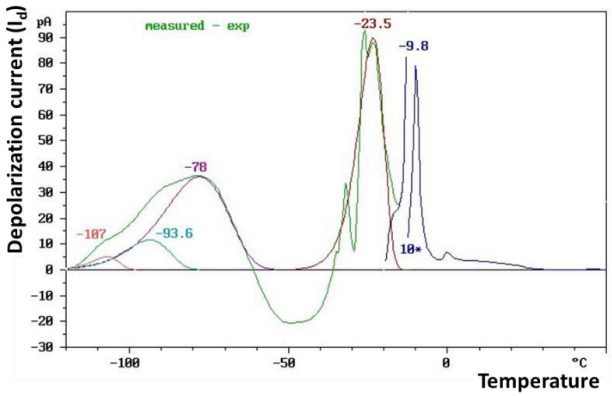

Figure 8
TSDC curve of sunflower oil

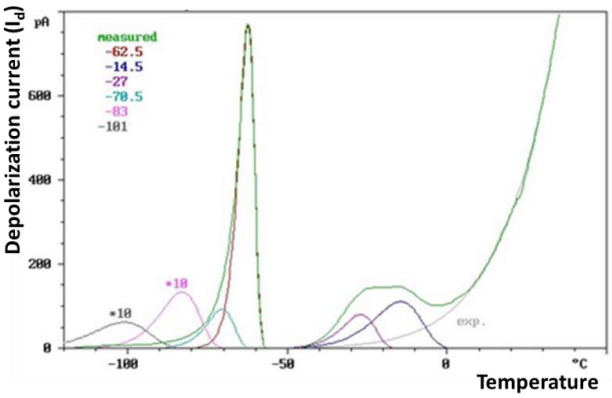

Figure 9
TSDC curve of castor oil

Castor oil's TSDC curve is also similar to its DMA results *(Figure 9)*: one separate, high intensity peak in the –100…–50 °C temperature range, at –62.5 °C, which represents α relaxation. This very high intensity peak (which almost reaches 700 pA depolarization current, much larger than the other oils' largest intensity) is also refers to the castor oil's highly polar nature due to its high content of ricinoleic acid.

Rapeseed oil has the lowest (–87.5 °C), and castor oil has the highest (–62.5 °C) glass transition temperature according to the TSDC measurement.

CONCLUSION

Four different types of vegetable oils (olive, rapeseed, sunflower and castor oil) was tested by dynamic mechanical analysis and thermally stimulated depolarization current. The oils showed similar behavior to macromolecules, thus they can be possible new plasticizers in the rubber industry. Furthermore, different fatty acid composition resulted in different transition processes.

Summarizing the results of DMA and TSDC measurements the following additional findings can be made:

1. We cannot assign a particular glass transition temperature, we can only determine a temperature range.
2. Glass transition temperature also depends on the measurement method.
3. The DMA curve represents the peaks in one block, while TSDC is a more sensitive method with more accurate values, but the sample preparation takes more time in this method.
4. DMA is advantageous if we want faster measurement, and less accurate results are sufficient for us.
5. Based on the DMA curves, I assume that the highest amount of fatty acid in the oils affects the glass transition temperature.
6. As shown in *Figure 10*, there are extreme differences between the identified glass transition temperatures for a given sample (the most outstanding differences are observed for olive and rapeseed oil).

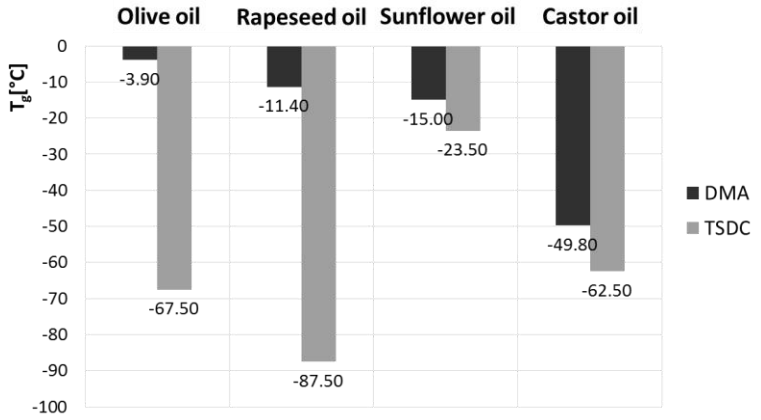

Figure 10
Comparison of DMA and TSDC results

7. In terms of the shape of the curves, castor oil showed the greatest similarity between the two methods, in addition to similar T_g values were also produced. Furthermore, the castor oil's curve shape approaches very well the typical thermomechanical curve of elastomers. This is presumably due to the high lactic acid content (close to 90%), which has a strongly polar character. This sample had the most intense depolarization current peak, approx. seven times larger the other oils'.
8. The curves of olive and sunflower oil also show similarities in both measurement methods, but their shape contains several peaks unlike castor oil. In the case of rapeseed oil, the curves of DMA and TSDC differ significantly in terms of their shape and intensity of peaks.

The transition temperatures can be used to calculate the activation energy, which is the basis of thermodynamic compatibility. The accurate fatty acid composition of the oil samples could be defined by Gas Chromatography-Mass Spectrometry, then the solubility parameter of the natural rubber and the oil plasticizers could be determined. Knowing these data, it is possible to give a theoretical estimation for the rubber mixtures' thermodynamic and chemical compatibility.

ACKNOWLEDGEMENT

The described article was carried out as part of the EFOP-3.6.1-16-2016-00011 *Younger and Renewing University – Innovative Knowledge City – institutional development of the University of Miskolc aiming at intelligent specialisation* project implemented in the framework of the Szechenyi 2020 program. The realization of this project is supported by the European Union, co-financed by the European Social Fund.

REFERENCES

[1] Samarth, N. B., Mahanwar, P. A. (2015). Modified Vegetable Oil Based Additives as a Future Polymeric Material — Review. *Open Journal of Organic Polymer Materials*, Jan., Vol. 5, No. 1, pp. 1–22.

[2] Csapó J., Csapóné Kiss Zs. (2003). *Élelmiszer-kémia*. Budapest, Mezőgazda Press.

[3] Orsavova, J., Misurcova, L., Ambrozova, J., Vicha, R., Mlcek, J. (2015). Fatty Acids Composition of Vegetable Oils and Its Contribution to Dietary Energy Intake and Dependence of Cardiovascular Mortality on Dietary Intake of Fatty Acids. *International Journal of Molecular Sciences*, June, Vol. 16, No. 6, pp. 12871–12890.

[4] Vingering, N., Oseredczuk, M., du Chaffaut, L., Ireland, J., Ledoux, M. (2010). Fatty acid composition of commercial vegetable oils from the French market analysed using a long highly polar column. *Oilseeds and fats, Crops and Lipids*, May, Vol. 17, No. 3, pp. 185–192.

[5] Lee, D.-S., Noh, B.-S., Bae, S.-Y., Kim, K. (1998). Characterization of fatty acids composition in vegetable oils by gas chromatography and chemometrics. *Analytica Chimica Acta*, Jan., Vol. 358, No. 2, pp. 163–175.

[6] Zambiazi, R. C., Przybylski, R., Zambiazi, M. W., Mendonça, C. B. (2007). Fatty acid composition of vegetable oils and fats. *B. Ceppa*, Jan./June, Vol. 25, No. 1, pp. 111–120.

[7] Binder, R. G., Applewhite, T. H., Kohler, G.O., Goldblatt, L. A. (1962). Chromatographie analysis of seed oils. Fatty acid composition of castor oil. *Journal of the American Oil Chemists' Society*, Dec., Vol. 39, No. 12, pp. 513–517.

[8] Conceição, M. M., Candeia, R. A., Silva, F. C., Bezerra, A. F., Fernandes, V. J., Souza, A. G. (2007). Thermoanalytical characterization of castor oil biodiesel. *Renewable and Sustainable Energy Reviews*, June, Vol. 11, No. 5, pp. 964–975.

[9] Salimon, J., Mohd Noor, D. A., Nazrizawati, A. T., Mohd Yusoff, M. F., Noraishah, A. (2010). Fatty acid composition and physicochemical properties of Malaysian castor bean ricinus communis L. seed oil. *Sains Malaysiana*, May, Vol. 39, No. 5, pp. 761–764.

[10] Szakács H., Varga Cs., Nagy, R. (2012). *Polimerek méréstechnikája.* Veszprém, University of Pannonia.

[11] Senatra, D. (2006). Comparative analysis of complex liquids based on a multiexperimental approach. *Advances in Colloid and Interface Science*, Dec., Vol. 128–130, pp. 65–75.

[12] Senatra, D., Gambi, C. M., Neri, A. P. (1981). Thermally stimulated dielectric polarization release in water-in-oil microemulsions. *Journal of Colloid and Interface Science*, Feb., Vol. 79, No. 2, pp. 443–453.

[13] Ihemaguba, C. L. (2018). *Using Physical Methods for the Investigation and Characterization of Fine Structure of Fluid Additives and Selected Polymeric Materials*. MSc thesis, University of Miskolc, Miskolc, Hungary.

[14] Zsoldos, G., Szoda, K., Marossy, K. (2017). Combined Mechanical and Electrical Study of Polymers of Biological Origin. In: *Proc. of the 4th International Conference on Competitive Materials and Technology Processes (IC-CMTP4)*, 3 March to 7 October 2016, Miskolc, Hungary. IOP Publishing Ltd IOP Conference Series: Materials Science and Engineering, Vol. 175.

[15] Mutlu, H., Meier, M. A. R. (2010). Castor oil as a renewable resource for the chemical industry. *European Journal of Lipid Science and Technology*, Jan., Vol. 112, No 1, pp. 10–30.

[16] Hedvig, P. (1977). *Dielectric spectroscopy of polymers*. Budapest, Akadémiai Kiadó.

Materials Science and Engineering, Volume 45, No. 1 (2020), pp. 29–36.
DOI: 10.32974.mse.2020.003

THE ROLE OF METALLOGRAPHY IN THE RESTORATION OF AN INCENSE BURNER FROM PERSIA

TAMÁS BUBONYI[1] – SZILVIA GYÖNGYÖSI[2] – LEA NAGY[3] – PÉTER BARKÓCZY[4] – ESZTER BAKONYI[5]

Abstract: Before the restoration of a metallic object, detailed analysis of the metal and the microstructure could provide useful information about the techniques used for producing it. Additionally, it is possible to obtain data about the metal and the object, which expands the knowledge about the origin of the object and its raw material. This study introduces this field through the metallographic analysis of an incense burner from Persia, from the Quajar period of the 19th Century Iran. The results of the metallographic investigation are not only used for the restoration work but also for archaeometry and archeology. The burner was made from a heterogeneous brass alloy. The antecedents of the burner were unknown so local heating was applied to avoid the brittle breakages. Selenium content was detected in the sulfide inclusions which shows a Near-East origin of the raw material.

Keywords: metallography, restoration, chemical analysis, selenium, brass

INTRODUCTION

An incense burner from Persia was examined *(Figure 1)*. This burner is owned by the Ferenc Hopp Museum of Asian Arts and is exhibited in Budapest. The burner was damaged, the body was broken, and some small part were missing. Lea Nagy made the repair and restoration of the burner [1]. Due to the large extent of deformation, it was an important question if the raw material was brittle or ductile. This basic property of the metal determines the best practices during the manufacturing process [2]. Additionally, it was necessary to complement the missing part. Chemical analysis was needed to choose the best alloy for the restoration [3, 16, 17]. However,

[1] Department of Physical Metallurgy, Metalforming and Nanotechnology, University of Miskolc
H-3515 Miskolc-Egyetemváros, Hungary
fembubo@uni-miskolc.hu
[2] Department of Solid State Physics, University of Debrecen
H-4026 Debrecen, Bem Square 18, Hungary
szilvia.gyongysi@science.unideb.hu
[3] University of Fine Arts
H-1062 Budapest, Andrássy str. 69–71, Hungary
nagy.lea@gmail.com
[4] Department of Physical Metallurgy, Metalforming and Nanotechnology, University of Miskolc
H-3515 Miskolc-Egyetemváros, Hungary
fembarki@uni-miskolc.hu
[5] Hungarian National Museum
H-1088 Budapest, Múzeum krt. 14–16, Hungary
bakonyi.eszter@gmail.com

the chemical composition by itself was not enough to make the suitable replacement. To determine the original production method was also necessary to approximate the original status and outlook after the repair [4, 11]. Therefore, a full metallographic description was necessary before the restoration and repair could begin [5, 13, 18].

The basic steps of the production can be identified by the status of the microstructure [6]. These steps are casting, plastic deformation and heat treatment [7]. Based on the alloy and the microstructure, basics of the production technology can be reverse engineered [8, 19]. A detailed quantitative description of the microstructure gives a chance for a more detailed analysis and description of the circumstances of the processing. Optical microscopy is the best investigation method for the microstructure, and additional SEM-EDS analysis helps to identify the different phases or precipitations based on their local composition. Sometimes the surface condition, possible layer is also important. In these cases, the SEM-EDS study also helps [9, 14, 15].

Metallographic analysis belongs to the destructive material testing methods [10]. Taking sample from the objects is necessary. This is not a problem before the restoration, however, the size of the samples in case of artifacts is small in almost every case, so it is important for the sample to represent the whole artifact [11]. In the case of the burner the damaged part has a graved lace like fine structure, so the relevant sample is consequently very tiny. To see the importance of the questions, a detailed analysis and description was performed, and the results are summarized in this article.

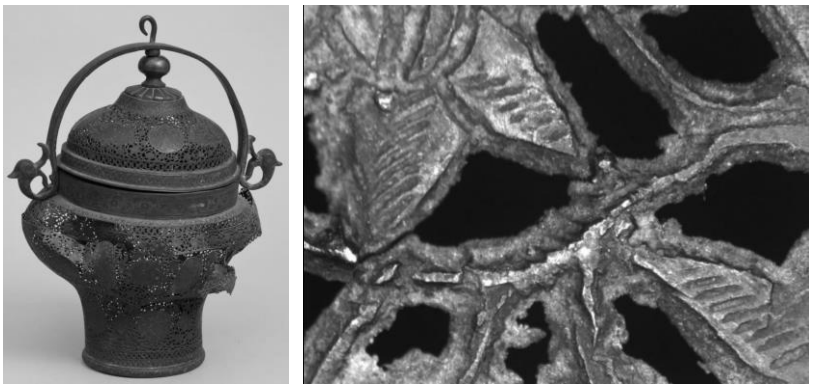

Figure 1
The examined incense burner and the lace like broken part in larger magnification

1. MATERIALS AND METHODS

A sample was cut from the lace like parts, and the cross-section of the sample was examined. The preliminary SEM-EDS analysis shows that the raw material of the burner is brass. Therefore, the sample was grinded and polished mechanically. The polishing was performed with 3 and 1 μm diamond particles. Immersion etching was applied using $FeCl_3$ solution. The microstructure was observed with a Zeiss AxioImager M1m microscope. The SEM-EDS analysis was made by Árpád Kovács at LISA

Strategic Research Infrastructure of the Faculty of Materials Engineering, University of Miskolc. A Zeiss EVO MA 10 SEM was used with an EDAX EDS system.

2. RESULTS AND DISCUSSION

As visible on *Figure 1*, the lace-like part of the burner is broken. The larger magnification shows the fine structure of this lace-like part. Elements with small cross sections hold the top of the burner. The picture suggests that this is a carved and inwrought part. A small piece of the material was removed and analysed with SEM-EDS. *Figure 2* shows the micrograph of this part.

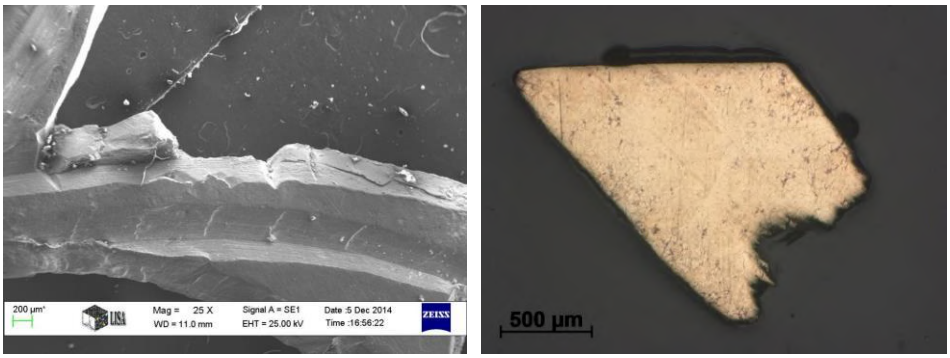

Figure 2
SEM micrograph taken from the examined part of the burner (left) and the prepared cross section of this sample (right)

The SEM micrograph of *Figure 2* clearly reveals the traces of carving, so this is the necessary technique of production and ornamenting the extensions. The surface of the sample was analysed. The analysis shows that the sample is brass with 30 w% zinc content. Additionally, 1 w% silver and extremely high 8 w% lead content was measured. Consequently, in the following tests, the sample was handled as brass. The lead content on the other hand was too high, so the cross section must be analysed as well to compare with the surface for identifying the extent of the corrosion. The corrosion process causes the segregation of lead to the surface of the metal.

The SEM –EDS analysis of the cross section of the sample shows 35.5 w% zinc content and 0.5–1 w% lead content. Silver was not detected in the bulk. This large difference of the lead content at the surface and the bulk shows a strong corrosion, which was not trivial at the first observation of the burner. As a result, the cleaning of the surface was necessary during the restoration. The zinc content suggests inhomogeneous brass which can be seen on *Figure 3*. The β islands and pins exists in an α matrix. The pins of β draw the dendritic structure of the raw material. This suggests a cast raw material. On the microstructure of *Figure 2*, the heterogeneous structure, where the top and the bottom of the sample contains more β than the central area of the cross section, can clearly be seen. This shows that a thin plate was cast, and this

plate was then manufactured. The large cooling rate caused the segregation at the surface area. This is supported by the dendritic-like structure as well. The differential interference contrast (DIC) micrographs of the sample *(Figure 4)* reveal the twin boundaries and small grains, which are typical after the recrystallization process. These can be observed mainly near the surface. The carving creates plastic deformation, and the microstructure shows that the material was heat-treated, annealed after carving. The fast cooling can produce brittle brass due to the β- β' transformation, and annealing can increase the ductility of the material.

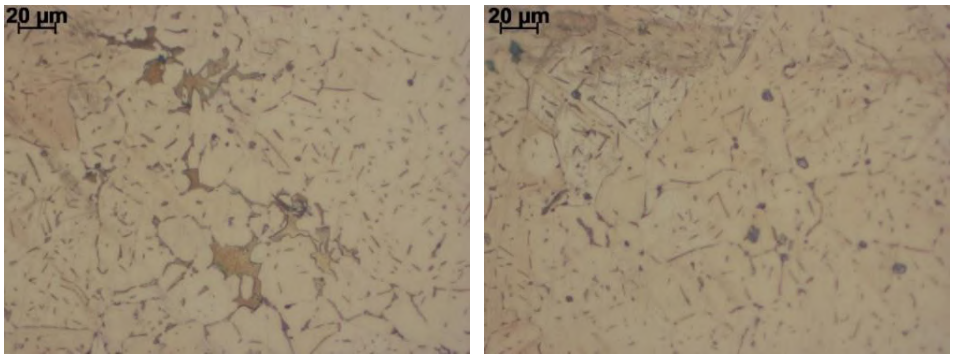

Figure 3
Optical micrographs from the microstructure of the burner

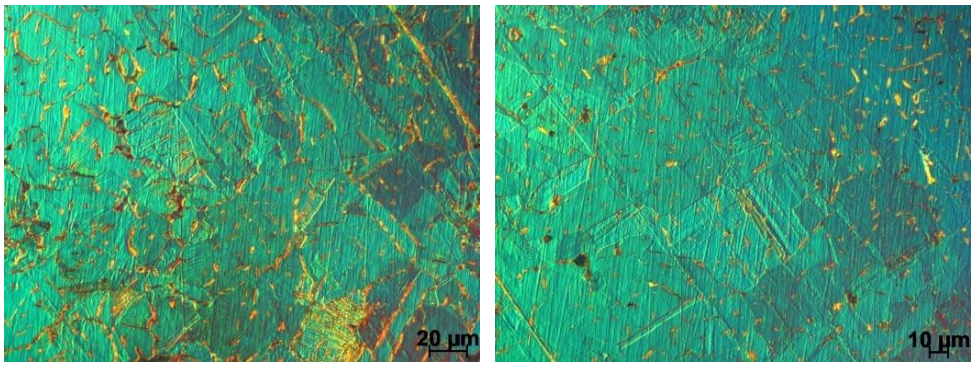

Figure 4
The microstructure of the examined sample illuminated and analysed by DIC technique

Next to the β, other phases-inclusions were revealed by the optical microscopic observation. Therefore, a detailed SEM-EDS analysis was performed. *Figure 5* shows the SEM micrographs, where the different analysed phases are marked with numbers. The left image shows the typical appearance of α (1) and β (2) phases. The α phase contains 35 w/w% zinc while the β contains 45.3 w% zinc. The right image

also shows the α (1) and the β (3, 4) phases with the same composition. It is interesting that the microstructure contains pure copper (2, 5) which shows that the alloying of the raw material was not properly performed. Comparing the above information with the plausible manufacturing method, it is possible that the alloy was produced only for this object.

On the left micrographs of *Figure 5*, number 3 denotes the lead inclusion. It is white in the SEM micrographs due to the larger atomic weight related to the surrounding. These inclusions appear to be pure lead, the copper cannot solve the lead either in liquid or solid state. Therefore, the lead forms smaller or larger drops during solidification, and solidifies in this form at the beginning of the cooling of the melt. *Figure 6* shows this in larger magnification, and the analysed drops are denoted by 1. Number 2 denotes phases in both micrographs, where the local chemical analysis detected a high content of selenium.

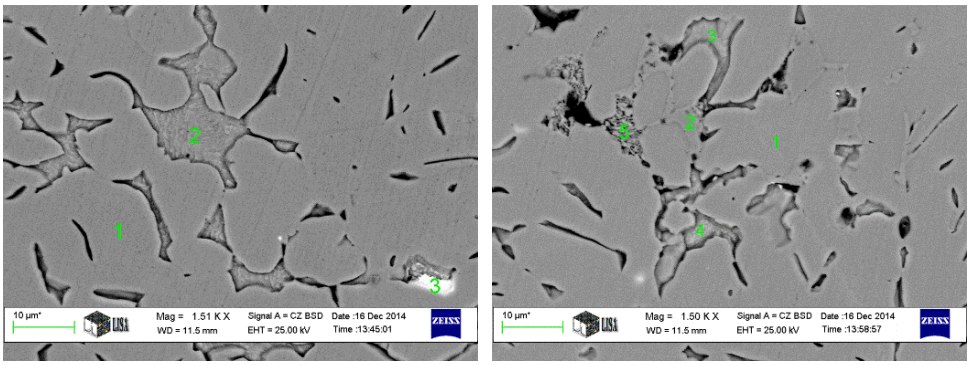

Figure 5
Different kinds of phases and the positions of the local chemical analysis in the microstructure of the sample from the burner

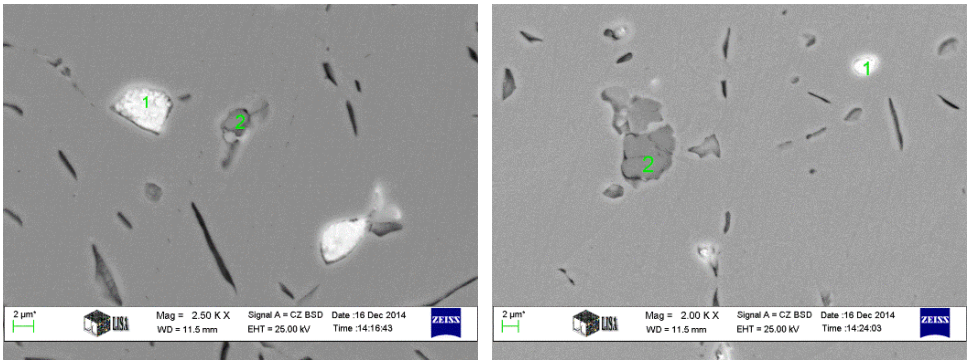

Figure 6
Positions of the local chemical analysis of selenium containing inclusions, and their morphology

These phases are basically copper-sulphide inclusions from the smelting process. Additionally, beside the sulphur these contain 9 w/w% selenium too. The sulphur and the selenium are chemically compatible and can substitute each other in the same chemical reactions. So, the sulphide copper ores can contain selenium, and the smelting process will be the same.

The copper-selenides are rare; therefore, they can be used as a trace of the origin of the ore. One typical place where selenides can be found is the Near-East, the estimated origin of the burner. Due to the large fossil deposition (oil basin) the selenium content of the copper ores can increase. This phenomenon and the inclusions show the origin of the burner next to the typology, the ornaments and the documentation.

The metallography of a small part of the burner revealed that the raw material of the burner is heterogeneous brass with some small-sized lead and sulfide inclusions. The possible manufacturing of the damaged lace-like part is: 1. casting a plate, 2. preparing the carved and inwrought pattern, 3. heat-treatment. The alloy could be brittle based on the chemical composition and the possible manufacturing method. A short-term local heat treatment was applied (~450 °C) before the bending of the material in the damaged parts. The extensions were made from common brass (C26000). The chemical composition of wire brass (C27000) is closer to the burner, although it has a higher tensile strength, and acts like a spring. The cold-rolled state was used for carving. First soldering was planned to fix the parts in the damaged area, but the structure was too fine for a successful application. Finally, sticking was used. Special high strength glue was applied due to the possible remaining elastic stresses.

CONCLUSIONS

An incense burner originated in Iran was examined before the restoration work. The burner was broken, and some parts were missing, so a large repair and substitution work was necessary. For this work the analysis of the chemical composition was necessary. The bulk material is brass (35.5 w% Zn and 0.5–1% lead). The material was cast to a plate, then ornamented by carving. After the carving the burner was annealed. The basic question of the repairing was the ductility of the raw material. This is a heterogeneous brass material, which can be brittle, especially if the estimated manufacturing method is taken into consideration. So, the local heating of the bent parts was suggested. Additionally, the lead content was extremely large at the surface, which indicates an intensive corrosion of the burner, so the cleaning was also suggested. During the metallographic analysis, copper-sulfide inclusions were found which have large selenium content. These inclusions are from the smelting process and were used as trace to point to the Near-East as the origin of the raw material. Based on this information the whole repair was made, and the object can be exhibited.

ACKNOWLEDGEMENT

The described article was carried out as part of the EFOP-3.6.1-16-2016-00011 *Younger and Renewing University – Innovative Knowledge City – institutional development of the University of Miskolc aiming at intelligent specialisation* project implemented in the framework of the Szechenyi 2020 program. The realization of this project is supported by the European Union, co-financed by the European Social Fund.

REFERENCES

[1] Nagy L. (2017). *Perzsa sárgaréz füstölőedény restaurálása*. Thesis, Budapest, University of Fine Arts.

[2] Hosford, W. F., Caddell, R. M. (2011). *Metal Forming, Mechanics and Metallurgy*. Cambridge University Press.

[3] Lutz, J., Pernicka, E. (1996). Energy dispersive X-ray analysis of ancient copper alloys: empirical values for precision and accuracy. *Archaeometry*, 38, pp. 313–323.

[4] Kienlin T. L. (2013). Copper and Bronze: Bronze Age Metalworking in Context. In: Fokkens, H., Harding, A. (eds.). *The Oxford Handbook of the European Bronze Age*. Oxford, Handbooks in Archaeology.

[5] Scott D. A. (1991). *Metallography and Microstucture of Ancient and Historic Metals*. Tien Wah Press Ltd., Singapore.

[6] Konečná, R., Fintová, S. (2012). Copper and Copper Alloys: Casting, Classification and Characteristic Microstructures, Copper *Alloys. Early Applications and Current Performance – Enhancing Processes*, Collini, L. (ed.), InTech, ISBN: 978-953-51-0160-4.

[7] Porter, D. A., Easterling, K. E., Sherif, M. Y. A. (2009). *Phase Transformations in Metals and Alloys*. Boca Raton, FL, CRC Press.

[8] Fadhil, A. A., Ghattas, M. S., Iskander, B. A., Ajeel, S. A., Enab, T. A. (2018). Structural characterization and detecting processes of defects in leaded brass alloy used for gas valves production. *Alexandria Engineering Journal*, Vol. 57, pp. 1301–1311.

[9] Cvikel, D., Cohen, M., Inberg, A., Klein, S., Iddan, N., Ashkenazi, D. (2017). Metallurgical characterization of brass sheet from the 19th-century Akko Tower Wreck (Israel). *Materials Characterization*, Volume 131, pp. 175–187.

[10] Vander Voort (g. F. (2004). *ASM Handbook 9: Metallography and Microstructures*. ASM International, printed in the USA.

[11] Czichos, H., Saito, T., Smith, L. (eds) (2011). *Handbook of metrology and testing*. Springer-Verlag, Berlin–Heidelberg.

[12] Dillmann, P., Béranger, G., Piccardo, P., Matthiesen, H. (eds.) (2007). *Corrosion of metallic heritage artefacts Investigation, conservation and prediction for long-term behaviour*. Cambridge, Woodhead Publishing Limited.

[13] Pollini, J., Giumlia-Mair, A. (2019). The statue of Germanicus fom Amelia: New discoveries. *American Journal of Archaeology*, Vol. 123, No. 4, pp. 673–686.

[14] Dillmann, P., Watkinson, D., Angelini, E., Adriaens, A. (eds.) (2013). *Corrosion and conservation of cultural heritage metallic artefacts*. Cambridge, Woodhead Publishing Limited.

[15] Mcneil, M. B., Little, B. J. (1992). Corrosion mechanisms for copper and silver objects in near-surface environments. *Journal of the American Institute for Conservation*, Vol. 31/3., pp. 355–366.

[16] Artioli, G. (ed.) (2010). *Scientific methods and cultural heritage: An introduction to the application of materials science to archaeometry and conservation science*. Oxford University Press.

[17] Varella, E. A. (ed.) (2013). *Conservation Science for the Cultural Heritage, Applications of Instrumental Analysis*. Springer-Verlag, Berlin–Heidelberg.

[18] Giumlia-Mair, A., Mráv, Zs. (2014). The aes Corinthium vessels from Egyed, Hungary. *Folia Archaeologica*, LVI.

[19] Benkő, E., Barkóczy, P. (2017). The archaeology of books. Medieval book clasps and other book fittings from Pilis Cistercian Monastery. In: Benkő, E., Kovács, Gy., Krisztina, O. (ed.). *Crafts and workshops in Hungary During the Middle Ages and the early modern period*. Budapest, Hungarian Academy of Sciences.

Materials Science and Engineering, Volume 45, No. 1 (2020), pp. 37–49.
DOI: 10.32974.mse.2020.004

THE EFFECT OF COREMAKING PARAMETERS ON THE THERMAL DISTORTION BEHAVIOUR OF RESIN-COATED SAND

IMRE BUDAVÁRI[1] – LÁSZLÓ VARGA[2]

Abstract: In the shell core making process, to achieve precise dimensions, good surface quality, and defect-free casting, it is essential to optimize the proper technological parameters. These parameters influence the properties of the core through the curing mechanism of the novolac binder. To avoid uneven deformation or defects during the pouring process, it is very important to understand the complex phenomenon that takes place at the core/metal interface. In the research work, the effect of the curing time and curing temperature on the hot distortion properties of resin coated sand was investigated. Tests were made using Hot-Distortion Tester laboratory equipment, where the deformation and degradation time was measured. It was established, that higher curing temperature and curing time lead to higher deformation and smaller thermal strength of the resin-coated sand cores.

Keywords: resin-coated sand, thermal load, hot-distortion, deformation, degradation

INTRODUCTION

The shell process, also called croning process, was developed in Germany during World War II by Johannes Croning. It is widely used for making shell moulds and shell cores for the manufacturing of small and medium-sized aluminium, cast iron and steel products. In this process, resin-coated sand or precoated shell sand is used as a moulding material. The coated sand is blown into a preheated core-box or dumped into a heated pattern plate. The resin is melted and then cured thus the core or the mould is hardened [1].

The resin-coated sand is characterized by good flowability, good strength, and good shakeout characteristics. Because of its advantageous properties complicated solid and also hollow cores can be produced that provide good surface finish, high level of dimensional accuracy and thus near-net shaped castings in the production [2], [3].

[1] Foundry Institute, University of Miskolc
H-3515 Miskolc-Egyetemváros, Hungary
budavari1987@gmail.com
[2] Foundry Institute, University of Miskolc
H-3515 Miskolc-Egyetemváros, Hungary
laszlo.varga.mak@gmail.com

To control the quality of sand cores or moulds, and to achieve improved production efficiency it is necessary to understand the curing mechanism of the phenol-formaldehyde based novolac resin since it has a significant impact on the properties of the produced shell core or mould [1].

According to the literature [4], the reaction between the novolac resin and the curing agent (so called hexa) is a multi-step polycondensation reaction that takes place at three stages: during.

In the coating, the core or mold making, and the metal pouring. In the coating process, when the hexa is added to the sand-resin mixture, the novolac is partially cross-linked. Using high precoating temperature [5] leads to a fully cured polymer that prevents proper coating, causing deterioration in the quality of the resin-coated sand. For example the hot-tensile strength can be reduced.

During the core making procedure, the resin-coated sand is blown into the heated core-box. In this stage, the resin is called A-resol, which creates a solid film around the sand grains. When the coated sand interacts with the high-temperature core-box the resin starts to melt and plastically flow between the sand grains. The novolac transforms into the B-resitol stage, which is a thermoplastic condition. Uprising the temperature of the sand mixture, the curing agent breaks down into formaldehyde and ammonia. The free formaldehyde reacts with the hydroxyl group of the phenol-formaldehyde novolac resin through an irreversible reaction. The resin transforms from a thermoplastic state to a thermosetting one, which is a fully cured state called C-resit, which can be characterized as hardened, rigid resin [6]. Different states of the resin during the core making process can be seen in *Figure 1*.

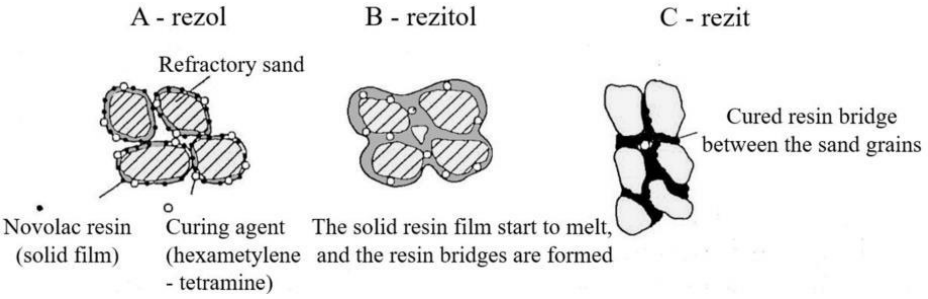

Figure 1

The transformation of the novolac resin during the core making procedure [6]

The extent of the cross-linking reaction can be controlled with the combination of curing time and curing temperature. The curing time is a time interval in which the resin-coated sand is exposed to heat in the core-box. The curing temperature means the elevated temperature at which the curing process takes place. Monitoring these two technological parameters during the core making process plays a vital role in achieving the desired mechanical strength of the core to withstand the handling, transporting and physical contact of the molten metal during the pouring process [5].

By increasing curing time and curing temperature, the desired wall thickness can be achieved. Using excessive high curing temperature results in an over-cured, brittle core, which may lead to erosion, cracking or breakdown of the core when it is interacting with the high-temperatured molten metal. On the other hand, the under-cured core may not have enough strength to withstand the mechanical loading induced by the handling process, causing early breakage. The other adverse effects are excessive thermoplastic relaxation and gas evolution during the pouring process. The curing temperature is generally between 204–316 °C [7].

To help the foundries in setting the optimum curing temperature, at which the crosslinking reaction will be fully completed, several studies [4], [8], [9] were carried out to investigate the structural changes before and after the curing reaction, while other studies [10], [11], [12] focused on the thermal degradation due to the thermal exposure. According to Woo Chun-Chiao et al. [4] the curing temperature should be higher than 150 °C and lower than 300 °C. The investigation showed that the shell cores possess their optimum strength at 260 °C without burning-out of the cross-linked resin.

In practice, the resin-coated sand is characterized by its physical properties such as grain-size distribution, loss on ignition (LOI), and cold and hot tensile strength [1]. Measuring of these properties cannot provide sufficient information about how does the chemically bonded sand core reacts when it is interacting with the high-temperature molten metal. At the core/metal interface a complex thermomechanical phenomenon takes place. When the liquid metal is poured into the mould, it contacts the sand core. As a result of the rising temperature, complex unfavorable reactions can be observed: polymorphous changes in the refractory sand, thermoplasticity, thermal deformation and degradation in the binder system. This phenomenon significantly affect the final casting shape, dimensional accuracy, and surface quality. In some cases, it may cause deformation, veining defects and early collapsing of the core. To prevent these defects it is important to apply proper core components, and proper technological parameters in the core making process [13].

To research the thermal behaviour of the chemically bonded sand cores, different methods are used. The first measuring device for the investigation of hot-distortion properties of sand cores was developed in 1966 by the British Cast Iron Research Association (BCIRA). In this case, a 115 mm × 25 mm × 6 mm sized specimen is heated from the bottom by a gas burner. The basics of the methodology of the BCIRA test device were presented in publication [14]. This device was further developed by the Simpson Gerosa Company. In the case of Hot Distortion Tester [15], the specimen is heated with a gas burner that is controlled with a gas flowmeter. The distortion of the specimen is measured with a displacement sensor of 0.01 mm accuracy. The loading force is constant, 0.3 N by the displacement sensor. The results of the investigation can be used to identify the thermal expansion, hot brittleness, burn-out rate and hot-strength of the chemically bonded sand core. The polish DMA apparatus [16] is another device that uses the principles of the BCIRA equipment. The rectangular cross-sectioned specimen is also heated from the bottom, however, in this case with a halogen radiator. The device has a complex automatic measurement system

such as a microprocessor-based system for the programming of the heating parameters, an automated drive for specimen movement with auto-positioning-, and a super-precise sensor. The temperature of the specimen can be measured through a pyrometer and an infrared thermal camera. The LRu-DMA apparatus [13] is a further developed device. In this case, two special heaters provide the thermal load for the specimen from the bottom and the top. A new way of measuring the thermal behaviour of sand cores was developed at Western Michigan University. The Thermal Distortion Tester [17] is used to measure the deformation of a sample of sand of 50 mm diameter and 8 mm thickness. With this apparatus, precise thermal loading can be set. The specimen loading is between 3.5–5 N. The longitudinal and the radial distortion of the sample can be measured.

Several research work [7], [17], [18], with most of the above-mentioned measuring devices were published in the last decades. Unfortunately, only a few publications are available about the Hot-Distortion Tester (developed by Simpson Gerosa company). In reference [15], Scott McIntyre and Scott M. Strobl presented the equipment through the describing of the thermal behaviour of resin-coated sand. The specimen is heated from the bottom and the distortion of the specimen is measured over time. The resulting hot-distortion curve based on the investigation can be seen in *Figure 2*.

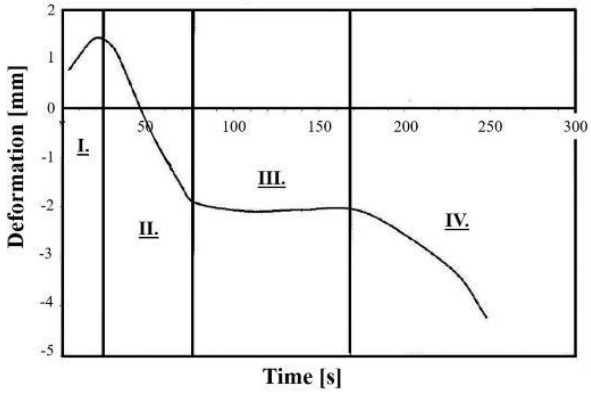

Figure 2
Hot-distortion curve of the resin-coated sand

The hot-distortion curve of the resin-coated sand can be divided into four-sections: upward deflection, thermoplastic relaxation, thermosetting, and thermal degradation – failure.

The specimen is exposed to the heat generated by the gas burner. Because of the uprising temperature of the sample, the sand begins to expand. In the case of quartz sand, polymorphous structural changes can be observed. Due to one-sided heating, thermal difference is developed in the specimen. The rate of heat expansion of the sand is greater at the heated side of the specimen than at the opposite side. This leads to the upward deflection of the sample that is recorded as positive deformation value. According to the literature [15] this stage is strongly determined by the type, shape,

size and bulk density of the sand. Higher positive deformation of the sand cores may lead to the dimensional inaccuracy of the casting.

Further thermal exposure leads to structural changes in the binder system. The resin bridges between the sand grains begin to soften, and the residual hexamethylene-tetramine decomposes to formaldehyde and ammonia. The viscosity of the resin drops, and the end of the specimen moves downward which is recorded as negative deformation values. If the core shows high plasticity it may result in the deflection of the core. In this case, the dimensions of the produced casting are outside of the required dimensional tolerances. On the other hand, low plasticity may result in hot tearing and veining defects.

The released formaldehyde reacts with the phenolic resin and further cross-linking takes place. This mechanism determines the thermosetting stage.

After continuous heat loading, the binder burns-out, which results the mechanical failure of the specimen. The length of time from initial heating to the mechanical failure of the specimen describes the hot strength of the resin binder. In case of low hot strength, early core breakage can occur during the casting process. On the other hand, high hot strength may result in poor shake-out characteristics of the core [15].

Investigation of the thermal behaviour of resin-coated sands with the Hot-Distortion Tester results in a better understanding of the effect of various components on the shell core characteristics. This may lead to more efficient production of quality castings.

1. MATERIALS AND METHODS

As it was mentioned above, the curing time and curing temperature strongly influence the properties of the resin-coated sand. Because of that, this paper aims to investigate the effect of these technological parameters on the thermal behaviour of resin coated sand using the Hot-Distortion Tester. Based on the hot-distortion curves, the authors focus on the analysis of the maximum deformation and degradation time of the samples.

The experiment was conducted at the sand laboratory of the Foundry Institute, Faculty of Materials Science and Engineering, University of Miskolc. In the course of our research work, the resin-coated sand used for making the hot-distortion samples was the PLASTSIL precoated sand. The applied curing time and curing temperature values are presented in *Table 1*.

Table 1

The applied technological parameters

Resin coated sand: PLASTSIL				
Curing time [s]	**Curing temperature [°C]**			
	240	**260**	**280**	**300**
15	Recording of hot-distortion curves Determination of max. deformation [mm] and degradation time [s]			
30				
60				
90				

The experimental process of this study (see *Figure 3*) can be divided into two parts. First, the physical properties of the resin-coated sand were investigated which include the determination of the moisture content, loss on ignition, grain size distribution and specific surface of the pre-coated resin sand. The second part of the investigation consisted of the preparation of the hot-distortion samples and the hot-distortion test.

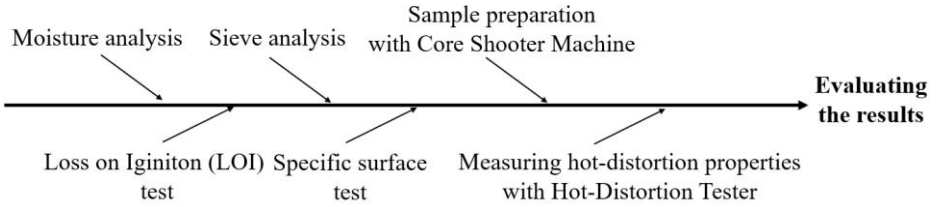

Figure 3
The steps of the experimental process

In the case of resin-coated sand, the moisture content is generally not a problem, because it evaporates during the hot coating process when the sand is heated to about 120–150 °C. If the moisture content is high, it slows down the curing rate of the binder system, which leads to the deterioration of core strength [1]. In this study, the resin-coated sand was dried at 120 °C in a Kern DBS-60 moisture analyzer. The drying process was finished when further weight changes could not be observed.

The loss on ignition (LOI) is a property that represents the resin content and the amount of different volatile organic compounds in the sand mixture. The LOI test of the pre-coated sand gives an approximation of the percentage of the resin content [1]. During the test, 2 grams of the dried sample was weighed into a ceramic crucible. The weight of the samples and the crucibles were measured with an OHAUS Adventurer-Pro analytical scale which has an accuracy of 0.0001 g. Three consecutive measurements were performed during the investigation. The three pieces of the crucible were heated up to 900 °C in an electric furnace. The holding time was 20 minutes. Then the samples were removed from the furnace and let to cool down to measure its weight. The process was repeated until the weight changes were not higher than 0.001 g. From the initial and residual weight, the percentage of the LOI was calculated.

In the research work, the determination of the granulometric properties of the resin-coated sand included the examination of the grain size distribution and the specific surface of the shell sand.

The grain size distribution and the specific surface strongly influence the strength properties and gas permeability of the sand core. According to the literature, it is necessary to remove the resin film from the sand grains before investigating these properties. Because of that, the PLASTSIL resin-coated sand sample was held at 900 °C for 1 hour. Then the grain size distribution of the uncoated sand grains was measured with a Fritch Analysette 3 Pro sieve shaker. The device has 7 pieces of meshes with aperture sizes of 0.063–, 0.1–, 0.2–, 0.315–, 0.6–, and 1.0 mm. The

sample weight was 50 g. The amplitude of the sieving was 2 mm and the sieving time was 15 minutes. After the sieving process, the retained sand on each mesh was weighted and from the results, the grain size distribution and the average grain-size were calculated. The average of two consecutive measurements was used for the evaluation.

To measure the actual specific surface of the uncoated sand (surface area per unit weight of the material), a DISA POF type sand specific surface testing apparatus was used. The investigation is based on the Blaine method. During the examination, 50 grams of sludge-free sand is placed in the burette of the equipment, and the volume of the sand is noted. Based on the time required for a fixed volume of air to pass through the sand sample, the actual specific surface can be evaluated by using the graph given by the producer of the equipment. The specific surface of the sand is derived from the average of three consecutive measurements. The coefficient of angularity describes the angularity of sand grains, which is the deviation from the spherical shape. It can be calculated as the quotient of the measured and the theoretical specific surface.

To investigate the deformation behaviour of the resin-coated sand, hot distortion tests were performed. With using a core blowing equipment, rectangular cross-sectioned specimens having dimensions of 114.3 mm × 25.4 mm × 6.35 mm were produced. During the process in each case, 5 pieces of samples were investigated with combinations of different curing time and curing temperature (see *Table 1*). The blowing pressure was 6 bar. The hot-distortion tests were conducted with a Hot-Distortion Tester. One end of the specimen is fixed, while on the other end of it a displacement sensor is placed. The sand specimen was heated from the bottom using the gas burner controlled by a gas flowmeter. The ratio of natural gas and the air was 50 : 30. When the specimen is exposed to heat, deformation can be observed that is recorded with the displacement sensor in time. The result of the investigation is presented in hot-distortion curves (see *Figure 2*). In *Figure 4* the core blowing machine and the Hot-Distortion Tester are shown.

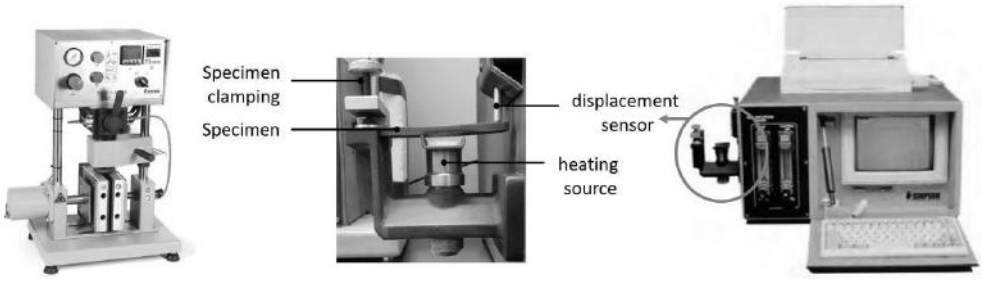

Figure 4
The Core blowing machine (left), and the Hot-Distortion Tester (right)

2. RESULT AND DISCUSSION

The results of the preliminary tests of the resin-coated sand are summarized in *Figure 5*. The bar graph shows the retained sand in the function of the different sizes of

the meshes. It can be established that the investigated sand grains mostly fall into three size regions: 0.1–0.2 mm, 0.2–0.315 mm and 0.315–0.6 mm. The average grain size was 0.23 mm. The sand has a high specific surface with a value of 205 cm^2/g. The high specific surface value of the sand can be attributed to the small grain size, the grooved surface quality and the angular morphology of the sand. This latter statement is confirmed by the calculation of the angularity coefficient, which has a value of 1.86.

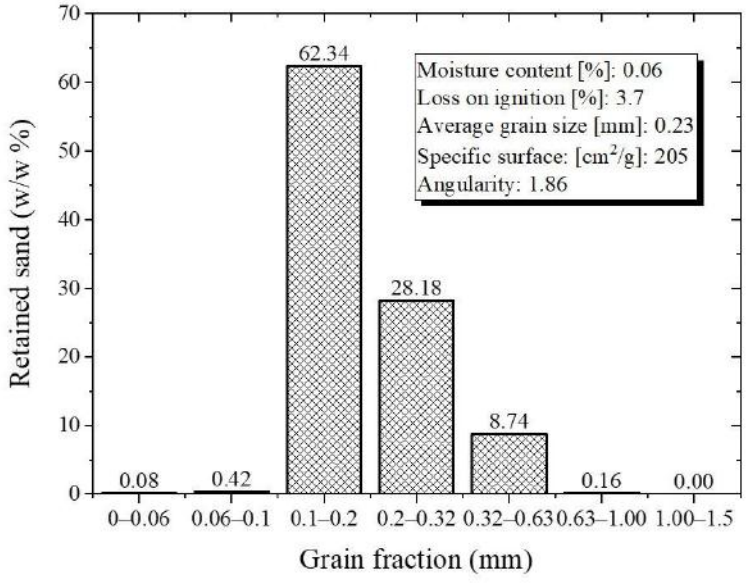

Figure 5

The grain-size distribution and the other physical properties of the resin-coated

It appears that the resin-coated sand has a low moisture content having a value of 0.06%. This means that the moisture will not adversely affect the curing of the resin. According to the loss on ignition test, the resin content of the PLASTSIL resin-coated sand is 3.4%. This high amount of resin content is typically used for shell mold and shell core during the cast irons and steel casting production.

During the experiments, 80 pieces of rectangular cross-sectioned samples were produced with a combination of different curing times and curing temperatures. Observation of the samples produced with different technological parameters is shown in *Figure 6*. It can be seen that the color of the produced samples changes from yellow to dark brown. According to the earlier literature, this color-changing gives information about the extent of curing. Unfortunately, several parameters affect the color of the resin-coated sand core during the manufacturing process. The color variation of the precoated sand is strongly influenced by the raw sand and its impurities,

the quantity of additives, etc. To determine the optimum curing conditions, it is advisable to investigate the strength and thermomechanical properties of the resin-coated sand.

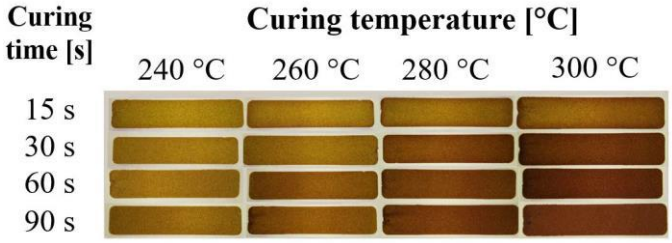

Figure 6
Resin-coated sand samples produced with different curing time and curing temperature

During the hot-distortion test, five pieces of samples were produced with a given curing temperature and curing time. From the recorded hot-distortion curves the max. deformation and degradation time were determined and average values were calculated. In *Figure 7*, those curves are presented that are closest to these average max. deformation and degradation times.

As can be seen, the hot-distortion curves show a similar tendency to the diagram published by Scott McIntyre and Scott M. Strobl [15]. The hot-distortion curves include the upward deflection/deformation, the thermoplastic relaxation, the thermosetting, and the thermal degradation – failure stages.

Analyzing the data, it can be established that the investigated technological parameters, the curing temperature and curing time have a significant impact on the thermomechanical properties of the resin-coated sand cores. Samples prepared with higher curing temperatures and longer curing times show higher deformation at the beginning stage of the heat exposure. The authors assume that this phenomenon may be explained with the curing mechanism of the novolac binder. The extent of cross-linking is lower in the case of samples produced with lower curing temperature and shorter curing time (see *Figures 7a* and *7b*). A large proportion of the resin could be in the B-resitol stage. This is the reason, why these samples exhibited larger thermoplastic deformation that is typical for thermoplastic polymers. This phenomenon is especially apparent in the case of samples produced with 240 °C and 260 °C cure temperatures. During exposure to heat, the allotropic transformation of the sand grains leads to volume expansion. If a larger proportion of the resin is in B-resitol state, then the expansion of sand grains is less impeded because the resin bridges between the grains can be deformed, contracted. When higher curing temperature and longer curing time have been applied, the extent of curing of the binder is greater. In this case, the proportion of the C-resit can be higher. The rigid binder bridges block the free expansion of the sand grains. In the outer layer of the hot-distortion samples, the effect of the volume expansion is greater, which results in greater upward deflection.

Based on the hot-distortion curves in *Figures 7c* and *7d*, it can be established, that higher curing temperature and longer curing time lead to a higher extent of the cross-linking of the binder. This results in smaller plasticity and thermosetting stage of the resin-coated sand samples. In the case of the PLASTSIL resin-coated sand, this effect can be strongly observed when the curing temperature is higher than 260 °C.

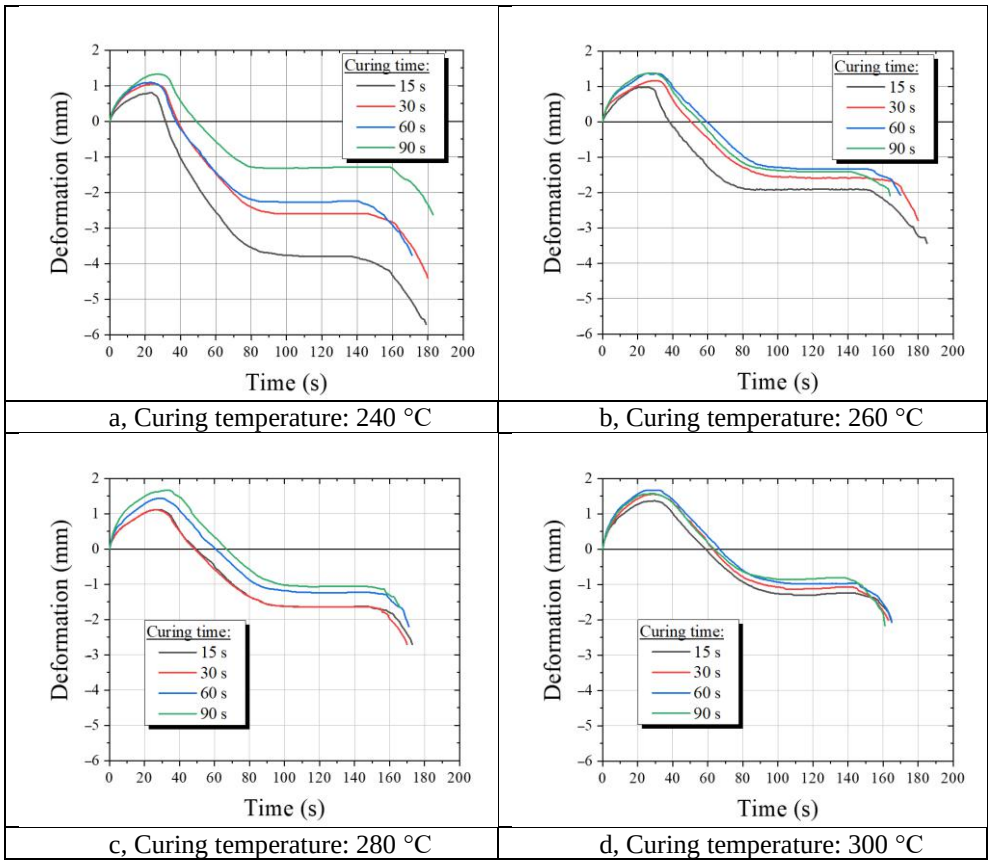

a, Curing temperature: 240 °C | b, Curing temperature: 260 °C

c, Curing temperature: 280 °C | d, Curing temperature: 300 °C

Figure 7
Results of the hot-distortion test

The curing time and curing temperature affect the thermal strength of the resin-coated sand samples as well. The rectangular cross-sectioned samples produced with higher curing temperature and longer curing time show shorter degradation time and smaller thermal strength. This results in the improved shakeout properties of the sand cores. The influence of the curing time on the degradation time of the resin-coated sand samples is stronger at curing temperatures higher than 260°C (see *Figures 7c–d*).

The maximum deformation and degradation time of the samples are summarized in *Figure 8*.

Summarizing the results of the research, it can be concluded that the curing temperature and curing time strongly influence the hot-distortion properties of resin coated sand cores. In the shell core making process it is recommended to set these two technological parameters with taking into consideration the requirements of the castings. If achieving high dimensional accuracy is the main goal, then it is advisable to use low curing temperature with short curing time. To improve the shake-out properties of the cores, higher curing temperatures need to be applied.

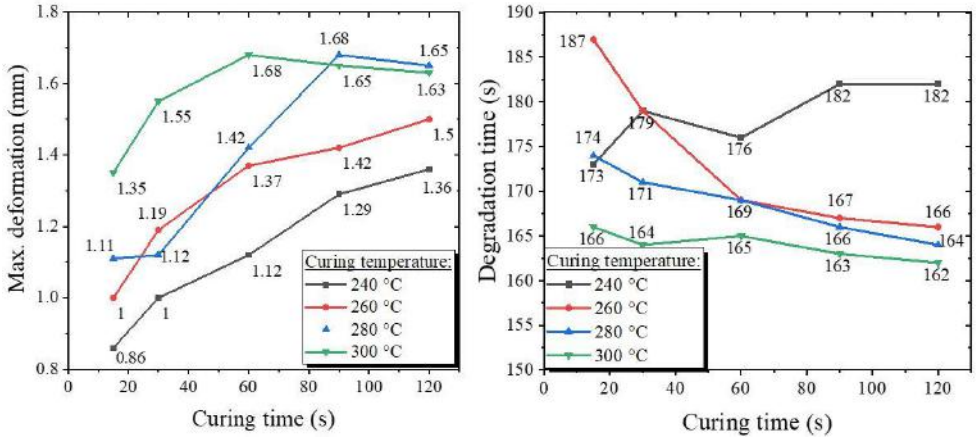

Figure 8
The effect of the curing time and curing temperature on the max deformation and degradation time

In the case of the investigated PLASTSIL resin-coated sand, the optimum conditions to produce sand cores would be 240 °C curing temperature and longer curing time to withstand the high thermal load of the molten alloy during the production of cast iron castings.

ACKNOWLEDGEMENT

The described article was carried out as part of the EFOP-3.6.1-16-2016-00011 *Younger and Renewing University – Innovative Knowledge City – institutional development of the University of Miskolc aiming at intelligent specialisation* project implemented in the framework of the Szechenyi 2020 program. The realization of this project is supported by the European Union, co-financed by the European Social Fund.

REFERENCES

[1] McIntyre, Scott (2008). Shell Molding and Shell Coremaking. In: *ASM Handbook Volume 15: Casting*. Editing ASM Handbook Committee, Materials Park, Ohio, pp. 598–616.

[2] Kerns, K. J., Thiel, J. (2009). Reinventing Shell Technology: Making Good „Scents" of an Ageless Process. *Trans. American Foundry Society,* Schaumburg, IL USA, Vol. 117, pp. 313–321., April 7–10.

[3] Recknagel, Ulrich (2011). Das Maskenformverfahren: Eine deutsche Innovation zur Gussherstellung seit 60 Jahren. *Giesserei Praxis*, Nr. 6, pp. 279–295.

[4] Chun-Chiao, Woo, Jie, Hu (1988). A Study of Phenolic Novolak Resin Chemistry in Relation to the Hot Method of Coating Shell Sand. *International Journal of Cast Metals Research*, Volume 1, Issue 3, pp. 171–175.

[5] Naiyu, H. et. al. (1993). Defects in Phenolformaldehyde Precoated Sand Cores and Molds. *Trans. American Foundry Society*, Schamburg, IL USA, Vol. 101, pp. 725–732.

[6] Eckart. F., Tilsch, W. (1993). Verfestigung (Härtung) der Formteile. In: *Formstoffe und Formverfahren.* Leipzig–Stuttgart, pp. 356–357.

[7] Gnanamurthy, S., Ramrattan, S., Gromala, B. (2017). Using Thermal Distortion Curves to Identify Cracking in Resin Coated Shell Cores for Aluminum Castings. *Trans. American Foundry Society*, Schaumburg, IL USA, Vol. 125, pp. 343–349., April 22–25.

[8] Shi, Yan, Wang, Li-feng (2016). Curing reaction and mechanism of phenol-formaldehyde novolac resins for foundry. *China Foundry*, May, Volume 13, No. 3, pp. 205–210.

[9] Shi, Yan, Wang, Li-feng (2004). Study on preparation of fast curing novolaks for the shell process. *China Foundry*, November, Volume 1, No. 2, pp. 106–111.

[10] Chiantore, O., Lazzari, M., Fontana, M. (1995). Thermal Decomposition of Phenol-Formaldehyde Foundry Resins. *International Journal of Polymer Analysis and Characterization*, Volume 1, Issue 2, pp. 119–130, published online 24 September 2006.

[11] Dungan, Robert S., Reeves, James B. III (2005). Pyrolysis of Foundry Sand Resins: A Determination of Organic Products by Mass Spectrometry. *Journal of Environmental Science and Health*, Part A: Toxic/Hazardous Substances and Environmental Engineering, Volume 40, Issue 8, pp. 1557–1567, published online 20 August 2010.

[12] Lytle, C. A., Bertsch, W., McKinley, M. (1998). Determination of novolac resin thermal decomposition products by pyrolysis-gas chromatography-mass spectrometry. *Journal of Analytical and Applied Pyrolysis*, Volume 45, pp. 121–131.

[13] Ignaszak, Z. (2018). Discussion on the Methodology and Apparatus for Hot Distortion Studies. *Archives of Foundry Engineering*, Volume 18, Issue 2, pp. 141–145.

[14] Morgan, A. D., Fasham, E. W. (1975). The BCIRA Hot Distortion Tester for Quality Control in Production of Chemically Bonded Sands. *Trans. American Foundry Society*, Schaumburg, IL USA, Volume 91, pp. 73–80.

[15] McIntyre, Scott, Strobl, Scott M. (1998). Adapting Hot Distortion Curves to Process Control. *Foundry Management & Technology, Sand Testing*, March, pp. 22–26.

[16] Jakubski, J., Dobosz, S. M. (2007). The thermal deformation of core and moulding sands according to the hot-distortion parameters investigations. *Achives of Metallurgy and Materials*, June, Volume 52, Issue 3, pp. 421–427.

[17] Oman, A. J., Ramrattan, S. N., Keil, M. J. (2013). Next Generation Thermal Distortion Tester. *Trans. American Foundry Society*, Schaumburg, IL USA, Volume 121, pp. 323–329., 6–9 April 2013.

[18] Dobosz, St. M., Grabarczyk, A., Major-Gabryś, K., Jakubski, J. (2015). Influence of Quartz Sand Quality on Bending Strength and Thermal Deformation of Moulding Sands with synthetic Binders. *Achives of Foundry Engineering*, Volume 15, Issue 2, pp. 9–12.

Materials Science and Engineering, Volume 45, No. 1 (2020), pp. 50–62.
DOI: 10.32974.mse.2020.005

EFFECT OF TIN ADDITION ON THE PROPERTIES OF ELECTROLESS NI-P COATINGS

MÁTÉ CZAGÁNY[1] – PÉTER BAUMLI[2]

Abstract: One of the advantageous properties of electroless Ni-P coatings is the good solderability, which is utilized in the electronic industry. However, the applied high-temperature required by the soldering process might lead to undesired transformation of the coating structure. Thus, the investigation of the thermal stability of the coating has become more and more important among scientists, as by adding a new, 3rd element to the coating, the stability of the coating's structure can be increased. In our research, the required conditions for the 3rd element were determined based on the hypothesis of kinetic stabilization, and tin (Sn) was found an appropriate alloying element. By adding $SnCl_2$ precursor salt to the bath, the main properties of the coating were investigated, such as chemical composition, thickness and appearance. Based on the experiments, 0.3 g/L $SnCl_2$ was determined as the optimal concentration with the applied bath composition. Subsequently, the thermal behaviour of the formed Ni-P-Sn coating was investigated by Differential scanning calorimetry (DSC) and X-ray diffraction analysis (XRD).

Keywords: Ni-P-Sn, electroless deposition, Ni-P coating, thermal stability

INTRODUCTION

The electroless Ni-P coatings, in addition to their outstanding mechanical properties (high hardness and wearability) and corrosion-resistance are preferred to be use in the fields of electronic industry as well, in order to facilitate the soldering process and improve the quality of the joint [1–2]. It is well-known, that these coatings are formed with a non-equlibrium phase-structure (nanocrystalline, amorphous) during the deposition, being thermodynamically unstable as a consequence. This means that at a sufficiently high temperature they endeavour to reach an equilibrium state. In the case of the two-component Ni-P coatings, this means the formation of crystalline Ni phase (fcc) and Ni_xP_y compounds (typically Ni_3P at T > 400 °C) accompanied with the coarsening of the grains [3]. These transformations might result in difficulties for high-temperature applications, as the mentioned properties are highly dependent on the thermal stability of the coatings, and might lead to the degradation of

[1] Institute of Physical Metallurgy, Metalforming and Nanotechnology, University of Miskolc, H-3515 Miskolc-Egyetemváros
femmatt@uni-miskolc.hu
[2] Institute of Physical Metallurgy, Metalforming and Nanotechnology, University of Miskolc, H-3515 Miskolc-Egyetemváros
baumlipeter@gmail.com

the formed joint [4]. The experimental findings show that the transformation temperature (i.e. thermal stability) of the non-equilibrium nano- or amorphous structure of the coatings can be increased by co-deposition of a 3rd element.

Studies of Ni-P coatings showed that the composition of the coatings (i.e. the P-content), and heat treatment conditions have an influence on the structural transformation of the coatings. Depending on the P-content, the coatings can be divided into 3 classes [5]: low- (1–5 wt.%), medium- (6–9 wt.%) and high-P (>10 wt.%) coatings. Similarly, the microstructure of the coatings varies depending on the P-content: from a P-supersaturated nanocrystalline solid solution (low-P content), through a mixture of nanocrystalline and amorphous phases (medium-P content) to a completely amorphous (high-P content) structure [6].

Hentschel et al. [7] studied the low-P coatings at atomic scales and found that P is segregated to the interface of the nanocrystallites (11 at.%) or to a lesser extent, forming a supersaturated solid solution inside the crystallite (1 at.%), which coincides with the findings of M. Czagany et al. [8–9]. In their view, as the P-content increases, the volume ratio of the interface of the crystallites increases to the detriment of the crystallite phases until the coating becomes completely amorphous. This observation was also confirmed by Farber et al. [10], observing the segregation of P at the interface of crystallites by 3D imaging, and measuring a 0.8 nm thick interface layer.

It is agreed, that the transformation temperature (i.e. thermal stability) of the coatings decreases with increasing P-content *(Table 1)*. In addition, coatings with lower P-content have a higher transformation activation energy than those with high P-content [5].

Table 1

Transformation temperature of electroless Ni-P coatings with different P-content

Type of the coating	**Transformation temperature**
Low-P (3–5 wt.%)	400–410 °C [7]
Medium-P (5–8 wt.%)	350 °C [11]
High-P (12 wt.%)	346 °C [5]
High-P (16 wt.%)	325 °C [5]

Similarly, several different studies report that the temperature of the formation of Ni_xP_y compounds can be increased by co-deposition of one (or more) new elements, i.e. by forming 3-or 4-component coatings, thereby maintaining the non-equilibrium structure of the coatings up to higher temperatures. The commonly used alloys and the obtained transformation temperatures are listed in *Table 2.*

Table 2

Transformation temperature of different 3-component Ni-P-Me coatings

Alloying element	**Coating composition (wt.%)**	**Transformation temperature, and heating rate**	**Formed compounds**
Cu	Ni-12,4P [12] Ni-1,7Cu-12,2 P [4] Ni-4,3Cu-12,3P [12]	341.9 °C (20 °C/min) 371 °C 363.7 °C (20 °C/min)	Ni_3P
W	Ni-8,4 P [15] Ni-10,9W-7,6P [13] Ni-4W-2P [14]	348 °C (10 °C/min) 406 °C (10 °C/min) 493 °C (40 °C/min)	Ni_3P, Ni_5P_2, NiP
Re	Ni-8,8P [6] Ni-6,8Re-8,2P [6] Ni-9P [15] Ni-7P-8Re [15]	339–362 °C (5–25 °C/min) 379–405 °C (5–25 °C/min) 382 °C (25 °C/min) 405 °C (25 °C/min)	Ni_3P, NiP, Ni_5P_2, $Ni_{0.21}$-$Re_{0.79}$

According to the literature, the thermal stability of Ni-P coatings can be increased by the 3rd element in the following ways: (a) by forming a solid solution with the matrix and inhibiting the diffusion of P atoms (delaying Ni_3P compound formation), or (b) forming compounds in the matrix, thus inhibiting the diffusion of P in the matrix and hindering the grain coarsening.

There is no reference to the segregation of the alloying element to the interface of nanocrystallites, but the interfacial segregation of P and the stabilizing effect provided by its segregation is known [7].

During our research, we aimed to delay the formation of Ni_3P compound in Ni-P coatings by adding a 3rd element (kinetic stabilization). This element had to meet the following 3 conditions:

1. It should not dissolve in Ni, or only to a small extent.
2. Preferably should not form a phosphide compound (if it does, the stability of the compound should be less than that of Ni_xP_y compounds).
3. The surface tension of the melt of the 3rd element should be less than the melt of Ni.

If these conditions are met, the 3rd element segregates to the interface of the crystallites, and expected to have a hindering effect on the nuclei formation of Ni_3P and crystalline Ni phases, achieved by the reduction of the diffusion coefficient of Ni and P atoms. Among the elements that can be deposited by electroless method [16], Sn was chosen as the alloying element. The approach of stabilizing the Ni-P coating based on these aspects is considered to be novel.

1. PRELIMINARY DESIGN AND EXPERIMENTAL

1.1. Conditions of using Sn as an alloying element

Sn can form 3 compounds with phosphorous [17]: Sn_4P_3, Sn_3P_4 and SnP_3, so it is necessary to compare the thermal stability of these compounds with Ni_xP_y compounds, using the free enthalpy values which are summarized in *Table 3*. For comparability, it is necessary to give these values in kJ/mol atom. Considering that our aim is to produce coatings with low and/or medium P-content, the concentration of P is rather low compared to Ni, so the required unit is kJ/mol-P atom. Based on the converted values, Ni_3P compound is the most stable of the studied phosphides, in agreement with literature [18].

For Sn_xP_y compounds, the assumed amount of Sn and P atoms is significantly smaller compared to Ni atoms, thus the free enthalpy of formation related to the total number of atoms is authoritative. As these values are lower than the corresponding values of Ni_xP_y compounds, the formation of these compounds is not expected. In the case of the 2-component Ni-Sn system [17], three Ni_xSn_y compounds are known also: Ni_3Sn, Ni_3Sn_2, Ni_3Sn_4. Although Ni dissolves in Sn, only to a small amount in the relevant temperature range of 300–450 °C. As for the Gibbs-energy of formation of Sn_xNi_y compounds, it is adequate to refer to the Gibbs-energies per the amount of Sn atoms *(Table 5)*. These values are also lower than of the Ni_xP_y compounds, so the formation of these compounds is not expected either. The surface tension of Sn melt is $\sigma_{lg} = 561 \frac{mN}{m}$, while for Ni is σ_{lg}: 1770–1800 $\frac{mN}{m}$ [21–22], assuming that Sn is expected to segregate to the interface of nickel crystallites. Thus, it can be concluded that Sn satisfies all three conditions for increasing the stability of the Ni-P coating.

Table 3

Gibbs-energies of formation of Ni_xP_y, Sn_xP_y and Sn_xNi_y compounds [19, 20]

Compound	Gibbs-energy of formation (ΔG_f)			
	at 298.15 K		at 900 K	
	[kJ/mol]	[kJ/mol atom]*	[kJ/mol]	[kJ/mol atom]*
Ni_3P	–212.380	–212.380	–188.058	–188.058
Ni_2P	–177.115	–177.115	–155.295	–155.295
Ni_5P_2	–421.249	–210.624	–375.617	–187.808
Sn_4P_3	–106.66	–15.237	14.13	2.019
Sn_3P_4	–143.37	–20.481	40.37	5.767
SnP_3	–87.59	–21.898	4.07	1.018
Ni_3Sn	–90.887	–90.887	–75.510	–75.510
Ni_3Sn_2	–151.421	–75.711	–117.236	–58.618

*for Ni_xP_y and Ni_xSn_y compounds the unit is kJ/mol-P and kJ/mol-Sn atom respectively

1.2. Deposition of Ni-P and Ni-P-Sn coatings

Ni-P and Ni-P-Sn coatings were deposited on pure Cu (dimension of 9 × 6 × 2 mm) and C45 steel (dimension of 10 × 7 × 3 mm) plates. In order to get a good adhesion between the substrates and the coating, the surface of the substrates was pre-treated by the following methods:

1) Grinding and polishing (down to the grade of 1 μm)
2) 5 min ultrasonic cleaning in acetone
3) Deoxidation by immersion in cc. HCl (35 m/m%) for 30 s
4) Activation in $PdCl_2$ solution

The composition and mean parameters of electroless baths are listed in *Table 4*. The Ni source was $NiSO_4 \cdot 6H_2O$, while $SnCl_2 \cdot 2H_2O$ served as Sn precursor. The effect of the Sn precursor was studied at different concentrations: 0.05–7.5 g/L, while the values of the other bath components remained unchanged. Na-acetate served as a complexing agent, thiourea acted as a stabilizer and the applied reducing agent was Na-hypophosphite.

Table 4

Composition and parameters of electroless Ni-P and Ni-P-Sn baths

Bath constituent, parameter	Concentration, values
Nickel sulphate (using $NiSO_4 \cdot 6H_2O$)	15 g/L
Sn(II)-chloride (using $SnCl_2 \cdot 2H_2O$)	0.05–7.5 g/L
Sodium acetate (using $CH_3COONa \cdot 3H_2O$)	13 g/L
Sodium hypophosphite (using $NaH_2PO_2 \cdot H_2O$)	14 g/L
Thiourea (CH_4N_2S)	1 mg/L
pH	6
Temperature, time	80 °C, 60 min
Bath volume	50 ml

1.3. Characterization methods

Surface morphology and cross-section of the coatings was analyzed by Scanning Electron Microscopy (HITACHI S-4800, Japan). The thermal behaviour of Ni-P and Ni-P-Sn coatings was studied by Differential Scanning Calorimetry (Netzsch STA 449 F1 Jupiter Simultaneous TG-DTA/DSC). The measurement was carried out in vacuum (10^{-4} mbar) to avoid any oxidation process with a heating rate of 10 °C/min to 600 °C. The phase structure of the coatings was investigated by Bruker D8 Discovery X-ray diffractometer, using Cu K-alpha radiation, 40 kV and 40 mA generator settings with a 10 min measurement time. Measurements were performed on previously heat-treated samples (at 400 °C) in an LT-S/1200 type furnace, using

Ar as shielding gas. The XRD measurement was carried out in the 3DLab Fine Structure Analysis Laboratory of the University of Miskolc.

2. RESULTS AND DISCUSSION

2.1. Microstructure and morphology of Ni-P and Ni-P-Sn coatings

The surface morphology of 2-component Ni-P coating is shown in *Figure 1*. The coating presents a semi-spherical, cauliflower-like structure on both the steel *(Figure1a)* and Cu substrate *(Figure 1b)*, in accordance with literature [18]. The thickness of the coatings is somewhat different, 19.8 μm on the surface of the steel while 15.8 μm on the Cu substrate. The P-content of the coatings, however is very similar, 3.67 wt.% on steel and 3.17 wt.% on copper, representing the group of low P content.

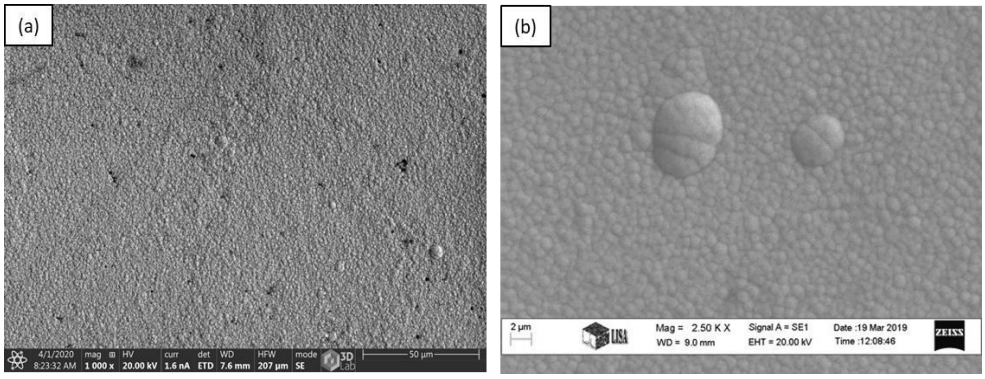

Figure 1
Surface morphology of electroless Ni-P coating, deposited on (a) C45 steel substrate, (b) pure Cu substrate

To study the effect of Sn alloying, baths with different $SnCl_2$ concentration were used. The chemical composition measured in the cross-section of the deposited coatings are listed in *Table 5*. With the use of 0.05 g/L $SnCl_2$ salt, no coating was formed, however by increasing its concentration, 3-component Ni-P-Sn coatings were successfully created. The concentration of Sn represents a persistent increase with the concentration of $SnCl_2$, but reaching concentrations of 3 and 7.5 g/L, almost pure and pure Sn coatings were formed respectively. In contrast, the P-content showed an inverse behaviour to the Sn concentration, the amount measured in the coating decreased constantly.

The thickness values of the coatings as a function of the $SnCl_2$ concentration are shown in *Figure 2*. The addition of 3 g/L $SnCl_2$ resulted in a 4 μm thick coating, which is approx. a quarter of the Sn-free Ni-P coating. However, with the addition of larger amount of Sn salt, the thickness further decreased, remaining below 1 μm.

Table 5
Composition of the coatings obtained on the surface of Cu substrates from baths with different $SnCl_2$ concentration

$SnCl_2$ concentration of the baths (g/L)	**Composition (wt.%)**		
	Ni	**P**	**Sn**
0	96.83	3.17	–
0.05	no coating		
0.3	92.08	2.32	5.60
0.75	87.46	3.67	8.87
1.5	83.75	0.99	15.26
3	0.80	0.58	98.62
7.5	0	0	100

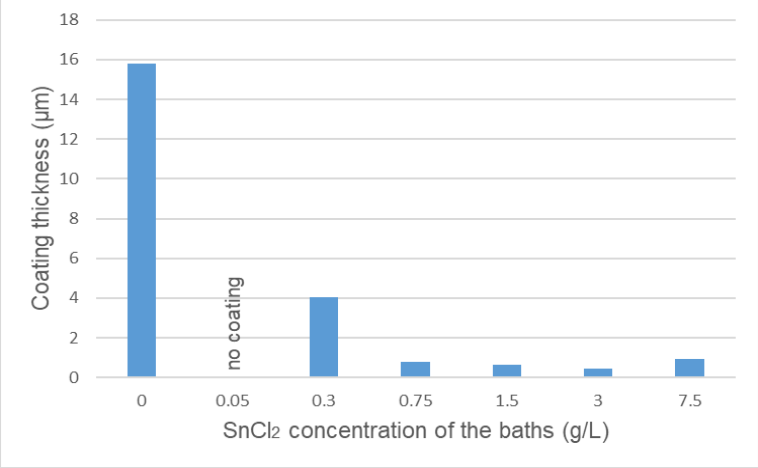

Figure 2
Thickness of the coatings deposited on Cu substrates as a function of $SnCl_2$ concentration

Based on the composition, the coatings obtained from baths with a concentration of 1.5 g/L $SnCl_2$ or less can be considered as Ni-P-Sn coatings. However, in the case of 1.5 g/L Sn salt, various Sn formations grown on the surface of the coating *(Figure 3a)*, thereby preventing its suitability as our goal was to obtain Ni-P coatings alloyed with Sn. At the same time, the thickness of the coating should also be considered. The surface of the thickest coating obtained by using concentration of 0.3 g/L $SnCl_2$ on the surface of Cu and C45 steel is shown in *Figure 3b* and *Figure 3c* respectively. The formed coating has a spot-like appearance on both substrates. The EDS measurements show that several successive layers grown on top of each other, with each spot indicating thinner areas *(Figure 3c)*.

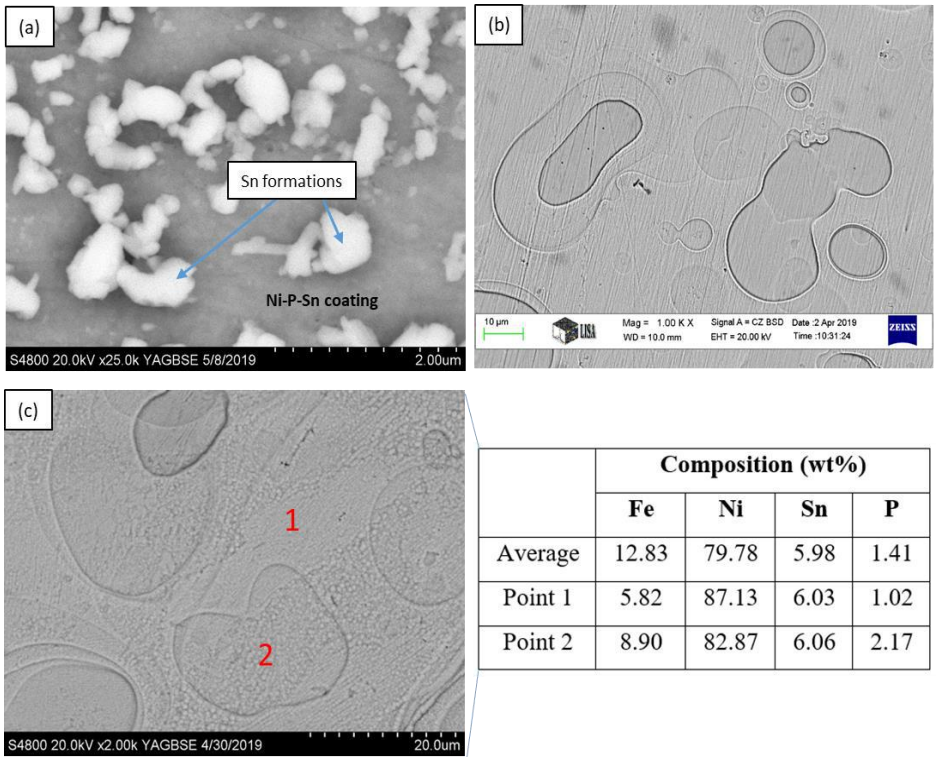

	Composition (wt%)			
	Fe	**Ni**	**Sn**	**P**
Average	12.83	79.78	5.98	1.41
Point 1	5.82	87.13	6.03	1.02
Point 2	8.90	82.87	6.06	2.17

Figure 3
SEM images of the surface of Ni-P-Sn coatings obtained from baths with (a) 1.5 g/L $SnCl_2$ concentration on top of Cu substrate, (b) 0.3 g/L $SnCl_2$ concentration on Cu substrate, (c) 0.3 g/L $SnCl_2$ concentration on C45 steel substrate

2.2. Thermal behaviour of Ni-P and Ni-P-Sn coatings

The thermal behaviour of the successfully produced Ni-P-Sn coatings from baths containing 0.75 g/L (Ni-P-Sn1) and 0.3 g/L (Ni-P-Sn2) $SnCl_2$ precursor salt was studied using DSC measurement. The obtained DSC graphs of the coatings are shown in *Figure 4*. The Ni-P coating indicates the characteristic exothermic peak, starting at 394 °C. According to the literature, this change refers to the transformation of the coating structure, i.e. the appearance of the Ni-phosphide compound(s), and the onset of the coarsening of Ni crystallites [11]. Although the Sn-containing coatings have smaller thickness, no exothermic process is observed in their case. As for the Ni-P-Sn1 coating, a lower intensity endothermic process starts at 398 °C, just like in the case of Ni-P-Sn2 sample, starting at 384 °C. The absence of an exothermic peak suggests that no Ni-phosphide compounds formed in the presence of Sn.

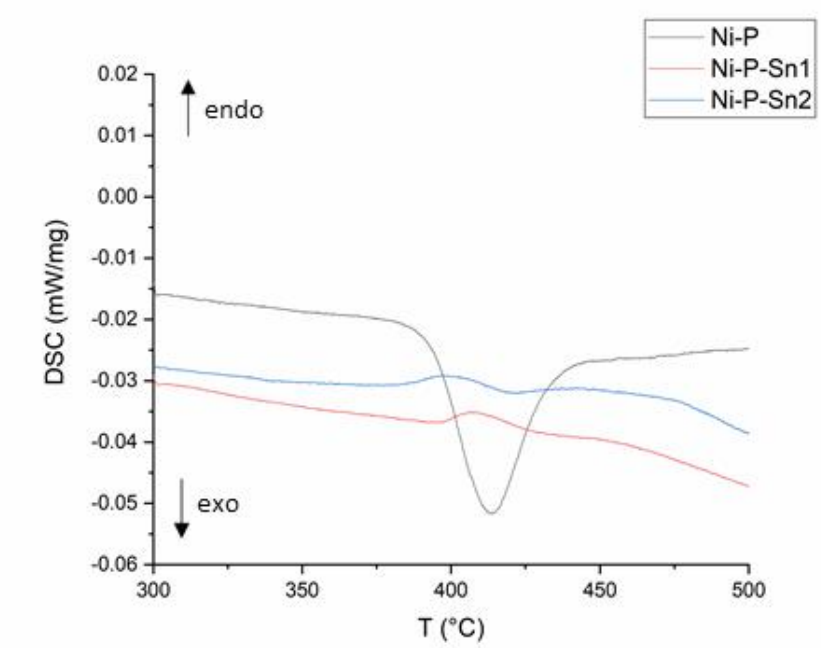

Figure 4
DSC graphs of Ni-P and Ni-P-Sn coatings deposited on Cu substrate

Figure 5 shows the X-ray diffraction patterns of Ni-P and Ni-P-Sn coatings deposited on Cu substrate and heat-treated at 400 °C. Reflections of Ni_3P compounds are observed in the case of the Ni-P coating. However, in the case of Sn-containing coatings there is no indication of the Ni_3P compounds. The (111) and (001) peaks of Cu for Cu K-beta, W L-alpha1 and W L-alpha2 radiation were detected with very small intensity, due to the high diffracting intensity of Cu substrate. The relevant peaks are marked and have their peak heights of 0.25% (K-beta) and 0.32% (L-alpha lines) relative to Cu (111) peak, in accordance with the monochromatization capability of the Göbel mirror given as >99.3% for Cu K-alpha radiation.

In order to acquire the phase composition of the measured samples, Rietveld refinement was applied with an emission profile containing Cu K-alpha, Cu K-beta and W L-alpha lines, which was defined by using NIST SRM 640d Si standard, thus all peaks and intensities could be assigned correctly to the relevant crystalline phases. The calculated values are shown in *Table 6*. Interestingly, the results show that there is some residual amorphous phase in all of the studied coatings. For the Ni-P coating, the amount of the crystallized Ni_3P is 6.7 wt.%, which is considerably reduced with the addition of Sn to the coatings (3.7 and 2.1 wt.%). Furthermore, the amount of the residual amorphous phase is also supressed, confirming the stabilization effect of Sn addition.

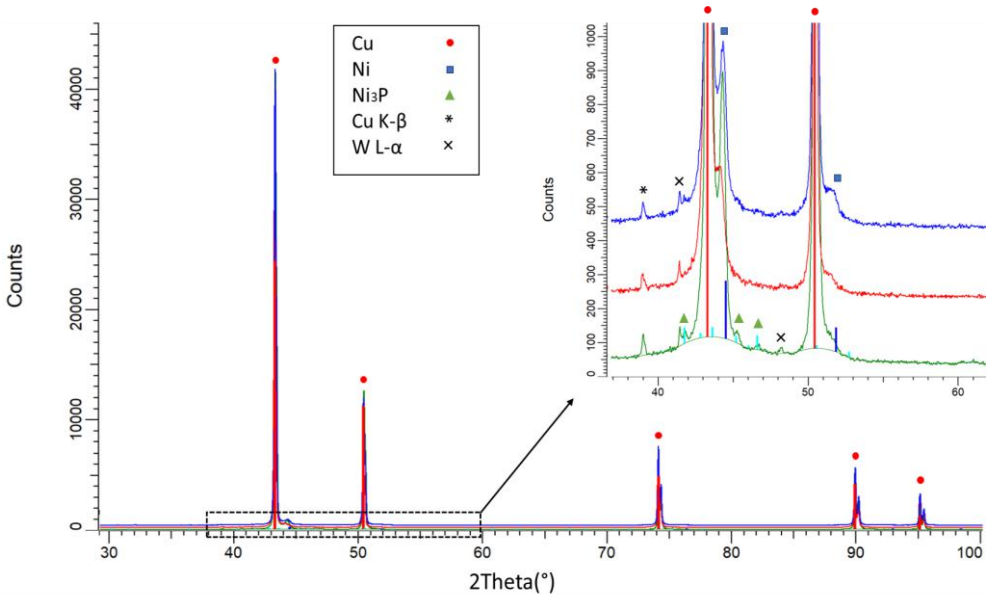

Figure 5
X-ray diffraction patterns of Ni-P and Ni-P-Sn coatings on Cu substrates, heat-treated at 400 °C

Table 6
Phase composition of the Ni-P and Ni-P-Sn coatings measured by XRD, calculated by Rietveld refinement

Phase	Phase composition (wt.%)		
	Ni-P	Ni-P-Sn1	Ni-P-Sn2
Ni	38.4	26.4	36.5
Ni_3P	6.7	3.7	2.1
Amorphous	54.9	69.8	61.4

CONCLUSION

Increasing the thermal stability of electroless Ni-P coatings is an important issue of both the literature and industry. As a first step, 3 base conditions required to stabilize the non-equilibrium structure of the coating were determined. As a result, tin (Sn) was chosen as a promising alloy for stabilization. Subsequently, the effect of the applied $SnCl_2$ precursor salt concentration was studied on the composition, thickness and appearance of the formed coating. Based on the results, the optimal $SnCl_2$ concentration ranged from 0.3 to 1.5 g/L, as no coating was formed at lower concentration, while Sn-based and pure Sn coatings formed with higher concentrations. Based

on the experiments, the Ni-P-Sn coating with appropriate composition and optimal thickness could be determined, which was achieved at a concentration of 0.3 g/L $SnCl_2$.

Subsequent DSC and XRD measurements confirmed that the formation of Ni_3P could be supressed by Sn co-deposition, thus the thermal stability of the coating could be successfully increased. Our future goal however, is to optimize the composition of the bath with regard to the appearance and thickness of the formed coating, as well as a deeper understanding of the processes taking place in the structure of the coating during heat treatment.

ACKNOWLEDGMENTS

The work of Máté Czagány is supported by the ÚNKP-19-3 New National Excellence Program of the Ministry for Innovation and Technology. The described study was carried out as part of the EFOP-3.6.1-16-2016-00011 *Younger and Renewing University – Innovative Knowledge City – institutional development of the University of Miskolc aiming at intelligent specialisation* project implemented in the framework of the Szechenyi 2020 program. The realization of this project is supported by the European Union, co-financed by the European Social Fund.

Our research was carried out as part of the GINOP-2.3.2-15-2016- 00027 *Sustainable operation of the workshop of excellence for the research and development of crystalline and amorphous nanostructured materials* project implemented in the framework of the Szechenyi 2020 program. The realization of this project is supported by the European Union.

REFERENCES

[1] Yoon, J. W., Noh, B. I., Jung, S. B. (2011). Comparative Study of ENIG and ENEPIG as Surface Finishes for a Sn-Ag-Cu Solder Joint. *J. Electron. Mater*, Vol. 40, No. 9, pp. 1950–1955.

[2] Yamamoto, K., Akahoshi, H., Kato, T., Kawamura, T., Koizumi, M., Satoh, R. (2008). An embrittlement mechanism of impact fracture of Sn–Ag–Cu solder joints on BGA using electroplated Ni/Au surface finishes. *IEEE Trans. Compon. Packag. Technol*, Vol. 31, pp. 849–858.

[3] Apachitei, I., Duszczyk, J., Katgerman, L., Overkamp, P. J. B. (1998). Electroless Ni–P Composite coatings: The effect of heat treatment on the microhardness of substrate and coating. *Scr. Mater*., Vol. 38, No. 9, pp. 1347–1353.

[4] Krasteva, N., Armyanov, S., Georgieva, J., Avramova, N., Fotty, W. (1995). Thermal Stability of Electroless NiMeP Amorphous Alloys. *J. Electron. Mater*, Vol. 24, No. 8, pp. 941–946.

[5] Keong, K. G., Sha, W., Malinov, S (2002). Crystallisation kinetics and phase transformation behaviour of electroless nickel–phosphorus deposits with high phosphorus content. *J. Alloy. Compd*., Vol. 334, pp. 192–199.

[6] Wojewoda-Budka, J., Wierzbicka-Miernik, A., Litynska-Dobrzynska, L., Szczerba, M. J., Mordarski, G., Mosiałek, M., Huber, Z., Zieba, P. (2016). Microstructure characteristics and phase transformations of the Ni-P and Ni-P-Re electroless deposited coatings after heat treatment. *Electrochim. Acta*, Vol. 209, pp. 183–191.

[7] Hentschel, T., Isheim, D., Kirchheim, R., Müller, F., Kreye, H. (2000). Nanocrystalline Ni-3.6 at.% P and its transformation sequence studied by Atom-probe Field-ion microscopy. *Acta mater*., Vol. 48, pp. 933–941.

[8] Czagány, M., Baumli, P., Kaptay, G. (2017). The influence of the phosphorous content and heat treatment on the nano-microstructure, thickness and micro-hardness of electroless Ni-P coatings on steel. *Appl. Surf. Sci.*, Vol. 423, pp. 160–169.

[9] Czagany, M., Baumli, P. (2017). Effect of pH on the characteristics of electroless Ni-P coatings. *J. Min. Metall. Sect. B-Metall*., Vol. 53, No 3, pp. 327–332.

[10] Farber, B., Cadel, E., Menand, A., Schmitz, G., Kircheim, R. (2000). Phosphorus Segregation in nanocrystalline Ni-3.6 at.% P alloy investigated with the tomographic Atom Probe (TAP). *Acta Mater*., Vol. 48, pp. 789–796.

[11] Keong, K. G., Sha, W., Malinov, S. (2002). Crystallization and phase transformation behaviour of electroless nickel-phosphorus deposits with low and medium phosphorus contents under continuous heating. *J. Mater. Sci.*, Vol. 37, pp. 4445–4450.

[12] Chen, J., Zou, Y., Matsuda, K., Zhao, G. (2017). Effect of Cu addition on the microstructure, thermal stability, and corrosion resistance of Ni–P amorphous coating. *Mater. Lett.*, Vol. 191, pp. 214–217.

[13] Tien, S. K., Duh, J. G., Chen, Y. I. (2004). Structure, thermal stability and mechanical properties of electroless Ni–P–W alloy coatings during cycle test. *Surf. Coat. Technol*., Vol. 177–178, pp. 532–536.

[14] Balaraju, J. N., Kalavati, Manikandanath, N. T., William Grips, V. K. (2012). Phase transformation behavior of nanocrystalline Ni–W–P alloys containing various W and P contents. *Surf. Coat. Technol.*, Vol. 206, pp. 2682–2689.

[15] Mencer, D. Electroless deposition of amorphous Ni–Re–P alloys from acidic hypophosphite solutions. *J. Alloy. Compd*., Vol. 306, pp. 158–162.

[16] Djokic, S. S. (2002). Electroless Deposition of Metals and Alloys. In: *Modern Aspects of Electrochemistry*. Conway, Brian, E., White, Ralph E. (eds.). The

Westaim Corporation, Fort Saskatchewan, Alberta, T8L 3W4, Canada, pp. 51–133.

[17] Baker, Hugh (ed.) (1992). *Alloy Phase Diagrams*. ASM Handbook, Vol. 3.

[18] Sudagar, J., Lian, J., Sha, W. (2013). Electroless nickel, alloy, composite and nano coatings-A critical review. *J. Alloys Cmpd.*, Vol. 571, pp. 183–204.

[19] Barin, I. (1993). Thermochemical Properties of Pure Substances. VCh, in 2 parts, Weinheim.

[20] Ganesan, R., Ciccioli, A., Gigli, G., Ipser. H. (2011). Thermochemical investigations in the tin–phosphorus system. *Int. J. Mat. Res*. (*formerly Z. Metallkd*.), Vol. 102, pp. 93–103.

[21] Keene, B. J. (1993). Review of data for the surface tension of pure metals. *Int. Mater. Rev.*, Vol. 38, No. 4, pp. 157–192.

[22] Kaptay, G., Báder, E., Bolyán, L. (2000). Interfacial Forces and Energies Relevant to Production of Metal Matrix Composites. *Mater. Sci. Forum*, Vols. 329–330, pp. 151–156.

Materials Science and Engineering, Volume 45, No. 1 (2020), pp. 63–76.
DOI: 10.32974.mse.2020.006

BEHAVIOUR AND TREATMENT OF METALS IN BURNING SYSTEM DURING BIOMASS COMBUSTION – LITERATURE REVIEW

TRUONG PHI DINH[1] – HELGA KOVÁCS[2] – ZSOLT DOBÓ[3]

Abstract: Biomass is a renewable energy resource and known as an excellent alternative option for the partial replacement of fossil fuels in energy production. Plants, as frequently used biomass energy sources, contain metals in a different amount. During biomass combustion, the emission of certain elements may lead to environmental pollution and health problems even if the biomass comes from a non-contaminated land. Hence, keeping the metals in the combustion system and avoid hazardous emissions is desirable. The same direction can be recognized by noble metals (NMs) and rare earth elements (REEs) as well, however, in these cases, the economic aspects are also considered. This paper briefly reviews the literature on metal contaminated biomass, phytoextraction, polluted biomass combustion, and the behavior of metals in combustion systems. Based on the literature review the fate of NMs and REEs during polluted biomass incineration has not been deeply investigated yet and requires further examination. Furthermore, capturing metals inside the burning system is also a huge challenge because a significant amount of metal compounds leaves the burning system with flue gas in solid and gaseous form. Besides, phytomining is a potential option for the extraction of NMs and REEs from the soil via plants. And, solid remains (bottom ash, fly ash) coming from contaminated biomass is a promising metal resource.

Keywords: metal, phytoextraction, disposal option, biomass combustion

INTRODUCTION

Biomass is a renewable energy resource including plant and animal materials. Its reservations are limitless. Besides that, biomass energy offers various environmental advantages such as reducing climate change, mitigating acid rain, water pollution, soil erosion, etc. Therefore, biomass is a potential energy resource to diversify world fuel supplies and substantially decrease greenhouse gas emissions [1]. According to reported data, biomass made up 64% of renewable energy's contribution [2] and it is anticipated to rise around double to triple in 2050 [3].

[1] Department of Combustion Technology and Thermal Energy, University of Miskolc
H-3515 Miskolc-Egyetemváros, Hungary
truong.dinh@uni-miskolc.hu
[2] Department of Combustion Technology and Thermal Energy, University of Miskolc
H-3515 Miskolc-Egyetemváros, Hungary
helga.kovacs@uni-miskolc.hu
[3] Department of Combustion Technology and Thermal Energy, University of Miskolc
H-3515 Miskolc-Egyetemváros, Hungary
zsolt.dobo@uni-miskolc

Generally, woody biomass has been known as an extensively used and the most plentiful resource of biomass. Statistically, more than one-third of the global lands are contaminated sites [4], called brownfields [5]. The real number even might be higher than which has been reported so far. According to the received data, mineral oil and metals are the most contaminants contributing 60% to contaminated lands [6]. Soil contamination in general and metals pollution in particular have serious negative effects on the ecosystem, human health, and the environment. Phytoextraction referring to plants accumulating metals (lead, cadmium, zinc, gold, silver, cerium, lanthanum, etc.) from the soil has been proven as an effective, environmentally friendly, safe, and low-cost remediation method to tackle the problem [7], [8]. The production of the phytoextraction process is a large amount of contaminated biomass that needs proper disposal and management. Thus, polluted biomass has been investigated with a dual purpose those are mitigating pollution problems through the phytoextraction process and producing energy.

1. PHYTOEXTRACTION

Phytoextraction is a soil remediation technology. During this process, plants accumulate metals from contaminated soils, transfer, and store them into the roots and above-ground parts of the plants with various distributions [9]. There are two types of plants can be efficiently used for phytoextraction those are hyperaccumulators and fast-growing species. Hyperaccumulators have been defined as plants that can accumulate huge amounts of metals in the soil without suffering [10]. Fast-growing species that have lower metals extracting ability than hyperaccumulators, however, their total biomass production is outstandingly higher such as poplar or willow [11], [12]. The lower limit for hyperaccumulation and studies corresponding to metals accumulated by plants are summarized in *Table 1*.

Table 1

Studies on metals accumulated by plants

Element	The lower limit for Hyperaccumulators (mg/kg)	Plant species	Concentration in plant (mg/kg)	Ref.
REEs	1,000	*Dicranopteris linearis* (fern)	4,438	[13]
		Dicranopteris dichotoma (fern)	2,231	[14]
		Hickory	(in leaves) 2,296	[15]
Silver	1	*Lupinus sp.* (blue lupin) – induced	126.000	[16]
		Amanita species (mushroom)	1,253.000	[17]
		Tobacco – induced	54.300	[18]
Gold	1	*Lupinus sp.* (blue lupin) – induced	6.300	[16]
		B. juncea (indian mustard) – induced	63.000	[19]
		Z. mays (corn) – induced	20.000	[19]

Element	The lower limit for Hyperac-cumulators (mg/kg)	Plant species	Concentration in plant (mg/kg)	Ref.
Platinum	1	*Berkheya coddii* (flowering plant) – induced	0.183	[20]
		Berkheya coddii (flowering plant)	(in leaves) 0.220 (in roots) 0.140	[21]
Palladium	1	*Berkheya coddii* (flowering plant) – induced	7.677	[20]
		Berkheya coddii (flowering plant)	(in leaves) 0.710 (in roots) 0.180	[21]
		Cannabis sativa (hemp)	30.336	[22]
Nickel	1,000	*Berkheya coddii* (flowering plant)	7,880	[23]
		Alssum lesbiacum (flowering plant)	10,000	[23]
Thallium	100	*Iberis intermedia* (herbaceous plant)	4,055	[24]
		Biscutella laevigata (flowering plant)	13,768	[24]
Cobalt	1,000	*Berkheya coddii* (flowering plant)	290	[25]
		Haumaniastrum robertii (flowering plant)	(in leaves) 4,304	[26]
Zinc	10,000	*Thlaspi caerulescens* (alpine pennygrass)	43,710	[27]
		Dichapetalum gelonioides (small semi-evergreen tree)	30,000	[27]
Lead	1,000	*Minuartia verna* (spring sandwort)	20,000	[27]
		Agrostis tenuis (grass)	13,490	[27]
Cadmium	100	*Thlaspi caerulescens* (alpine pennygrass)	2,130	[27]
		Arabidopsis halleri (flowering plant)	267	[28]
Copper	1,000	*Angiopteris sp. nov.* (fern)	3,535	[29]
		Anisopappus davyi (sunflower)	3,504	[29]
Manga-nese	10,000	*Phytolacca acinosa* (herbaceous plant)	(in leaves) 12,180	[30]
		Chengiopanax sciadophylloides (flowering tree)	(in leaves) 23,200	[31]
Chro-mium	300	*Leersia hexandra* (grass)	(in leaves) 2,978	[32]
Arsenic	1,000	*Pteris vittata* (brake fern)	3,280–4,980	[33]
		Pityrogramma calomelanos (fern)	(in leaves) 8,350	[34]

Phytoextraction is not only used for removing metals from contaminated areas but also offers the possibility for exploiting metals from mill tailings, overburdens, low-grade ores, or mineralized soil that is not economic by traditional mining methods [35]. In the economic aspect, NMs are potential candidates for phytomining because of their high value. However, only a few studies can be found in the case of Silver, Gold [35], [36]. While, the information about others like Platinum, Palladium, Rhodium,

Osmium, etc is very limited and even zero. Specifically, the phytoextraction of precious metals in contaminated soils has not been investigated that deserves more attention because of dual advantages including soil remediation and economic benefit.

2. TREATMENT AND DISPOSAL OF BIOMASS USED FOR PHYTOEXTRACTION

Phytoextraction is a soil remediation process that uses plants to uptake pollutants from brownfields and transports them into the plants. Polluted lands remediation and contaminates biomass formation occur simultaneously. It means that the environmental hazard is just transferred from soil to biomass. Hence, the phytoextraction process encounters a serious problem that is the production of large quantities of highly contaminated biomass, it needs proper disposal and management. Several methods of contaminated biomass treatments including composting, compaction, direct disposal, leaching, thermal conversion (pyrolysis, gasification, combustion) have been investigated so far [37], [38]. The pre-treatment step includes composting, compaction, and pyrolysis to decrease biomass volume and remove excess water. This lowers the cost of transportation to the disposal site and enhances the technical parameters. After this step, considerable quantities of polluted material still exist. On the other hand, direct disposal, leaching, incineration (gasification, combustion) known as final disposal methods [39]. The treatment techniques of phytoextraction biomass disposal are shortly described in *Table 2*. Among the aforementioned approaches, combustion has been recognized as the most feasible, economically acceptable, environmentally effective pathway [38], [39].

Table 2

Treatment techniques of phytoextraction biomass disposal, based on [38], [39]

Process	Step	Advantages	Disadvantages
Composting	Pretreatment	• Reduce volume and water content, decreases the costs of handling and transportation	• Time-consuming (2-3 months) • End-product needs to be treated as hazardous waste • In laboratory scale
Compaction	Pretreatment	• Volume reduction leads to cost transportation reduction • Shorter time compared to composting • Recovery of metals	• Special equipment is required • End-products (remaining biomass, leachates) should be treated as hazardous waste
Direct disposal	Final disposal	• Simple and time effectiveness	• Expensive and limited dumping sites • Slow reduction of polluted material • Serious environmental problems • This method has been forbidden
Leaching	Final disposal	• Recovery of metals	• No technology
Pyrolysis	Pretreatment	• High volume reduction, increases the energy density of biomass and decreases the	• Solid product fraction needs to be treated as hazardous waste

Process	Step	Advantages	Disadvantages
		costs of handling and transportation • Useful end-product	
Gasification	Final disposal	• High volume reduction, toxic metals enriched in solid residual • Lowering harmful climate change via CO_2 mitigation	• Undesired products such as tar, ash, etc., are formed • Technical and environmental problems during the utilization of syngas produced from contaminated biomass
Combustion	Final disposal	• High volume reduction, toxic metals enriched in solid residual • Produce energy	• Undesirable emissions of CO, NO_x, fly ash and solid, gaseous metal compounds

3. BIOMASS COMBUSTION

Combustion is a thermal conversion process and recognized as the best way for contaminated biomass final disposal. Combustion degradates material in the presence of excess oxygen/air at high temperatures over 900 °C [40]. The benefits of combustion technology are more than 90% volume reduction and toxic metals enriched in solid residual. Additionally, combustion is not only a disposal method for polluted biomass but also a promising energy producing solution. Nonetheless, the combustion of polluted biomass results in diverse environmental issues such as undesirable emissions of CO, NOx, fly ash, and solid, gaseous metal compounds. Where solid and gaseous metal compounds are the main concern of polluted biomass combustion, further investigations of these compounds during the combustion of biomass fuels (polluted and unpolluted) would be imperative, because many studies have proven than metals emission could arise even if the biomass feedstock comes from a non-contaminated land [41], [42].

Metals enter the combustion chamber subsequently exit in one of the three following forms: solid residues in the combustor (bottom ash); solid particles in the flue gas (fly ash); and the exhausted gas (flue gas). The fate of metals during combustion in ashes reported by different studies is presented in *Table 3*, which shows that most of the metals were detected in bottom ash and cyclone ash. Nonetheless, in another work, Vassilev et al [43] concluded that more than 90% of Cd, Hg, Sb, Se, and V are volatilized during biomass combustion, and higher than 50% volatilization in case of As, Cr, Pb, or Zn.

Table 3

Distribution of metals in some boiler ashes mg/kg, based on [44]

Metal	Bottom ash			Cyclone ash		Filter ash			Flue dust
	[45]	[46]	[47]	[45]	[47]	[45]	[46]	[47]	[47]
As	9.2	<3.0	3.0	25.6	1.9	5.1	16.0	0.7	0.2
Ba	534.9	330.0	–	671.4	–	206.4	2000.0	–	–
Cd	1.1	<0.3	1.2	2.3	8.6	1.9	3.0	6.6	1.9
Co	6.7	2.5	9.7	11.5	3.7	6.4	8.0	0.6	0.2

Metal	Bottom ash			Cyclone ash		Filter ash			Flue dust
	[45]	[46]	[47]	[45]	[47]	[45]	[46]	[47]	[47]
Cr	24.6	15.0	187.0	128.1	50.7	10.1	24.0	15.2	4.6
Cu	12.8	<10.0	147.1	31.6	51.6	18.9	60.0	29.9	8.8
Fe	5230.9	–	11756.8	8136.0	4442.2	1988.3	–	384.1	116.9
Mn	4864.0	–	12293.0	7144.0	5700.0	5020.0	–	779.0	228.0
Ni	28.5	19.0	27.1	68.3	14.6	24.5	67.0	3.5	1.1
Pb	29.0	<3.0	43.4	36.1	22.5	23.4	49.0	27.5	8.2
Ti	160.0	–	–	179.0	–	982.0	–	–	–
V	–	95.0	32.2	–	10.3	–	140.0	2.0	0.6
Zn	99.2	160.0	485.9	252.0	946.7	61.7	480.0	511.1	150.8
Hg	0.005	<0.030	0.003	0.007	0.030	0.014	<0.300	0.283	0.084

Several studies have been carried out corresponding to the metals flow calculations [48] and the distribution of metals during woody biomass combustion [43], [49]–[51]. Besides, the fate of metals during combustion of different feedstocks like waste [52], [53], sludge [54], [55], poultry litter [56], [57], contaminated oil [58], co-combustion [59], [60] also have been investigated.

The volatilization of metals is one of the major factors influencing the distribution of metals in biomass combustion [43]. It is dependent on the boiling point, the lower boiling point leads to the higher volatilization of metal.

The combustion temperature has been proven as the main parameter influencing the fate of metals during biomass combustion. Jimenez et al [61] combusted olive residue *(orujillo)* and analyzed the concentrations of Cr, Mn, Fe, Co, Ni, Cu, Zn, Ga, As, and Pb in sub-micrometer aerosols at different furnace temperatures (1,100, 1,300, and 1,450 °C) in an entrained flow reactor. The results revealed that almost metals (except Co, Ga, and Mn) were enriched in fine particles by increasing combustor temperature. Hu et al [62] investigated the impact of the combustion temperature, moisture content, chlorine on metals (Zn, Pb, Cu, Mn, and Cd) transferring into flue gas of sewage sludge combustion. According to the results, the higher burning temperature caused the higher selected metals content in the flue gas. It was also found that a higher moisture content decreased the transfer Cd, Zn, and Pb into the flue gas, but it had a slight effect on Cu and Mn. Furthermore, added chlorine during sewage sludge combustion promoted to release Cs, Zn, and Pb into the flue gas, but it had little influence on Cu and Mn. Likewise, Belevi and Langmeier [63] studied the evaporation behavior of Zn, Sn, Cu, Sb, Cd, and Pb during municipal solid waste combustion in a furnace temperature range of 500−900 °C. It was indicated that higher burning temperature caused an increase in transfers of target metals into the gaseous phase, except Sb. The authors also revealed, the residence time increase (from 10 to 120 min) resulted in higher evaporation of Zn, Cu, Cd, Pb, and it showed a slight effect in the case of Sb. Likewise, several studies investigated the influence of combustor temperature on the behavior of metals during the combustion of different kinds of feedstocks such as contaminated woody biomass [64], sewage sludge

[65], waste [66], [67], poultry litter, co-combustion [68]. These results showed the same connection between the burning temperature and distribution of metals.

Besides that, the effect of flue gas temperature on the behavior of metals during biomass combustion has been rarely investigated. Polluted biomass *(Populus tremula)* was combusted to analyze the impact of flue gas temperature [69]. According to the results, more metals (Ag, Co, Cr, Cu, Fe, Ga, Mg, Mn, Ni, Pb, Si, Sn, Ti, V, and Zr) could be condensed on fly ash particles and captured inside the combustion system by decreasing flue gas temperature from 250 to 150 °C. The study also revealed that more than 50% of the total metals input (except Ni) could not be detected in bottom ash and fly ash as seen in *Figure 1*. This means that, during contaminated biomass combustion, these metals likely were volatized and exited the combustion system in gaseous form.

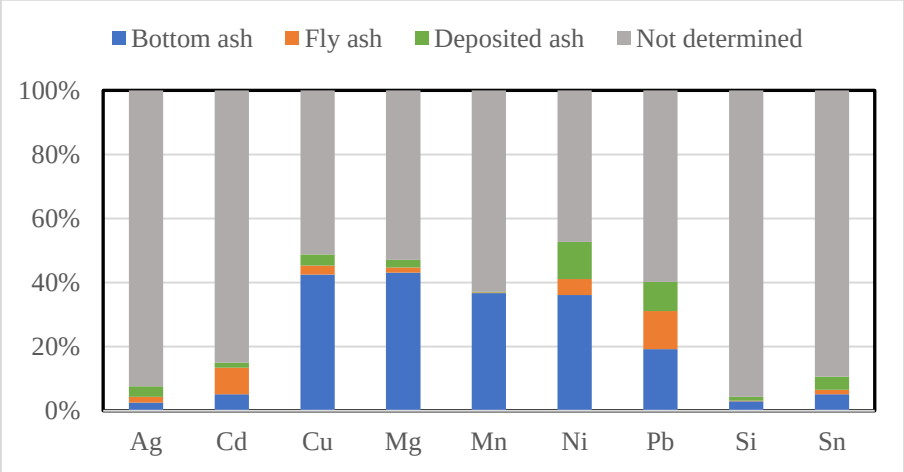

Figure 1
Metal flow in contaminated biomass combustion, based on [69]

Residence time and moisture content are recognized as the secondary influencing factors on the fate of metals during combustion. It has been reported that longer reaction time leads to more volatilization of metals while, an increase of moisture content in feedstocks may decrease the emissions of metals [62], [70].

The distribution of metals during combustion also influenced by the presence of chlorine. It was found that the increase of chlorine content in the combustion chamber results in a higher concentration of metals in flue gas [62], [70]. That can be explained by decreasing volatility temperature [71].

It has been indicated that the lack of oxygen accelerates metals volatilization due to the less formation of metal oxides that have higher volatility temperature than metal elements [72], [73].

The partitioning of metals in biomass combustion also depends on the type of furnace. Lu et al. [74] stated that in terms of the influence of the combustor type, the

horizontal tube furnace resulted in a higher metals volatilization compared to the entrained tube furnace.

Generally, the distribution of metals during biomass combustion depends on various factors such as feedstock properties, reactors, operating conditions (combustion temperature, flue gas temperature, pressure, oxygen, residence time), the boiling point of metals, presence of chlorine, etc. It can be said that the fate of NMs and REEs during contaminated biomass combustion has not been investigated yet. Moreover, the capture of metals inside the combustion system is a huge challenge because more than 50 percent of metals emit in the gaseous phase according to recent research. These tasks need further investigation so far. Additionally, during combustion process metals are enriched in bottom ash, especially in fly ash. Thus, the concentration of metals in the ash might be high enough for extraction and the solid remains coming from contaminated biomass is a promising metal resource.

CONCLUSIONS

Based on the literature review it can be stated that various studies are corresponding to the behavior of heavy metals during contaminated combustion. However, the investigation of NMs and REEs in the burning system is extremely limited and requires further examination.

Furthermore, developing a technique to capture (and possibly recover) metals is also the potential gap of knowledge. Since, according to several recent studies, a significant amount of metal compounds is leaving the burning system with flue gas in solid and gaseous form without ensuring their capture and treatment. It can be said that capturing metals inside the burning system is challenging and it has not been fully solved yet as well.

Additionally, phytomining is a potential option for the extraction of NMs and REEs from the soil via plants. And, solid remains coming from contaminated biomass is a promising metal resource.

ACKNOWLEDGMENT

The research was carried out as part of the *More efficient exploitation and use of subsurface resources* project of the University of Miskolc, implemented in the framework of the Thematic Excellence Program funded by the Ministry of Innovation and Technology of Hungary. (Grant Contract reg. nr.: NKFIH-846-8/2019)

REFERENCES

[1] U.S. Energy and I. Administration (2019). *DOE-EIA International Energy Outlook 2019*.

[2] Smil, Vaclav (2017). *Energy Transitions: Global and National Perspectives*. Praeger, ABC CLIO.

[3] Johansson, T. B., Patwardhan, A. P., Nakićenović, N., and Gomez-Echeverri, L. (2012). *Global energy assessment: toward a sustainable future*. Cambridge University Press.

[4] Abhilash, P. C., Dubey, R. K., Tripathi, V., Srivastava, P., Verma, J. P., Singh, H. B. (2013). Remediation and management of POPs-contaminated soils in a warming climate: Challenges and perspectives. *Environ. Sci. Pollut. Res.*, Vol. 20, No. 8, pp. 5879–5885.

[5] Alker, S., Joy, V., Roberts, P., Smith, N. (2000). The definition of brownfield. *J. Environ. Plan. Manag.*, Vol. 43, No. 1, pp. 49–69.

[6] Panagos, P., Van Liedekerke, M., Yigini, Y., Montanarella, L. (2013). Contaminated sites in Europe: Review of the current situation based on data collected through a European network. *Journal of Environmental and Public Health*, Vol. 2013, pp. 1–11.

[7] Mahar, A. et al. (2016). Challenges and opportunities in the phytoremediation of heavy metals contaminated soils: A review. *Ecotoxicol. Environ. Saf.*, Vol. 126, pp. 111–121.

[8] Khan, F. I., Husain, T., Hejazi, R. (2004). An overview and analysis of site remediation technologies. *J. Environ. Manage.*, Vol. 71, No. 2, pp. 95–122.

[9] Salt, D. E. et al. (1995). Phytoremediation: a novel strategy for the removal of toxic metals from the environment using plants. *Bio/technology*, Vol. 13, No. 5, p. 468.

[10] van der Ent, A., Baker, A. J. M., Reeves, R. D., Pollard, A. J., Schat, H. (2013). Hyperaccumulators of metal and metalloid trace elements: Facts and fiction. *Plant and Soil*, Vol. 362, No. 1–2, pp. 319–334.

[11] Kovacs, H., Szemmelveisz, K., Palotas, A. B. (2013). Solubility analysis and disposal options of combustion residues from plants grown on contaminated mining area. *Environmental Science and Pollution Research*, Vol. 20, No. 11. pp. 7917–7925.

[12] He, J. et al. (2013). Cadmium tolerance in six poplar species. *Environ. Sci. Pollut. Res.*, Vol. 20, No. 1, pp. 163–174.

[13] Zhenggui, W. et al. (2001). Rare earth elements in naturally grown fern Dicranopteris linearis in relation to their variation in soils in South-Jiangxi region (Southern China). *Environ. Pollut.*, Vol. 114, No. 3, pp. 345–355.

[14] Miao, L., Ma, Y., Xu, R., Yan, W. (2011). Environmental biogeochemical characteristics of rare earth elements in soil and soil-grown plants of the Hetai goldfield, Guangdong Province, China. *Environ. Earth Sci.*, Vol. 63, No. 3, pp. 501–511.

[15] Robinson, W. O. (1943). The occurrence of rare earths in plants and soils. *Soil Science*, Vol. 56, No. 1. pp. 1–6.

[16] Anderson, C. W. N., Stewart, R. B., Moreno, F. N., Gardea-Torresdey, J. L., Robinson, B. H., Meech, J. A. (2003). Gold phytomining. Novel Developments in a Plant-based Mining System. *Proc. Gold 2003 Conf. New Ind. Appl. Gold*, No. 2, pp. 35–45.

[17] Borovička, J., Řanda, Z., Jelínek, E., Kotrba, P., Dunn, C. E. (2007). Hyperaccumulation of silver by Amanita strobiliformis and related species of the section Lepidella. *Mycol. Res.*, Vol. 111, No. 11, pp. 1339–1344.

[18] Krisnayanti, B. D., Anderson, C. W. N., Sukartono, S., Afandi, Y., Suheri, H., Ekawanti, A. (2016). Phytomining for artisanal gold mine tailings management. *Minerals*, Vol. 6, No. 3, pp. 1–11.

[19] Anderson, C., Moreno, F., Meech, J. (2005). A field demonstration of gold phytoextraction technology. *Miner. Eng.*, Vol. 18, No. 4, pp. 385–392.

[20] Walton, D. (2002). *The phytoextraction of gold and palladium from mine tailings: this thesis is presented in fulfilment of the requirements for the degree of Master of Philosophy*. Massey University.

[21] Nemutandani, T., Dutertre, D., Chimuka, L., Cukrowska, E., Tutu, H. (2006). The potential of Berkheya coddii for phytoextraction of nickel, platinum, and palladium contaminated sites. *Toxicol. Environ. Chem.*, Vol. 88, No. 2, pp. 175–185.

[22] Aquan, Hendra Michael (2015). *Phytoextraction of Palladium and Gold from Broken Hill Gossan*. Massey University, Palmerston North, New Zealand.

[23] Robinson, B. H., Brooks, R. R. Howes, A. W., Kirkman, J. H., Gregg, P. E. H. (1997). The potential of the high-biomass nickel hyperaccumulator Berkheya coddii for phytoremediation and phytomining. *Journal of Geochemical Exploration*, Vol. 60, No. 2, pp. 115–126.

[24] Anderson, C. W. N. et al. (1999). Phytomining for nickel, thallium and gold *J. Geochemical Explor.*, Vol. 67, No. 1–3, pp. 407–415.

[25] Robinson, B. H., Brooks, R. R., Clothier, B. E. (1999). Soil amendments affecting nickel and cobalt uptake by Berkheya coddii: potential use for phytomining and phytoremediation. *Ann. Bot.*, Vol. 84, No. 6, pp. 689–694.

[26] Brooks, R. R. (1977). Copper and cobalt uptake byHaumaniastrum species. *Plant and Soil*, Vol. 48, No. 2, pp. 541–544.

[27] Reeves, R., Baker. *Metal-accumulating plants. Phytoremediation of Toxic Metals: Using Plants to Clean Up the Environment*. John Wiley, Vol. 6, Jan.

[28] Bert, V., Bonnin, I., Saumitou-Laprade, P., De Laguérie, P., Petit, D. (2002). Do Arabidopsis halleri from nonmetallicolous populations accumulate zinc and cadmium more effectively than those from metallicolous populations? *New Phytol.*, Vol. 155, No. 1, pp. 47–57.

[29] Malaisse, F., Brooks, R. R., Baker, A. J. M. (1994). Diversity of vegetation communities in relation to soil heavy metal content at the Shinkolobwe copper/cobalt/uranium mineralization, Upper Shaba, Zaire. *Belg. J. Bot.*, Vol. 127, No. 1, pp. 3–16.

[30] Xue, S. G., Chen, Y. X., Reeves, R. D., Baker, J. M., Lin, Q., Fernando, D. R. (2004). Manganese uptake and accumulation by the hyperaccumulator plant Phytolacca acinosa Roxb. (Phytolaccaceae). *Environ. Pollut.*, Vol. 131, No. 3, pp. 393–399.

[31] Mizuno, T., Emori, K., Ito, S. I. (2013). Manganese hyperaccumulation from non-contaminated soil in Chengiopanax sciadophylloides Franch. et Sav. and its correlation with calcium accumulation. *Soil Sci. Plant Nutr.*, Vol. 59, No. 4, pp. 591–602.

[32] Zhang, X. H., Liu, J., Huang, H. T., Chen, J., Zhu, Y. N., Wang, D. Q. (2007). Chromium accumulation by the hyperaccumulator plant Leersia hexandra Swartz. *Chemosphere*, Vol. 67, No. 6, pp. 1138–1143.

[33] Ma, L. Q., Komar, K. M., Zhang, W., Cai, Y., Kennelley, E. D. (2001). A fern that hyperaccumulates arsenic. *Nature*, Vol. 411, No. 6836, pp. 438–438.

[34] Visoottiviseth, P., Francesconi, K., Sridokchan, W. (2002). The potential of Thai indigenous plant species for the phytoremediation of arsenic contaminated land. *Environ. Pollut.*, Vol. 118, No. 3, pp. 453–461.

[35] Sheoran, W., Sheoran, A. S., Poonia, P. (2009). Phytomining: A review. *Miner. Eng.*, Vol. 22, No. 12, pp. 1007–1019.

[36] Sheoran, V., Sheoran, A. S., Poonia, P. (2013). Phytomining of gold: A review. *J. Geochemical Explor.*, Vol. 128, pp. 42–50.

[37] Ghosh, M., Singh, S. P. (2005). A review on phytoremediation of heavy metals and utilization of its byproducts. *Appl. Ecol. Environ. Res.*, Vol. 3, No. 1, pp. 1–18.

[38] Kovacs, H., Szemmelveisz, K. (2017). Disposal options for polluted plants grown on heavy metal contaminated brownfield lands – A review. *Chemosphere*, Vol. 166, pp. 8–20.

[39] Sas-Nowosielska, A., Kucharski, R., Małkowski, E., Pogrzeba, M., Kuperberg, J. M., Kryński, K. (2004). Phytoextraction crop disposal – An unsolved problem. *Environ. Pollut.*, Vol. 128, No. 3, pp. 373–379.

[40] Koppejan, J., Van Loo, S. (2012). *The handbook of biomass combustion and co-firing*. Routledge.

[41] Pöykiö, R., Mäkelä, M., Watkins, G., Nurmesniemi, H., Dahl, O. (2016). Heavy metals leaching in bottom ash and fly ash fractions from industrial-scale BFB-boiler for environmental risks assessment. *Transactions of Non-ferrous Metals Society of China (English Edition)*, Vol. 26, No. 1. pp. 256–264.

[42] Sarabèr, A. J. (2014). Co-combustion and its impact on fly ash quality; Full-scale experiments. *Fuel Processing Technology*, Vol. 128. pp. 68–82.

[43] Vassilev, S. V., Baxter, D., Vassileva, C. G. (2014). An overview of the behaviour of biomass during combustion: Part II. Ash fusion and ash formation mechanisms of biomass types. *Fuel*, Vol. 117, No. PART A. pp. 152–183.

[44] Nzihou, A., Stanmore, B. (2013). The fate of heavy metals during combustion and gasification of contaminated biomass-A brief review. *Journal of Hazardous Materials*, Vol. 256–257. pp. 56–66.

[45] Li, L., Yu, C., Bai, J., Wang, Q., Luo, Z. (2012). Heavy metal characterization of circulating fluidized bed derived biomass ash. *Journal of Hazardous Materials*, Vol. 233–234. pp. 41–47.

[46] Dahl, O., Nurmesniemi, H., Pöykiö, R., Watkins, G. (2009). Comparison of the characteristics of bottom ash and fly ash from a medium-size (32 MW) municipal district heating plant incinerating forest residues and peat in a fluidized-bed boiler. *Fuel Processing Technology*, Vol. 90, No. 7–8. pp. 871–878.

[47] Narodoslawsky, M., Obernberger, I. (1996). From waste to raw material - The route from biomass to wood ash for cadmium and other heavy metals. *J. Hazard. Mater.*, Vol. 50, No. 2–3, pp. 157–168.

[48] Kovacs, H., Szemmelveisz, K., Koós, T. (2016). Theoretical and experimental metals flow calculations during biomass combustion. *Fuel*, Vol. 185, pp. 524–531.

[49] Obernberger, I., Biedermann, F., Widmann, W., Riedl, R. (1997). Concentrations of inorganic elements in biomass fuels and recovery in the different ash fractions. *Biomass and Bioenergy*, Vol. 12, No. 3. pp. 211–224.

[50] Valmari, T., Kauppinen, E. I., Kurkela, J., Jokiniemi, J. K., Sfiris, G., Revitzer, H. (1998). Fly ash formation and deposition during fluidized bed combustion of willow. *J. Aerosol Sci.*, Vol. 29, No. 4, pp. 445–459.

[51] Kovacs, H., Szemmelveisz, K., Palotas, A. B. (2015). Environmentally Sound Combustion of Ligneous Plants Grown, *in Heavy Metal-Contaminated Soil*. pp. 261–277.

[52] Yuan, C. S., Lin, H. Y., Wu, C. H., Liu, M. H. (2005). Partition and size distribution of heavy metals in the flue gas from municipal solid waste incinerators in Taiwan. *Chemosphere*, Vol. 59, No. 1, pp. 135–145.

[53] Zhang, H., He, P. J., Shao, L. M. (2008). Fate of heavy metals during municipal solid waste incineration in Shanghai. *J. Hazard. Mater.*, Vol. 156, No. 1–3, pp. 365–373.

[54] Corella, J., Toledo, J. M. (2000). Incineration of doped sludges in fluidized bed. Fate and partitioning of six targeted heavy metals. I. Pilot plant used and results. *J. Hazard. Mater.*, Vol. 80, No. 1–3, pp. 81–105.

[55] Van de Velden, M., Dewil, R., Baeyens, J., Josson, L., Lanssens, P. (2008). The distribution of heavy metals during fluidized bed combustion of sludge (FBSC). *J. Hazard. Mater.*, Vol. 151, No. 1, pp. 96–102.

[56] Lynch, D. et al. (2014). Behavior of heavy metals during fluidized bed combustion of poultry litter. *Energy and Fuels*, Vol. 28, No. 8, pp. 5158–5166.

[57] Abelha, P. et al. (2003). Combustion of poultry litter in a fluidised bed combustor. *Fuel*, Vol. 82, No. 6, pp. 687–692.

[58] Pavageau, M. P. et al. (2004). Partitioning of Metal Species during an Enriched Fuel Combustion Experiment. Speciation in the Gaseous and Particulate Phases. *Environ. Sci. Technol.*, Vol. 38, No. 7, pp. 2252–2263.

[59] Sippula, O., Lamberg, H., Leskinen, J., Tissari, J., Jokiniemi, J. (2017). Emissions and ash behavior in a 500 kW pellet boiler operated with various blends of woody biomass and peat. *Fuel*, Vol. 202, pp. 144–153.

[60] Xiao, Z. et al. (2015). Energy recovery and secondary pollutant emission from the combustion of co-pelletized fuel from municipal sewage sludge and wood sawdust. *Energy*, Vol. 91, pp. 441–450.

[61] Jiménez, S., Pérez, M., Ballester, J. (2008). Vaporization of trace elements and their emission with submicrometer aerosols in biomass combustion. *Energy and Fuels*, Vol. 22, No. 4, pp. 2270–2277.

[62] Hu, Y., Wang, J., Deng, K., Ren, J. (2014). Characterization on heavy metals transferring into flue gas during sewage sludge combustion. *Energy Procedia*, Vol. 61. pp. 2867–2870.

[63] Belevi, H., Langmeier, M. (2000). Factors determining the element behavior in municipal solid waste incinerators. 2. Laboratory experiments. *Environmental Science and Technology*, Vol. 34, No. 12. pp. 2507–2512.

[64] Delplanque, M. et al. (2013). Combustion of Salix used for phytoextraction: The fate of metals and viability of the processes. *Biomass and Bioenergy*, Vol. 49, pp. 160–170.

[65] fan Zhang, Y. et al. (2018). Volatility and partitioning of Cd and Pb during sewage sludge thermal conversion. *Waste Manag.*, Vol. 75, pp. 333–339.

[66] Peng, T. H., Lin, C. L., Wey, M. Y. (2014). Development of a low-temperature two-stage fluidized bed incinerator for controlling heavy-metal emission in flue gases. *Appl. Therm. Eng.*, Vol. 62, No. 2, pp. 706–713.

[67] Sørum, L., Frandsen, F. J., Hustad, J. E. (2004). On the fate of heavy metals in municipal solid waste combustion. Part I. Devolatilisation of heavy metals on the grate. *Fuel*, Vol. 83, No. 11–12. pp. 1703–1710.

[68] Xue, Z., Zhong, Z., Lai, X. (2020). Investigation on gaseous pollutants emissions during co-combustion of coal and wheat straw in a fluidized bed combustor. *Chemosphere*, Vol. 240, No. 124853, pp. 1–8.

[69] Kovacs, H., Dobo, Z., Koos, T., Gyimesi, A., Nagy, G. (2018). Influence of the Flue Gas Temperature on the Behavior of Metals during Biomass Combustion. *Energy and Fuels*, Vol. 32, No. 7, pp. 7851–7856.

[70] Chanaka Udayanga, W. D., Veksha, A., Giannis, A., Lisak, G., Chang, V. W. C., Lim, T. T. (2018). Fate and distribution of heavy metals during thermal processing of sewage sludge. *Fuel*, Vol. 226, No. March, pp. 721–744.

[71] Barton, R. G., Clark, W. D., Seeker, W. R., Fate of metals in waste combustion systems. *Combust. Sci. Technol.*, Vol. 74, No. 1–6, pp. 327–342.

[72] Obernberger, I., Brunner, T., Bärnthaler, G. (2006). Chemical properties of solid biofuels-significance and impact. *Biomass and Bioenergy*, Vol. 30, No. 11, pp. 973–982.

[73] Guo, F., Zhong, Z., Xue, H., Zhong, D. (2018). Migration and Distribution of Heavy Metals During Co-combustion of Sedum plumbizincicola and Coal. *Waste and Biomass Valorization*, Vol. 9, No. 11, pp. 2203–2210.

[74] Lu, S. et al. (2012). Comparison of trace element emissions from thermal treatments of heavy metal hyperaccumulators. *Environ. Sci. Technol.*, Vol. 46, No. 9, pp. 5025–5031.

Materials Science and Engineering, Volume 45, No. 1 (2020), pp. 77–83.
DOI: 10.32974.mse.2020.007

THE INFLUENCE OF REFLUX TEMPERATURE ON THE YIELD OF TRANSPORTATION FUELS DURING PLASTIC WASTE PYROLYSIS

ZSOLT DOBÓ[1] – TAMARA MAHNER[2] –
GERGŐ KECSMÁR[3] – GÁBOR NAGY[4]

Abstract: The operational parameters of the reflux play an important role during a plastic waste pyrolysis process as it recirculates the heavy hydrocarbons into the reactor for further molecule scissoring. The impact of the reflux temperature on the pyrolysis oil composition was investigated and the results are summarized in this paper. A plastic waste blend containing HDPE, LDPE, PP and PS was pyrolyzed in a laboratory scale batch reactor in the reflux temperature range of 150–300 °C, while the obtained pyrolysis oil was further processed by atmospheric distillation. Results show that by decreasing the reflux temperature the yield of gasoline range hydrocarbons can be significantly enhanced: 285 $g/kg_{solid\ waste}$ gasoline yield was measured at 300 °C reflux temperature, while 150 °C resulted 446 $g/kg_{solid\ waste}$. Additionally, the pyrolysis gas yield containing mostly C_1-C_4 hydrocarbons is also enhanced by lowering the reflux temperature. Results show, that producing gasoline and diesel range hydrocarbons from plastic wastes through pyrolysis is a viable method to reduce the accumulation of plastic wastes and could provide value added transportation fuels.

Keywords: Plastic waste, pyrolysis, reflux temperature

INTRODUCTION

Plastic waste generation and accumulation became a serious problem in the world. The global plastic waste generation reached 302 Mt in 2015, while the total plastic waste ever generated from primary plastics had reached 5,800 Mt [1]. By projecting current global waste management trends to 2050, it is assumed that the primary plastic waste generated will be around 26,000 Mt [1]. 29.1 Mt of plastic ended up in waste stream in the EU during the year of 2018 [2]. About 24.9% of this plastic waste was landfilled, 32.5% was recycled while 42.6% was utilized for energy recovery [2]. As the amount of plastic waste continuously increases, some alternative methods are being developed

[1] Institute of Energy and Quality, University of Miskolc
H-3515 Miskolc-Egyetemváros, Hungary
zsolt.dobo@uni-miskolc.hu
[2] Institute of Energy and Quality, University of Miskolc
H-3515 Miskolc-Egyetemváros, Hungary
mtami0203@gmail.com
[3] Institute of Energy and Quality, University of Miskolc
H-3515 Miskolc-Egyetemváros, Hungary
kecsm.gerg@gmail.com
[4] Institute of Energy and Quality, University of Miskolc
H-3515 Miskolc-Egyetemváros, Hungary
nagy.gabi@uni-miskolc.hu

including pyrolysis, which is a promising method to generate value-added liquid fuel suitable for transportation as it can reduce the carbon footprint of the transportation industry and optimize waste management towards zero landfilling [3].

The pyrolytic products can be divided into a gas, liquid, and solid fraction. Based on the process parameters the gas/liquid ratio can be changed. The influencing factors of plastic waste pyrolysis were investigated by several researchers such as temperature [4–6], pressure [7, 8], time [5, 9], type of reactor [10, 11], catalyst [12–14] and plastic waste material used [15–20]. Very limited information can be found in the literature about the reflux temperature influence on the pyrolysis oil composition [21]. Therefore, the main goal of this study is to investigate the impact of the reflux temperature change on the plastic waste pyrolysis process. A batch reactor equipped with a reflux condenser was utilized for pyrolysis runs, while the pyrolysis oils were further processed by atmospheric distillation to determine the transportation fuel yields.

1. MATERIALS AND METHODS

The pyrolysis runs were performed in a laboratory scale batch reactor equipped with a temperature controlled reflux. The reflux is a simple shell-and-tube heat exchanger, where the temperature and the flow rate of the cooling air can be adjusted in order to control the temperature of the pyrolysis vapors exiting the reflux. The vapors exiting the reflux are condensed in a secondary, water cooled heat exchanger and the liquid product (pyrolysis oil) is collected in a product container at room temperature. The remaining gases were collected in a sample bag and flared after the measurements. *Figure 1* shows the schematic illustration of the measurement system.

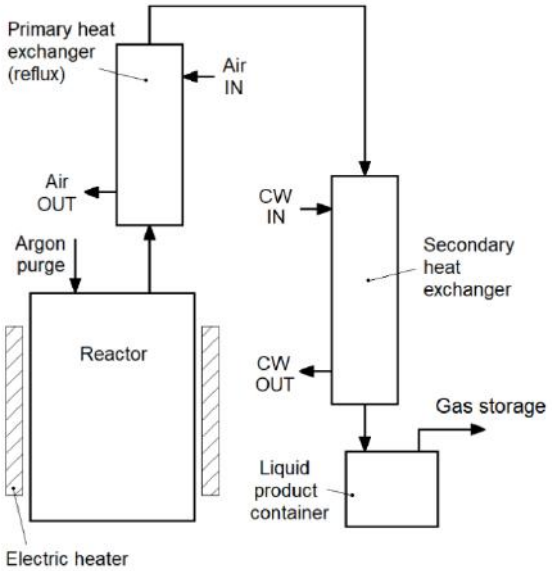

Figure 1
Schematic illustration of the measurement system

A mixture of PP, LDPE, HDPE and PS was used representing the typical plastic demand in the European Union in 2018 [2]. Based on the data found in [2] the solid plastic waste blend used in this study contained 34.8% PP, 31.6% LDPE, 22.0% HDPE and 11.6% PS. 200 g solid waste blend was loaded into the reactor in each case, while the temperature of the reactor heater was set to 700 °C. Four pyrolysis measurements were performed while the reflux temperature was gradually increased from 150 °C to 300 °C with 50 °C increments. The obtained pyrolysis oils were further processed by atmospheric distillation to separate the gasoline and diesel range hydrocarbons. The 20–200 °C range was considered as gasoline, while the 200–350 °C was considered as diesel range hydrocarbons.

2. RESULTS

The mass distribution of the products at different reflux temperatures is summarized in *Table 1*.

Table 1

The distribution of products at different reflux temperatures

Reflux temperature, °C	**Gas, %**	**Liquid (oil), %**	**Solid, %**
150	32.2	62.5	5.3
200	27.9	66.7	5.4
250	17.8	76.7	5.5
300	15.4	80.7	3.9

Based on the obtained results it can be stated that the temperature of the reflux has a significant impact on the liquid and gas yield. The influence is not evident in the case of solid residues. The main function of the reflux is to capture heavy hydrocarbon molecules and return them into the reactor for further molecule scissoring. Typically, the heavier hydrocarbon molecules have higher boiling temperatures as well, thus, it is supposed that by decreasing the reflux temperature the amount of lighter hydrocarbon molecules is increased in the final pyrolytic liquid product. It follows that the gaseous product is intensified as the reflux temperature decreases. This effect lowers the total liquid product during the pyrolysis process. Additionally, the more evaporation-condensation cycle increases the time necessary to complete the pyrolysis process as seen in *Figure 2*, where the pyrolysis vapor temperatures exiting the reflux are depicted during the pyrolysis runs. Based on these results it can be stated that by increasing the reflux temperature the pyrolysis oil yield can be increased while the time necessary to finish the pyrolysis can be decreased.

The results of the atmospheric distillation is shown in *Figure 3*. It can be seen that by lowering the reflux temperature the amount of the gasoline range hydrocarbons in pyrolysis oil can be significantly intensified. The presence of hydrocarbons with boiling temperatures higher than 350 °C even at 150 °C reflux temperature indicates that the efficiency of the reflux is low.

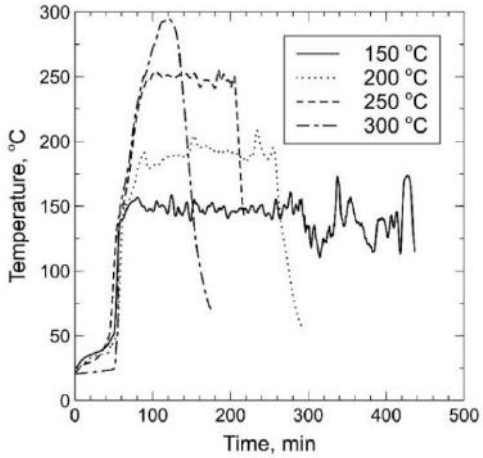

Figure 2
Typical temperature stability of vapors exiting the reflux.
The heating procedure of the reactor started at zero minute

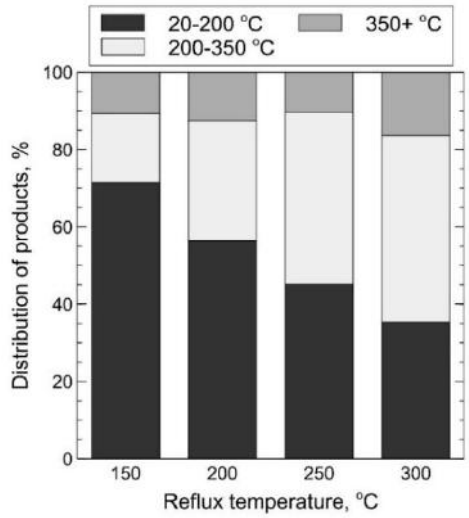

Figure 3
Distribution of different products in pyrolysis oil

Thus, an important conclusion is that reflux design might also play an important role in the pyrolysis process. Although the amount of pyrolysis oil decreases by decreasing the reflux temperature, the gasoline yield increases as shown in *Figure 4*. The highest gasoline yield of 446 g/$kg_{solid\ waste}$ was measured at 150 °C reflux temperature, which is roughly 0.6 L/$kg_{solid\ waste}$ by considering 0.75 g/ml density. On the other side,

the highest diesel yield of 390 g/kg$_{\text{solid waste}}$ was measured at 300 °C reflux temperature. These results show, that lowering the reflux temperature is a viable method in cases when maximizing gasoline production is desirable.

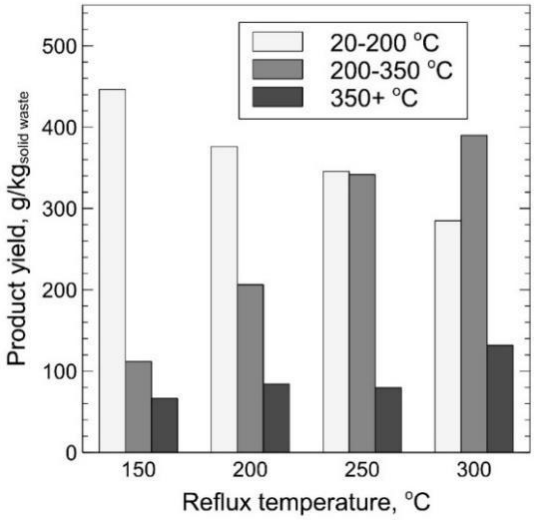

Figure 4
Yields of gasoline (20–200 °C) and diesel (200–350 °C) range hydrocarbons

Based on these results, both the gasoline yield and the flammable gaseous pyrolysis product yield can be significantly enhanced by lowering the reflux temperature. The gaseous product contains mainly C_1-C_4 hydrocarbons, thus, the heating value and the flow rate of the gas might be high enough to cover the heat requirement of the reactor. Investigating this assumption is one possible direction of the research. Additionally, eliminating the distillation residue (350+ °C portion), i.e. converting it into fuel product would be an important requirement.

CONCLUSIONS

The influence of the reflux temperature on the gasoline and diesel yield during plastic waste pyrolysis was experimentally investigated in an electrically heated batch reactor. The plastic waste blend contained PP, LDPE, HDPE and PS in a ratio representing the typical plastic demand in the EU in 2018. Results show, that although the pyrolysis oil yield is decreasing by lowering the reflux temperature, the gasoline yield increases as the reflux recirculates the heavy hydrocarbon molecules into the reactor for further molecule scissoring. The highest gasoline yield of 446 g/kg$_{\text{solid waste}}$ was measured at 150 °C reflux temperature while the highest diesel yield of 390 g/kg$_{\text{solid waste}}$ was measured at 300 °C reflux temperature.

ACKNOWLEDGMENT

The presented study was carried out as part of the EFOP-3.6.1-16-2016-00011 *Younger and Renewing University – Innovative Knowledge City – institutional development of the University of Miskolc aiming at intelligent specialisation* project implemented in the framework of the Szechenyi 2020 program. The realization of this project is supported by the European Union, co-financed by the European Social Fund.

REFERENCES

[1] Geyer, R., Jambeck, J. R., Law, K. L. (2017). Production, use, and fate of all plastics ever made. *Science Advances*, 3, pp. 1–5.

[2] Plastics – the facts 2019. *An analysis of European plastics production, demand and waste data*. https://www.plasticseurope.org/application/files/9715/7129/9584/FINAL_web_version_Plastics_the_facts2019_14102019.pdf

[3] Faussone, Gian Claudio (2017). Transportation fuel from plastic: Two cases of study. *Waste Management*, 73, pp. 416–423.

[4] Sogancioglu, M., Ahmetli, G., Yelm E. (2017). A comparative study on waste plastics pyrolysis liquid products quantity and energy recovery potential. *Energy Procedia*, 118, pp. 221–226.

[5] López, A., de Marco, I., Caballero, B. M., Laresgoiti, M. F., Adrados, A. (2011). Influence of time and temperature on pyrolysis of plastic wastes in a semi-batch reactor. *Chemical Engineering Journal*, 173, pp. 62–71.

[6] Kalargaris, I., Tian, G., Gu, S. (2017). The utilization of oils produced from plastic waste at different pyrolysis temperatures in a DI diesel engine. *Energy*, 131, pp. 179–185.

[7] Murata, K., Sato, K., Sakata, Y. (2004). Effect of pressure on thermal degradation of polyethylene. *Journal of Analytical and Applied Pyrolysis*, 71, pp. 569–589.

[8] Miranda, R., Yang, J., Roy, C., Vasile, C. (2001). Vacuum pyrolysis of commingled plastics containing PVC I. kinetic study. *Polymer Degradation and Stability*, 72, pp. 469–491.

[9] Diaz Silvarrey, L. S., Phan, A. N. (2016). Kinetic study of municipal plastic waste. *International Journal of Hydrogen Energy*, 41, pp. 16352–16364.

[10] Sharuddin, S. D. A., Abnisa, F., Daud, W. M. A. W., Aroua, M. K. (2016). A review on pyrolysis of plastic wastes. *Energy Conversion and Management*, 115, pp. 308–326.

[11] Butler, E., Devlin, G., McDonnell, K. (2011). Waste polyolefins to liquid fuels via pyrolysis: review of commercial state-of-the-art and recent laboratory research. *Waste and Biomass Valorization*, 2, pp. 227–255.

[12] Miandad, R., Barakat, M. A., Aburiazaiza, A. S., Rehan, M., Nizami, A. S. (2016). Catalytic pyrolysis of plastic waste: a review. *Process Safety and Environmental Protection*, 102, pp. 822–838.

[13] Miandad, R., Barakat, M. A., Rehan, M., Aburiazaiza, A. S., Ismail, I. M. I., Nizami, A. S. (2017). Plastic waste to liquid oil through catalytic pyrolysis using natural and synthetic zeolite catalysts. *Waste Management*, 69, pp. 66–78.

[14] Buekens, A. G., Huang, H. (1998). Catalytic plastics cracking for recovery of gasoline-range hydrocarbons from municipal plastic wastes. *Resources, Conservation and Recycling*, 23, pp. 163–181.

[15] Kunwar, B., Cheng, H. N., Chandrashekaran, S. R., Sharma, B. K. (2016). Plastics to fuel: a review. *Renewable and Sustainable Energy Reviews*, 54, pp. 421–428.

[16] Kumar, S., Singh, R. K. (2011). Recovery of hydrocarbon liquid from waste high density polyethylene by thermal pyrolysis. *Brazilian Journal of Chemical Engineering*, 28, pp. 659–667.

[17] Miranda, R., Yang, J., Roy, C., Vasile, C. (2001). Vacuum pyrolysis of commingled plastics containing PVC I. kinetic study. *Polymer Degradation and Stability*, 72, pp. 469–491.

[18] Kunwar, B., Cheng, H. N., S.R. Chandrashekaran, S. R., Sharma, B. K. (2016). Plastics to fuel: a review. *Renewable and Sustainable Energy Reviews*, 54, pp. 421–428.

[19] Sogancioglu, M., Yel, E., Ahmetli, G. (2017). Investigation of the effect of polystyrene (PS) waste washing process and pyrolysis temperature on (PS) pyrolysis product quality. *Energy Procedia*, 118, pp. 189–194.

[20] Sinn, Hansjörg, Kaminsky, Walter, Janning, Jörg (1976). Processing of plastic waste and scrap tires into chemical raw materials, especially by pyrolysis. *Angewandte Chemie International Edition*, 15, pp. 660–672.

[21] Seth, D., Sarkar, A. (2004). Thermal pyrolysis of polypropylene: effect of reflux-condenser on the molecular weight distribution of products. *Chemical Engineering Science*, 59, pp. 2433–2445.

Materials Science and Engineering, Volume 45, No. 1 (2020), pp. 84–95.
DOI: 10.32974.mse.2020.008

A COMPARATIVE STUDY OF NON-MONOTONICITY FOR UNIDIRECTIONAL AND CROSS ROLLING OF NIOBIUM SHEET

VIKTOR GÁL[1] – MÁTÉ SZŰCS[2] –
GÁBOR SZABÓ[3] – GYÖRGY KRÁLLICS[4]

Abstract: Under cold forming conditions, a niobium plate with 50 × 50 × 4 mm size was rolled using two different types of technology. In first one, the size and properties of the plates were changed by a unidirectional successive multi-step procedure. In another one, cross-rolling with the same reduction was used to achieve the changes in size and properties. Following the experiments, 3D finite element process modelling was performed with DEFORM software in order to determine the deformation history and state of the two processes for the same plate thickness. This factor is directly related to the microstructure of the material and its related change. The performed process modelling was controlled by comparing the measured and calculated rolling forces and torques.

Keywords: sheet rolling, finite element modelling, non-monotonic deformation, niobium

INTRODUCTION

Cross rolling, by changing the workpiece orientation and changing the deformation path, is a way of tailoring texture development to reduce the anisotropic properties of the workpiece [1]. The sample to the rolling plane is rotated by 90° about the normal direction (ND). The most commonly used sequence of stages for cross rolling are the following: Two step cross rolling (TSCR), also known as pseudo-cross rolling, where direction is changed after achieving 50% of the total reduction *(Figure 1.a)*.; Multistep cross rolling (MSCR), also known as true cross rolling, where direction is changed after each pass *(Figure 1.b)*; Clock rolling *(Figure 1.c)* may be one more way of achieving cross rolling by continuously changing the rolling direction by 90° about ND and if the rotation is 180° instead of 90°, it is called as reverse rolling. Alteration in the rolling direction or deformation path changes the substructure formed in the previous path of deformation, and hence affects the deformation

[1] Institute of Material Science and Technology, University of Miskolc
H-3515 Miskolc-Egyetemváros, Hungary
metgv@uni-miskolc.hu
[2] Institute of Physical Metallurgy, Metal Forming and Nanotechnology, University of Miskolc
H-3515 Miskolc-Egyetemváros, Hungary
femszmat@uni-miskolc.hu
[3] Institute of Metallurgy, University of Miskolc
H-3515 Miskolc-Egyetemváros, Hungary
szabogabor@uni-miskolc.hu
[4] Institute of Physical Metallurgy, Metal Forming and Nanotechnology, University of Miskolc
H-3515 Miskolc-Egyetemváros, Hungary
femkgy@uni-miskolc.hu

texture. Cross rolling leads to rolled product of comparatively uniform mechanical properties in all directions.

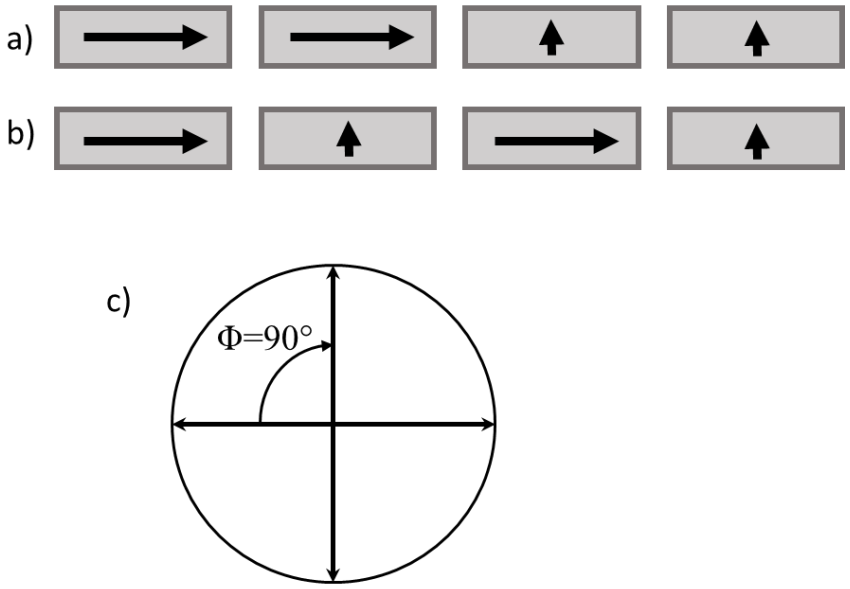

Figure 1
Cross rolling sequences: a) Two-step cross rolling (TSCR)
b) Multistep cross-rolling (MSCR) c) Clock rolling

In present work, the objective of the modelling is to demonstrate the non-monotonic nature of the process, indicating that it is non-monotonic, resulting fine grains and a special crystallographic texture.

1. STRAIN HISTORY IN METAL FORMING

The permanent deformation of the samples is demonstrated by the strain trajectory approach as initiated by Ilyushin [2], representing the deviatoric strain tensor ***(e)*** in a five-dimensional vector space as:

$$e_1 = \sqrt{\frac{3}{2}} \ln V'_{11},\ e_2 = \sqrt{2}\left(\ln V'_{22} + \frac{1}{2} \ln V'_{11} \right), \\ e_3 = \sqrt{2} \ln V'_{12},\ e_4 = \sqrt{2} \ln V'_{23}, e_5 = \sqrt{2} \ln V'_{31} \tag{1}$$

where $\ln V'$ is the logarithmic deviatoric strain tensor. Some examples for the strain trajectories are shown in *Figure 2*. Trajectory #1 is monotonic, #2 is nearly monotonic, #3 is simple non-monotonic and #4 is cyclic non-monotonic.

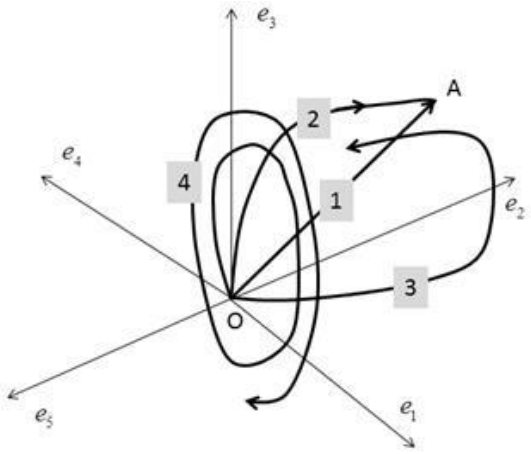

Figure 2
Examples for the strain trajectories in the five-dimensional vector space

In order to appreciate the measure of the non-monotonicity of deformation, consider the nearly monotonic trajectory #2 [3]. During deformation, the endpoint of the strain vector travels along the curved OA trajectory. The ideally monotonic deformation corresponds to the straight-line OA. Therefore, at the deformation time '*t*' the measure of non-monotonicity is given as:

$$NM(t) = \frac{\bar{\varepsilon}(t)}{\bar{\varphi}(t)} \geq 1 \tag{2}$$

where $\bar{\varepsilon}(t)$ is the total equivalent strain $\bar{\varepsilon} = \int_0^t \dot{\bar{\varepsilon}}\, dt$, which is equivalent to the length of the trajectory, and $\bar{\varphi}(t)$ is the equivalent logarithmic strain, which equals the length of the straight trajectory OA. In the case of non-monotonic deformation, the complete trajectory is separated into *n* nearly monotonic portions. For each part the $(NM)_i$ is determined as the ratio of the length of the local trajectory part and the straight segment connecting its end points. In this case, the measure of non-monotonicity of the whole deformation is given as:

$$NM = \sum_{i=1}^{n} (NM)_i \tag{3}$$

The larger the value of *NM*, the higher the degree of non-monotonicity of deformation. It should be noted that although all $(NM)_i$ values are larger than one, *NM* may decrease with increasing strain as the end points of the segments may vary during the development of the deformation trajectory.

Strain path change was suggested by Schmitt et al. [4] to measure the change of the direction of the plastic strain tenzor corresponding to the pre strain and to the subsequent strain modes

$$\cos\phi = \frac{\ln \mathbf{V}_{pr} : \ln \mathbf{V}_{sub}}{\left\|\ln \mathbf{V}_{pr}\right\| \left\|\ln \mathbf{V}_{sub}\right\|} \tag{4}$$

Change in strain path offers an additional parameter during the processing of materials to alter the microstructure and crystallographic texture, and thereby the mechanical properties of the product [5], [6], [7], [8]. In the literature, quite a few articles deal with the finite element simulation of cross rolling [9].

2. EXPERIMENTAL ROLLING OF NIOBIUM

The 4 mm thick niobium sheets were unidirectional- and cross rolled at room temperature without any front- and back tension. The other two sizes of material are the same with 50 mm. Both rolling experiments consists of four passes to reach the final thickness of material. The rolls' diameter was 220 mm, and their surfaces were lubricated with a mineral oil-based mixture. The rolling force and torque were recorded in the whole process by an HBM type data acquisition system. *Figure 3* shows the final shapes of sheets which was obtained by the two different technique.

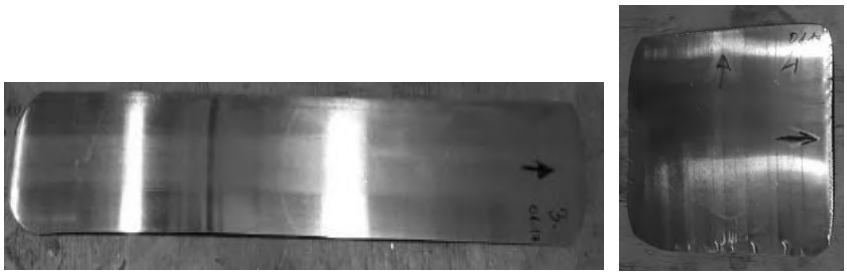

a) b)

Figure 3

Final shape of rolled niobium after a) the unidirectional- and b) cross rolling

In cross rolling, the material rotated clockwise with angle of $\Phi = 90°$ around its normal axes (perpendicular to sheet plane) before each pass. The entry and final thickness per pass are detailed in *Table 1*. The rolling speed was 30 m/min for each pass.

Table 1

Entry and final thicknesses of unidirectional- and cross rolling per pass

	Unidirectional rolling		**Cross rolling**		
Pass number	h_0 **(mm)**	h_f **(mm)**	h_0 **(mm)**	h_f **(mm)**	**Φ (°)**
1.	4.02	3.46	4.02	3.47	–
2.	3.46	2.98	3.47	3.00	+90°
3.	2.98	2.51	3.00	2.55	–90°
4.	2.51	2.02	2.55	2.11	+90°

3. FINITE ELEMENT ANALYSIS OF NIOBIUM ROLLING

The three-dimensional problem was solved by DEFORM software to simulate the unidirectional- and cross rolling process as well. The rolled material was assumed to be plastic, which flow curves was described by the *Equation (5)*.

$$\sigma_y = \left(A + B\bar{\varepsilon}^n\right)\left(1 + C\ln\dot{\varepsilon}^*\right), \quad \dot{\varepsilon}^* = \bar{\dot{\varepsilon}} / \bar{\dot{\varepsilon}}_{ref} \tag{5}$$

where the material constants are A = 140 MPa, B = 214 MPa, n = 0.525, C = 0.1061, while the roll was rigid. The perfect cylindrical surface of the roll was approximated by 8,000 polynomials. Due to the symmetry of the problem, it was used a half-thick model with a symmetry plane in the middle. In order to achieve the appropriate number of elements in the thickness direction, 8-node brick type mesh elements with a size of 0.48 × 0.44 × 0.71 mm were used. The total number of elements was 31,000. After the last simulated pass, a minimal distortion of hexahedral mesh was observed, so we used the initial mesh for whole process. The simulation was performed with a constant time step, calculated with the conjugate gradient solver algorithm with direct iteration.

A cold rolling problem was calculated, with an initial plate temperature of 20 °C, and it was assumed that the property of the material did not change during the rolling because of the temperature change. Between each pass, the material was to cool back to ambient temperature of 20 °C. A m = 0.4 Kudo-type friction factor between the plate and cylinder surfaces was used. In the validation process of finite element simulation, the friction factor was modified to minimize the difference between the measured- and calculated force. In *Figure 4* and *5*, the diagrams show the measured and calculated rolling force as a function of time.

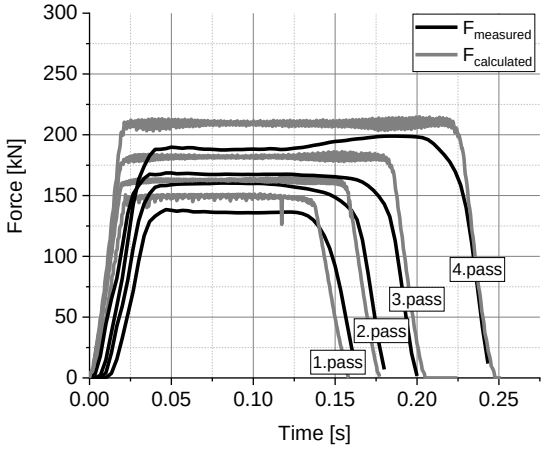

Figure 4
Measured- and calculated force of unidirectional rolling

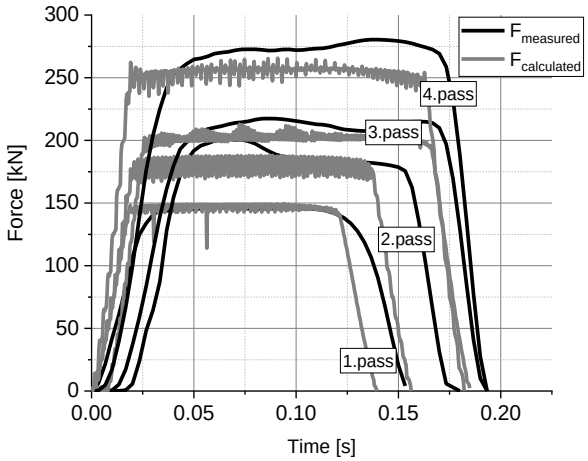

Figure 5
Measured- and calculated force of cross rolling

After the running the simulation, the strain quantities were obtained in six different points through the half thickness of the material. Three of them were selected on the plane of longitudinal section (they are point A, B and C in *Figure 6*) and the other three at the edge of sheet in the same relative coordinates. The relative coordinates of the analysed points along the *z* axis are the followings, $r_A = 0.0$ $r_B = 0.5$, $r_C = 1.0$, $r_D = 0.0$ $r_E = 0.5$ and $r_F = 1.0$. Each of them are related to the initial position of sheet as it is illustrated by *Figure 6*.

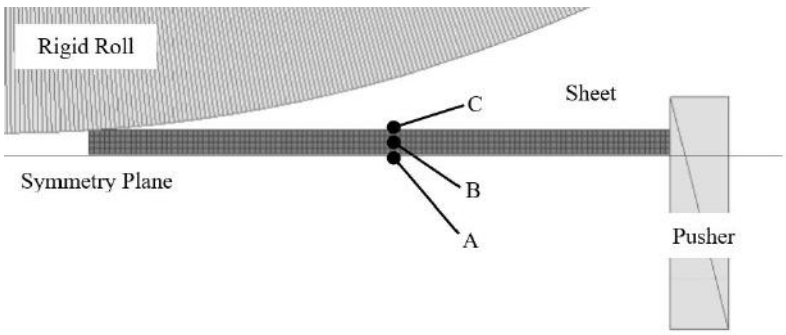

Figure 6
Longitudinal section of 3D finite element model with the position of points A, B and C

4. CALCULATION RESULTS OF FINITE ELEMENT ANALYSIS

Below mentioned figures show the analysed quantities in terms of forming time for the unidirectional- and cross rolling as well. The diagrams contain the logarithmic

equivalent- $\bar{\varphi}$, the total equivalent plastic strain $\bar{\varepsilon}$ and the parameter of non-monotonicity *NM* for the whole experimental rolling. The calculation results were obtained in six different material points shown by *Figures 7–12.*

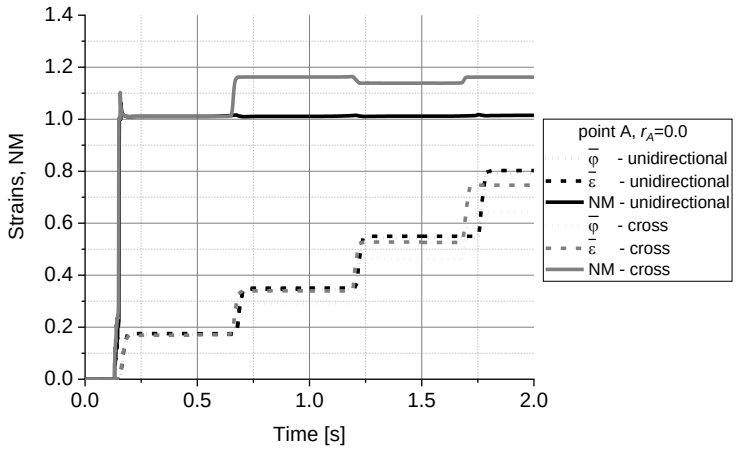

Figure 7
Logarithmic equivalent-, total equivalent strain and NM parameter in terms of time for point A

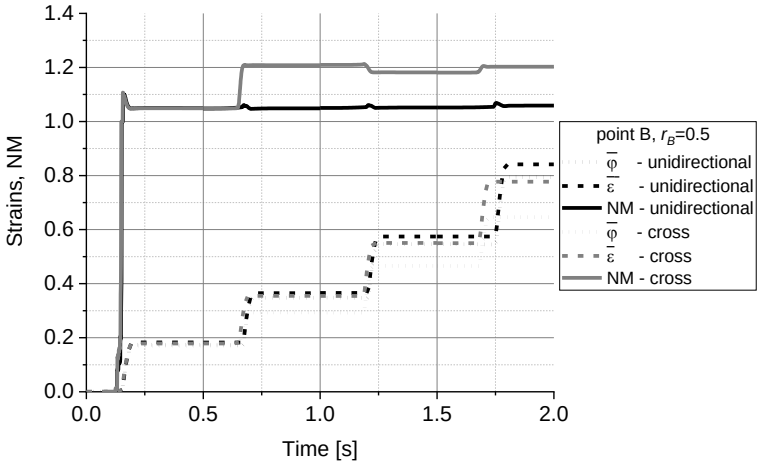

Figure 8
Logarithmic equivalent-, total equivalent strain and NM parameter in terms of time for point B

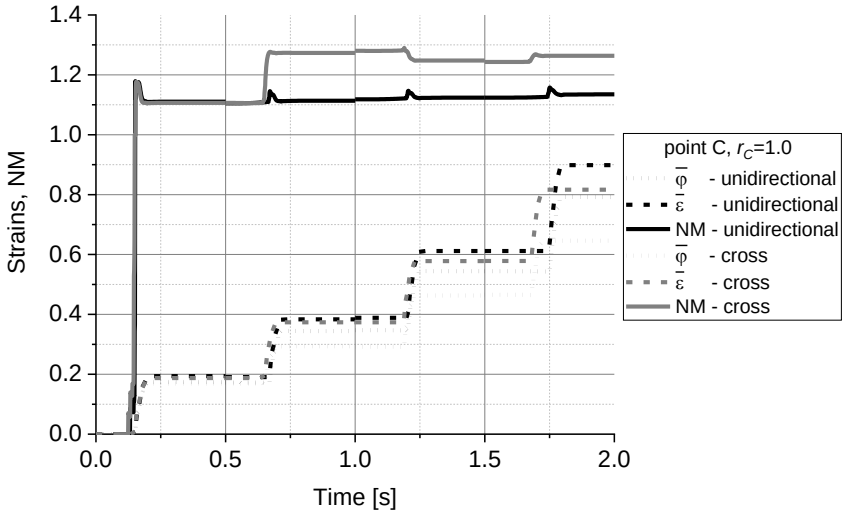

Figure 9
Logarithmic equivalent-, total equivalent strain and NM parameter in point C

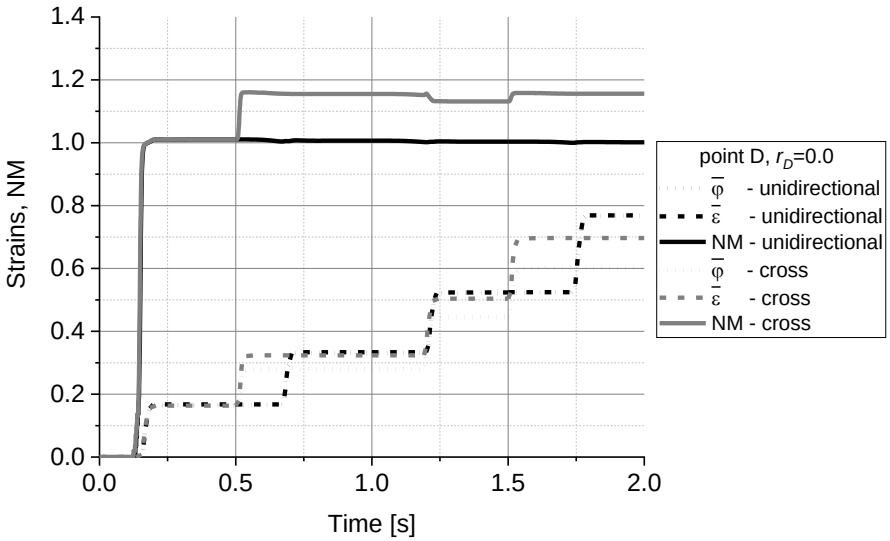

Figure 10
Logarithmic equivalent-, total equivalent strain and NM parameter in point D

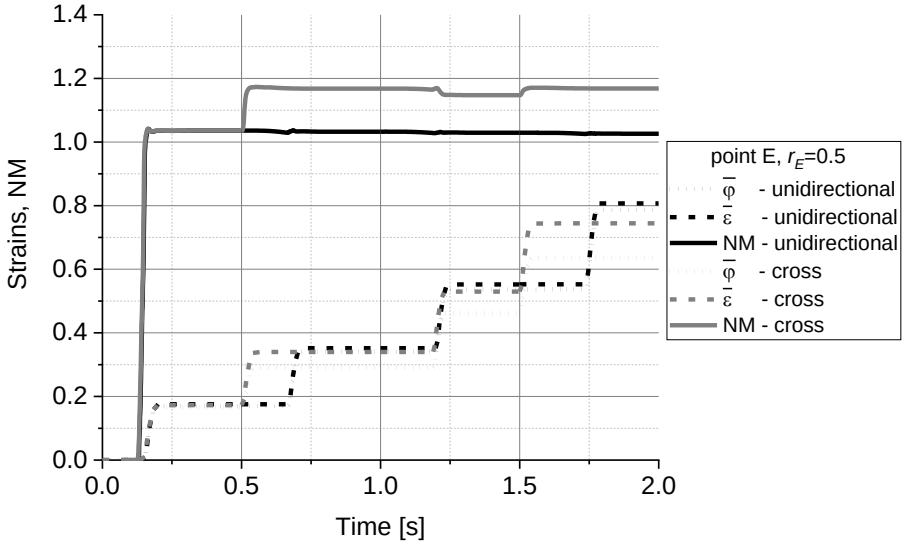

Figure 11
Logarithmic equivalent-, total equivalent strain and NM parameter in point E

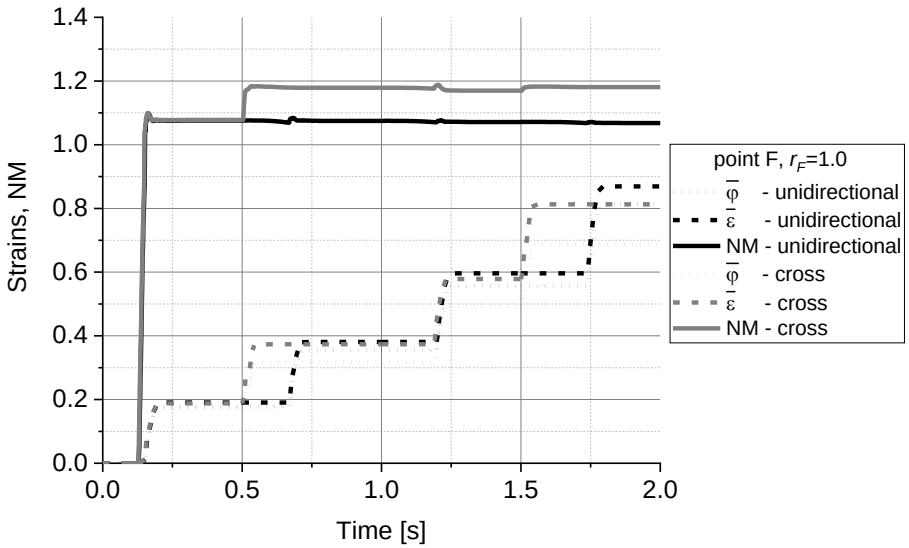

Figure 12
Logarithmic equivalent-, total equivalent strain and NM parameter in point F

A significant difference was observed in *NM* parameter of rolling methods. Cross rolling shows higher values of *NM* in each material points that confirms a higher degree of non-monotonicity of deformation. *Figure 13* shows the calculated cos ϕ parameter of cross rolling in terms of transition between the passes. The parameter was investigated in different points of sheet. The horizontal dashed line designates the cos ϕ = 1.0 which is a constant value and characterizes unidirectional rolling process in terms of monotonicity for each investigated material points.

Since both parameters show significant differences between the plastically formed sheets, it is highly recommended to study and measure the materials microstructure more deeply. In addition, it is expected a significant difference in crystallographic texture as well. On the other hand, the three-dimensional simulations provide input data of texture simulation with a relative high accuracy.

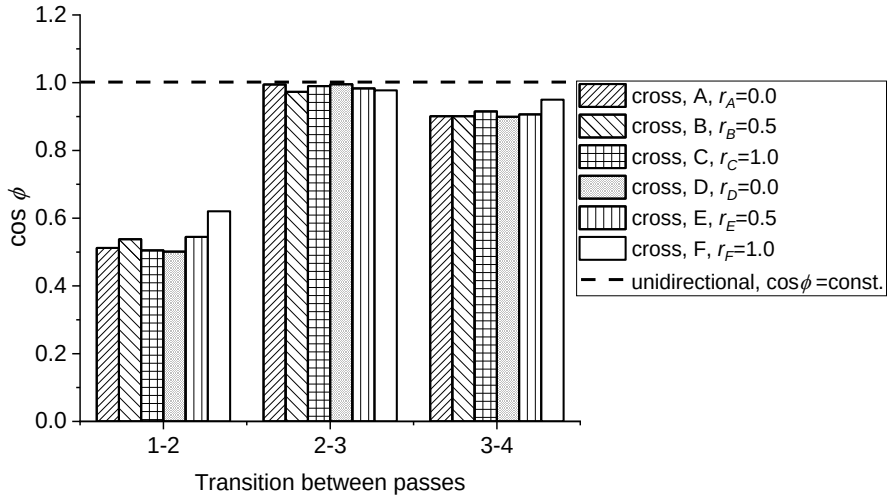

Figure 13
Comparison of cos ϕ parameter obtained two different rolling processes

CONCLUSION

Three-dimensional finite element models were established to simulate the experimental rolling. Calculations were validated by the measured rolling force per pass. The difference between the calculated and measured data was minimized iterative while the friction factor was modified several times.

The effects of two different rolling methods on the non-monotonicity and mechanical quantities of material were studied by numerical calculations when the investigated sheets have the same initial geometry. We observed a relative high difference in the value of non-monotonicity of unidirectional- and cross rolling that indicates a significant microstructural changes of niobium sheet.

ACKNOWLEDGEMENTS

The research was carried out at the University of Miskolc, within the framework of the Thematic Excellence Program funded by the Ministry of Innovation and Technology of Hungary. (Grant Contract reg. nr.: NKFIH-846-8/2019)

The described study was carried out as part of the EFOP-3.6.1-16-2016-00011 *Younger and Renewing University – Innovative Knowledge City – institutional development of the University of Miskolc aiming at intelligent specialisation* project implemented in the framework of the Széchenyi 2020 program. The realization of this project is supported by the European Union, co-financed by the European Social Fund.

REFERENCES

[1] Rout, M., Pal, S. K., Singh, S. B. (2015). Cross Rolling: A Metal Forming Process. In: Davim, J. (ed.). *Modern Manufacturing Engineering. Materials Forming, Machining and Tribology*. Springer International Publishing, Switzerland.

[2] Ilyushin, A. A. (1990). *Mehanika splosnoj sredi*. SSSR, Izdatelstvo Moskovskogo Universiteta, p. 196.

[3] Krallics, G., Malgyn, D. (2005). Finite element simulation of equal channel angular pressing. In: Burhanettin, Altan (ed.). *Severe Plastic Deformation: Towards Bulk Production of Nanostructured Materials*. 612 p. New York, Nova Science Publishers Inc., p. 445.

[4] Schmitt, J. H., Shen, E. L., Raphanel, J. L. (1994). A parameter for measuring the magni- tude of a change of strain path: Validation and comparison with experiments on low carbon steel. *International Journal of Plasticity*, 10, pp. 535–551.

[5] Catorceno, Litzy Lina Choquechambi, de Abreu, Hamilton Ferreira Gomes, Padilha, Angelo Fernando (2018). Effects of cold and warm cross-rolling on microstructure and texture evolution of AZ31B magnesium alloy sheet. *Journal of Magnesium and Alloys*, 6, pp. 121–133.

[6] Gurao, N. P., Sethuraman, S., Suwas, Satyam (2011). Effect of strain path change on the evolution of texture and microstructure during rolling of copper and nickel. *Materials Science and Engineering A*, 52, pp. 7739–7750.

[7] Davenport, S. B., Higginson, R. L., Sellars, C. M., Withers, P. J., van Houtte, P., Brown, L. M., Prangnell, P. (1999). The Effect of Strain Path on Material Behaviour during Hot Rolling of FCC Metals. *Philosophical Transactions: Mathematical, Physical and Engineering Sciences*, Vol. 357, No. 1756, Deformation Processing of Metals, pp. 1645-1661.

[8] Koohbor, Behrad, Serajzadeh, Siamak (2012). Influence of deformation path change on static strain aging of cold rolled steel strip. *International Journal of Advanced Manufacturing Technology*, 61, pp. 901–909.

[9] Rout, Matruprasad, Pal, Surjya K., Singh, Shiv B. (2016). Finite element simulation of a cross rolling process. *Journal of Manufacturing Processes*, 24, pp. 283–292.

Materials Science and Engineering, Volume 45, No. 1 (2020), pp. 96–105.
DOI: 10.32974.mse.2020.009

SOME RESEARCH RESULTS OF CONVENTIONAL MINERAL FILLERS USED IN ROAD CONSTRUCTION

RÓBERT GÉBER[1] – BELLA UDVARDI[2] – ISTVÁN KOCSERHA[3]

Abstract: This paper presents and summarizes some research results which were carried out by the Institute of Ceramics and Polymer Engineering, University of Miskolc in the last few years.

In order to achieve the best results extended literature review was made. Mineral fillers were tested from different Hungarian locations in order to reveal their role in asphalt pavements. Particle size distribution, morphology, specific surface area and air void of fillers were determined, as well as different adsorption tests were also made.

The performed tests give useful information about the behaviour of mineral fillers in asphalt pavements, especially about the cohesion between the particles and bitumen.

Keywords: asphalt, hydrophilic, microstructure, mineral filler, oil adsorption, Rigden void, surface

INTRODUCTION

Asphalt: the most common pavement material

Asphalt materials consist of a mixture of mineral aggregates and bitumen. The mineral skeleton of this composite system builds up from different fractions of rocks. The maximum carrying capacity of asphalt pavements can be reached by a precisely controlled technology which consists not only of the mixing mineral aggregates with bitumen but appropriate compacting [1].

The finest parts of mineral materials in asphalt pavements are called fillers of which particle sizes are under 0.063 mm [2]. Their particle size distribution (PSD) is extremely important in asphalt technology. Particle size and polydispersity, morphology, volume fraction and packing highly affect both the viscosity of bitumen and the performance of pavement [3, 4, 5, 6]. The presence of fines – owing to their surface properties – also affects the adsorption ability of bitumen [7].

[1] Institute of Ceramics and Polymer Engineering, University of Miskolc
H-3515 Miskolc-Egyetemváros, Hungary
robert.geber@uni-miskolc.hu
[2] Institute of Ceramics and Polymer Engineering, University of Miskolc
H-3515 Miskolc-Egyetemváros, Hungary
ubella07@gmail.com
[3] Institute of Ceramics and Polymer Engineering, University of Miskolc
H-3515 Miskolc-Egyetemváros, Hungary
istvan.kocserha@uni-miskolc.hu

The properties of fillers fundamentally affect the contact with bitumen, therefore the properties of asphalt mastics (= bitumen + filler) and pavements [8, 9]. Cohesion, contact and absorption ability depend mainly on particle size (polydispersity), fineness modulus, specific surface, porosity and mineral composition (possibly the CaO content [10]) of fines. According to Clopotel and Bahia [11], the adsorption of bitumen components is proportional to the specific surface area (SSA) of fillers and at the same time it is independent from the mineral composition. Morphology, i.e. the geometry and shape of fillers affect the internal friction of mixture [12].

The role of mineral fillers in asphalt mixtures has been expansively investigated by several researchers. In their work, Grabowski and Wilanowicz [4] looked for quantitative relationship between some features of limestone fillers (such as particle size distribution, Rigden Void between filler particles, sphericity, surface texture and specific surface) and their stiffening properties. Their results showed significant difference between the structure of fillers and the above mentioned features. A number of tests were made by Ishai and Craus [6] on different mineral materials. They used the packing volume concept and described specific rugosity as an important parameter of packing which characterizes well the geometrical irregularity of mineral materials and eventually affects the properties of asphalt mixtures. Shashidar and his colleagues [13, 14] tested the effect of particulate mineral materials of asphalt mixtures on the rheological properties in their researches. According to them, the interaction between the particles, their agglomeration, particle shape and orientation in a given volume decrease packing, which affect the stiffness of asphalt pavements. Liao and his associates [15] tested the role of mineral fillers in asphalt mastics in point of stiffening effect and failure. According to their results, the amount of fillers significantly affects the stiffening of mastics. The higher the amount of filler is the higher is the stiffness of mastics.

According to Sakharov [16], the effect of fillers is based on the fact that they play an interactive role with their fineness and surface characteristics. They have a relatively high specific surface area in the mineral skeleton of asphalt mixtures, therefore they are able to adsorb a great part of bitumen.

Lisihina [17] executed tests on different (basic and carbonate) rocks concerning the adsorption of bitumen. According to the Author, these materials are able to absorb much more binders on their unit surfaces than acidic rocks. Lisihina stated that fillers with high porosity can absorb the components of bitumen in a selective way (selective diffusion).

In addition, a number of researchers [4, 6, 18, 19, 20] have also made experiments on asphalt mixtures with the use of mineral fillers. According to Hu et al. [21] the strength and structure of asphalts are highly affected by the contact between fillers and bitumen. The greater the binding force between mineral particles and bitumen is, the higher the strength of asphalt pavement is.

According to the above mentioned, the contact between fillers and bitumen depends on the adsorption processes taking place on their interface. Physical adsorption is affected by the porosity and the specific surface area of the fillers. According to numerous research articles, the bond between bitumen and siliceous

fillers is mechanical (generated by the Van der Walls forces) while the bond between bitumen and another filler (for example limestone) is chemical.

The amount of pores, cracks and small crystals stuck on the surface of filler particle increase the specific surface area, therefore affect the adsorbable amount of bitumen. Compared to other particles, specific surface area of fillers in mineral skeleton of asphalt mixture is considerably higher, therefore they are able to adsorb great part of bitumen in compound. It is practical to use material from ground basic, carbonate rocks as fillers. These rocks are hydrophobic which is favourable in view of adsorption of binder material [8]. When choosing fillers, mineral composition has a great importance, that is, material has to be pure. Presence of clay minerals is unfavourable for instance, as it decreases mechanical strength, resistance to mechanical weathering, and finally leads to failure of pavement sooner than planned.

Geometry, size, and surface activity of fillers all affect the relation with bitumen. Examination of physical-chemical mechanisms on the surface was made by Craus et al. [22]. They stated that greater surface activity of mineral materials promotes the strength of bond on filler-bitumen boundary and increase quantity of adsorbed bitumen.

According to Maidanova and Rozental [23], the following factors affect the adsorption of bitumen: specific surface area and activity of mineral filler, as well as the amount of SARA (saturates, aromatics, resins and asphaltenes) fractions of bitumen. In their opinion, there is an adsorption boundary within the bitumen-filler structure which influences the specific surface area of filler. They also stated that aromatic oils play a significant role in the adsorption phenomena. Aromatic oils and saturates form the greater part of bitumen. These components are responsible for plasticity, fluidity and elasticity of bitumen [24].

In his summary work, Lesueur [25] characterized limestone as a kind of “active filler”. In his opinion, asphaltenes building up bitumen presumably surround limestone particles through an adsorption layer. He also assumed that these adsorption layers are formed not only in case of limestone but every time independently from filler type.

Gou et al. [26] examined the effect of adsorption ability of mineral fillers on chemical and rheological properties of bitumen. Their results showed, which were obtained on asphalt mastics samples, that polar fractions of binder material can absorb on the surface of fillers. They also stated that the amount of adsorption is significantly influenced by the mineral composition of surface and also the specific surface area of fillers. In another research work of Gou et al. [27], the bitumen-filler interaction was observed by atomic force microscopy. They found that the effective thickness of bitumen on the filler surface was around 1 μm.

Taking into account the above literature results and methods, the test were performed. The experimental results may promote more accurate experience in the cohesion between bitumen and mineral fillers and their applicability in road construction.

1. MATERIALS AND METHODS

1.1. Sample preparation

During the research the Authors have examined conventional mineral materials used in asphalt technology (limestone, andesite, dolomite). The samples are originated from Hungarian locations. Limestone fillers were previously ground by the manufacturers. Andesite and basalt rocks were available in 2/4 mm fractions, which were ground in planetary ball mill after washing and drying. After grinding, fine fillers were fractioned by a standard sieve of 0.063 mm nominal particle size. Samples were then dried to weight constancy and closed air-proof for further examinations.

1.2. Testing methods

Particle size distribution (PSD) of the ground material was measured by a HORIBA LA-950V2 laser diffraction particle size analyzer in wet mode using distilled water as dispersing media and sodium-pyrophosphate as dispersing agent applying the Fraunhofer-theory as evaluation method. Before the measurements 1-minute ultrasonic treatment was applied on the samples for better dispersion.

For morphological tests Carl Zeiss EVO MA10 scanning electron microscope (SEM) was used. High resolution electron micrographs were taken in different magnifications for further observation. The aim of this technique was to observe morphology and geometrical features of fillers.

Specific surface area (SSA) of the fillers (by BET-method) was determined by TriStar 3000 instrument (manufactured by Micromeritics). The method of this instrument is based on physical absorption and capillary condensation, and it works in volumetric mode. The fine filler samples were prepared with the use of SMARTPREP instrument. Adsorption-desorption isotherms, BET-specific surface area of samples were determined.

Hydrophilic coefficient of fillers was determined by sedimentation method. 5 grams of fine materials were weighed and put in a 25 ml measuring cylinder. In parallel, 10 ml of water and 10 ml of kerosene were poured into the cylinder. Fillers and liquids were thoroughly mixed together then the cylinders were filled with more liquid and closed with plugs. Volume of fillers was determined after 72 hours of sedimentation.

The air voids (or Rigden Void, RV) of dry compacted fillers were measured using the Rigden-apparatus, according to MSZ EN 1097-4:2008 standard [28]. To calculate RV, specific gravity of fillers is required, which were measured by pycnometric method. The knowledge of RV is useful in designing asphalt mixes and it is a good indicator for estimating stiffness.

German Filler Test [12] was done on the samples in order to determine the ability of oil adsorption. 15 grams of oil was mixed together with 45 grams of filler. A ball was tried to be formed from the mixture. If it was successful and the particles were held together by the oil, more filler – in 5 grams increments – was added. If the

mixture did not stick together anymore, the cohesion between the particles and oil was loosen. The reason of this is that oil filled the voids between the particles.

2. RESULTS AND DISCUSSION

Table 1 contains all of the relevant test results, which were obtained during the researches.

Table 1
Test results of mineral fillers

	Mineral filler			
	Limestone #1	**Limestone #2**	**Andesite**	**Basalt**
Average particle diameter, d_{50} [μm]	16.82	13.77	5.58	10.45
BET specific surface area, SSA [m^2/g]	0.93	1.55	4.62	2.99
Specific gravity, ρ [g/cm^3]	2.717	2.820	2.791	2.960
Rigden Void [%]	41.5	47.9	40.6	40.2
Oil adsorption (according to German filler test) [g]	95	50	75	75
Hydrophilic coefficient, η [–]	0.73	0.59	0.83	0.69

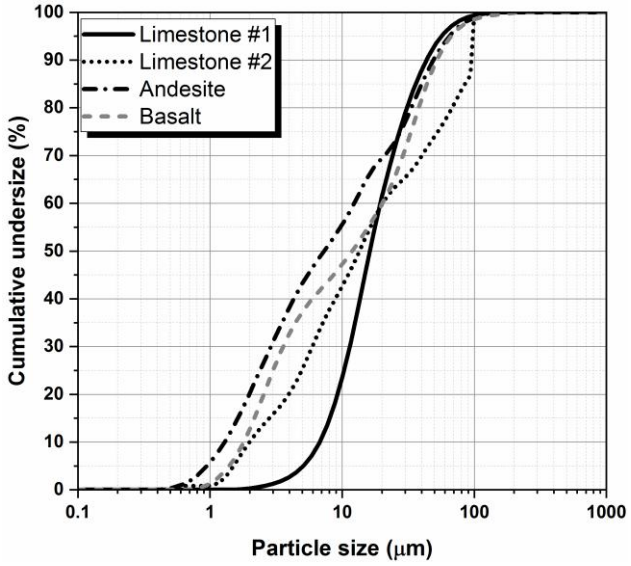

Figure 1
Particle size distribution of fillers

Figure 1 demonstrates the particle size distributions of fillers. According to the particle size distributions 80% of particles are smaller than 0.063 mm, in all cases. Based on the given data, it can be stated that andesite has the lowest average value (average particle size, d_{50}), with 5.58 µm. Limestone #1 has the highest median value with 16.82 µm. The reason for the differences between the average particle sizes of fillers is the way the rocks were ground. Limestones were ground by the manufacturers using industrial apparatus, while andesite and basalt were ground by the Authors in a lab scale.

In SEM micrograph *(Figure 2. a)* and b) of the limestones, relatively bigger, solid calcite particles can be seen. Small particles adhered on the surface of bigger particles. Bigger planar faces and planar fractures formed on other particles during grinding, especially in case of Limestone #1. Based on this, we can conclude a relatively small surface area which is favourable in view of bitumen quantity to be used.

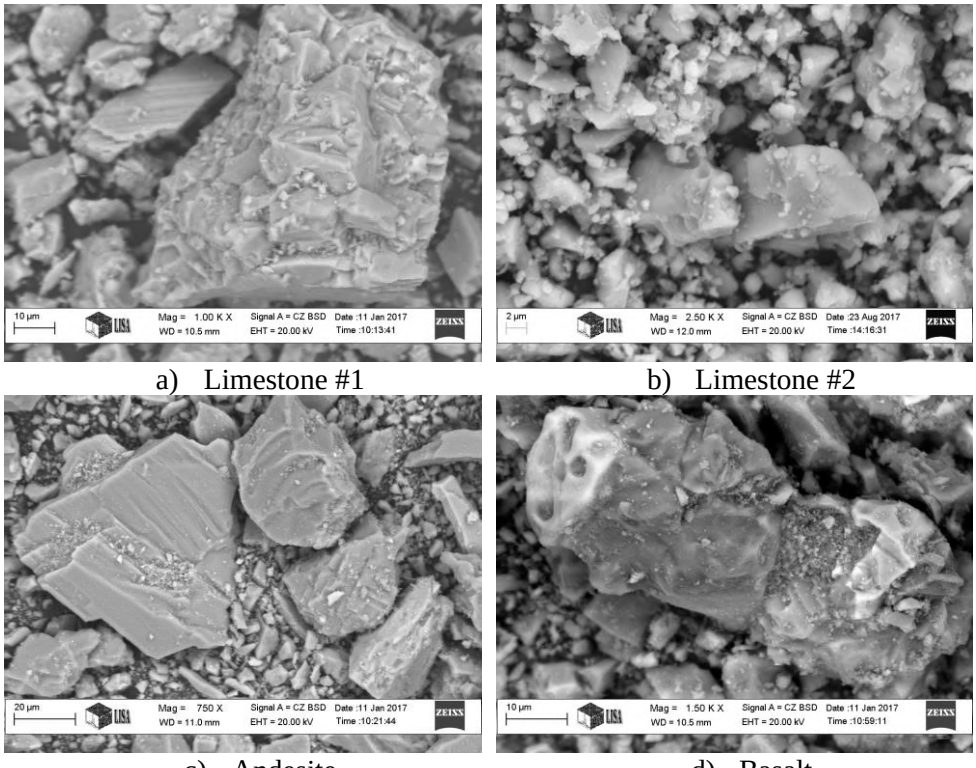

a) Limestone #1 b) Limestone #2

c) Andesite d) Basalt

Figure 2
SEM micrographs of fillers

A considerable polydispersity of the sample is well visible on the micrograph of andesite *(Figure 2. c)*. Besides the bigger, planar faced particles a great quantity of fine particles also occurs, but great part of them is of submicron size. We can observe

that fine particles adhered to the surface of the bigger particles. Particles formed during grinding have characteristically sharp edges and uneven fracture surfaces. Particles are considerably solid, there is no obvious trace of large pores, nevertheless the great number of submicronic particles refer to extensive specific surface area.

Polydispersity of the material fraction can also be observed on the SEM micrograph of basalt *(Figure 2. d)*. Just like in case of andesite, basalt also has those submicronic particles which may refer to extensive specific surface.

According to the N_2 adsorption tests the lowest specific surface area belongs to the Limestone #1 (0.93 m^2/g), while andesite has the highest SSA value (4.62 m^2/g). SSA values of the limestones are favourable referred to the quantity of bitumen to be used in asphalt mixture production. In case of using limestone as filler we do not need to calculate with excess of bitumen. Nevertheless, application of andesite may result in increased bitumen requirement, which affects, mainly worsens other features of the asphalt mixture (bleeding, rutting).

According to the void volume of the dry compacted fillers, Basalt has the lowest (40.2%), Limestone #2 has the highest (47.9%) RV values, which is related to particle size distribution. As Limestone #2 contains a relatively higher amount of coarser particles than the other samples, therefore the space between the particles (interparticle void) is higher.

Based on the results of Kandhal et al. [12], the German filler test is on one hand a standard for the rate of the Rigden Void and on the other hand provides information about the adsorption ability of the fillers. During the use of the method, hydraulic oil fills the air void among the particles of the filler used in the maximum extent. Besides, the oil layer formed on the surface of the particles presumably promotes better adherence of the particles to each other.

Research results showed that Limestone #1 was able to bind unit value of oil in the greatest volume (95 g), while Limestone #2 was able to bind the smallest volume (50 g). This presumes that voids content among Limestone #1 particles is small, therefore oil is able to hold a greater number of particles. However, voids content of Limestone #2 is high as it is able to hold only a minimal number of particles.

Determination of hydrophilic coefficient is based on the comparison of water and oil adsorption ability of the filler. Oil, like bitumen is an apolar material. However, during the examinations the Authors have used kerosene instead of oil, as this liquid has the same features as oil in view of the experiment, but due to its lower density sedimentation of the particles is faster. This is rather important, as value of the hydrophilic coefficient can be defined from the volume ratios (i.e. $V_{water}/V_{kerosene}$) of sedimented particles in these liquids. If the ratio value is more than 1, filler is hydrophilic; if it is less than 1, it is hydrophilic. Based on Ref. [8], hydrophilic coefficient of the good filler used in asphalt pavements is 0.7–0.85. Based on the results all the examined fillers are hydrophobic. Limestone #2 has the lowest ($\eta = 0.59$) hydrophilic coefficient, while andesite has the highest ($\eta = 0.83$). Hydrophilic coefficient of Limestone #1 and Andesite are in the optimal range, therefore these materials are able to form a good relationship with bitumen.

Based on a previous research result of the Authors [29] hydrophilic coefficient value of fillers ground from carbonate rocks (limestone, dolomite) is affected also by particle size. They found that the highest the ratio of fine particles in the given fraction is, the lowest the hydrophilic coefficient value will be. Liquid surrounds particles as a kind of layer. The thicker the layer surrounding the particles in the kerosene is, the better relation between this apolar liquid and the mineral material can be formed. Therefore, the higher the sedimentation volume of the particles in the kerosene is, the lower their hydrophilic coefficient will be.

CONCLUSIONS

The aim of this article was to present some research results, which were carried out on different mineral materials used in asphalt pavements. It can be stated, that particle size distribution have a great influence not only on the specific surface area and air void, but the cohesion between the fillers and bitumen. The results of the performed tests, contribute to a better understanding of the interaction between filler and bitumen.

ACKNOWLEDGEMENT

The described article was carried out as part of the EFOP-3.6.1-16-2016-00011 *Younger and Renewing University – Innovative Knowledge City – institutional development of the University of Miskolc aiming at intelligent specialisation* project implemented in the framework of the Szechenyi 2020 program. The realization of this project is supported by the European Union, co-financed by the European Social Fund.

REFERENCES

[1] Wang, L., Liu, H., Zhao, S. (2010). Aggregate gradation design of asphalt mixture with stone-to-stone contact based on fuller's model. *Journal of Shanghai University (English Edition)*, Vol. 14, pp. 387–390.

[2] ÚT 2-3.301-1:2010 Hungarian Road Paving Technical Specification (e-UT 05.02.11). *Útépítési aszfaltkeverékek*. Aszfaltbeton (AC); Magyar Útügyi Társaság (MAÚT), 2010. február 15.

[3] Chen, J., Kuo, P., Lin, P., Huang, C., Lin, K. (2008). Experimental and theorethical characterization of the engineering behavior of bitumen mixed with mineral filler. *Materials and Structures*, Vol. 41, pp. 1015–1024.

[4] Grabowski, W., Wilanowicz, J. (2008). The structure of mineral fillers and their stiffening properties in filler-bitumen mastics. *Materials and Structures*, Vol. 41, pp. 793–804.

[5] Kim, Y. R., Little, D. N. (2004). Linear viscoelastic analysis of asphalt mastics. *Journal of Materials in Civil Engineering*, Vol. 16, No. 2, pp. 122–132.

[6] Ishai, I., Craus, J. (1996). Effects of Some Aggregate and Filler Characteristics on Behavior and Durability of Asphalt Paving Mixtures. *Transportation Research Record: Journal of the Transportation Research Board*, No. 1530, pp. 75–85.

[7] Loorents, K.-J., Said, S. F. (2009). On mineralogical composition of filler and performance of asphalt concrete. *International Journal of Pavement Engineering*, Vol. 10, Issue 4, pp. 299–309.

[8] Gezentsvey, L. B. (1960). *Road asphalt concrete*. Moscow, Stroynadat.

[9] Anderson, D. A. (1996). Influence of fines on performance on asphalt concrete mixtures. *International Center for Aggregates Research (ICAR)*, 4th Annual Symposium, University of Texas at Austin (CD-ROM).

[10] Wang, H., Al-Qadi, I., Faheem, A., Bahia, H., Yang, S., Reinke, G. (2011). Effect of mineral filler characteristics on asphalt mastic and mixture rutting potential. *Transportation Research Record: Journal of the Transportation Research Board*, Vol. 2208, pp. 33–39.

[11] Clopotel, C., Bahia, H. (2013). The effect of bitumen polar groups adsorption on mastics properties at low temperatures. *Road Materials and Pavement Design*, Vol. 14 (Suppl. 1), pp. 38–51.

[12] Kandhal, P. S., Lynn, C. Y., Parker, F. (1998). Characterization tests for mineral fillers related to performance of asphalt paving mixtures. *NCAT Report*, No. 98–2, pp. 1–26.

[13] Shashidhar, N., Chollar, B. H., Rheological properties of asphalts with particulate additives. *ACS Division of Fuel Chemistry*, Vol. 41, No. 4, pp. 1307–1316.

[14] Shashidhar, N., Shenoy, A. (2002). On using micromechanical models to describe dynamic mechanical behavior of asphalt mastics. *Mechanics of Materials*, Vol. 34, No. 10, pp. 657–669.

[15] Liao, M. C., Chen, J. S., Tsou, K. W. (2012). Fatigue Characteristics of Bitumen-Filler Mastics and Asphalt Mixtures. *Journal of Materials in Civil Engineering*, Vol. 24, Issue 7, pp. 916–923.

[16] Sakharov, P. V. (1935). Methods for designing asphalt mixtures. *Transport and roads of the city*, No. 12.

[17] Lisihina, A. I. (1962). *Dorozhnye pokrytiya i osnavaniya s primeneniem bitumov i degtei.* Avtotransizdat, Moscow (In Russian).

[18] Cooley, L., Stroup-Gardiner, A. M., Brown, E. R., Hanson, D. I., Fletcher, M. O. (1998). Characterization of asphalt-filler mortars with Superpave binder tests. *Journal of Association of Asphalt Paving Technologists*, Vol. 67, pp. 42–65.

[19] Harris, B. M., Stuart, K. D. (1995). Analysis of mineral fillers and mastics used in stone matrix asphalt. *Journal of Association of Asphalt Paving Technologists*, Vol. 64, pp. 54–95.

[20] Kavussi, A., Hicks, R. G. (1997). Properties of bituminous mixtures containing different fillers. *Journal of Association of Asphalt Paving Technologists*, Vol. 66, pp.153–186.

[21] Hu, S., Zhang, H., Wang, J. (2006). Research on alkaline filler flame-retarded asphalt pavement. *Journal of Wuhan University of Technology*, Vol. 21, No. 3, pp. 146–148.

[22] Craus, J., Ishai, I., Sides, A. (1978). Some physico-chemical aspects of the effect and the role of the filler in bituminous paving mixtures. *Journal of Association of Asphalt Paving Technologists*, Vol. 47, pp. 558–588.

[23] Maidanova, N. V., Rozental, D. A. (2006). Asphalt adsorption in relation to the surface area of the mineral filler and content of aromatic oils. *Russian Journal of Applied Chemistry*, Vol. 79, No. 8, pp. 1386–1387.

[24] Paliukaité, M., Vaitkus, A., Zofka, A. (2014). Evaluation of bitumen fractional composition depending on the crude oil type and production technology. Selected Papers, The 9th International Conference "Environmental Engineering" 22–23 May 2014, Vilnius, Lithuania.

[25] Lesueur, D. (2009). The colloidal structure of bitumen: Consequences on the rheology and on the mechanisms of bitumen modification. *Advances in Colloid and Interface Science*, Vol. 145, pp. 42–82.

[26] Guo, M., Bhasin, A., Tan, Y. (2017). Effect of mineral fillers adsorption on rheological and chemical properties of asphalt binder. *Construction and Building Materials*, Vol. 141, pp. 152–159.

[27] Guo, M., Tan, Y., Yu, J., Hou, Y., Wang, L. (2017). A direct characterization of interfacial interaction between asphalt binder and mineral fillers by atomic force microscopy. *Materials and Structures*, Vol. 50, p. 141.

[28] MSZ EN 1097-4:2008. *Tests for mechanical and physical properties of aggregates*. Part 4: Determination of the voids of dry compacted filler. Standard.

[29] Géber, R., Kocserha, I., Gömze, L. A. (2013). Influence of composition and particle size distribution on the properties of limestone and dolomite asphalt fillers. *Materials Science Forum*, Vol. 729, pp. 344–349.

Materials Science and Engineering, Volume 45, No. 1 (2020), pp. 106–114.
DOI: 10.32974.mse.2020.010

THE EFFECT OF ALUMINIUM DROSS ON FIRED BRICK PRODUCTS

ALEXANDRA HAMZA[1] – ISTVÁN KOCSERHA[2] – ANDREA SIMON[3]

Abstract: In this research, the usability of aluminium dross – an industrial by-product – as an additive for the brick industry was investigated. Brick clay was used to prepare the mixtures, to which different amounts (6–24 wt%) of dross were added. The optimal moisture content (20 wt%) required for forming was determined in preliminary experiments. Volume and weight changes during drying and firing were calculated. Compressive strength, bulk density and water absorption tests were performed on the fired samples. As the most often used additives of the brick industry (e.g. sawdust and petroleum coke) may interact with a possible new additive during firing, mixtures containing 3.35 wt% sawdust and 1 wt% petroleum coke were also prepared. Our results showed that increasing the amount of dross reduced drying and firing shrinkage as well as body density, but increased water absorption. Compressive strength varied inversely to the dross content.

Keywords: additive, aluminium dross, ceramics, fired clay bricks, industrial by-product, recycling

INTRODUCTION

In the production of industrial products, almost always a by-product is created, the storage and disposal of which causes many problems for companies. Industrial waste accumulates over time and causes serious environmental and health damage in the long run [1, 2]. Aluminium industry is one of the industries producing the largest amount of hazardous waste – more than 4.5 billion kilograms of aluminium waste per year worldwide [3, 4, 5]. For this reason, it is important to recycle these industrial wastes and to create products that are useful to society and harmless to the environment.

One of the by-products of aluminium production is the slag, which is formed by the oxidation of molten aluminium due to the metal-air contact. The alumina generates a long, continuous layer on the surface of the melt, thus a certain amount of metallic aluminium is also present in this layer. Salt treatment is used to minimize oxidation [6, 7]. Typically, two different types of slag are distinguished: primary or

[1] FIEK, University of Miskolc
H-3515 Miskolc-Egyetemváros, Hungary
femhamza@uni-miskolc.hu
[2] Institute of Ceramic and Polymer Engineering, University of Miskolc
H-3515 Miskolc-Egyetemváros, Hungary
istvan.kocserha@uni-miskolc.hu
[3] Institute of Ceramic and Polymer Engineering, University of Miskolc
H-3515 Miskolc-Egyetemváros, Hungary
femandi@uni-miskolc.hu

white slag and secondary or black slag. 15–20% and 10% of aluminum can be recovered from white and black slag, respectively. Various methods, such as pyrometallurgy or hydrometallurgy, are developed to use slags as a secondary raw material but the amount of the recovered, usable material is small [8, 9].

The dross formed during the smelting of secondary aluminium has very little value so far, so researchers tend to neglect this by-product [8]. However, the generated solid waste can be used in the ceramic industry, including brick production. Fired brick is one of the most widely used building materials, made mainly using primary materials (clay, sand, water and other organic materials) [10]. The workability of numerous industrial by-products is being investigated, such as waste from the paper industry, cigarette butts, fly ash, sludge from textile sewage treatment plants, plastic fiber, straw, rice husk ash, granulated blast furnace slag, rubber, soda pulp, sawdust and red mud [11, 13, 14, 15, 16]. However, for each additive, it is important to examine their effect on the properties of the finished product.

In this experiment, the usability of dross originating from the smelting of secondary aluminium was investigated. The drying and firing shrinkage, weight loss, bulk density, water absorption and compressive strength of the samples were measured.

1. MATERIALS AND METHODS

1.1. Materials

The samples were prepared using yellow clay with low carbonate content as raw material. Its mineral composition was analysed by X-ray Powder Diffraction (Rigaku Miniflex II, Cu Kα, 2θ range from 3 to 90°). Quantitative results were obtained by Rietveld full-profile refinement analysis. The XRD pattern and the mineral composition of the clay are shown in *Figure 1* and *Table 1*.

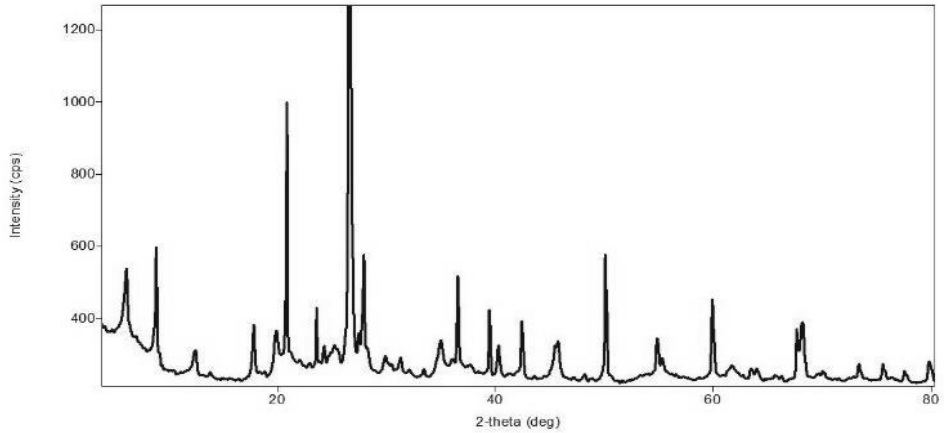

Figure 1
XRD pattern of the yellow clay

Table 1
Mineral composition of the yellow clay

Phase	Q	I	M	A	SM	G	K	M	C	D	CH	AM	WC
Quantity	41.1	24.2	5.0	5.5	6.1	3.3	6.7	4.4	–	–	2.3	10	6.6

(Q: quartz; I: illite; M: muscovite; SM: smectite; A: albite; G: goethite; K: kaolinite; M: microcline; C: calcite; D: dolomite; CH: chabazite; AM: amorphous content; WC: water content)

The main components of the dross were also identified by X-ray Powder Diffraction. The main phases of the dross were corundum, spinel, nordstrandite, wurtzite, sylvine and fluorite. The dross had a moisture content of 6 wt%, so it was dried before use.

Sawdust and petroleum coke, the most commonly used additives in the brick industry, were used as additional additives. Sawdust is one of the most commonly used pore-forming additives, which generates pores during firing and thus improves the thermal insulation of brick products. Petroleum coke is also added for the same reason. During the preparation of the mixtures, 3.35 wt% sawdust and 1 wt% petroleum coke, based on the dry weight of the clay, were added.

1.2. Mixture preparation

Table 2
Composition of the prepared mixtures in wt%

Clay/Dross	100/0	94/6	88/12	82/18	76/24

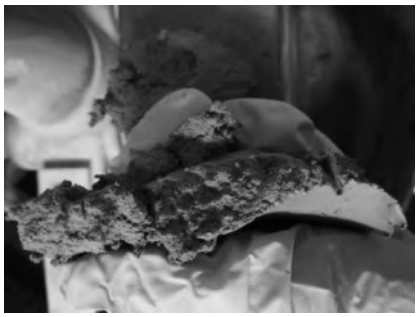

Figure 2
Homogenized mixture

Figure 3
Hermetically sealed mixtures

Two experimental series were made. In the first series only clay, dross and water were mixed. The clay was used without drying, with a moisture content of 6.6 wt%. This amount was taken into account when adjusting the moisture content. Dross and clay were mixed in their dry state by a laboratory pan mill. The amount of dross was 0, 6,

12, 18 and 24 wt%. In the second series, 3.35 wt% sawdust and 1 wt% petroleum coke, based on the dry weight of the clay, were added, and the dross content was also varied between 0–24 wt%. The moisture content was set to 20 wt% in both cases. Dross-clay mixtures were prepared at the ratios described in *Table 2*. The homogenized mixtures *(Figure 2)* were conditioned airtight for 24 hours after mixing *(Figure 3)*.

1.3. Sample preparation

After the conditioning, 16 samples with a diameter of 24 mm and a height of 50 mm were prepared from the mixtures by extrusion with a KEMA PVP 5/s equipment *(Figure 4)*. No cracks appeared on the extruded samples. The samples were then dried in a laboratory drying chamber to constant weight for 48 hours. The dried samples were fired at 860 °C and kept for 1 hour, the heating rate was 150 °C/hour. After cooling, the samples were removed from the furnace *(Figure 5)*. No cracks appeared on the samples after firing.

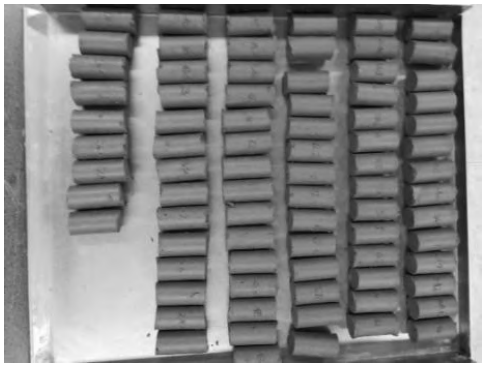

Figure 4
Extruded samples

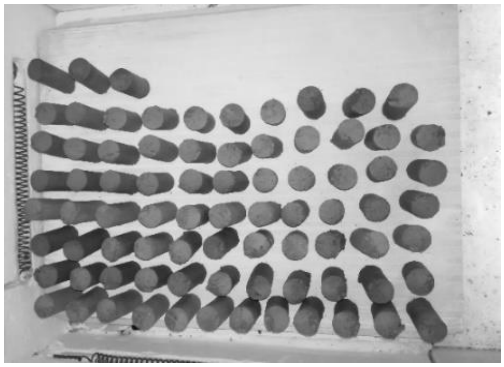

Figure 5
Fired samples

2. RESULTS AND DISCUSSION

2.1. Drying and firing shrinkage

As a result of the rise in temperature, various physical and chemical processes take place in the brick products during firing. Therefore, it is important to know the effect of certain materials on the drying *(Figure 6)* and firing *(Figure 7)* shrinkage and weight changes, as dimensional changes must be taken into account in advance during production. Therefore, the effect of the increasing amount of dross on these properties was examined. For each setting, measurements were performed on 10 extruded samples.

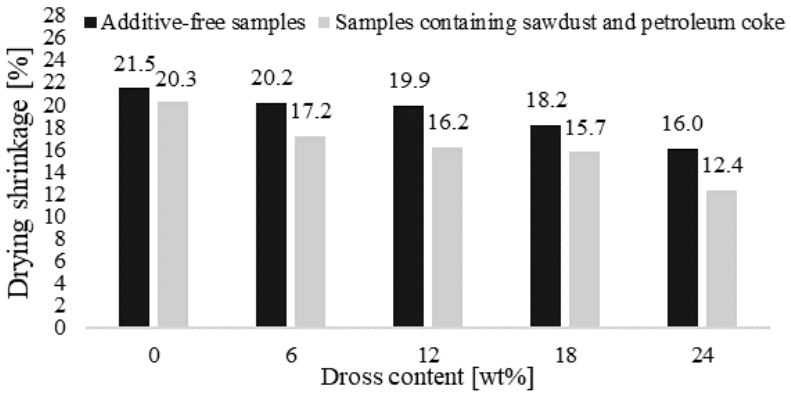

Figure 6
The effect of dross content on drying shrinkage

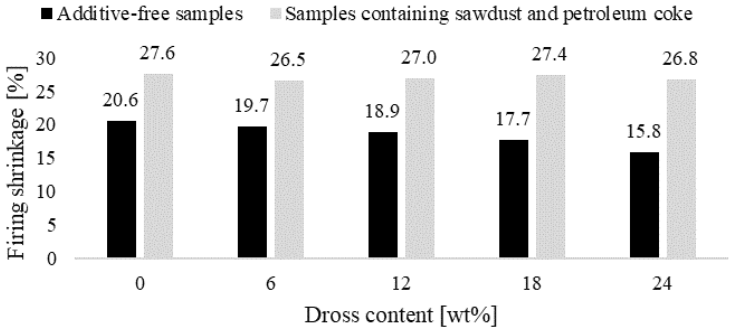

Figure 7
The effect of dross content on firing shrinkage

It can be seen in *Figure 6*, that the drying shrinkage of the samples decreases with increasing the amount of the dross. In the additive-free series, the drying shrinkage was reduced by 34% compared to the dross-free samples with the addition of 24 wt% dross while the series containing sawdust and petroleum coke showed a 40% decrease. Firing shrinkage also decreased with increasing dross content, but not as intensely as the drying shrinkage.

2.2. Water absorption and bulk density

To perform the measurement, the dried, fired samples were weighed using a digital balance, then placed into a pan and poured with distilled water until they were completely covered. The samples were heated and boiled for 3 hours (from the boiling of the water), making up for the amount of evaporated water. During the boiling the open pores were saturated with water. After boiling, the samples were cooled down

to room temperature and weighed again after soaking up the water from their surface. The test was performed on 10 fired samples for each series.

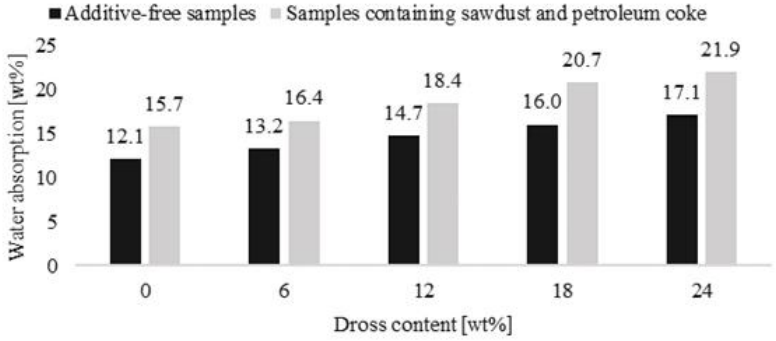

Figure 8
The effect of dross content on water absorption

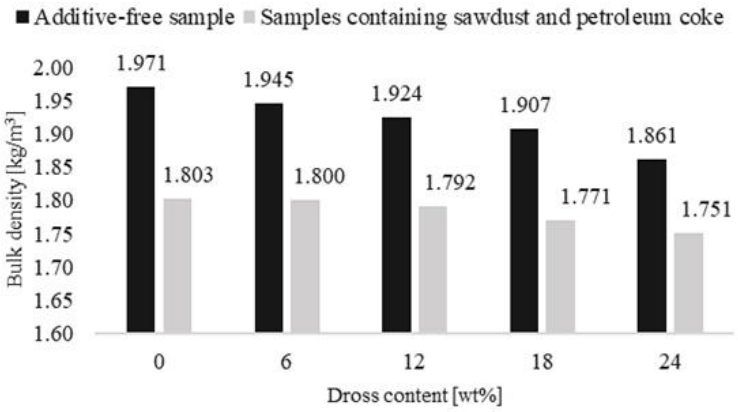

Figure 9
The effect of dross content on bulk density

The hydrostatic method was used to determine the bulk density 6 samples were measured per setting. The measurement was performed using a digital balance and a device developed for this measurement. The samples were placed in a hanging basket and immersed into distilled water. The device was fixed to a digital balance to measure the weight of the water displaced by the sample.

In both series, the water absorption increased directly with the amount of dross *(Figure 8)*, thus the addition of dross increased the amount of open pores. Adding 24 wt% dross resulted in a 30% increment compared to the dross-free samples in both series. Water absorption and bulk density are closely related, and it follows that increasing the proportion of dross reduced the bulk density of the samples.

2.3. Compressive strength

Compressive strength is one of the most important features for building materials. The measurement was performed on 10 samples per mixture, using a laboratory testing instrument with a measuring range of 10 t. As parallel surfaces are required for the measurement, the contact surfaces of the samples were ground to be parallel.

According to *Figure 10*, compressive strength significantly decreased with increasing the amount of dross, as the average compressive strength of dross-free samples was 30 MPa, which decreased to 21.12 MPa with the addition of 24 wt% dross. Compressive strength also decreased in the case of additive-free samples, but not to the same extent.

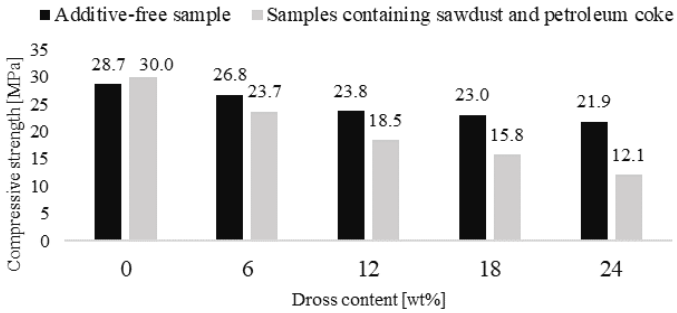

Figure 10
The effect of dross content on compressive strength

CONCLUSIONS

Our experiments have shown that drying and firing shrinkage decreased by increasing the amount of dross. As for the additive-free series, the drying shrinkage decreased from 21.5% to 16%, while for the series containing both sawdust and petroleum coke, it decreased from 20.3% to 11.5%. This is a favorable result, as it shows, adding dross can reduce the drying sensitivity and the resulting problems.

Water absorption increased with the amount of dross. In the case of 24 wt% dross content, the increment was 6% and 5% for the series containing additives and without additives, respectively. The addition of dross increases the proportion of open pores. Bulk density of the samples did not change significantly.

The most remarkable change was observed in compressive strength. Compared to the dross-free samples, the samples having 24 wt% dross content had 60% and 24% lower values for the series with and without additives, respectively.

ACKNOWLEDGEMENT

The research work is supported by the GINOP 2.2.1-15-2016-00018 project in the framework of the New Széchenyi Plan of Hungary, co-financed by the European Social Fund. The described study was carried out as part of the EFOP-3.6.1-16-2016-

00011 *Younger and Renewing University – Innovative Knowledge City – institutional development of the University of Miskolc aiming at intelligent specialisation* project implemented in the framework of the Széchenyi 2020 project. The realization of this project is supported by the European Union, co-financed by the European Social Fund.

REFERENCES

[1] Mahinroosta, Mostafa, Allahverdi, Ali (2018). Hazardous aluminum dross characterization and recycling strategies: A critical review. *Journal of Environmental Management*, Vol. 223, pp. 452–468.

[2] Xiao, Y., Reuter, M. A., Boin, U. (2005). Aluminium recycling and environmental issues of salt slag treatment. *J. Environ. Sci. Health*, Vol. 40, pp. 1861–1875.

[3] Abdulkadir, A., Ajayi, A., Hassan, M. I. (2015). Evaluating the chemical composition and the molar heat capacities of a white aluminum dross. *Energy Proced*., Vol. 75, pp. 2099–2105.

[4] Davida, E., Kopac, J. (2013). Aluminum recovery as a product with high added value using aluminum hazardous waste. *Journal of Hazardous Materials*, Vol. 261, pp. 316–324.

[5] Macaskie, L. E., Mikheenko, I. P., Yong, P., Deplanche, K., Murray, A. J., Paterson-Beedle, M. et al. (2010). Today's wastes, tomorrow's materials for environmental protection. *Hydrometallurgy*, Vol. 104, pp. 483–487.

[6] Tripathy, A. K., Mahalika, S., Sarangi, K., Tripathy, B. C., Sanjay, K., Bhattacharya, I. N. (2019). A pyro-hydrometallurgical process for the recovery of alumina from waste aluminium dross. *Minerals Engineering*, Vol. 137, pp. 181–186.

[7] Tenorio, J. A. S., Espinosa, D. C. R. (2002). Effect of salt/oxide interaction on the process of aluminum recycling. *Journal of Lights Metals*, 2, pp. 89–93.

[8] Ramaswamy, Parvati, Ranjit, Shravan, Bhattacharjee, Sushmit, Gomes, Sylvester Avijit (2019). Synthesis of high temperature (1,150 °C) resistant materials after extraction of oxides of Al and Mg from Aluminum dross. *Materials Today: Proceedings*, Vol 19, pp. 670–675.

[9] Meshram, Arunabh, Jain, Anant, Gautam, Divyansh, Singh, Kamalesh Kumar (2019). Synthesis and characterization of tamarugite from aluminium dross: Part I. *J. Environ. Manage*., Vol. 232, pp. 978–984.

[10] Kocserha, I., Gömze, L. A., (2010). Friction properties of clay compounds. *Applied Clay Science*, Vol. 48/3., pp. 425–430.

[11] Junge, K. (2000). Additives in the brick and tile industry. *Ziegelindustrie International*, 12, pp. 25–39.

[12] Xuanye, Z. (2003). The use of residual materials in the Chinese brick and tile industry. *Ziegelindustrie International*, Vol. 4, pp. 22–27.

[13] Ducman, V., Kopar, T. (2007). The influence of different waste additions to clay- product mixtures. *Materials and Technology*, Vol. 41/6., pp. 289–293.

[14] Kristaly, F., Gömze, L. A., Papp, I. (2010). The Transformation of Added Vegetal Waste Materials during. *Clay Brick Firing Materials Science Forum*, Vol. 659, pp. 37–42.

[15] Raut, S. P., Ralegaonkar, R. V., Mandavgane, S. A. (2011). Development of sustainable construction material using industrial and agricultural solid waste: A review of waste-create bricks. *Construction and Building Materials*, Vol. 25, Issue 10, pp. 4037–4042.

[16] Kocserha, I., Hamza, A., Géber, R. (2018). The effects of red mud on clay compounds. *IOP Conf. Series: Materials Science and Engineering*, 426, 012026.

Materials Science and Engineering, Volume 45, No. 1 (2020), pp. 115–124.
DOI: 10.32974.mse.2020.011

THE INVESTIGATION OF SODIUM LAURYL SULPHATE AS FOAM STABILIZER IN CEMENT FOAMS

ALEXANDRA HAMZA[1] – ISTVÁN KOCSERHA[2]

Abstract: In this study, we investigated hydrogen-peroxide foamed cement foams to which we used sodium-lauryl-sulfate (SLS) as a foam stabilizing additive. The specimens were prepared cement, water, hydrogen peroxide, expanded perlite and the aforementioned foam stabilizer. The substances listed were applied in two series. In one the amount of foam stabilizer additive was 0.01 wt%, while in the other it was twice 0.02 wt% relative to the weight of the cement. The samples were foamed with a 30% hydrogen-peroxide solution in 4 wt%, 6 wt% and 8 wt%. As a result, we obtained specimens with a body density of 450–660 kg/m^3. The prepared samples had 0.89–2.24 MPa compressive strength on the 28th day. In addition, we examined the macro structure of the specimens.

Keywords: cement foam, body density, foam stabilizing, compressive strength, porosity

INTRODUCTION

Cement foam belongs within to the group of lightweight concretes, with a wide range of bulk densities from 300 to 2,000 kg/m^3. Research on this topic has been carried out since 1980 [1, 2]. Cement foam is a low density and high porosity building material, which we can prepare using by various methods. There are three common forms of making cement foams, which can be made by blowing air, using precursor foam or mixing a chemical foaming additive [3, 4, 5].

There are two types of chemical foaming additives: the most common one is aluminum paste and the other type is hydrogen-peroxide [6, 7, 8]. Hydrogen-peroxide is a strong oxidizing agent that is stable at low pH, however it decomposes in the presence of increasing alkalinity. As a result, the strong alkaline property of fresh cement slurry is a propitious condition for catalyzing the decomposition of hydrogen peroxide. Nevertheless, these are elements in the cement that further catalyze the decomposition process [9]. During the decomposition process bubbles are formed in the cement matrix which these promotes the production of high porosity cement foam. The degree of porosity and compressive strength are closely related. In this context it is not sufficient to determine only the percentage by the volume of the total

[1] FIEK, University of Miskolc
H-3515 Miskolc-Egyetemváros, Hungary
femhamza@uni-miskolc.hu
[2] Institute of Ceramic and Polymer Engineering, University of Miskolc
H-3515 Miskolc-Egyetemváros, Hungary
istvan.kocserha@uni-miskolc.hu

air content, since the mechanical properties are also strongly influence by the shape, size, and distribution of the pores [10, 11].

Fresh cement foam ages through a number of interrelated processes, which reduces the stability of the foam. Such a destabilizing process is fluid flow. As fluid flows, the fluid layers become thinner, thus causing the collapse of the foam sample resulting. The simultaneous presence of bubbles of different sizes improves fluid drainage. However, the presence of smaller and larger size bubbles leads to the diffusion of gases due to different internal pressures [12, 13]. Larger size bubbles also reduce the stability of the foam as the size of the bubble is directly related to the buoyancy force. As a result, the larger the bubbles the faster leave the system, which in dangers the preservation of the foam structure [14]. The bulk density and stability of cement foam can be affected by the addition of appropriate additives, these substances are increased by the viscosity of the solution [15]. Significant in current cement foam production foaming agents are added to create pores in the cement slurry. This is supported by applying various foam stabilizing additives [16, 17, 18]. A number of foam stabilizers have been investigated, such as calcium stearate, sodium-lauryl-ether-sulfate and sodium-lauryl-sulfate [15, 19].

In this study, we used sodium-lauryl-sulfate (SLS) as a foam stabilizer for the preparation of hydrogen peroxide foamed cement foams. During the tests, we changed the amount of foaming agent from 4 to 8 wt% and the foam stabilizing additive, then we observed the effect of these on the bulk density as well as the compressive strength of the specimens.

1. MATERIALS AND SPECIMEN DETAIL

1.1. Cement

CEM II / B-M (V-LL) 32.5 R composite Portland cement was used as raw material for the tests, which contains fly ash and limestone additives in an amount of 21–35 wt%. A quick-setting cement has a positive impact on the stability of the cement foam. Therefore, we chose rapid cement instead of conventional cement of normal setting time.

1.2. Foaming agent

Hydrogen peroxide is a strong oxidizing agent in which the oxygen atoms are peroxo-bonded to each other. The binding energy of the peroxo-bond is not high. Therefore hydrogen peroxide is thermodynamically unstable, thus quite decomposable, this decomposition process is used to produce cement foams. During the decomposition process water and oxygen are formed [9]. The rate of decomposition of H_2O_2 depends on the alkalinity of the solution: at pH = 10.3 the rate of decomposition is 4-5 times higher than in neutral water [20, 21]. This property is also preferential for the production of cement foams, as fresh cement sludges are strongly alkaline in nature. A 30 wt% hydrogen-peroxide solution was used to prepare the specimens.

1.3. Foam stabilizer

Foam stabilizing additives to play an important role in the production of cement foam, whereas it greatly effects the foam structure formed and the stability of the fresh cement foam produced by the foaming additive. The stabilizers used are generally surfactants which reduce the surface tension of the water. Synthetic surfactants can be further divided into anionic, cationic, amphoteric and non-ionic tensides. Anionic surfactants are the most common due to their low cost [22]. For this reason, sodium-lauryl-sulfate (SLS) was chosen, which belongs to the group of anionic surfactants with a molecular weight of 288.38 g/mol.

1.4. Other additives

As a further, expanded perlite (ANZO P2) was added, which is one of the most popular admixtures in lightweight concrete due to its low body density and excellent thermal insulation. During production, the crude mined perlite is heated to 760–1,100 °C at this temperature, the substance becomes pyroplastic and the water inside it becomes water vapor and increases 4–20 times the original volume of the substance [23, 24]. The energy properties of the expanded perlite are excellent. Due to its high water absorption capacity, it facilitates the post-treatment of concrete. As water-saturated expanded perlite provides water for the later hydration of the cement [25]. In our previous studies, we found that applying expanded perlite during the preparation of cement foams resulted in a more stable fresh cement foam. For this reason, we included in the formula for cement foams. A superplasticizer additive (Mapei Dynamon NG 1012) was also for production of cement foams. This ensured that the cement slurry had sufficient consistency to be field moulds.

1.5. Cement foam preparation

Cement foams were prepared from cement, expanded perlite, water, superplasticizer, foaming agent and foam stabilizer additives. Two series were prepared with different amounts of foam stabilizer. In the first series, the amount of foam stabilizer – relative to the weight of the cement – blended in the mixture was 0.01 wt% while in the other series this amount of double (0.02 wt%). For both series, we made specimens by mixing different volumes of hydrogen peroxide, which we adjusted to 4, 6, and 8 wt%. The w/c ratio was 0.6 in all mixtures, which includes the amount of water introduced with hydrogen peroxide.

The first step in sample preparation was to mix about 30% of the mixing water with the expanded perlite in order to reduced its dusting *(Figure 1)*. The perlite was then added to the weighed out cement. The amount of mixing water remaining was divided in to two parts. The superplasticizer was added to one part, and we dissolved the foam stabilizing additive in the other part *(Figure 2)*.

Figure 1
Expanded perlite mixed with water

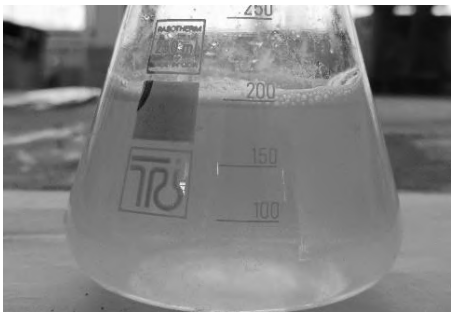

Figure 2
SLS dissolved in water

The moistened expanded perlite and cement were mixed with each other by an electric mixer *(Figure 3)*. After we obtained a homogeneous mixture we added the superplasticizer and the water containing the foam stabilizing additive. The cement slurry was further mixed with intensive mixing, the mixing time was 2 minutes, during which time the superplasticizer made the cement paste reasonably fluid *(Figure 4)*. Finally, diluted (30 wt%) H_2O_2 as the foaming agent was added to the cement slurry. The incorporation of hydrogen-peroxide was carried out by intense mechanical stirring for 10 seconds.

Figure 3
Mixing cement and perlite

Figure 4
Fresh cement slurry after mixing

The cement paste was filled into 70 × 70 × 70 mm moulds after mixing the hydrogen-peroxide. Then the moulds were vibrated with a vibrating table so that the slurry would fill the template evenly. Two hours after casting, top of the samples were removed with a wire. After 24 hours, the moulds decomposition was also performed *(Figure 5)*. The samples had been cured for 28 days at 22 °C under water.

Figure 5
Specimens after template disassembly

2. TESTING OF SPECIMEN

2.1. Compressive strength

The samples were fractured at 28 days of age for compressive strength testing. Three specimens were tested for all mixtures. The compressive strength test was performed with an INSTRON electromechanical tensile-pressure device. The results of compressive strength are included in Table 1 and graphically illustrated in *Figure 6*.

Table 1
Compressive strength and body density of specimen

	Compressive strength [MPa]			**Body Density [kg/m^3]**		
Content of H_2O_2	4 wt%	6 wt%	8 wt%	4 wt%	6 wt%	8 wt%
SLS 0.01wt%	2.24	1.85	1.37	662	557	472
SLS 0.02wt%	1.48	1.20	0.84	615	533	456

As it is shown in *Figure 6* the compressive strength of the samples with 0.02 wt% SLS was lower that of samples made with 0.01 wt% foam stabilizer. The compressive strength of specimens prepared with 4 wt% hydrogen peroxide decreased from 2.24 MPa to 1.48 MPa by doubling the amount of SLS. Numerical values are summarized in *Table 1*.

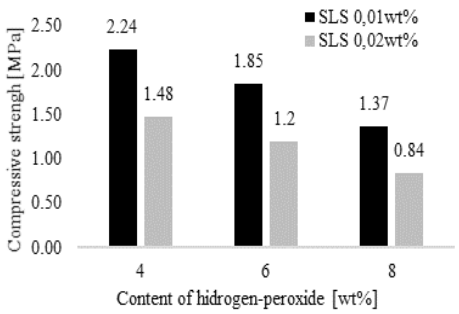

Figure 6
Compressive strength

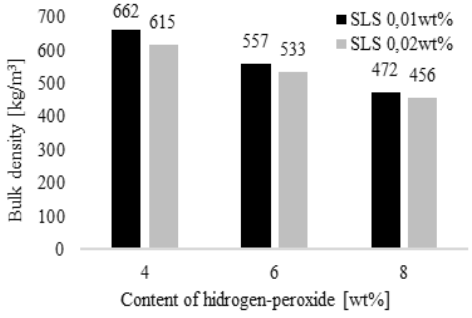

Figure 7
Bulk density

2.2. Bulk density of specimens

The samples were dried at 105 °C to constant weight. Bulk density was calculated for three samples per mixtures. After drying, lengths and weight of the specimens were measured and bulk density was calculated as mass per unit volume. According to *Table 1* that doubling of foam stabilizing additive did not have significant impact on the value of bulk density. Analyzing *Figure 7* it can be seen that, the bulk density of the cubes made with 4 wt% H_2O_2 foaming additive showed a 7% decrease while the amount of foam stabilizer was doubling. For specimens containing 6 wt% and 8 wt% H_2O_2, this reduction was 4.5% in both cases.

2.3. Distribution of average pore size

Macro images were taken of the fracture surface of the specimens. Macrographs of the samples are shown in *Figure 8*. In the captured images, the diameters of the pores were measured using software called ImageJ, then the values were averaged for each specimen. From the pore size measurements *(Table 2)*, it can be concluded that as the amount of hydrogen-peroxide was boosted the pore diameters were increased. In this case the 0.01 wt% SLS mixing was clearly visible, larger pores were formed than when the 0.02 wt% mixing was used.

Table 2
Distribution of average pore size

	0.01 wt% SLS			0.02 wt% SLS		
Content of H_2O_2	4 wt%	6 wt%	8 wt%	4 wt%	6 wt%	8 wt%
Pore size [mm]	1.607	2.741	3.775	1.386	2.019	2.378

Figure 8 shows that as the ratio of hydrogen-peroxide increased, the pores which were differed more and more from the spherical shape. The sample was prepared with 0.01 wt% SLS and 8 wt% foaming additive showed the most distorted pore structure.

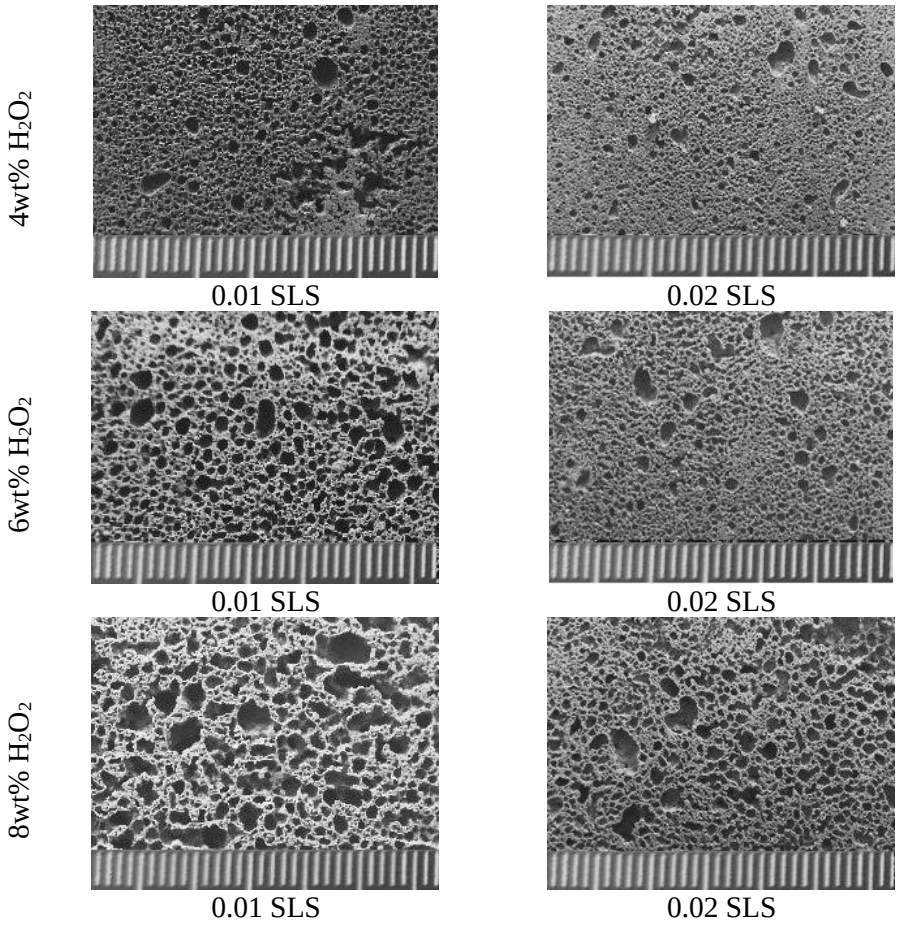

Figure 8
Macro structure of samples

CONCLUSIONS

Foam stabilizer additives promote the formation of an appropriate cement foam structure. It is most optimal for the foams to form spherical pores in an even distribution, which results in a stable fresh cement foam. For this purpose, we need to optimize a number of things, such as the w/c ratio, the amount of foaming and stabilizing additives, because the best combination of these materials gives the best results.

Investigations have revealed, that doubling the amount of SLS showed lower compressive strength values in all cases. Samples made with 0.02 wt% SLS had ~35% lower compressive strength than the series containing 0.01 wt% foam stabilizer. For instance, the compressive strength of cubes prepared with 4 wt% hydrogen-peroxide decreased from 2.24 MPa to 1.48 MPa.

The bulk density of specimens did not change significantly by doubling the amount of foam stabilizer. The bulk density of the specimens made with 4 wt% H_2O_2 foaming additive showed a 7% decrease while in the case of specimens containing 6 wt% and 8 wt% hydrogen-peroxide respectively this reduction was 4.5%.

The macro structure of specimens prepared with two different amounts of SLS differed from each other significantly. The largest divergences were in the case of the cubes prepared with 8 wt% H_2O_2 content. The samples with a foam stabilizer content of 0.01 wt% showed a rather deformed picture at this foaming additive content. In addition, the average pore size of the cement foam was larger than in the case of the 0.02 wt% foam stabilizer.

According to these results based on, it can be said that, increasing the amount of foam stabilizing additive resulted in a uniform pore distribution and pore size. In contrast, the results of the compressive strength test showed a significant decrease.

ACKNOWLEDGEMENT

The described study was carried out as part of the EFOP-3.6.1-16-2016-00011 *Younger and Renewing University – Innovative Knowledge City – institutional development of the University of Miskolc aiming at intelligent specialisation* project implemented in the framework of the Széchenyi 2020 program. The realization of this project is supported by the European Union, co-financed by the European Social Fund.

REFERENCES

[1] Naveen Kumar, K., Vijayan, D. S., Divahar, R., Abirami, R., Nivetha, C. (2020). An experimental investigation on light-weight concrete blocks using vermiculite. *Materials Today: Proceedings*, Vol. 20, pp. 987–991.

[2] Pang, X., Singh, J., Jimenez, W. C. (2018). Characterizing gas bubble size distribution of laboratory foamed cement using X-ray micro-CT. *Construction and Building Materials*, Vol. 167, pp. 243–252.

[3] Feneuil, B., Roussel, N., Pitois, O. (2019). Optimal cement paste yield stress for the production of stable cement foams. *Cement and Concrete Research*, Vol. 120, pp. 142–151.

[4] Huang, Z., Zhang, T., Wen, Z. (2015). Proportioning and characterization of Portland cement-based ultra-lightweight foam concretes. *Construction and Building Materials*, Vol. 79, pp. 390–396.

[5] Mounanga, P., Gbongbon, W., Poullaina, P., Turcry, P. (2008). Proportioning and characterization of lightweight concrete mixtures made with rigid polyurethane foam wastes. *Cement and Concrete Composites*, Vol. 30, pp. 806–814.

[6] Mohammed, H., Hamad, A. J. (2014). A classification of lightweight concrete: materials, properties and application review. *International Journal of Advanced Engineering Applications*, Vol. 7, pp. 52–57.

[7] Dey, V., Bonakdar, A., Mobasher, B. (2014). Low-velocity flexural impact response of fiber-reinforced aerated concrete. *Cement and Concrete Composites*, Vol. 49, pp. 100–110.

[8] Hamza, A., Simon, A. (2019). Effect of Treated Aluminum Dross on the Properties of Foamed Concretes. *Materials Science and Engineering*, Vol. 44, No. 2, pp. 32–42.

[9] Hao, L., Wang, R., Zhang, L., Fang, K., Men, Y., Qi, Z., Jiao, P., Tian, J., Liu, J. (2014). Utilizing cellulase as a hydrogen peroxide stabilizer to combine the biopolishing and bleaching procedures of cotton cellulose in one bath. *Cellulose*, Vol. 21, pp. 777–789.

[10] Hilal, Ameer A., Thom, N. H., Dawson, A. R. (2015). On void structure and strength of foamed concrete made without/with additives. *Construction and Building Materials*, Vol. 85, pp. 157–164.

[11] Kearsley, Elizabeth Paulina (1999). *The effect of high volumes of ungraded fly ash on the properties of foamed concrete*. PhD thesis, University of Leeds.

[12] Guignot, Sylvain, Faure, Sylvain, Vignes-Adler, Michèle, Pitois, Olivier (2010). Liquid and particles retention in foamed suspensions. *Chemical Engineering Science*, Vol. 65, pp. 2579–2585.

[13] Saint-Jalmes, Arnaud (2006). Physical chemistry in foam drainage and coarsening. *Soft Matter*, 2 (10), p. 836.

[14] Jones, M. R., Ozlutas, K., Zheng, L. (2016). Stability and instability of foamed concrete. *Magazine of Concrete Research*, Vol. 68 (11), pp. 542–549.

[15] Siva, M., Ramamurthy, K., Dhamodharan, R. (2015). Sodium salt admixtures for enhancing the foaming characteristics of sodium lauryl sulphate. *Cement and Concrete Composites*, Vol. 57, pp. 133–141.

[16] Ghorbani, S., Sharifi, S., de Brito, J., Ghorbani, S., Jalayer, M. A., Tavakkolizadeh, M. (2019). Using statistical analysis and laboratory testing to evaluate the effect of magnetized water on the stability of foaming agents and foam concrete. *Construction and Building Materials*, Vol. 207, pp. 28–40.

[17] Panesar, D. K. (2013). Cellular concrete properties and the effect of synthetic and protein foaming agents. *Construction and Building Materials*, Vol. 44, pp. 575–584.

[18] Li, Tian, Huang, Fangmei, Zhu, Jiang, Tang, Jinhui, Liu, Jiaping (2020). Effect of foaming gas and cement type on the thermal conductivity of foamed concrete. *Construction and Building Materials*, Vol. 231, 117197.

[19] Wang, Zhenjun, Liu, Liang, Zhou, Junxiang, Zhou, Changjun (2016). Impacts of potassium permanganate ($KMnO_4$) catalyst on properties of hydrogen peroxide (H_2O_2) foamed porous cement slurry. *Construction and Building Materials*, Vol. 111, pp. 72–76.

[20] Haines, R. I., McCracken, D. R. (1989). Decomposition of hydrogen-peroxide under coolant chemistry condition. *Proceedings of the Water Chemistry of Nuclear Reactor Systems*, Vol. 5, pp. 309–310.

[21] Wu, Linda, Shoesmith, David W. (2014). An Electrochemical Study of H_2O_2 Oxidation and Decomposition on Simulated Nuclear Fuel (SIMFUEL). *Electrochimica Acta*, Vol. 137, pp. 83–90.

[22] Zhu, Han, Chen, Longlong, Xu, Jie, Han, Qinghua (2020). Experimental study on performance improvement of anionic surfactant foaming agent by xanthan gum. *Construction and Building Materials*, Vol. 230, 116993.

[23] Wang, Liang, Liu, Peng, Jing, Qiangshan, Liu, Yuanzhen, Wang, Wenjing, Zhang, Yu, Li, Zhu (2018). Strength properties and thermal conductivity of concrete with the addition of expanded perlite filled with aerogel. *Construction and Building Materials*, Vol. 188, pp. 747–757.

[24] Kapeluszna, Ewa, Kotwica, Łukasz, Pichór, Waldemar, Nocuń-Wczelik, Wiesława (2020). Cement-based composites with waste expanded perlite, Structure, mechanical properties and durability in chloride and sulphate environments. *Sustainable Materials and Technologies*, Vol. 24, e00160.

[25] Lura, P., Bentz, D. P., Lange, D. A., Kovler, K., Bentur, A. (2004). Pumice aggregates for internal water curing. *International RILEM Conference on the Advances in Concrete through Science and Engineering*, 26 Evanston, IL, pp. 137–151.

Materials Science and Engineering, Volume 45, No. 1 (2020), pp. 125–135.
DOI: 10.32974.mse.2020.012

INVESTIGATION OF ALUMINUM DROSS – GLASS MIXTURES

ALEXANDRA HAMZA[1] – ANDREA SIMON[2]

Abstract: Aluminium dross treated with hydrometallurgical process mainly consists of spinel, wurtzite and alumina. This composition makes the dross to be a promising secondary raw material for the ceramic industry. Many application fields (refractory, concrete, cement, alumina) are presented in the literature. However, as for the glass industrial application, there are limited research results available. In this study, the effect of aluminum dross and cyclone powder on the properties of melted glasses was investigated. Four drosses and two types of cullet (float and packaging glass) were used. The melting behaviour of the glasses and the mixtures were characterized by heating microscopy. Mineral phases of the raw and the melted materials were identified as well.

Keywords: aluminium dross, glass, glass colour, phases, heating microscopy, glass foaming

INTRODUCTION

One of the most important environmental issues is the handling of the waste materials. Especially the hazardous wastes can generate serious problems, as even their disposal need a lot of preparation and monitoring. One of the environment-friendly solutions is the recycling of the disposed waste materials. Industrial waste can be recycled in many fields, as raw material for road construction, buildings, glasses, glass-ceramics or composites.

Residues of metallurgical slags or drosses can be used as a replacement material for crushed stones in road constructions [1–6]. Using drosses or slags can enhance the friction behaviour and the wear resistance of the road. According to Yoshimura et al. [7], slags are suitable candidates as raw materials of refractory materials. The main phases of slags were $MgAl_2O_4$ and AlN, which may generate cracks during the firing. However, the appearance of the cracks did not influence the mechanical properties of the products. Treated drosses can be recycled in the production of calcium-aluminate [8] or other ceramic products [9–11].

Based on the composition of the slags/drosses *(Table 1)*, they can be mainly used in the preparation of MAS (MgO-Al_2O_3-SiO_2) glasses or glass-ceramics [12–17]. Properties of the glass-ceramic products are determined by the crystalline phases,

[1] FIEK, University of Miskolc
H-3515 Miskolc-Egyetemváros, Hungary
femhamza@uni-miskolc.hu
[2] Department of Ceramics and Polymer Engineering, University of Miskolc
H-3515 Miskolc-Egyetemváros, Hungary
simon.andrea@uni-miskolc.hu

the composition of the glass and the nucleating agents [18]. The most important crystal-forming additives are ZrO_2, TiO_2, P_2O_5 and Cr_2O_3 [19]. Another perspective for the drosses are the ceramic glazes. Chemical resistance of the glaze can be enhanced by adding waste materials (float glass, granite, limestone) to the ingredients of the glaze [20]. This increase is due to the crystalline phases appeared in the glaze. Glasses are materials similar to the glazes. López-Delgado et al [26] studied CaO-Al_2O_3-SiO_2 (CAS) glasses to describe the vitrification of the Ald (Al dust). Silica sand, calcium carbonate and aluminium-rich waste, as a source of Al_2O_3, were used as raw materials. However, in the presence of humidity, toxic gases such as H_2, NH_3 and H_2S can be formed:

$$2Al + 3H_2O \rightarrow 3H_2\,(g) + Al_2O_3 \quad (1)$$

$$2AlN + 3H_2O \rightarrow 2NH_3\,(g) + Al_2O_3 \quad (2)$$

$$Al_2S_3 + 3H_2O \rightarrow 3H_2S\,(g) + Al_2O_3 \quad (3)$$

Table 1

Oxide composition (wt%) of some drosses

Reference		[7]	[8]	[21]	[22]	[23]	[24]	[25]	[26]
Oxides	Al_2O_3	84	65	63.29	67.3	87.57	64.8	68.18	66.2
	MgO	11	14	0.45	6.03	4.2	3.2	9.73	8.7
	SiO_2	2	13	6.36	4.14	2.77	4	13.04	
	CaO	1	3	20.2	4.83	0.85	0.93	0.82	3.9
	Na_2O	0.7	0.5	0.36	1.7	1.86	2.75	1.69	2.5
	K_2O	0.4	0.4	–	0.61	0.26	0.51	0.52	1.36
	Fe_2O_3	0.3	2	0.32	1	0.25	1.5	1.8	1.4
	TiO_2	0.3	1.5	–	0.69	0.13	–	0.61	1.46
	ZnO	–	–	0.93	–	–	–	–	1.45
	MnO	–	–	0.73	0.18	0.11	–	0.32	
	Al								16.5
AF**		A	B	C	D	D	E	C	F

* *average particle size*

** *AF: application field, A = refractory, B: Ca-aluminate, C: concrete, D: cement, E: η- Al_2O_3, F: glass*

This literature review shows that the applicability of aluminium dross as raw material for the glass industry has been limitedly studied and/or published. However, the composition of the treated aluminium dross may be suitable as a raw material for the glass industry, depending on the composition of the glass to be manufactured.

1. MATERIALS AND METHODS

4 types of dross (A-D), the cyclone fraction (coded as E), and two types of cullet (float and packaging glass) were used as raw materials. The phases of the drosses were identified by a Rigaku Miniflex II (Cu Kα, 2θ 3–90°, step size 0.02°, room temperature) table top X-ray diffractometer, with a PDXL2 software to evaluate the results. The Rietveld complete profile fitting procedure was used to quantify the phases. The chemical (oxide) composition of the glasses was measured using a ZEISS EVO MA10 scanning electron microscope equipped with an EDAX detector. Melting behaviour of the mixtures was studied with a Camar Elettronica MicrOVis heating microscope, in the 25–1,200 °C temperature range.

Powder mixtures were blended in a laboratory mixer for 5 minutes at 200 rpm. The glass:dross weight ratio was 9 : 1. The mixtures were placed into a porcelain crucible and heated up in a laboratory furnace to 1,300 °C according to *Figure 1*. After the melting, samples were left in the furnace to cool down to room temperature. Photos were taken on the melted-cooled samples with a Huawei P20 Lite device.

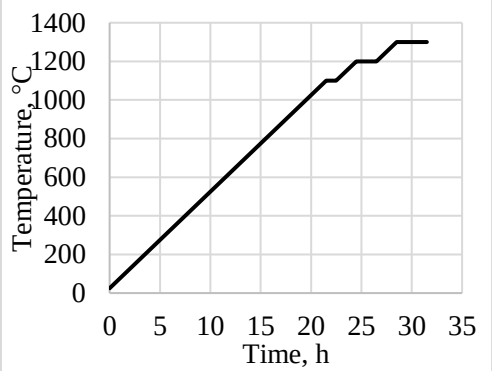

Figure 1
Heating profile

2. RESULTS AND DISCUSSION

The composition of the glasses *(Table 2)* is very similar. The main constituents are SiO_2, Na_2O and CaO. Small amounts of MgO, Al_2O_3, K_2O and Fe_2O_3 were also identified. The packaging glass contains a little more CaO, Al_2O_3 and Fe_2O_3 than the float glass. The main phases of the drosses *(Table 3)* are corundum, spinel and wurtzite. In addition, drosses contain salts (fluorite, halite, sylvite) and other compounds, like bayerite, calcite or periclase. Cyclone fraction has the highest amount of salt. Metallic aluminium and amorphous phase can only be found in the cyclone powder. Dross A and D has the highest amount of wurtzite, which can generate NH_3 gas in the presence of water. The ratio of spinel and corundum in the dross depends on the Mg content of the pristine alloy.

Table 2

Oxide composition (wt%) of the glasses

	SiO_2	Al_2O_3	MgO	CaO	Na_2O	K_2O	Fe_2O_3	S	F
Float*	69.1	0.83	3.28	8.00	12.8	0.29	0.51	0.19	<0.3
Packaging*	68.3	1.5	2.15	9.11	10.5	0.67	1.21	0.110	<0.3

**+other: MnO, TiO_2, P_2O_5 <0.075%*

Table 3

Mineral composition (wt%) of the drosses

Phase	Formula	Dross code				
		A	B	C	D	E
Corundum	Al_2O_3	**21.95**	**16.58**	**12.998**	**43.77**	**6.85**
Spinel	$MgAl_2O_4$	**55.33**	**65.1**	**71.14**	**32.07**	**53.07**
Wurtzite	AlN	**18.06**	**6.09**	4.86	**19.34**	**17.24**
Fluorite	CaF_2				1.74	3.36
Halite	NaCl	1.80	1.06	0.78	1.14	2.22
Sylvite	KCl	0.6	0.13	0.11	0.37	
Bayerite	$Al(OH)_3$		0.63	8.54	0.06	
Calcite	$CaCO_3$	2.26	0.40	1.57	1.52	1.21
Periclase	MgO	–				2.57
Aluminium						2.48
Amorphous						**11**
Total salt content		2.40	1.19	0.89	3.25	5.58

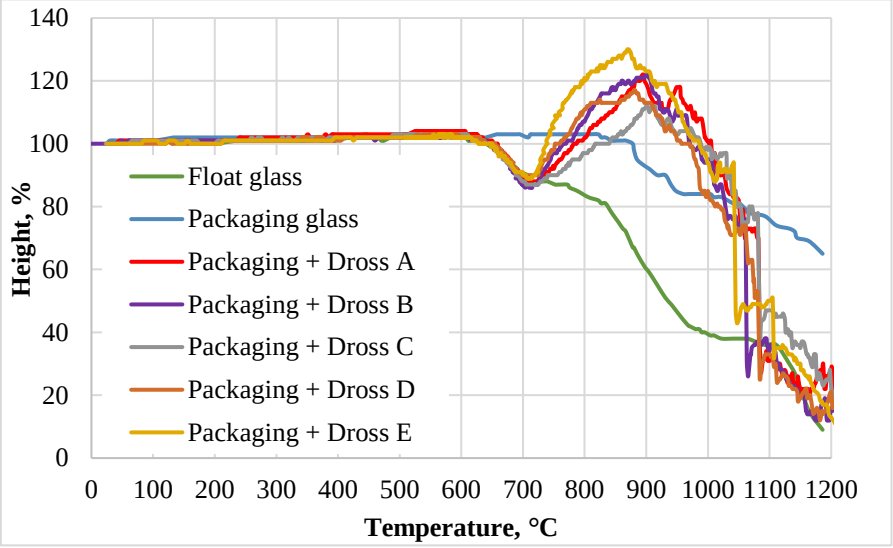

Figure 2

Heating microscopy profiles of the mixtures

Thermal properties (melting behaviour) of the glass/dross mixtures were investigated by heating microscopy. Melting profiles *(Figure 2)* of float and packaging glasses are quite similar, but float glass has lower characteristic temperatures. The addition of drosses reduced the sintering temperature of the packaging glass/dross mixtures, but increased the sphere-half sphere temperatures *(Table 4)*. However, the melting point temperature decreased in the presence of the drosses. These drosses contain salts that can reduce the melting temperature of the mixtures. All mixtures showed a foaming process between 700–1,050 °C due to the presence of AlN and $CaCO_3$, which generates gas development during the heating.

Table 4

Characteristic temperatures of the heating microscopy stages

	Sintering (°C):	**Softening (°C):**	**Sphere (°C):**	**Half sphere (°C):**	**Melting (°C):**
Float glass	671	827	855	931	981
Packaging glass	702	828	884	1,014	1,112
Packaging + Dross A	678	775	942	1,030	1,084
Packaging + Dross B	669	794	923	1,030	1,063
Packaging + Dross C	667	839	925	1,055	1,084
Packaging + Dross D	675	–	951	1,032	1,076
Packaging + Dross E	671	–	954	1,045	1,045

Figure 3 and *4* presents the photos of the melted mixtures. The signs of foaming are clear for the float glass + dross A and D mixtures. In the float glass + dross B and C mixtures, only small bubbles appeared at the walls of the crucible. Float glass + dross E sample was completely free from bubbles. The re-melted float glass had a slight greenish shade. Melted float glass + dross mixtures showed brown/amber colour. Float glass + dross B and C mixtures had a matte, strong brown colour, due to the change in the valence number of Fe ions. Float glass + dross E was the clearest mixture, where the glass phase is colour, but transparent, unlike the re-melted glass. This sample had less dense cracks than the pristine glass.

As for the packaging glass, the re-melted glass had no bubbles. Packaging glass + dross A, C and D had signs of small bubbles. Packaging glass + dross B sample contained more bubbles placed at the wall of the crucible. Re-melted packaging glass, and mixtures with dross B and E turned to green. Mixture with dross C had strong, greenish-brownish colour. Mixture A and D had brown shade. The colour of the glasses depends on the valence state of the ions and oxides in the glass structure. Every melted sample left a glassy coating on the inner part of the crucibles, due to the relatively high salt content.

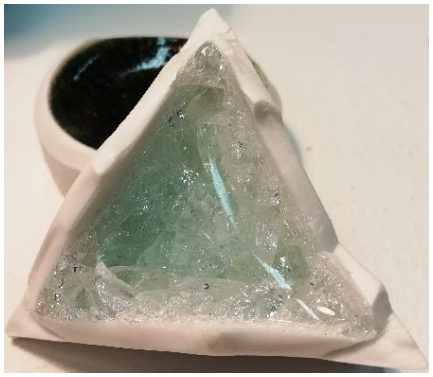

Float glass

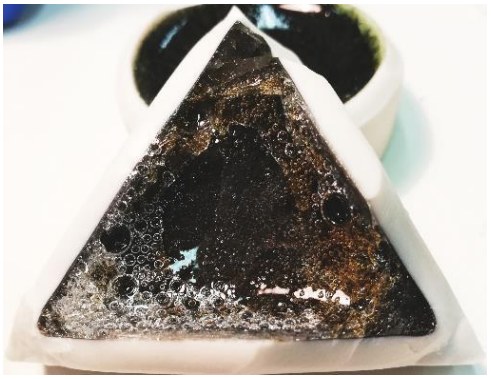

Float glass + Dross A

Float glass + Dross B

Float glass + Dross C

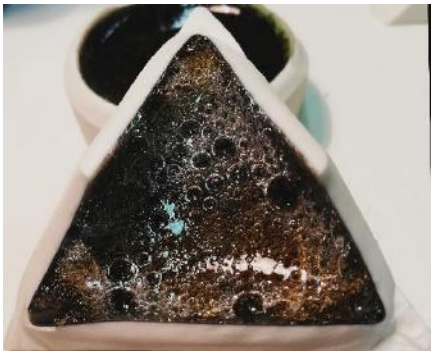

Float glass + Dross D

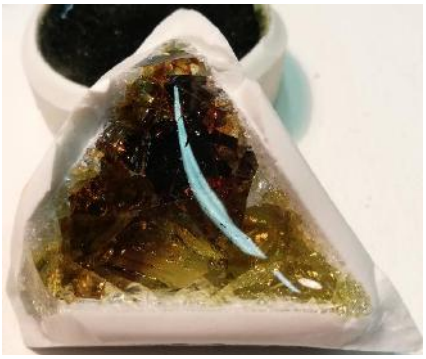

Float glass + Dross E

Figure 3
Photographs of the float glass based samples

Packaging glass

Packaging glass + Dross A

Packaging glass + Dross B

Packaging glass + Dross C

Packaging glass + Dross D

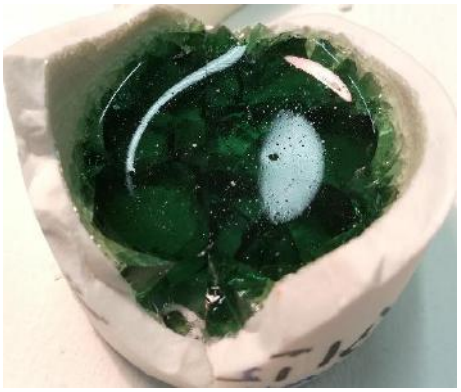

Packaging glass + Dross E

Figure 4

Photographs of the packaging glass based samples

Based on the X-ray diffraction analysis, the melted mixtures contain mainly amorphous phases with a small amount of crystalline phases. Quartz phase occurred in every sample as the main crystalline phase. In the re-melted float glass sodalite ($Na_4Al_3ClSi_3O_{12}$) was indicated by the analysis. In the float glass + dross C mixture, akermanite ($Ca_2Mg(Si_2O_7)$) was identified. Sodalite is a feldspathoid mineral of the tectosilicates which can appear in blue, grey, yellow, green, or pink colours [27]. Akermanite is a member of the sorosilicate group, which can be gray, green, brown, or colorless [28]. These phases can also be responsible for the colour change of the glasses.

CONCLUSION

In this study, the applicability of aluminium drosses with different composition as a raw material for the glass industry was investigated. Melting behaviour of different glass mixtures with 4 types of dross (A-D), cyclone fraction (coded as E), and two types of cullet (float and packaging glass) was characterized by heating microscopy. The shape of the melting profiles of the float and packaging glasses is quite similar but the float glass starts to melt at lower temperature. The addition of drosses increased the sphere-half sphere temperatures of the packaging glass/dross mixtures, but reduced the sintering and melting point temperature. The salt content of the drosses can reduce the melting point temperature of the mixtures. Independently from the dross type, all mixtures showed a foaming process between 700–1,050 °C which is due to the presence of AlN and $CaCO_3$. In both glasses, dross A and D generated bubbles during the melting. Dross B generated more bubbles in the packaging glass than in the float glass. Depending on the exact composition of the dross and the type of the glass, the dross changes the colour of the glass to green, brown or amber. The colour of the glasses depends on the valence state of the ions and oxides in the modified glass structure.

Based on the X-ray diffraction analysis of the re-melted mixtures, small amount of crystalline phases as quartz, sodalite, akermanite were found beside the amorphous fraction. Higher temperature and more time is needed to ensure the complete dissolution of the dross constituents to the glass. These phases can also contribute to the modification of the glass colour.

ACKNOWLEDGEMENT

The research work is supported by the GINOP2.2.1-15-2016-00018 project in the framework of the New Széchenyi Plan of Hungary, co-financed by the European Social Fund.

The described study was carried out as part of the EFOP-3.6.1-16-2016-00011 *Younger and Renewing University – Innovative Knowledge City – institutional development of the University of Miskolc aiming at intelligent specialisation* project implemented in the framework of the Széchenyi 2020 program. The realization of this project is supported by the European Union, co-financed by the European Social Fund.

REFERENCES

[1] Haritonovs, V., Zaumanis, M., Brencis, G., Smirnovs, J. (2013). Asphalt Concrete Performance with Conventional and Waste Aggregates. *Int. J. Pavement Res. Technol*., Vol. 6, No. 5, pp. 505–510.

[2] Ézsiás L. (2012). Kohászati salakok – a zúzottkövek megújult alternatívái az aszfaltgyártás területén. *Az Aszfalt*, Vol. 17, No. 1, pp. 16–20.

[3] Fang, F. T., Chong, Y. C., Nyunt, T. T., Loi, S. S. (2013). Development of Environmentally Sustainable Pavement Mix. *Int. J. Pavement Res. Technol*., Vol. 6, No. 4, pp. 440–446.

[4] Chen, J.-S., Wei, S.-H. (2016). Engineering properties and performance of asphalt mixtures incorporating steel slag. *Construction and Building Materials*, Vol. 128, pp. 148–153.

[5] Masoudi, S., Abtah, S. M., Goli, A. (2017). Evaluation of electric arc furnace steel slag coarse aggregate in warm-mix asphalt subjected to long-term aging. *Construction and Building Materials*, Vol. 135, pp. 260–266.

[6] Asi, I. M., Qasrawi, H. Y., Shalabi, F. I. (1986). Use of steel slag aggregate in asphalt concrete mixes. *Canadian Journal of Civil Engineering*, Vol. 34. pp. 902–911.

[7] Klaus, B., Horn, P. (1986). *Robot Vision*. Cambridge, MA, MIT Press.

[8] Yoshimura, H. N., Abreu, A. P., Molisani, A. L., de Camargo, A. C., Portela, J. C. S., Narita, N. E. (2008). Evaluation of aluminum dross waste as raw material for refractories. *Ceramics International*, 34, pp. 581–591.

[9] Pickens, John W., Morris, Edward L. (2001). *Process for preparing calcium aluminate from aluminum dross.* US Patent 6238633B1. https://www.google.tl/patents/US6238633 [Accessed May 20, 2020].

[10] Yerushalmi, Daniel, Sarko, Leonard (1995). *Method of recycling aluminum dross*. US Patent 5424260, https://www.google.tl/patents/US5424260 [Accessed May 20, 2020].

[11] Yerushalmi, Dan (1992). *Aluminum dross recovery process*. US 5102453 Patent, https://www.google.tl/patents/US5102453 [Accessed May 20, 2020].

[12] Stewart, Donald L. Jr., VanLinden, Jan H. L. (1993) *Process for the removal of salts from aluminum dross*. US 5227143 Patent, https://www.google.tl/patents/US5227143 [Accessed May 20, 2020].

[13] Rawlings, R. D., Wu, J. P., Boccaccini, A. R. (2006). Glass-ceramics: Their production from wastes. *A Review. Journal of Materials Science*, February 2006, Volume 41, Issue 3, pp 733–761., DOI:10.1007/s10853-006-6554-3.

[14] Bernardo, E., Varrasso, M., Cadamuro, F., Hreglich, S. (2006). Vitrification of wastes and preparation of chemically stable sintered glass-ceramic products. *Journal of Non-Crystalline Solids*, 352, pp. 4017–4023.

[15] He, F., Zheng, Y., Xie, J. (2014). Preparation and Properties of CaO-Al2O3-SiO2 Glass-ceramics by Sintered Frits Particle from Mining Wastes. *Science of Sintering*, 46, pp. 353–363.

[16] Hauwa, Isa (2011). A review of glass-ceramics production from silicate wastes. *International Journal of the Physical Sciences*, 23 November, Vol. 6 (30), pp. 6781–6790.

[17] Wang, Jing, Cheng, Jinshu, Tang, Liying, Tian, Peijing (2003). Effect of Nucleating Agents and Heat Treatments on the Crystallization of Magnesium Aluminosilicate Transparent Glass-ceramics. *Journal of Wuhan University of Technology-Mater. Sci. Ed*., Feb. 2013. DOI 10.1007/s11595-013-0642-4.

[18] Khater, G. A. (2010). Glass-ceramics in the CaO–MgO–Al2O3–SiO2 system based on industrial waste materials. *Journal of Non-Crystalline Solids*, 356, pp. 3066–3070.

[19] Shao, Hua, Liang, Kaiming, Zhou, Feng, Wang, Guoliang, Hu, Anming (2005). Microstructure and mechanical properties of MgO–Al2O3–SiO2–TiO2 glass–ceramics. *Materials Research Bulletin*, 40, pp. 499–506.

[20] Zanotto, Edgar Dutra (2010). A bright future for glass-ceramics. *American Ceramic Society Bulletin*, Vol. 89, No. 8, pp. 19–27

[21] da Silva, R. C., Pianaro, S. A., Tebcherani, S. M. (2012). Preparation and characterization of glazes from combinations of different industrial wastes. *Ceramics International*, 38, pp. 2725–2731.

[22] Mailara, Gireesh, Sujay Raghavendra, N, Sreedhara, B. M, Manu, D. S, Hiremath, Parameshwar, Jayakesh, K. (2016). Investigation of concrete produced using recycled aluminium dross for hot weather concreting conditions. *Resource-Efficient Technologies*, June, Volume 2, Issue 2, p. 68–80.

[23] Puertas, F., Blanco-Varela, M. T., Vazquez, T. (1999). Behaviour of cement mortars containing an industrial waste from aluminium refining. Stability in Ca(OH)2 solutions. *Cement and Concrete Research*, 29, pp. 1673–1680.

[24] Ewais, E. M. M., Khalil, N. M., Amin, M. S., Ahmed, Y. M. Z., Barakat, M. A. (2009). Utilization of aluminum sludge and aluminum slag (dross) for the manufacture of calcium aluminate cement. *Ceramics International*, December, Volume 35, Issue 8, pp. 3381–3388.

[25] Das, B. R., Dash, B., Tripathy, B. C., Bhattacharya, I. N., Das, S. C. (2007). Production of g-alumina from waste aluminium dross. *Minerals Engineering*, 20, pp. 252–258.

[26] Shinzato, M. C., Hypolito, R. (2005). Solid waste from aluminum recycling process: characterization and reuse of its economically valuable constituents. *Waste Management*, Volume 25, Issue 1, pp. 37–46.

[27] López-Delgado, Aurora, Tayibi, Hanan, Pérez, Carlos, Alguacil, Francisco José, López, Félix Antonio (2009). A hazardous waste from secondary aluminium metallurgy as a new raw material for calcium aluminate glasses. *Journal of Hazardous Materials*, 165, pp. 180–186.

[28] https://www.mindat.org/show.php?id=3701&ld=1&pho= [Accessed May 20, 2020].

[29] https://www.mindat.org/min-70.html [Accessed May 20, 2020].

Materials Science and Engineering, Volume 45, No. 1 (2020), pp. 136–142.
DOI: 10.32974.mse.2020.013

TEXTURE ANALYSIS AND CORROSION TESTING OF ALUMINIZED CARBON STEEL C45

HAWKAR J. MUHAMMED[1] – MÁRTON BENKE[2] –
DÁNIEL KONCZ-HORVÁTH[3] – ZSOLT SÁLYI[4] – TAMÁS I. TÖRÖK[5]

Abstract: The texture of hot-dip aluminized carbon steel C45 has been studied. Hot-dip aluminized (HDA) samples were prepared by laboratory experiments. The structure and crystal orientation of the topcoat layer of an aluminized specimen was analyzed through X-ray diffraction. The outcome of XRD reveals that the phase formed after removing the excess aluminum from the top surface (ripples) of the coated sample was FeAl, a non-stochiometric intermetallic with a Fe/Al atomic ratio of 1/1, but it also contains some impurity atoms, which cannot be identified with XRD. These impurity atoms modify the lattice plane distance d values of the FeAl phase, and as a result, the reflections shift. Lattice orientation of such a phase was found to be (110). Corrosion testing of the hot air-exposed (at 700 °C and for several hours) aluminized specimens were also performed, which revealed the still quite high wet corrosion (that is the salt water exposure at ambient air) resistance of the so modified outermost surface zone consisting of iron aluminides formed during the prior high-temperature exposure.

Keywords: Aluminizing, XRD, poles figure, iron aluminides, corrosion resistance

INTRODUCTION

Protection against oxidation and in general corrosion is essential to avoid degradation of the structure's material. Concurrently considering the structure of the coated material and interlayer(s) formed between the substrate and coated material is of primary importance due to the need to perpetuate stable structure withstanding even

[1] Institute of Metallurgy, University of Miskolc
H-3515 Miskolc-Egyetemváros, Hungary
hawkar@uni-miskolc.hu
[2] Institute of Physical Metallurgy, Metalforming, and Nanotechnology, University of Miskolc
H-3515 Miskolc-Egyetemváros, Hungary
fembenke@uni-miskolc.hu
[3] Institute of Physical Metallurgy, Metalforming, and Nanotechnology, University of Miskolc
H-3515 Miskolc-Egyetemváros, Hungary
femkhd@uni-miskolc.hu
[4] Institute of Physical Metallurgy, Metalforming, and Nanotechnology, University of Miskolc
H-3515 Miskolc-Egyetemváros, Hungary
femsalyi@uni-miskolc.hu
[5] Institute of Metallurgy, University of Miskolc
H-3515 Miskolc-Egyetemváros, Hungary
fektt@uni-miskolc.hu

in harsh environments at high temperature. Several researchers have studied the structure of aluminized carbon steel to depict the essential consistency of the coating layers. For example, the morphology structure at the coating/substrate interface was studied by Gul Hameed Awan and Faiz ul Hasan [1] and found on the XRD pattern that the interface was orthorhombic Fe_2Al_5 phase. Others, like Smiglewicz et al. [2] prepared samples of a specific Fe-Al binary alloy for studying its microstructure and phase changes at varying temperatures. They used a special VIM (vacuum induction melting) technique for producing the Fe-Al alloy casting/sample with 58 at.% aluminum. To modify the solidified sample microstructure (e.g., for grain refining), they also added small amounts (in total less than 0.2%) boron, carbon, and zirconium to the binary Fe-Al alloy. By XRD examinations, they identified the $FeAl_2$ phase present in the FeAl alloy prepared with the given composition, which coincides well with the phases appear in the Fe-Al equilibrium phase diagram [3]. Alboom et al. [4], while studying the structure of hot-dip aluminized steel and using several techniques (EDX, EBSD-Mapping, APT) combined with DFT calculations, detected two kinds of phases, $\theta(Fe_4Al_{13})$ and $\eta(Fe_2Al_{5+x})$ just beneath the aluminum cover layer.

In practice, several intermetallic layers that formed during any industrial HDA process, most often show a rather dis-ordered crystallographic structure. Nevertheless, the challenge from their exact identification point of view is that these intermetallic layers are usually fragile and never form an "ideal" stack of thermodynamically stable multilayers.

In our case, after preparing the aluminum-coated C45 steel specimens by the HDA process in one of our laboratories, the primary aim of our investigation was to measure the structure and crystal orientation of the coated sample's inner interdiffusion Fe-Al layer employing the XRD facilities available at the Institute of Physical Metallurgy, Metalforming, and Nanotechnology. In addition to that, a few preliminary laboratory corrosion testing experiments were also performed to see the high-temperature oxidation resistance behavior of the aluminized C45 steel specimens, because the primary aim of such aluminizing surface treatment of carbon steels is to enhance the corrosion resistance.

1. MATERIALS AND METHODS

Carbon steel C45 has been chosen considering their favorable mechanical properties and relatively cheap. Samples were off from a steel rod of 32 mm diameter, then cleaned, ground, and polished. For the hot-dip aluminizing route picked to aluminize carbon steel C45 samples, the molten bath was prepared in a graphite crucible with 98.01% aluminum content. Dipping time was set at 2.5 minutes, and the temperature of the commercially pure aluminum melt was 800 ± 2 °C. The disc shape steel samples were pickled in HCl solution (for de-scaling), then were ultrasonically degreased in acetone and stored in ethanol prior to aluminizing.

1.1. The XRD examinations

Due to the rather uneven original surface of the aluminized sample shown in *Figure 1*, first, it had to be prepared for the XRD analysis. The required flatness was achieved by grinding the top rippled surface of the sample; then, the specimen was mounted. X-ray diffraction was utilized to study the phase beneath the top surface of the aluminum and crystal lattice orientation at the top layer of coated aluminum. The applied Bruker D8 Advance type uses cobalt K-α radiation, and it was equipped with an Eulerian cradle. Besides the XRD phase analysis, the texture measurement was also performed on the sample to reveal the preferred orientation of the Fe-Al phase formed. The pole figure was measured up to a 75° tilting degree, and the absorption correction was carried out with ferritic steel powder.

1.2. Hot air corrosion testing

In this part of our studies, first, the hot-dip aluminized samples *(Figure 1)* were exposed to hot air (at 700 °C and for about 24 hours) in an electric resistance furnace in order to check the extent of the surface aluminum coatings transformation to the heat-affected and so modified surface zone mostly consisting of different iron aluminides [6].

Figure 1
Photos of three aluminized steel samples produced by the laboratory hot-dip aluminizing at 2.5 min. dipping time

2. RESULTS AND DISCUSSION

After careful removal of the excess aluminum from the surface of the aluminized steel discs, the so flattened specimens could be examined by our XRD device. The result of phase analysis detected by XRD is depicted in *Figure 2*. It is revealed that the phase in the interdiffused top layer below the solidified outermost excess aluminum coverage is a non-stochiometric intermetallic FeAl, i.e., with a Fe/Al atomic ratio is very close to 1/1, but it also contains some impurity atoms that have crystal lattice distance that differs from FeAl, which cannot be identified with XRD. These impurity atoms modify the d values of the FeAl phase, and as a result, the reflections shift *(Figure 2)*. From the XRD results of the interdiffused layer, one could conclude that this aluminized layer contains an aluminum content that might reach around 50 at.%. This observation

is also consistent with [2]. It is also apparent from the relative intensities of the FeAl phase that this phase is strongly textured. Texture measurements on the FeAl intermetallic phase revealed that the preferred orientation was (110) *(Figure 3)*. According to this, the vast majority of (110) planes of the FeAl phase are parallel with the sample's surface.

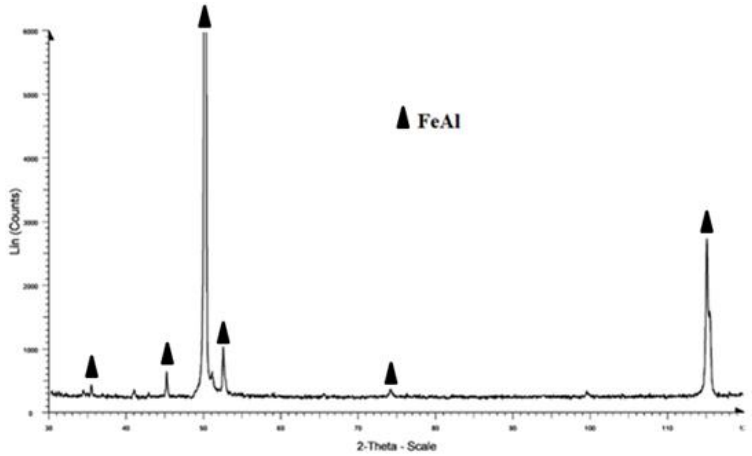

Figure 2

XRD-pattern of aluminized steel C45 interdiffused layer developed during 2.5 dipping time and recorded after removal of the topmost excess aluminum coverage

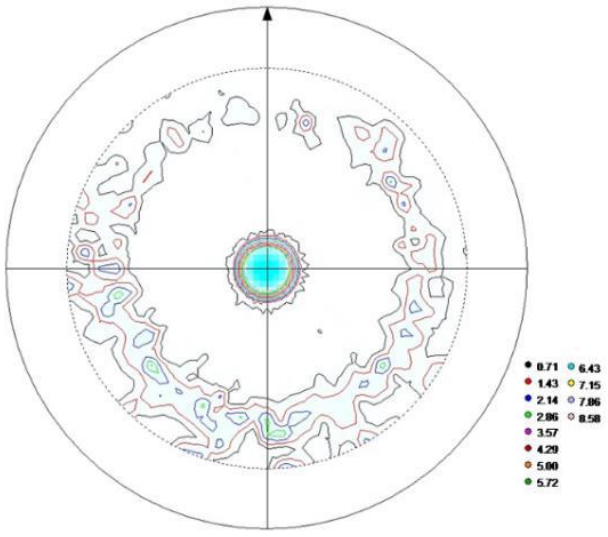

Figure 3

Pole figure of the FeAl intermetallic phase of {110}

High density appears in the middle of the pole figure, which means that the majority of the FeAl phase is oriented. It also can be observed that pole density is above 8 in the middle of the poles figure, which confirms that the developed texture is strong.

Carbon steel sheets aluminized in highly sophisticated and well-controlled industrial lines [6] have a surface aluminum coating of only around a few tens of micrometers. Under our laboratory conditions, however, the excess liquid aluminum was not shaved off either mechanically or using a so-called air knife. Hence, the disc-like steel specimen carried with it much excess adhering liquid aluminum that resulted in a somewhat uneven surface coverage (*Figures 1* and *4a*) after free (i.e., uncontrolled) cooling and solidification in ambient air. *Figure (4c)* shows the optical microscopy image of aluminized steel samples revealed three different zones; (1) steel substrate, (2) intermetallic, and (3) top aluminum.

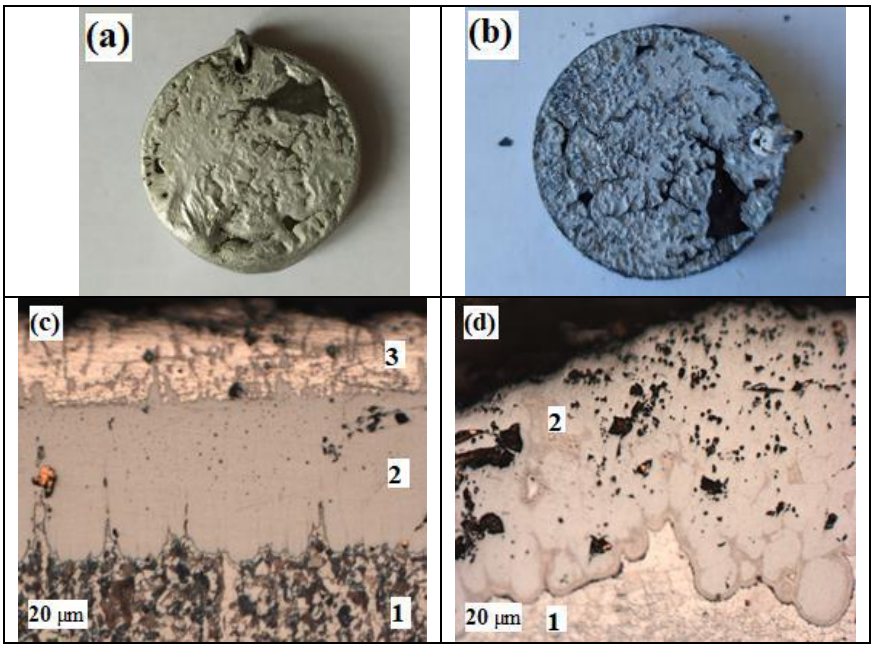

Figure 4

(a) Aluminized specimen (carbon steel C45 disc) with excess aluminum solidified on the top after removing the sample from the molten bath
(b) Aluminized specimen after hot air exposure at 700 °C for several hours showing a much-thinned aluminum surface coverage
(c) Aluminized specimen (carbon steel C45 disc) cross-section (OM image) revealing the layer structure of the hot-dip aluminized sample with 2.5 min dip time
(d) Partially oxidized intermetallic layer of the same sample after hot air exposure at 700 °C for 24 hours

After exposure to hot air inside the furnace, the topcoat surface, which is considered to be aluminum, has transformed (burn-off). Exposure to hot air causes the surface of aluminized steel to initiate a thin protective layer of aluminum oxide that can withstand against further oxidation, nevertheless, the aluminum beneath the aluminum oxide act as a reservoir to healing the top surface of the aluminum and produce aluminum oxide, hindering the oxidation progress inward steel substrate at least for a longer period compared to bare carbon steel. An aluminized sample is shown in *Figure (4a)* and its oxidized counterpart /i.e., after exposed to hot air for several hours/ is placed next to it in *Figure (4b)* just for visual comparison. As it is seen in *Figure (4b)* much of the original excess aluminum coverage not only thinned considerably but also developed a different surface morphology caused by the surface melting effect of the rather high temperature (~ 700 °C) that is a few tens degrees above the melting point of pure aluminum. *Figure (4d)* shows the optical microscopy image for the aluminized samples after exposure to hot air; the structure indicates that the aluminum top layer transformed to intermetallic, only two layers can be seen IM and substrate with some inclusions (oxide) in the intermetallic zone.

Otherwise, as it is well known [6], a relatively thin (<100μm) surface aluminum coatings at higher temperatures will diffuse inwards and form iron-aluminum intermetallic phases relatively fast. It means that in such cases and after several hours [5], it will be the alloyed aluminum surface of the initially aluminum-coated steel, which should resist any further attack of corrosion. And, indeed, it was observed after the neutral salt spray (standard NSS testing) exposure of 96 hours performed in one of our laboratories, that the originally white areas well covered with a thick aluminum layer did resist well the chemical attack of the neutral aqueous salt (NaCl) solution in the air at 35 °C. Moreover, even the originally bare-like small surface regions, where the outer surface must have consisted of iron aluminides, showed only some light brownish discoloration and formation of an only hardly detectable amount of rust-like surface corrosion products formed in the humid and wet salty air environment at around room temperature.

CONCLUSIONS

XRD phase analysis and texture analysis performed on the hot-dip aluminized C45 type steel specimen revealed that the formed FeAl phase is oriented in such a way that the (110) planes are parallel with the surface of the specimen. This result suggests that the FeAl intermetallic phase formed oriented instead of a random manner.

Exposing the hot-dip aluminized specimens to high temperature (700 °C in our case) in hot air must have caused the almost full conversion of the thinner (i.e., <100 μm) aluminum-coated areas to form iron aluminides in a few hours. Therefore, the high-temperature corrosion attack of air (i.e., via the iron oxide scale formation) can be mitigated, i.e., slowed down, as long as the aluminum content of the iron aluminides, something like an aluminum reservoir surface zone, can supply aluminum to form a thin protective aluminium oxide at the outermost surface of the HDA steel products.

As the wet corrosion resistance of commercially pure aluminum is quite high, and even higher than that of zinc, as long as the HDA coated carbon steel is covered with a coherent and sound aluminum layer, its wet corrosion resistance in neutral aqueous environments is also high; and such advantageous properties of the HDA coated carbon steels should contribute well to their even wider applications as that of today.

ACKNOWLEDGMENTS

The described article was carried out as part of the EFOP-3.6.1-16-2016-00011 *Younger and Renewing University – Innovative Knowledge City – institutional development of the University of Miskolc aiming at intelligent specialization* project implemented in the framework of the Szechenyi 2020 program. The realization of this project is supported by the European Union, co-financed by the European Social Fund.

REFERENCES

[1] Awan, G. H., ul Hasan, F. (2008). The morphology of coating/substrate interface in hot-dip-aluminized steels. *Mater. Sci. Eng. A*, Vol. 472, No. 1–2, pp. 157–165.

[2] Śmiglewicz, A., Jabłońska, M., Rodak, K., Tomaszewska, A. (2016). Study of the structure and thermal properties of intermetallics from Fe-Al system. *Acta Phys. Pol. A*, Vol. 130, No. 4, pp. 1004–1006.

[3] Kubaschewski, O. (1982). *IRON-Binary Phase Diagrams*. Berlin, Springer-Verlag.

[4] Van Alboom, A., Lemmens, B., Breitbach, B., De Grave, E., Cottenier, S., Verbeken, K. (2017). Multi-method identification and characterization of the intermetallic surface layers of hot-dip Al-coated steel: $FeAl_3$ or Fe_4Al_{13} and Fe_2Al_5 or Fe_2Al_{5+x}. *Surf. Coatings Technol.*, Vol. 324, pp. 419–428.

[5] Kobayashi, S., Yakou, T. (2002). Control of intermetallic compound layers at interface between steel and aluminum by diffusion-treatment. *Mater. Sci. Eng. A*, Vol. 338, No. 1–2, pp. 44–53.

[6] *Hot-dip aluminum-coated steel sheets, Nippon Steel Product Catalog*, https://www.nipponsteel.com/product/catalog_download/pdf/U034en.pdf.

Materials Science and Engineering, Volume 45, No. 1 (2020), pp. 143–152.
DOI: 10.32974.mse.2020.014

EXPERIMENTAL OVERVIEW OF STANDARD POLYCONDENSATION AND RING OPENING POLYMERIZATION METHODS OF PLLA

TIBOR HORVÁTH[1] – KÁLMÁN MAROSSY[2] – TAMÁS J. SZABÓ[3]

Abstract: The polylactic acid (PLA) is a well-known and widely used biodegradable biopolymer. The PLA could be produced by standard polycondensation and ring opening polymerization (ROP) technique. Each method has special requirements in order to synthesize polymers with appropriate properties and process efficiency. In this work both methods were applied to produce Poly-L-lactic (PLLA). During the experiments, method specific but various process parameters have been used. Regarding the ROP polymerization, a new oligomer separation method has been introduced. The base of this newly applied technique is the PLA oligomers' solubility in acetone and subsequent precipitation in water. The extracted crystal-like oligomers could be used for further polymer synthesis. The produced samples were analysed by FTIR and DSC methods to identify the structures and define the physical and chemical properties of synthetized materials. Over the polymerizations PLLA was plastified by adding of glycerol-dioleate.

Based on the trials' experiences the standard polycondensation and the ring opening processes have been compared and the effect of plasticizer was defined.

Keywords: PLLA, polycondensation, ring opening polymerization, FTIR, DSC, plasticizer

INTRODUCTION

The polylactic acid (PLA) is a natural sourced and - in case of proper circumstances – biodegradable aliphatic polyester used as pure or composite material on many fields of applications like medical, food industrial or other general purposes [1]. The lactic acid is a chiral molecule having two stereoisomers D-lactic acid and L-lactic acid as shown in *Figure 1.* By using of stereoisomers three different PLA types like the mostly crystalline poly(L-lactic)acid (PLLA), poly(D-lactic)acid (PDLA) and the mainly amorphous poly(DL-lactic)acid (PDLLA) can be synthetized [2] [3].

In general, the mostly used polymerization types for PLA are the standard polycondensation and the ring-opening polymerization [4]. In case of polycondensation

[1] Institute of Ceramic and Polymer Engineering, University of Miskolc
H-3515 Miskolc-Egyetemváros, Hungary
horvath.tibor70@upcmail.hu
[2] BorsodChem Zrt.
H-3500 Kazincbarcika, Bolyai tér 1, Hungary
kalman.marossy@borsodchem.eu
[3] Institute of Ceramic and Polymer Engineering, University of Miskolc
H-3515 Miskolc-Egyetemváros, Hungary
polsztam@uni-miskolc.hu

mainly low molar mass can be realized but new technologies are already available which suitable for producing PLA with appropriate molar mass [5]. From the other hand mostly the ROP method is used in that case when the high molar mass is required [6]. The polycondensation is a relatively simple but time-consuming process. Although the ROP method is also based on thermal polymerization of lactic acid but it is better form time demand point of view compared to the standard polycondensation, but it is more complicated technique [7].
Synthesis experiments have been carried out to test both methods. In case of PLLA produced by polycondensation method the material was plastified with adding of glycerol-dioleate.

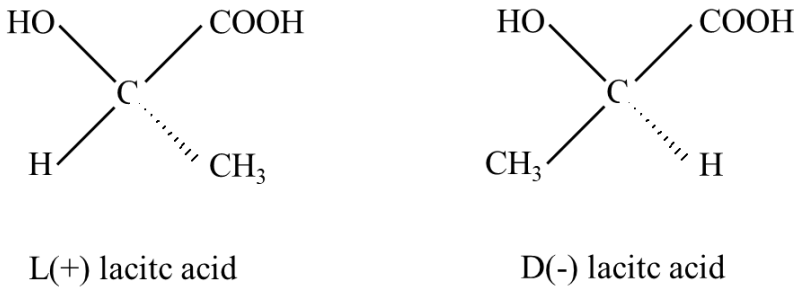

Figure 1
Stereoisomers of lactic acid [8]

1. MATERIALS AND METHODS

1.1. Materials

For the experiments, pure (general purity >90%; stereochemical purity of materials >99% L lactic acid was purchased from Musashino Chemical Laboratory Ltd. Stannous-octoate ($C_{16}H_{30}O_4Sn$) [9] [10] as catalyst and glycerol-dioleate ($C_{32}H_{72}O_5$, 536 $g \cdot mol^{-1}$) was used. These additional materials were ensured by University of Miskolc.

1.2. Methods and equipment

HEIDOLPH Laborota 400 efficient with joined Vacuubrand ME 1C type vacuum pump as basic equipment was used either to polycondensation or ring-opening processes. In case of ROP method higher temperature level had to be reached (180–220 °C) therefore the basic equipment was combined with 1260 VELP Arex-6 Digital additional apparatus. For weighing Precisa XR 2055SM machine was used. The laboratory with tools and equipment were provided by KISANALITIKA Kft.

All synthesized polymer samples have been analyzed by Fourier-transform infrared spectroscopy (FTIR) and Differential scanning calorimetry (DSC) methods. BRUKER Tensor 27 equipment was used for FTIR analysis, in case of DSC DSC131 Evo equipment was applied with dT/dt = 10 °C min^{-1} heating/cooling rates.

The analytical equipment was provided by Institute of Ceramic and Polymer Engineering at University of Miskolc.

Figure 2
HEIDOLPH Laborota 400 efficient with Vacuubrand ME 1C type vacuum pump as basic set-up for polycondensation

1.3. Synthesis of PLA by polycondensation method

During the experiment, the general steps of basic method were used and followed. Pure L-lactic acid was used as raw material. An appropriate amount (400 ml) of L-lactic acid has been added to a 1,000 cm^3 glass flask.

In the first step of polymerization the system was heated up to 80–120 °C to remove the water content of basic L-lactic acid solution. The time duration of this phase was 1 hour and 40 minutes. Then the temperature was set to 180 °C for 2 hours and 30 minutes to remove the organic solvents and remained water. In the last (polymerization) step 1%(V/V) catalyst was added to the system and gradually heated up to 160 °C. This step was continued for 72 hours. The system pressure was adjusted to 100mb for all of three steps and the reaction mixtures were stirred continuously.

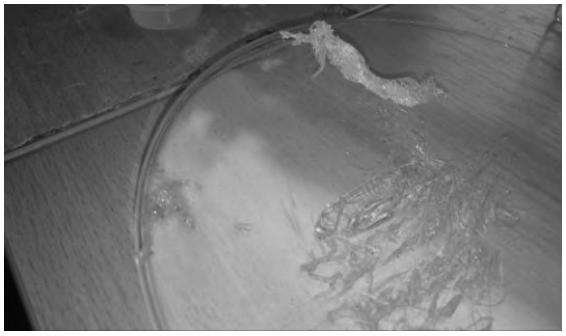

Figure 3
Strongly viscous PLLA samples taken from polymerization process

During the pre-polymerization and polymerization white, crystalline-like material was observed and removed from the neck of the flask and identified as lactide which is a by-product of the process. This lactide can be used for ring-opening process in case of ROP method.

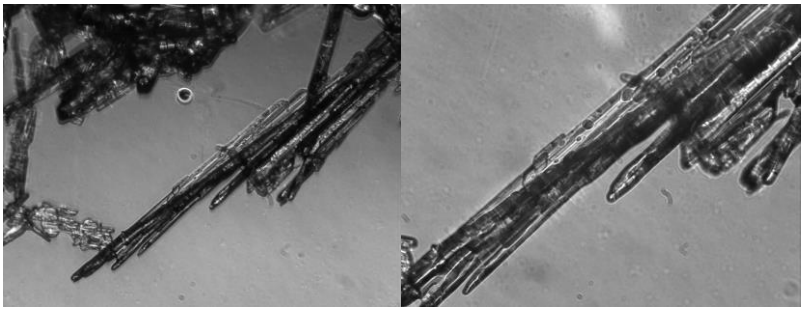

Figure 4
Microscopic images of L-lactides

Over the polycondensation the plastification of prepared PLLA samples was also carried out. During the experiment 6 g PLLA and 2 wt% (0,12 g) glycerol-dioleate as plasticizer were added to a 250 ml rounded reaction flask. The mixture was heated up to 160 °C under vacuum with continuous stirring and held on this environment for 1 hour.

1.4. Synthesis of PLA by ROP method

For ring-opening polymerization the same equipment with a small modification has been used. To be able to reach higher temperatures (200–220 °C), an additional heating apparat (1260 VELP Arex-6 Digital) was adapted to the system. In general, the ROP method can be divided for four steps as *dehydration*, *polymerisation*, *depolymerisation* and *ring-opening-polymerization*. The pressure was set to 100mb and the reaction mixtures were stirred continuously. For dehydration phase, various temperatures were used from 80 to 120 °C. The temperature for polymerisation was adjusted to 160 °C, for depolymerisation to 180–210 °C and for ROP it was set to 140 °C. Various reaction times were used for different steps.

During the lactide production phase of ROP a new material separation method was tested. The root problem is the removal of lactides and oligomers. In case of lactides, the lactide crystals already started to condensate in the neck part of reaction flask. Lactides could be removed periodically with scratching the inner surface of reaction flask. The other major problem was the removal of oligomers. It could be done in molten phase or as solution. The most efficient solvent for PLA is the chloroform [11]. Regarding this technique, to get the lactides and oligomers in solid phase a specific precipitant – like methanol – need to be used. [12] [13]. As the cost efficiency is a key aspect of industrial scaled usage of an alternative process, a more cost friendly method could be developed and tested.

In case of this newly applied method acetone was used as solvent, and then the lactides and oligomers were precipitated in distilled water. Thereafter the solid phase could be separated by filtration and dried in laboratory dryer at 40 °C for 4 hours. The extracted solid oligomers could be used to synthesize PLA with ROP polymerisation method. This process is going to be discussed in separated article.

Figure 5

Oligomers solved in acetone, precipitated and filtered & dried lactic acid oligomers

2. RESULTS AND DISCUSSION

2.1. Determination of sample materials' structure by Fourier Transform Infrared Spectroscopy (FTIR) method

All of the produced samples were analyzed by FTIR method to get information about and identify the structures of produced materials.

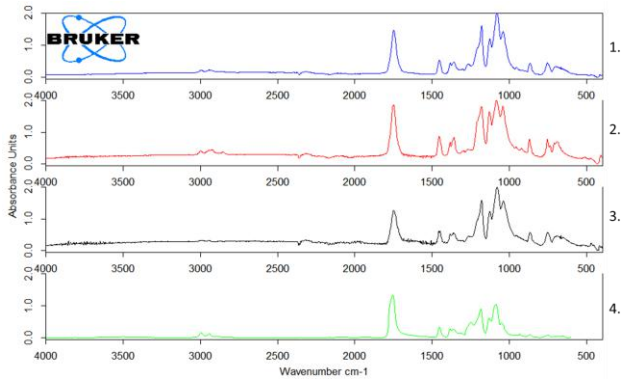

Figure 6

FTIR spectra of literature reference PLA (1) polycondensation produced PLLA (2), plasticized PLLA (3) and ROP method produced PLLA (4) samples

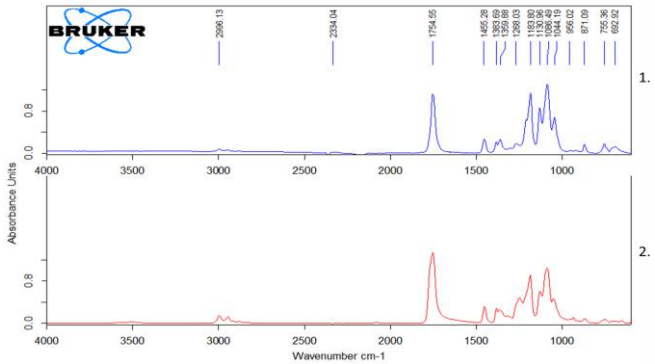

Figure 7

FTIR spectra of reference PLA (1) and lactic-acid oligomers (2) solved in acetone and precipitated in distilled water

The molecular structure related spectra of PLLA samples produced by polycondensation and ROP methods, as well as the plasticized PLLA are shown in *Figure 6*. The spectra of oligomers separated by the newly applied acetone dissolving method shown in *Figure 7*. Equalities have been observed and validated between the samples' FTIR spectra and reference library standard FTIR spectrum [14]. Therefore all analyzed polymers were identified as polylactic acid.

2.2. Differential Scanning Calorimetry (DSC) analysis of sample materials

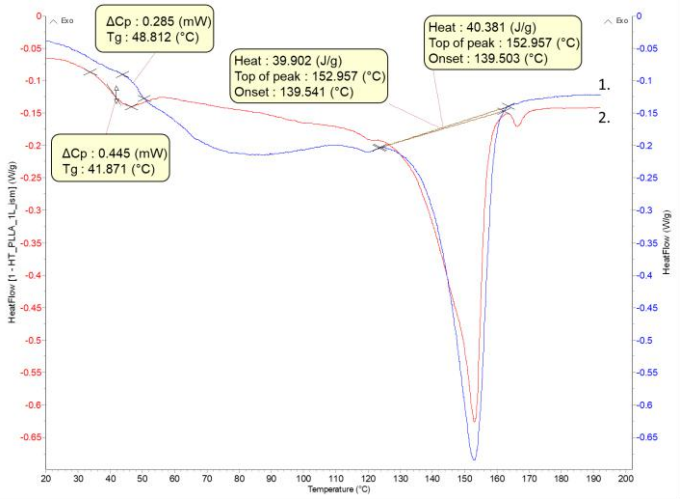

Figure 8

DSC curves of PLLA produced by polycondensation method (1) and its plasticized alternative (2)

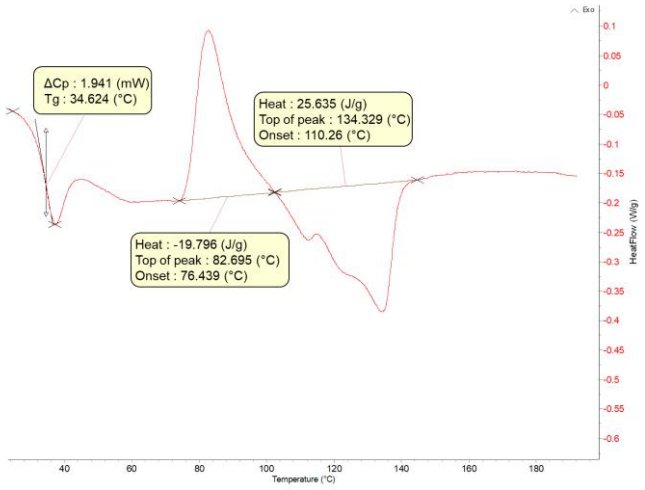

Figure 9
DSC curve of ROP method produced PLLA

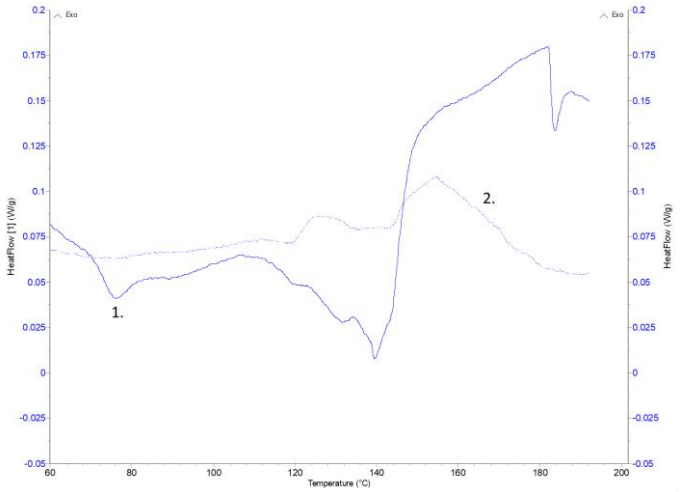

Figure 10
DSC curves (1.: first heating run, 2.: second heating run) of lactic-acid oligomers solved in acetone – precipitated in distilled water

Based on the DSC curves the Tg of polycondensation produced PLLA (*Figure 8*) was found at 48.8 °C. The Tg of its plasticized alternative was at 41.9 °C that validated that the glycerol-dioleate is an appropriate plasticizer for PLLA. Regarding the PLLA that was produced by ROP method the Tg=34.6 °C (*Figure 9*) was lower than in case of polycondensation produced PLLA that is referring to lower molar mass.

In case of alternative approach of lactic-acid oligomer removal, the DSC curves (*Figure 10*) proofing the absence of longer molecular chains as there are no thermoplastic material specific inter-structural processes like glass transition, recrystallization and degradation [15], i.e. the molar mass of this material is extremely low. This low molar mass of polymers is preferential for purpose of post-polymerization.

SUMMARY

The standard polycondensation is a quite time-consuming polymerization type for PLA as the release and removal of water is getting difficult as the process is progressed. Over that, to reach high molar mass is depends on parameters like temperature, system pressure, the general and stereochemical purity or raw material and the type of additives such as the catalysts.

The ring opening technique is much more time efficient method compared to the standard polycondensation, but from the other hand it is also more complicated. In this work both methods were applied to produce PLLA from L-lactic acid. Over the obvious time savings, higher molar mass can be reached with ROP technique but the process parameters need to be chosen carefully. This aspect of ROP method is recently under investigation, the results are going to be published in a separated study. The time need of polycondensation experiment was 72 hours and only 33 hours were used up for ROP method. Regarding the ROP polymerization, the process-time can be reduced by the adjustment of higher temperature of lactide production phase which is the most time-consuming part of this method, but this step needs to be done carefully to prevent the degradation of material.

In case of ROP technology related experiments, a new oligomer separation and removal method was successfully applied. This new approach aimed the separation and removal of oligomers is solid phase. During this process, the reaction mixture was cooled down to get into solid phase. Then this solid material was dissolved in an appropriate volume of pure acetone. The solution was passed into distilled water and the precipitated solid lactic acid oligomers were filtrated then dried. This powdered material which was identified as PLA by FTIR method could be used as basic material for post-polymerization.

ACKNOWLEDGMENT

This research was supported by the European Union ant the Hungarian State, cofinanced by the European Regional Development Fund in the framework of the GINOP – 2.3.4.-15-2016-00004 project, aimed to promote the cooperation between the higher education and the industry.

REFERENCES

[1] Babu, R. P., O'Connor, K., Seeram, R. (2013). Current progress on bio-based polymers and their future trends. *Progress in Biomaterials.* Vol. 2 (1), pp 1–16.

[2] Bodnár I. (2002). *Potenciálisan biodegradábilis, politejsav bázisú polimerek szintézise és vizsgálata*. Doktori (PhD-) értekezés, Debreceni Egyetem, Alkalmazott Kémiai Tanszék.

[3] Mehta, R., Kumar, V., Bhunia, H., Upadhyay, S. N. (2005). Synthesis of Poly(Lactic Acid): A Review. *Journal of Macromolecular Science; Part C*, Polymer Reviews, Vol. 45 (4), pp. 325–349.

[4] Jamshidian, M., Tehrany, E. A., Imran, M., Jacquot, M. (2010). Poly-Lactic Acid: Production, Applications, Nanocomposites, and Release Studies. *Comprehensive Reviews In Food Science and Food Safety*, Vol. 9, pp. 552–571.

[5] Hartmann, M. H. (1998). High-molecular-weight polylactic acid polymers. In: Kaplan, D. L. (ed.). *Biopolymers from renewable resources*. Berlin, Springer, pp. 367–411.

[6] Lopes, M. S., Jardini, A. L., Filho, R. M. (2014). Synthesis and Characterizations of Poly (Lactic Acid) by Ring-Opening Polymerization for Biomedical Applications. *Chemical Engineering Transactions*, Vol. 38, pp. 331–336.

[7] Singla, P., Kaur, P., Mehta, R., Berek, D., Upadhyay, S. N. (2012). Ring-Opening Polymerization of Lactide Using Microwave and Conventional Heating. *Procedia Chemistry*, Vol. 4, pp. 179–185.

[8] Lipsa, R., Tudorachi, N., Vasile, C. (2010). Poly polymers(α-hydroxyacids) in biomedical applications: synthesis and properties of lactic acid. *E-Polymers*, Vol. 10 (1), pp 1–43.

[9] Kaavessina, M., Chafidz, A., Distantina, S., Al-Zahrani, S. M. (2016). Characterization of Poly (lactic acid) Synthesized Via Direct Polycondensation With Different Treatments Of $SnCl_2$ As a Catalyst. *ARPN Journal of Engineering and Applied Sciences*, Vol. 11, No. 16, pp. 9992–9998.

[10] Puaux, J. P., Banu, I., Nagy, I., Bozga, G. (2007). A study of L-lactide ring-opening polymerization kinetics. *Macromol Symp.*, pp. 318–326.

[11] Oliveira, J., Brichi, G. S., Marconcini, J. M., Mattoso, L. H. C., Glenn, G. M., Medeiros, E. S. (2014). Effect of Solvent on the Physical and Morphological Properties of Poly(Lactic Acid) Nanofibers Obtained by Solution Blow Spinning. *Journal of Engineering Fibers and Fabrics*, Vol. 9, Issue 4, pp. 117–125.

[12] Parray, J. A., Yaseen Mir, M., Shameem, N. (2019). *Sustainable Agriculture: Biotechniques in Plant Biology*. Singapore, Springer, p. 320.

[13] Singh, V. M. (2008). *Synthesis of Polylactide with Varying Molecular Weight and Aliphatic Content: Effect on Moisture Sorption*. Master Thesis, Drexel University USA, PA.

[14] Cuiffo, M., Snyder, J., Elliot, A., Romero, N., Kannan, S., Halada, G. (2017). Impact of the Fused Deposition (FDM) Printing Process on Polylactic Acid (PLA) Chemistry and Structure. *Applied Sciences*, Vol. 6, 579, pp 1–14.

[15] Cao, X., Mohamed, A., Gordon, S. H., Willett, J. L., Sessa, D. J. (2003). DSC study of biodegradable poly(lactic acid) and poly(hydroxy ester ether) blends. *Thermochimica Acta*, 406, pp. 115–127.

Materials Science and Engineering, Volume 45, No. 1 (2020), pp. 153–162.
DOI: 10.32974.mse.2020.015

THE GRANULOMETRIC FEATURES AND PERMEABILITY EXAMINATION OF NO-BAKE RESIN BONDED SAND CORES

HENRIETTA HUDÁK[1] – LÁSZLÓ VARGA[2]

Abstract: A lot of natural and even more artificial sand is used in foundry technology. Foundry sand is the main element of sand mixtures from which molds or sand cores are made. The features of sand are determined by the below factors: chemical and mineralogical composition, sand grain's size, grain size distribution, sand grain's shape and the quality of the surface. Samples made from different foundry sand are used during the research whose features were examined with a new qualification system and then its connection with the gas permeability of sand cores were also analyzed.

Keywords: granulometry, grain size, grain morphology, grain shape, permeability

INTRODUCTION

Sand cores play a significant role in the production of high quality castings; therefore, the knowledge on the features of sand cores is of utmost importance. The thermal, mechanical and granulometric features of sand cores affect their deformation, gas permeability and shakeout. [1, 2]

Appropriate core sand mixtures are to be used in order to meet the requirements of castings. The main components of foundry molding and core sand mixtures, the different types of heat-resistant particulates (natural or synthetic sand) vary in their physical and chemical features, for example in the sand grain's size, shape, grain size distribution, chemical composition, surface structure, hardness, density, heat resistance, thermal expansion and thermal conductivity. [3, 4]

These features' knowledge contributes to opting for the adequate raw material needed for a zero-defect production, although these properties' examination is not able to provide a full picture of the features of foundry sand cores. The granulometric analysis carried out with sieve and image analyses is also inaccurate. In the case of the traditional sieve analysis, the sieve holes could clog, break, get damaged or during shake the sand grains could fragment. During the image analysis, the sand grains are measured in a random layout; consequently, significant differences can occur by the measurement of irregular particles. [5, 6] In case of sand cores, the optimal permeability and the adequate mechanical features can have a significant effect by the

[1] Institute of Foundry, University of Miskolc
H-3515 Miskolc-Egyetemváros, Hungary
ontheni@uni-miskolc.hu
[2] Institute of Foundry, University of Miskolc
H-3515 Miskolc-Egyetemváros, Hungary
ontvlaci@uni-miskolc.hu

optimal choice of granulometric features also; hence the precise and complex qualification of these parameters is essential. As a matter of fact, the current qualification of granulometric features primarily describes the base sand, not the features of sand cores. One of the reasons for introducing a new type of qualification system is to draw comparisons among the features of sand cores made from different base sands.

1. THE QUALIFICATION METHOD

By the application of the new qualification system and the introduction of the Core Quality Index (CQ_i), the characteristics in connection with the granulometric features of sand cores could be defined with a single value. The point of the qualification is that this single index incorporates the sand volume in the sand core, the surface of the total sand quantity and the bulk density which independent from the material density. Thus, it can be applied for the complex qualification of the features of sand cores.

The definition of CQ_i – Core Quality Index:

$$CQ_i = \frac{Air\ quantity\ \%}{SM}\ (-) \tag{1}$$

where:

Air quantity %: Percentage of the air in the sand core (%)

SM: Sand Module (cm)

$$SM = V_{sand}\ /A_{sand}\ (cm) \tag{2}$$

where:

V_{sand}: The volume of sand in the sand core or part of the sand core (cm^3)

A_{sand}: The total surface area of the sand in the sand core or part of the sand core (cm^2)

The following data is required to determine the Core Quality Index and the Sand Module value:

- V_{core}: The volume of the sand core (cm^3),
- m_{sand}: The mass of the sand core (mass of the sand) (g),
- ρ_{sand}: The density of the sand (material density of the sand) (g/cm^3),
- A_{BLAINE}: The specific surface area of the sand (cm^2/g).

In practice, besides the determination of base sand density and specific surface area the volume and the mass of samples to be examined is necessary.

By the application of the Core Quality Index the features of different base sands can be compared. With the CQ_i the granulometric and bulk density relations of sand cores can be independently qualified from the base sand quality and the size of sand core (dimensions).

2. MATERIALS AND MEASUREMENT

During the research, the factors determining the permeability were examined by the new qualification method. An important parameter is the shape of a sand grain. The shape of a sand grain beyond the binding strength affects the compactibility of the

sand mixture and its permeability. Hence sand types with different grain shapes were chosen.

We used two different quartz sand:

1. GBM 45 quartz sand – Badger Sand Mine (USA),
2. Polish quartz sand, ŚREDNI – Grudzeń-Las sand-pit (Poland), and synthetic sand:
3. Bauxite sand W55.

An aspect of selection was to have sands with different shapes although with similar average grain size; as a result, the effect of different grain shapes on gas permeability could be detected.

The results of the granulometric analysis of the investigated sands show summarized in *Table 1*.

Table 1

Measurement data of the investigated sands

	GBM 45	***ŚREDNI***	***Bauxite sand W55***
Average granularity, d_{50} (mm)	0.303	0.319	0.325
AFS granularity number (–)	61.7	52.66	57.44
Homogeneity degree (%)	44	64	55
Angularity coefficient (–)	1.14	1.38	1.08
Specific surface, A_{BLAINE} (cm^2/g)	105	125	100
Density (g/cm^3)	2.65	2.6	3.1
Bulk density (g/cm^3)	1.6	1.45	1.91
pH (–)	6.8	5.73	6.3
Grain shape	sub-rounded	angular	rounded

The results of the sieve analysis of the investigated sands show in *Figure 1*.

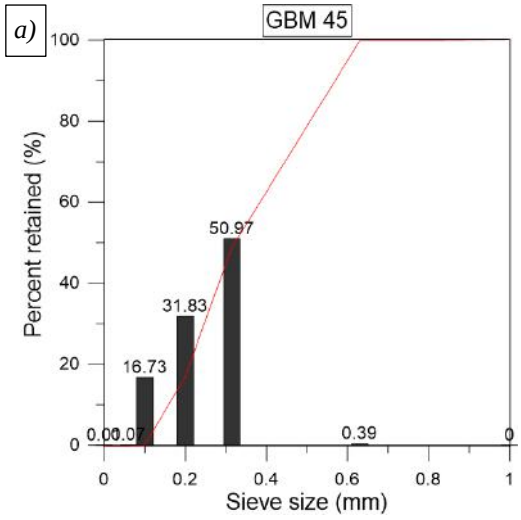

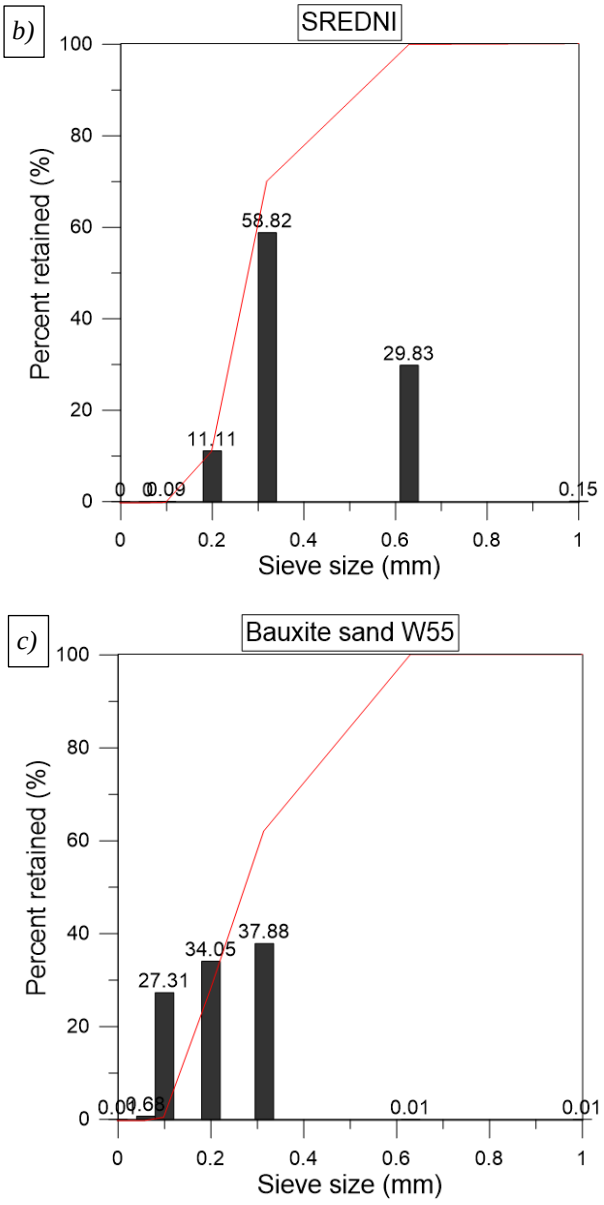

Figure 1

Sand grain size distribution of a) GBM 45 quartz sand, b) ŚREDNI quartz sand and c) Bauxite sand W55

The stereo microscope and scanning electron microscope (SEM) images of the investigated sands, as well as the results of EDS analysis are shown in *Figure 2*.

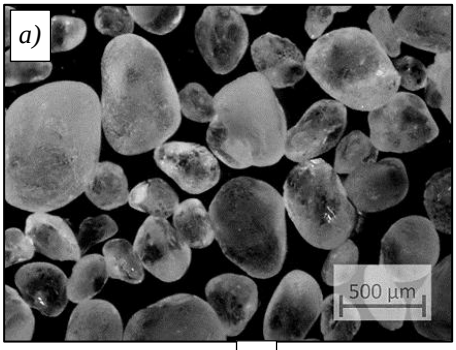
a)
500 µm

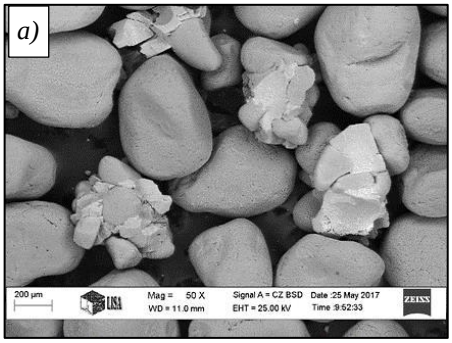
a)

a)

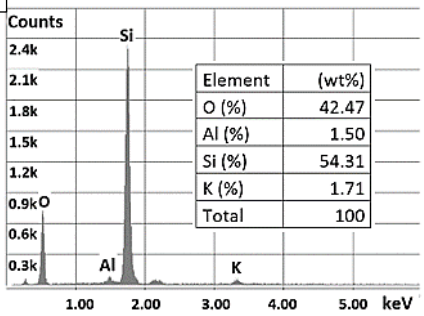
Counts
Si
2.4k
2.1k
1.8k
1.5k
1.2k
0.9k
O
0.6k
0.3k
Al
K
1.00
2.00
3.00
4.00
5.00
keV
Element (wt%)
O (%) 42.47
Al (%) 1.50
Si (%) 54.31
K (%) 1.71
Total 100

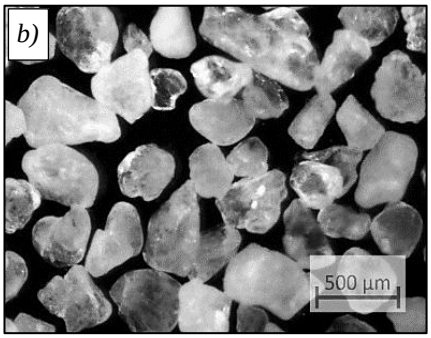
b)
500 µm

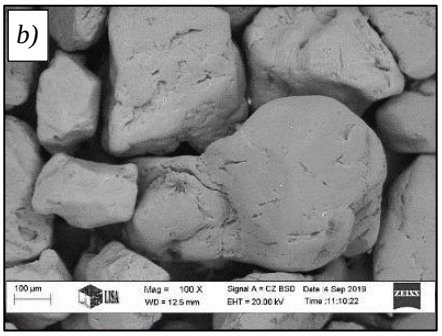
b)

b)

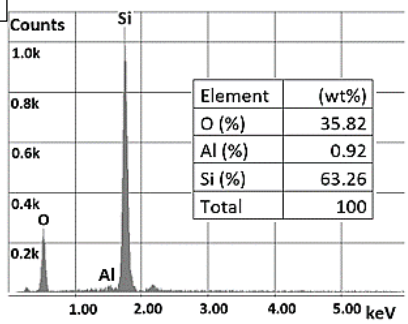
Counts
Si
1.0k
0.8k
0.6k
0.4k
O
0.2k
Al
1.00
2.00
3.00
4.00
5.00
keV
Element (wt%)
O (%) 35.82
Al (%) 0.92
Si (%) 63.26
Total 100

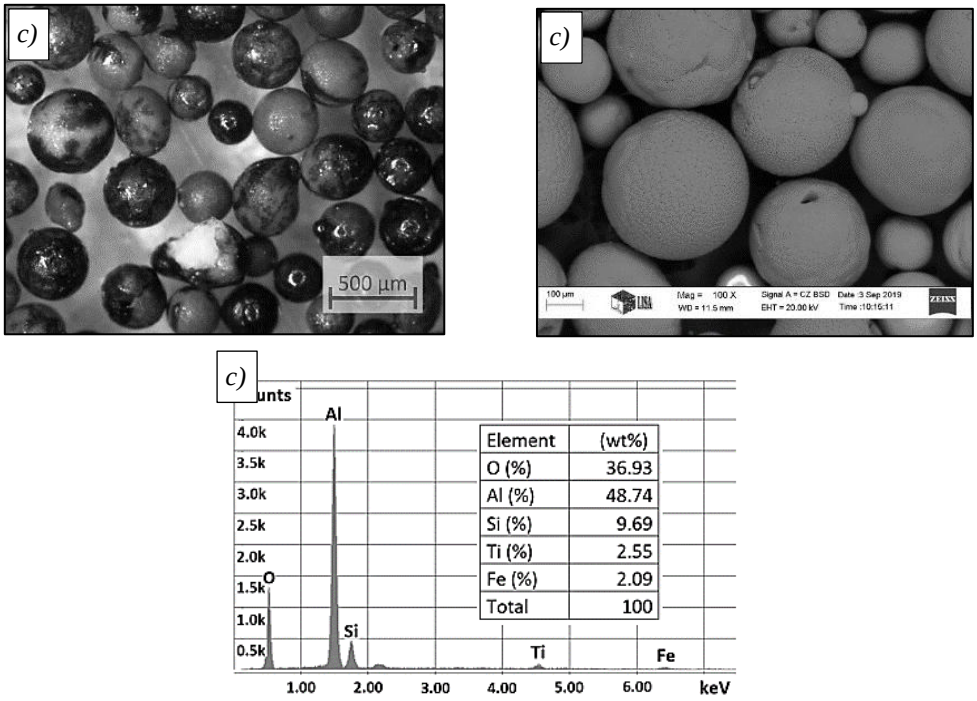

Figure 2

Stereo microscopy image and scanning electron microscopy (SEM) image with EDS analysis of a) GBM 45 quartz sand, b) ŚREDNI quartz sand and c) Bauxite sand W55

Based on the result of the granulometric analysis, it can be defined that the applied sands consist of 3 fractions and the grain size distribution of the investigated sands is different. The Polish quartz sand contains fine grains whereas Bauxite sand contains rough grains in a larger quantity. The elemental analysis shows that their components are diverse.

The sand mixture used for making specimen was made with phenolic resin (Furtolit 4003) and a catalyst as set by the recipe (Härter RS 20). The quantity of the phenolic no-bake resin needed to the mixture was 1% of the sand quantity, the catalyst was 40% of the resin quantity. In all cases, the sand mixture was made with a laboratory mixer for 2*1 minutes (for 1 minute with a catalyst and 1 minute with the resin). After the preparation of sand mixtures and within the shortest period of time and keeping a stable temperature (circa 20–22 °C), standard Ø50 × 50 mm cylindrical samples were made with a traditional sand rammer machine and with the different rams of 3, 5, 7 and 9. The process of preparing the specimens is illustrated in *Figure 3*.

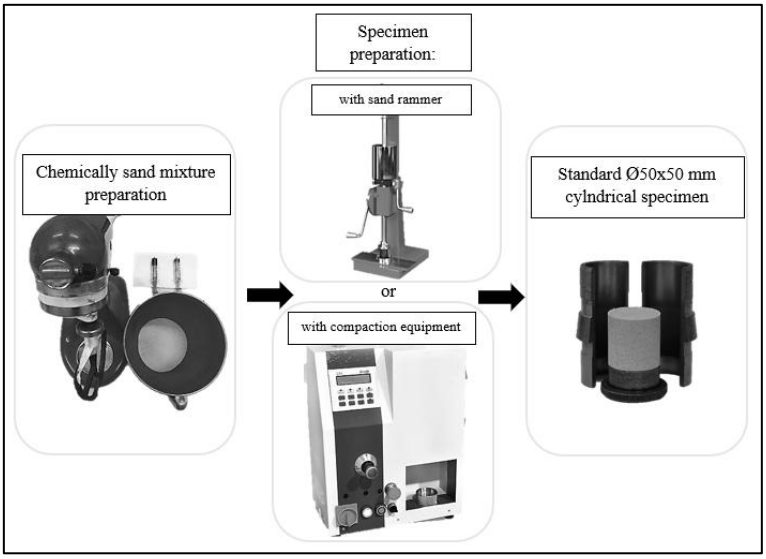

Figure 3
The process of specimen preparation

3. THE PERMEABILITY TEST

The permeability on the solidified cylindrical samples was measured by a tube with inflatable lining. The measurement results are given by the average of 2 measurements value.

Figure 4
The DISA type permeability measuring device and accessory for sand cores measuring

The CQ_i and permeability values of the specimens made of three different sands with different compaction forces (different ramming numbers) are shown in *Figure 5.*

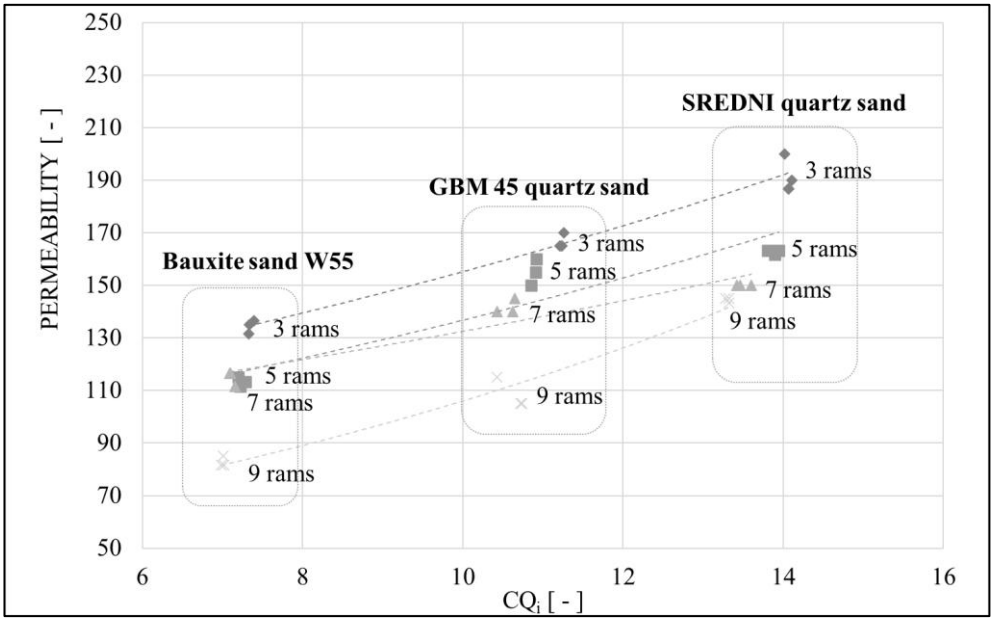

Figure 5

The permeability test values as a function of Core Quality Index (CQ_i) in the case of the three investigated sands

The sand cores with the lowest CQ_i were made from Bauxite sand; this sand type from the three was the rounded with the lowest specific surface area. The sand cores with the highest CQ_i were made from Polish silica sand; this sand type is the most angular with the largest specific surface area. In case of all three sand types by increasing the ramming, it is visible that the permeability has decreased and CQ_i has gone down slightly too since the air quantity in the sand cores has reduced. According to literature data, the permeability of samples made from more angular sand with higher specific surface area is worse than of samples made from more rounded sand with lower specific surface area, but our results have shown even the opposite. The rounded grains in compressed in the sand core get into less contact with each other; as a consequence, the core becomes more permeable among the sand grains for releasing gases. By Bauxite sand, the smaller grains fill the space among the larger grains better; therefore, the permeability worsens.

In order to eliminate the effects of the mixed grain structure by the GBM 45 quartz sand other examinations were carried out on samples made from sand mixture with different fractions per size. To get different grain sizes, the chosen GBM 45 quartz sand was divided with sieving into fractions per size, as follows:

- fine fraction – 100–200 μm;
- medium fraction – 200–315 μm;
- and coarse fraction – 315–630 μm.

In case of sand mixtures made from the fractioned sand, the specimens were made with the Multiserw-Morek compaction machine with the pressure of 1 MPa or 100 N/cm^2 for 20 seconds.

The permeability and CQ_i values of the specimens made of fractionated GBM 45 quartz sand are shown in *Figure 6*.

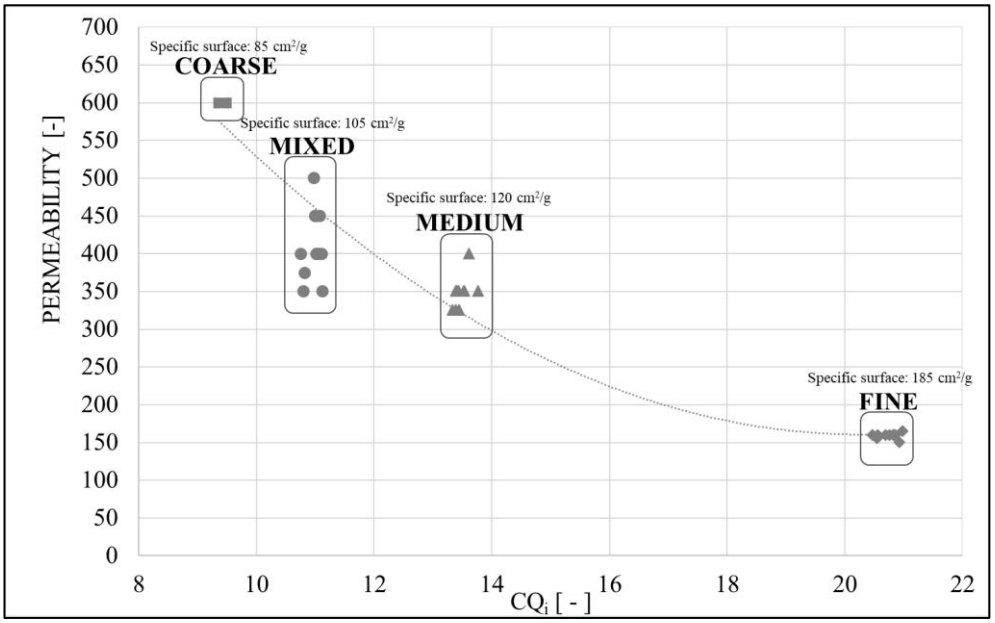

Figure 6
The permeability test values as a function of Core Quality Index (CQ_i) in the case of the fractionated GBM 45 quartz sands

The results showed that the permeability of samples made from the coarse fractioned sand mixture was the highest (the value exceeded the measurement threshold limit), although this fraction possessed the lowest CQ_i value. The lowest permeability was detected by sand cores made from fine fractions compared to the values of sand cores made from coarse or medium fractions. In case of samples made from different sand mixtures, containing air proportion is nearly the same, so there is no difference in the bulk density. Based on the measurement results, it can be verified that the permeability of sand cores (besides having the same voids content) made with the same production parameters (same content and quality of binder, same bulk density) with the coarse fraction is higher than of those sand cores containing medium or fine fractions. Despite samples made from different fractions possessing almost equal air percentage, that is, there is no significant alteration in their bulk density, their permeability can vary due to the different shape of 'channels' (voids) among sand grains. When the grain structure is mixed, variable permeability values can be detected due

to the inhomogeneous distribution of smaller grains compared to the systems of homogeneous grain structure.

CONCLUSION

The main purpose of the research was to reveal the correlation between the Core Quality Index (CQ_i) and the permeability of sand cores.

Sand core samples made from dissimilar foundry sands (GBM 45 quartz sand, ŚREDNI quartz sand and Bauxite sand W55) are used during the investigation whose features were analyzed with a new qualification method and then its relationship with the gas permeability of sand cores were also examined.

As the measurement results show, there is a correlation between the new qualification method and the permeability values. The diverse foundry sands can be easily compared with this qualification method introduced otherwise the different density values would make it difficult.The new type of qualification method makes it possible to predict the gas permeability of sand cores containing different base sands, thus making them easier to the planning of the characteristic feature.

ACKNOWLEDGEMENT

The authors are grateful to Árpád Kovács from the Institute of Physical Metallurgy, Metal Forming and Nanotechnology at the University of Miskolc for the scanning electron microscopy images.

REFERENCES

[1] Flemming, E., Tilch, W. (1993). *Formstoffe und Formverfahren*. Deutscher Verlag für Grundstoffindustrie, Leipzig, Stuttgart.

[2] Bakó K. (1976). *Öntödei formázóanyagok*. Budapest, Műszaki Könyvkiadó.

[3] Brown, J. R. (1999). Foseco Non-Ferrous Foundryman's Handbook. Foseco International Ltd, Butterworth-Heinemann, Oxford.

[4] Bakó K., Sándor J., Szabó Zs., Szíj Z. (1986). *Öntvények gyártástechnológiája*. Budapest, Műszaki Könyvkiadó.

[5] Dargai V., Polzin, H., Varga L., Dúl J. (2015). Öntödei homokok granulometriai tulajdonságainak meghatározása képelemzéssel. *XXIX. microCAD International Multidisciplinary Scientific Conference*, 9–10 April 2015, Conference Proceedings, Miskolc, pp. 1–7.

[6] Dargai, V., Polzin, H., Varga, L. (2018). Die Bestimmung der granulometrischen Eigenschaften von Gießereisanden mittels dynamischer Bildanalyse. *GIESSEREI PRAXIS*, 4/2018, pp. 19–22.

Materials Science and Engineering, Volume 45, No. 1 (2020), pp. 163–170.
DOI: 10.32974.mse.2020.016

SYNTHESIS AND CHARACTERIZATION OF MAGNETIC NANOPARTICLES FOR BIOLOGICAL SEPARATION METHODS

ÁGNES MÁRIA ILOSVAI[1] – EMMA SZŐRI-DOROGHÁZI[2] –
ÁDÁM PREKOB[3] – LÁSZLÓ VANYOREK[4]

Abstract: In our work, we successfully combined sonochemical production with the combustion method to produce magnetic nanoparticles. Iron (II)-acetate and iron (III)-citrate precursors were used in the synthesis, which in both cases were dispersed in 400 g/mol polyethylene glycol (PEG 400) using a high-efficiency ultrasonic technique (Hielscher homogenizer). The magnetic nanoparticles were bound to DNA to test their applicability in DNA separation processes. Plasmid DNA from *Escherichia coli (E. coli)* is well suited for carrying out the above assays. The magnetic particle morphology and size distribution were investigated by transmission electron microscopy (TEM), the nanoparticles were characterized by a high degree of dispersion. The functional groups on the surface of the particles were identified by Fourier transform infrared spectroscopy (FTIR) and hydroxyl groups were detected. The iron oxide forms of the sample were identified with X-ray diffraction (XRD), which were magnetite, maghemite and hematite phases. The dispersibility of nanoparticles in aqueous media was characterized by measuring the electrokinetic potential (using DLS) of the particles and due to the hydroxyl groups, its surface was sufficiently dispersible.

Keywords: nanoparticles, magnetite, TEM, FTIR, XRD, DNA

INTRODUCTION

In this research, we prepared and characterized magnetic iron oxide nanoparticles. Our goal was to produce nanoparticles that can be well dispersed in aqueous medium forming a stable dispersion. Due to their favorable properties, they are suitable for biological applications like DNA binding assays. At the moment, the commercially available DNA separation kits operating on a similar principle are available at high prices (Anti-DYKDDDDK antibody magnetite, of which 10 ml: approximately HUF 570,000) [1].

[1] Institute of Chemistry, University of Miskolc
H-3515 Miskolc-Egyetemváros, Hungary
ilosvaiagnes001@gmail.com
[2] Institute of Chemistry, University of Miskolc
H-3515 Miskolc-Egyetemváros, Hungary
emma.szdoroghazi@uni-miskolc.hu
[3] Institute of Chemistry, University of Miskolc
H-3515 Miskolc-Egyetemváros, Hungary
prekob.a@gmail.com
[4] Institute of Chemistry, University of Miskolc
H-3515 Miskolc-Egyetemváros, Hungary
vanyorekl@gmail.com

Many production processes are already known according to literature like sol-gel technology, microemulsion process, hydrothermal synthesis, high-temperature decomposition, precipitation synthesis, and sonochemical (ultrasonic) process [2]. Magnetic nanoparticles are used in many fields, including the pharmaceutical, food, and electronics industries, but we also find examples of their biological, geochemical, chemical, and electronic applications [2, 3].

Magnetic fluids and aqueous nanoparticles, which are particularly useful in biological and medical diagnostic applications, have been used as contrast agents in MRI (magnetic resonance imaging) studies. Magnetic particles have also been successfully tested in targeted transport of active substances during hyperthermia, and in magnetic cell separation processes [4–11]. Particles with different (polymer) coatings are widely used in DNA purification [12–15]. Most magnetic materials used for DNA purification have a complex composition, making them expensive to produce. Our choice of topic was influenced by the high price of the used commercial materials so we tried and successfully prepared magnetic iron oxide nanoparticles with properties similar to commercially available magnetites with a cheaper production process.

1. MATERIALS AND METHODS

For the production of magnetite nanoparticles iron (II) acetate, $Fe(CO_2CH_3)_2$ (Aldrich Chemistry) and iron (III) citrate, $FeC_6H_5O_7 \cdot xH_2O$ (PanReac AppliChem) salts were used, in both cases dispersed in polyethylene glycol with a molecular weight of 400 g/mol, $HO(C_2H_4O)_nH$ (Merck). For the synthesis, we used a high-efficiency ultrasonic homogenizer, Hielscher UIP1000hdT. The morphological characterization of the particles was performed by transmission electron microscopy (TEM; FEI Technai G), the functional groups were identified by Fourier transform infrared spectroscopy (FTIR; Bruker Vertex 70 FTIR spectroscope). The phase composition was determined by X-ray diffraction measurement (XRD; Rigaku Miniflex). To measure the electrokinetic potential of the particles, dynamic light scattering (DLS; Malvern, Zetasizer Nano-ZS) was used. The carbon content of the samples was determined with a CHNS (Vario MACRO) analyzer. The efficiency of DNA binding assays was confirmed by gel electrophoresis.

2. PRODUCTION OF MAGNETIC NANOPARTICLES AND DNA BINDING ASSAY

In this work, we would like to present magnetic nanoparticles from two different precursors: **sample A1** [iron (II) acetate] and **sample D1** [iron (III) citrate].

Both samples were prepared the same way, only the precursor type was changed. During the synthesis, 2 g of the precursor was used for **sample A1** (for **sample D1**: 3.47 g), which was dispersed in 20 g of polyethylene glycol (PEG) with a molecular weight of 400 g/mol using a high-efficiency ultrasonic homogenizer (Hielscher UIP1000hdT). After finishing the sonochemical treatment, the polyethylene glycol was burned using a Bunsen burner, thus creating iron oxide samples with magnetic

properties. Since **sample A1** was stable in aqueous medium, only the **D1 sample** had to be stabilized. For this purpose 5 different stabilizers were used: *PVP K30* (Polyvinylpyrrolidone); *PVA 115000* (polyvinyl alcohol); *CMC* (carboxymethylcellulose); *PEG 1000* (polyethylene glycol 1000) and *clay mineral* (sodium bentonite).

During the DNA binding examinations of the samples, the first step was mixing the DNA and the magnetic nanoparticles (MNPs) in a certain ratio (**sample A1**: 2 mg/ml; **sample D1**: around 2 mg/ml and 20 mg/ml). After the bonding of the DNA on the MNPs surfaces, they were collected at the bottom of the tube using a strong magnet. The supernatant fraction was also sampled, followed by washing of the samples. This is followed by the separation of DNA molecules from particles. Finally, the DNA eluted from the surface of the particles was placed in a separated sample holder *(Figure 1)*.

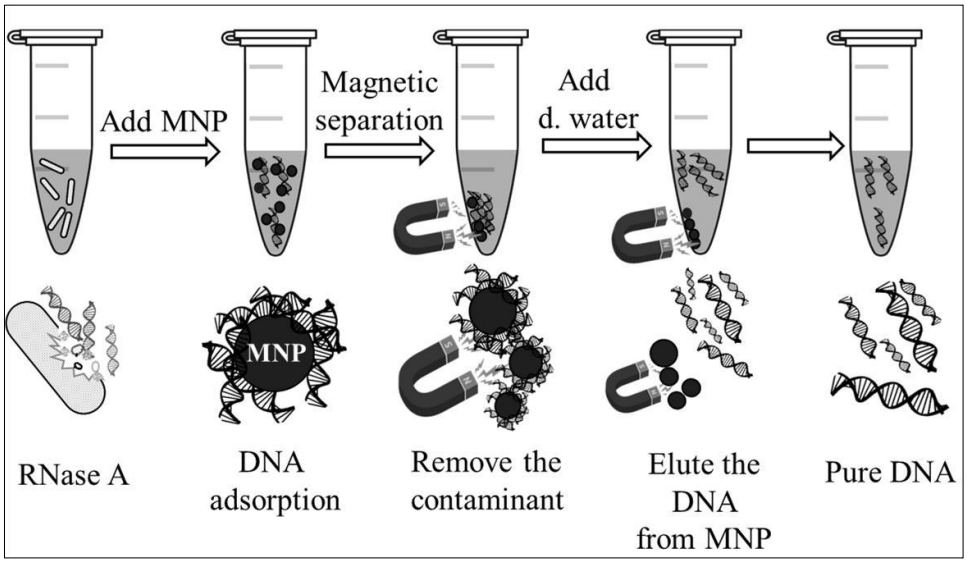

Figure 1
Outline of DNA binding test

3. EXPERIMENTAL RESULTS AND THEIR EVALUATION

The samples were first examined by transmission electron microscopy, with which the particle size and the morphology of the particles were characterized.

The granular structure can be well observed in the TEM images of both **sample A1** and **D1** *(Figure 2)*, so in both cases, we made size distribution diagrams using the "ImageJ" software *(Figure 3/A, B)*. The diagrams show that the average particle size of **sample A1** *(Figure 3/A)* was 14.4 nm, while the average particle size of **sample D1** *(Figure 3/B)* was 23.9 nm.

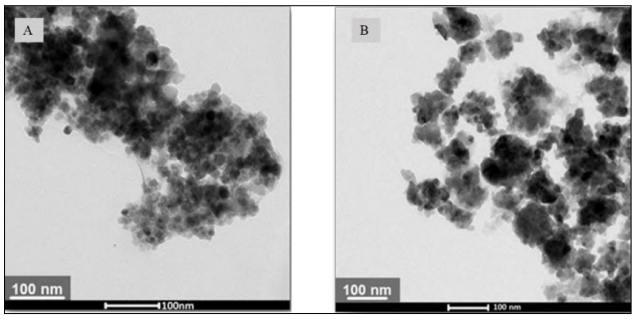

Figure 2
*TEM recording of **sample A1** and **D1***

Using Fourier transform infrared spectroscopy (FTIR), the functional groups on the surface of the particles were identified *(Figure 3/C, D)*. Comparing the spectra, it can be said that in both cases the valence vibrations of the Fe-O and OH groups can be found, C = C valence vibrations can also be seen in the mentioned samples, and C-O bonds can also be identified. Asymmetric and symmetric CH bonds can also be observed for **sample D1**.

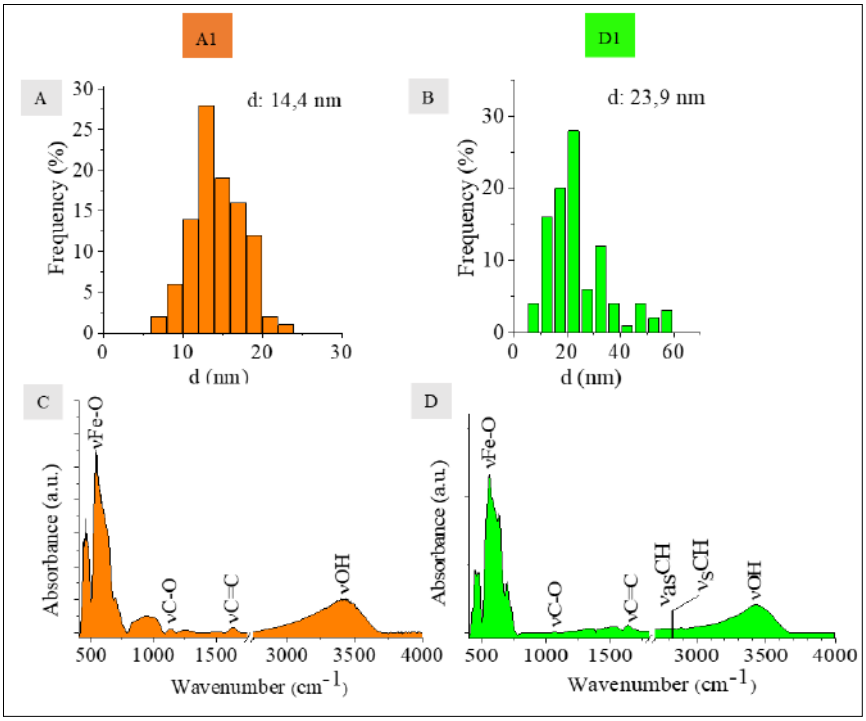

Figure 3
Size distribution diagrams (A, B) and FTIR spectra (C, D)

CHNS elemental analysis was performed on the samples to find out the exact amount of carbon because this may affect the ability of the particles to bind DNA. Elemental analysis showed that the carbon content in **sample A1** was 5.1 w/w%, while in **sample D1** this ratio was more than twice, 10.75 w/w% by number.

The phase composition of the samples was determined by X-ray diffraction (XRD) measurement. In case of sample A1 the results revealed *(Figure 4/A)* that there were three different iron oxide phases in the sample: magnetite (Fe_3O_4), hematite (α-Fe_2O_3) and maghemite (γ-Fe_2O_3). The sample contained 61.8 w/w% maghemite, the magnetite content was 19.9 w/w%, and the amount of hematite was 18.3 w/w%. In case of the **sample D1** *(Figure 4/B)* only two phases were detected, 93.2 w/w% maghemite and 6.8 w/w% hematite. In the case of **sample D1**, the ratio of the non-magnetic phase (hematite) was reduced (6.8 w/w%).

Based on the DLS results *(Figure 4/C)*, the deprotonation of the hydroxyl groups on the surface of the magnetic nanoparticles resulted in a negative zeta potential with an average of –20.3 mV. By reducing the zeta potential, the stability of aqueous dispersions made of nanoparticles can be increased.

The zeta potential of **sample D1** was also measured *(Figure 4/D)*, which showed an average of –4.1 mV, which is less negative than the determined potential for **sample A1** (–20.3 mV).

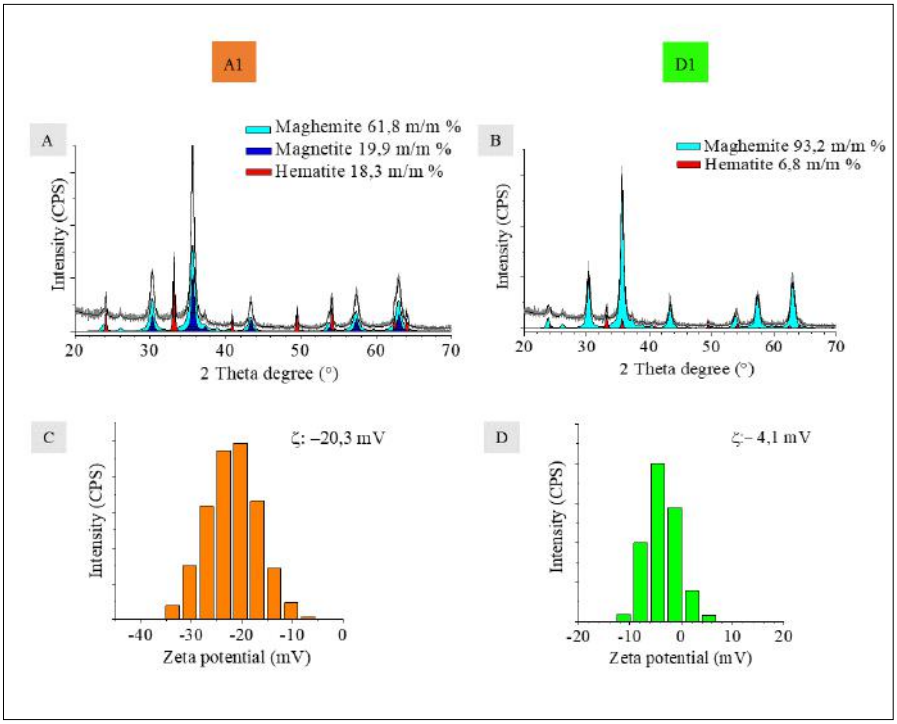

Figure 4

X-ray diffractograms (A, B) and Zeta potential distribution diagrams (C, D)

Both samples were tested in DNA binding assays. For **sample A1** *(Figure 5)*, the order of the samples in the gel electrophoresis assays was as follows:

Column 1: Positive control (+): plasmid DNA purified from *E. coli*

Column 2: MW marker (molecular weight marker): 1 kb DNA molecular weight marker

Column 3: Sample from supernatant fraction

Column 4, 6, 8: Negative control (–)

Column 5: DNA sample recovered from the MNP (eluted) (EF = elution fraction)

Column 7: Sample taken from the second elution of the DNA-MNP mixture (eluted DNA)

The test results showed that in the case of **sample A1**, the DNA bonds well to the surface of the particles and can be eluted from there *(Figure 5/A1)*. The DNA was able to bind reversibly because the red fluorescent band indicating the presence of DNA detached from the surface of the particles (lane 5 on the gel plate) is visible.

For *Figure 5/D1* the positive control (+) is the first column, which also contains plasmid DNA from *E. coli*. Next to it is the MW marker, which is a 1 kb DNA molecular weight marker, 3–4. columns denote the F1 fraction, the 5–6. columns are the supernatant fraction of DNA samples. The 7–8. column shows EF (column 7: about 2 mg/ml sample D1 + DNA sample; column 8: about 20 mg/ml sample D1 + DNA sample), which is the fraction taken from the DNA fraction separated from the DNA-MNP system.

For **sample D1** *(Figure 5/D1)*, only a faint mark is seen in EF (columns 7–8), suggesting that the DNA-binding ability of **sample D1** worked very well and we could not use this elution method, which was used for **sample A1**. In the further research more tests will be executed with this sample using new eluents.

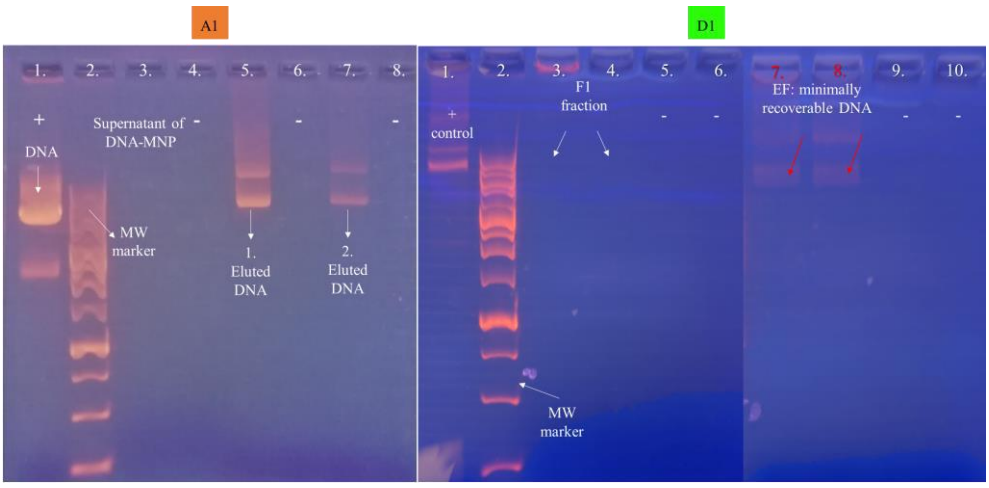

Figure 5
Investigation of reversible DNA binding by gel electrophoresis on samples A1 and D1

CONCLUSION

Magnetic nanoparticles were prepared using different iron precursors (**sample A1**: iron (II) acetate, **sample D1**: iron (III) citrate) and characterized by XRD, TEM, DLS and FTIR methods. The synthesis of magnetic iron oxides was accomplished by combining two modern methods, the sonochemical and the combustion methods. A recipe (**sample A1**) was also created with which we could produce a material suitable for DNA purification, which is more economical to prepare than the others available on the market.

ACKNOWLEDGEMENTS

The described article/presentation/study was carried out as part of the EFOP-3.6.1-16-2016-00011 *Younger and Renewing University – Innovative Knowledge City – institutional development of the University of Miskolc aiming at intelligent specialisation* project implemented in the framework of the Szechenyi 2020 program. The realization of this project is supported by the European Union, co-financed by the European Social Fund.

REFERENCES

[1] Anti-DYKDDDDK tag Affinity Beads (Binds to FLAG® tag sequence), Abcam. Available: https://www.abcam.com/ (2020. 04. 29.).

[2] Tóth, I. (2013). *Synthesis of variable-sized magnetite nanoparticles and their surface modification by polianionic coatings*. Dissertation (Doctoral dissertation), University of Szeged.

[3] Szebeni, J. (2011). Nanomedicine: Application of Nanotechnology in Medicine. Opportunities in Neuropsychiatry. Nanomedicine Research and Training Center, Semmelweis University, Bay Zoltán Public Foundation for Applied Research, Budapest, Uni. Miskolc, Faculty of Health, Miskolc, *Neuropsychopharmacologia Hungarica*, Vol. XIII, No 1, p. 17.

[4] McKeehan, L. W. (1940). Optical and Magnetic Properties of Magnetite Suspensions, Surface Magnetization in Ferromagnetic Crystals. *Phys. Rev*., Vol. 57, No. 12, pp. 1177–1178., June 15, 1940.

[5] Bee, A., Massart, R., Neveu, S. (1995). Synthesis of very fine maghemite particles. *Journal of Magnetism and Magnetic Materials*, Vol. 149, pp. 6–9.

[6] Blanco-Mantecon, M., O'Grady, K. (2006). Interaction and size effects in magnetic nanoparticles. *Journal of Magnetism and Magnetic Materials*, Vol. 296, pp. 124–133., Jan 2006.

[7] Fauconnier, N., Bée, A., Roger, J., Pons, J. N. (1999). Synthesis of aqueous magnetic liquids by surface complexation of maghemite nanoparticles. *Journal of Molecular Liquids*, Vol. 83, pp. 233–242., Dec 1999.

[8] Pankhurst, Q. A., Connolly, J. S., Jones, S. K., Dobson, J. (2003). Applications of magnetic nanoparticles in biomedicine. *Journal of Physics; Applied Physics*, Vol. 36, pp. R167–R181., July 2003.

[9] Gupta, A. K., Gupta, M. (2005). Synthesis and surface engineering of iron oxide nanoparticles for biomedical applications. *Biomaterials*, Vol. 26, No. 18, pp. 3995–4021., June 2005.

[10] Jain, T. K., Richey, J., Strand, M., Leslie-Pelecky, D. L., Flask, C. A., Labhasetwar, V. (2008). Magnetic nanoparticles with dual functional properties: Drug delivery and magnetic resonance imaging. *Biomaterials*, Vol. 29, No 29. pp. 4012–4021., Oct. 2008.

[11] Munnier, E., Cohen-Jonathan, S., Linassier, C., Douziech-Eyrolles, L., Marchais, H., Soucé, M., Hervé, K., Dubois, P., Chourpa, I. (2008). Novel method of doxorubicin–SPION reversible association for magnetic drug targeting. *International Journal of Pharmaceutics*, Vol. 363, No. 1–2, pp. 170–176., 3 Nov 2008.

[12] Saiyed, Z. M., Bochiwal, C., Gorasia, H., Telang, S. D., Ramchand, C. N. (2006). *Application of magnetic particles (Fe_3O_4) for isolation of genomic DNA from mammalian cells*. Department of Biochemistry, Faculty of Science, Maharaja Sayajirao University of Baroda, Sayajigunj, 7 July 2006.

[13] Yuanling, S., Jianbo, L., Yanhui, W., Chaofan, D., Yanna, L., Weiyan, S., Chuannan, L. (2017). A chemiluminescence biosensor based on the adsorption recognition function between Fe_3O_4@SiO_2@GO polymers and DNA for ultrasensitive detection of DNA. *Spectrochimica Acta Part A: Molecular and Biomolecular Spectroscopy*, University of Jinan, China, Vol. 178, pp. 1–7.

[14] Rahnama, H., Sattarzadeh, A., Kazemi, F., Ahmadi, N., Sanjarian, F., Zand, Z. (2016). Comparative study of three magnetic nano-particles ($FeSO_4$, $FeSO_4/SiO_2$, $FeSO4/SiO_2/TiO_2$) in plasmid DNA extraction. *Analytical Biochemistry*, Vol. 513, pp. 68–76.

[15] Nahid, S., Alireza, A., Mina, J., Monireh, F. (2016). Functionalization of Fe_3O_4@SiO_2 magnetic nanoparticles with nicotinamide and in-vitro DNA interaction. *Journal of Molecular Liquids*, Vol. 224, pp. 227–233.

Materials Science and Engineering, Volume 45, No. 1 (2020), pp. 171–181.
DOI: 10.32974.mse.2020.017

COMPLEX CHARACTERIZATION OF IRREGULAR EUTECTIC STRUCTURE

KASSAB AL-OMARI[1] – ARNOLD RÓNAFÖLDI[2] – ZSOLT VERES[3]

Abstract: Al-12.6Si alloy was solidified in a vertical Bridgman-type furnace equipped with a rotating magnetic inductor to induce the flow in the melt. The eutectic alloy was solidified unidirectionally by a growth rate of v = 0.1 mm/s, by a temperature gradient of G = 6 K/mm and with or without magnetic stirring. The interlamellar distances, the length, and orientation of Si lamellas were investigated by using new measuring methods.

Keywords: Eutectic solidification, Irregular eutectic, Rotation Magnetic Field RMF, interlamellar distances (λ,)

INTRODUCTION

The investigation of pattern formation in Al alloys has been the topic of several research studies, [1]. The formation of microstructures during solidification plays an important role in determining the properties of metal products [2]. Depending on the applied processing parameters and on the physical parameters of the material, a wide variety of solidified microstructures are observed in the course of the casting, welding, and other solidification processes.

The melt flow is an important parameter that affects the microstructure developing during solidification. The melt flow can be categorized into natural and forced convection. The contraction (or expansion) when the densities of the solid and liquid phases are different and the presence of the gravitational force during solidification are the two main reasons that cause the natural convection. The forced convection is a convection which is due to externally applied conditions. The melt flow can be controlled by a rotating magnetic field (RMF). The melt flow induced by RMF leads to macrosegregation in radial and axial directions, which leads to a change of phase ratio and distribution [3] [4] [5].

The combination of the Al-Si component improves the mechanical properties by which the wide range of application of the Al-Si eutectic alloy can be explained. The solidification of Al-Si eutectic alloys generally takes place at 12.6 w% of Si and at

[1] Institute of Physical Metallurgy, Metal forming & Nanotechnology, University of Miskolc
H-3515 Miskolc-Egyetemváros, Hungary
kassabalomari1992@gmail.com
[2] Institute of Physical Metallurgy, Metal forming & Nanotechnology, University of Miskolc
H-3515 Miskolc-Egyetemváros, Hungary
[3] Institute of Physical Metallurgy, Metal forming & Nanotechnology, University of Miskolc
H-3515 Miskolc-Egyetemváros, Hungary
vezso3838@gmail.com

an equilibrium temperature of 577 °C. The structure of Al-Si eutectic alloy shows two phases – they are as follows: Al solid solution phase as a matrix and a lamella-like Si particle. [6] [7]

The first theoretical explanation of the regular structure was developed by Jackson and Hunt in 1966. They simplified the problem of diffusion ahead of the solidification front by assuming a planar interface solidification and identical undercooling of melt in front of the solid phases which grow together from the melt of eutectic composition [8]. Many other explanations are based on the Jackson and Hunt model which developed new approaches in order to explain the relationship between the different parameters like the growth rate of the solid phase(v), undercooling of the melt (ΔT), temperature gradient (G) and the microstructural parameters such as the interlamellar distances λ and lamella length. [9] [10] [11] [12].

Experimentally, the Al-Si eutectic alloy has an irregular eutectic structure; owing to the growth of lamella with an undefined orientation and with different length, the microstructural measurements became a complex task for researchers.

Usually, the characterization of the eutectic structure means comparing two places in different samples and give a "fine/finer" or "coarse/coarser" description *(Figure 1)* [13]. These descriptions which are out of any numerical indication, are not enough to characterize the eutectic structure.

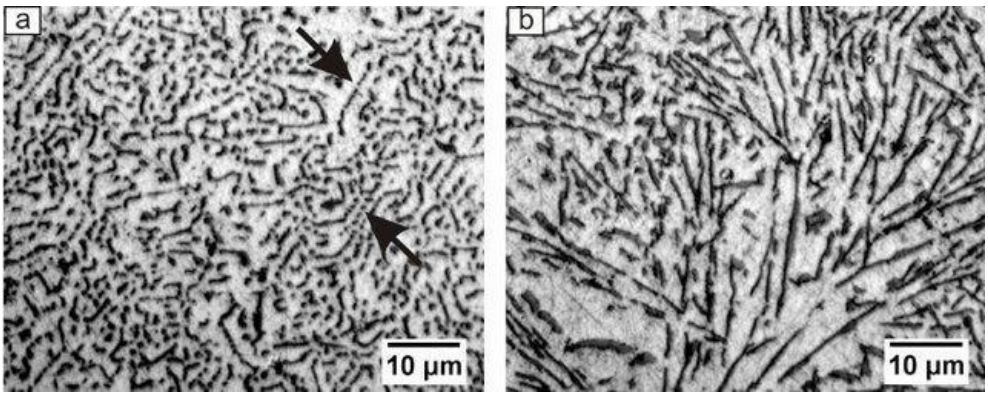

Figure 1
(a) Fine, and (b) coarse Al-Si eutectic structure [13]

On the other side, direct measurements were performed to characterize the interlamellar distances [14], on the transverse section (perpendicular to the growth direction) or on the longitudinal section (parallel to the growth direction) *(Figure 2a)*.

Among others, Clapham and Smith consider the line intercept method to measure the interlamellar distances, where the measurements are done by draw line in a "Wheatsheaf" formation of the eutectic lamellae, with their axes lying perpendicular to the quenched interface. Each line crosses several lamellae nearly at right angles *(Figure 2b)* [15] [16] [17].

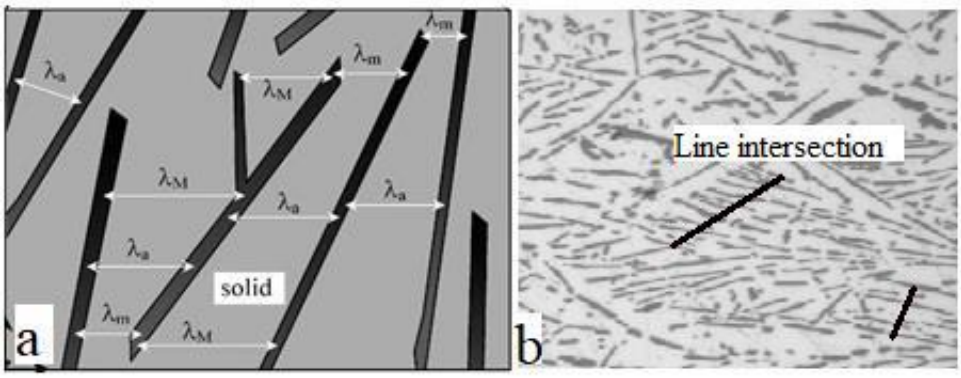

Figure 2

(a) Direct measurements (λ_m: minimum, λ_M: maximum, λ_a: average interlamellar distances) (b) line intercept method (M = 500)

There are a lot of Si eutectic lamellas with different growing directions in the eutectic Al alloys therefore the measurements of the interlamellar distances become very complicated. The two above methods (direct measurement and line intercept method) try to represent the eutectic structure with a limited number of measurements on the selected parts of the sample. Owing to this fact, the results of these methods highly depend on the examiner and the human factor.

Some researchers don`t believe in the previous method and use the "Fiber spacing method" as an alternative method to measure the interlamellar distances [18] [19]. Originally, the aim of this method was to measure the distance between the primary dendritic arms on primary phases in the dendritic structures where the number of particles (N) and the area (A) were taken into account to calculate the spacing (λ). [$\lambda = (A/N)^{0.5}$]. However, two valuable factors are missing from the fiber spacing method namely the particular area for each component (phase ratio) and the eutectic size factor.

Based on the previous reasons, the present paper suggests a new measuring method for measuring the interlamellar distances. For a better characterization of the eutectic structure, the measurement of further parameters of Si lamellae is suggested by us.

1. COMPLEX CHARACTERIZATION OF AN IRREGULAR EUTECTIC

Characterizing the irregular eutectic structure has been a big challenge for researchers because every eutectic lamella has a different length, thickness, and angle which represent the inclination between the axis of the lamellae and the direction of the solidification movement.

The distance between the lamellar spans a wide range as well, therefore we suggest to use the following three kinds of parameters to describe the irregular eutectic structure: the average interlamellar distance, the length and the angle of lamella.

By means of the image analysis software, we use the "Specific perimeter method" to measure the average interlamellar distance (λ), see *Equation (1)*

$$\lambda = 2 * \frac{A_p * (1 - A_f)}{N * P_o} \quad (1)$$

Where:

- P_0: is the average perimeter of the silicon lamella in the investigated microscopic photos (μm); it can be measured by image analysis software.
- N: Number of the eutectic lamellae.
- A_p: Area of the microscopic photo (μm^2).
- A_f: Area fraction of the eutectic lamellae in the eutectic structure.

Near the average lamellae distance, we measure the length of lamellae, which is equal to the Ferret diameter. The Ferret diameter can be defined as the distance between two parallel tangential lines restricting the object perpendicular to that direction *(Figure 3a)*. The new image processing techniques allow us to measure the Ferrets diameter for each object (every eutectic Si lamella) and analyze them. The measured Ferret diameters were divided into ranges and the percentage distribution of lamellas belonging to the given ranges were investigated.

In addition, the angle measurement has been performed as well. The angle measurements describe the orientation between the axis of the eutectic silicon lamella and the axis of direction of solidification front movement *(Figure 3b)*. A percentage relation between the above-mentioned size ranges and the angle distribution in that range was created.

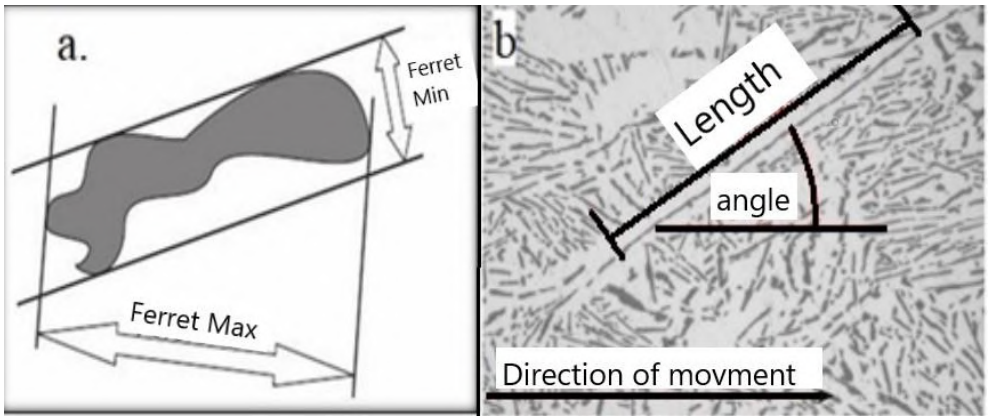

Figure 3

(a) Description of Ferret diameter. (b) The different measured parameters in Al-Si eutectic alloy (M = 500)

2. VALIDATION OF THE SPECIFIC PERIMETER METHOD

The new method has to be validated; a sample of Al-12.6 Si alloy was used for this purpose. This composition is the eutectic composition of the Al-Si alloys which contains only eutectic structure in equilibrium.

The validation process shall be performed on a different structure therefore the eutectic sample has been solidified under the effect of forced melt flow. Rotating Magnetic Field (RMF) was used for creating a magnetic stirring during solidification. Different flow velocities were used by changing the magnetic induction intensity from 0 mT (without stirring) to 150 mT.

Under the influence of magnetic stirring, a finer eutectic structure develops and the Si composition distribution changes; this phenomenon is called "macrosegregation". Due to the macrosegregation, the primary phase α and the primary silicon solidify alongside with the eutectic structure, but our research concern only the investigation of the eutectic structure.

The solidified samples were sectioned longitudinally and prepared by grinding, polishing, and etching in HF acid. The specimens were studied by Light Microscopy and Image J image analysis software.

The microscopic photos were taken by using the mosaic photo technique; The mosaic acquisition is a processing system to make large expanses of the target area on the object sample close to the resolution limit of light microscopy. To take a mosaic photo, a larger image is created from a series of smaller images individually collected orderly across a sample.

2.1. Interlamellar spaces

The present work recommends the specific perimeter method as a valid method for characterizing the interlamellar distances. This recommendation is based on several tens or more of validity tests. The validity of the specific perimeter method was tested on different Al-Si eutectic structure and compared with the Direct measurement method. The result shows a promising method because the error percentage does not exceed 2% in some cases, which makes the invented method a precise and fast measurement method. *Table 1* shows an example of some validation tests for random eutectic structures in the Al-Si eutectic specimen.

Table 1

Validation tests of the special Perimeter method

Number of tests	Magnetic induction (mT)	Surrounding structure	Interlamellar distance [µm]		Standard deviation
			Specific Perimeter method	Real hand Measurements	
1	0	Eutectic structure	3.64	3.7	0.04
2	0	Eutectic structure	3.8	3.5	0.2
3	0	Eutectic structure	3.45	3.6	0.1
4	150	Eutectic structure	3.35	3.3	0.03
5	150	Primary Al- Phase	2.26	2.4	0.09
6	150	Primary Si phase	4.32	4.4	0.05

It proves to be a complex task to measure the interlamellar distances owing to the formation of α primary phase and primary silicon in the stirred microstructure. Three different appearance of eutectic structure grow depending on the surrounding phase i.e. it has been found that a fine eutectic structure forms near the primary α phase, while a coarse eutectic structure grows near the primary silicon, and lastly the well-known eutectic structure forms where there are no primary structures nearby. *(Figure 4)*

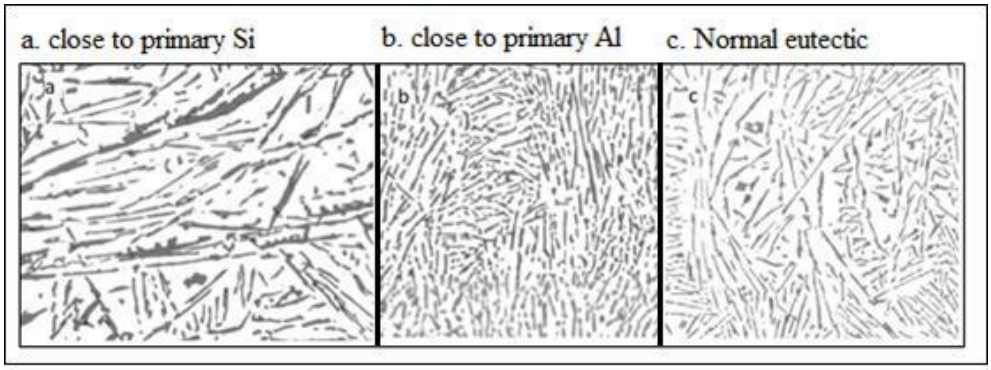

Figure 4
Different structures of eutectic type, (M = 500).
(v = 0.1 mm/s, G = 6 K/mm, magnetic intensity = 150 mT)

Owing to the aforementioned facts, it is not recommended to characterize the interlamellar distances without considering the place of eutectic structure; the average value was calculated for each type and given in *Table (2)*. The process of studying the effect of primary phases on the eutectic structure will be described in our following paper.

Table 2
Measurements of the interlamellar distances

Eutectic group	Distance (μm) ± 0.2
Without RMF	3.7
With RMF main eutectic structure	3.5
With RMF close to primary Si	4.06
With RMF near to primary Al	1.99

2.2. Length of lamellae

As mentioned before, the length measurements were performed by measuring the Ferret diameter of each Si eutectic lamellae. An image analysis software has been used to measure them.

The length measurements were analysed by categorizing the size of the eutectic Si lamella into different ranges starting from (0–10) and ending with (290–300) μm. In this way, we can investigate the size at which the effect of RMF will be the largest one. *Figure 5* shows the size ranges percentage both in the stirred and non-stirred parts.

The fine eutectic structure range (i.e. < 10μm) has the largest percentage both in the stirred and non-stirred parts. However, 95% of fine eutectic can be observed in the stirred part while 75% of it can be observed in the non-stirred specimen. The mechanisms of size reduction due to the magnetic fields applied during solidification are not yet well understood, but some authors state that they are due to the fragmentation of the primary arms of dendrites that act as nuclei [20], [21]; it can be true for large eutectic Si lamellas as well. Others state that they are due to the pressure differences caused by the oscillation of liquid that causes cavitation and consequently some nucleation of embryos [22], [23]. Yet, others claim that there is an undercooling effect due to the magnetic intensity [22]. There is some general agreement that the mass transportation of the cooled liquid from the mould perimeter to the hotter regions increases the solidification rate [22]. The mass transportation provides an opportunity to solute undercooling [20], [21].

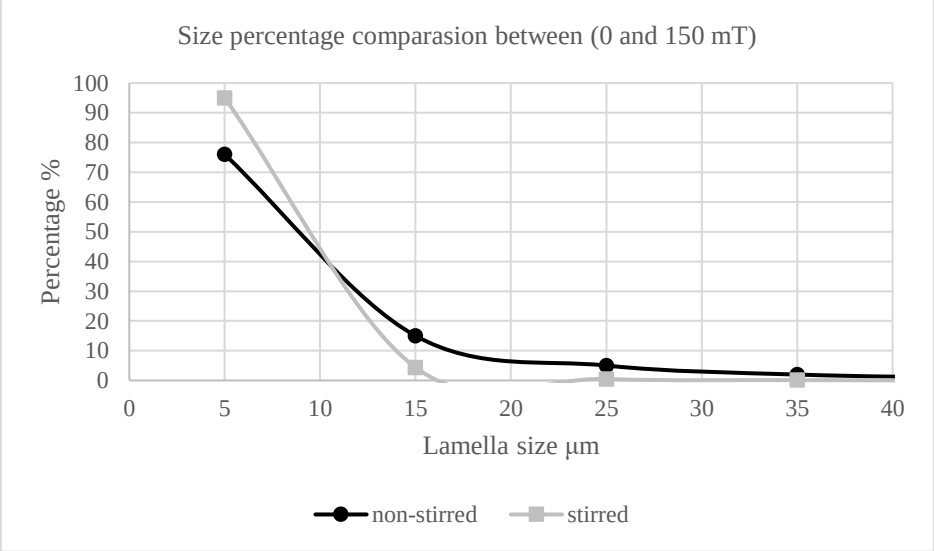

Figure 5
Si lamella size percentage of Al-Si eutectic sample with 0 and 150 mT

2.3. Angle measurements

The angle of the lamella describes the inclination degree between the axis of the eutectic silicon lamellas and the direction of the solidification movement.

The size measurements show the large effect of RMF on fine eutectic Silicon. Therefore, an angle distribution curve was created for calculating the effect of RMF on the angle of fine eutectic Si lamellas *(Figure 6)*.

When the solidification process takes place without the effect of the forced melt flow, 60% of the fine eutectic lamella tends to orient in a 45° from the sample axis.

Figure 6 shows a decreasing at 45° angle range percentage when RMF is switched on. This percentage will reduce to 35% by applying 150 mT. It means that the orientations of Si lamellas are more diverse when using RMF than those without RMF.

These large orientation differences suggest that the Si lamellas do not have an epitaxial growth in case of using RMF at 50 Hz as most of the Si lamellas without RMF seem to have.

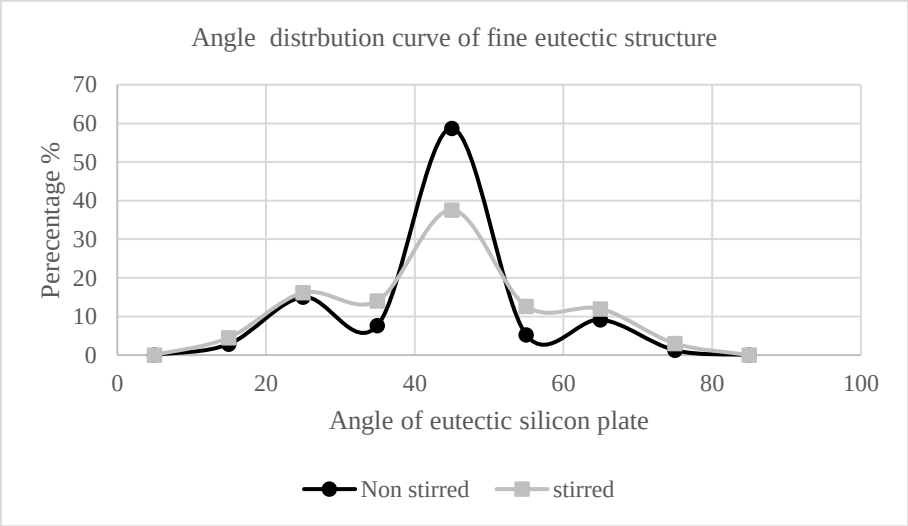

Figure 6
The angle distribution curve of fine eutectic Si lamella (<1μm) of Al-Si eutectic specimen

CONCLUSION

A newly developed complex characterizing method was used to describe the irregular eutectic structure. Three parameters were characterized.

a) The average interlamellar distance λ was characterized by using the specific perimeter method which proves its validity when it is compared with the other methods used recently.
b) The length of the eutectic Si lamellas was characterized by using an image analysis software in order to measure the Ferret diameter of every Si lamella.
c) The angle of the eutectic Si lamellae, where it was measured by determining the inclination degree between the axis of the Si lamella and the direction of the solidification front movement.

When Al-Si eutectic alloy is solidified under the effect of magnetic stirring induced by RMF, the microstructure will respond by reducing the length of the eutectic Si lamella. It results in more disorientations in the eutectic silicon lamella, and different eutectic appearances which means different interlamellar distances.

Based on our investigation, the used characterization method is good enough to characterize the different parameters in an irregular eutectic structure because it is a fast measurement, considers every single lamella and an accurate measurement with an error percentage which does not exceed 0.2%.

ACKNOWLEDGMENT

The described article was carried out as part of the EFOP-3.6.1-16- 2016-00011 *Younger and Renewing University – Innovative Knowledge City –institutional development of the University of Miskolc aiming at intelligent specialization* project implemented in the framework of the Szechenyi 2020 program. The realization of this project is supported by the European Union, co-financed by the European Social Fund.

REFERENCES

[1] Karma, A., Rappel, W.-J. (1998). Quantitative phase-field modeling of dendritic growth in two and three dimensions. *Phys. Rev. E.*, Vol. 57, No. 4, pp. 4323–4349.

[2] Dantzig, J., Rappaz, M. (2009). *Solidifcation*. Switzerland, EPFL Press.

[3] Tiller, W., Jackson, K., Rutter J., Chalmers, B. (1953). The redistribution of solute atoms during the solidification of metals. *Acta Metallurgica*, Vol. 1, No. July, pp. 428–437.

[4] Svéda, M., Sycheva, A., Kovács, J., Rónaföldi, A., Roósz, A. (2014). The effect of rotating magnetic field on the solidified structure of Sn–Cd peritectic alloys. *Materials Science Forum*, Vols. 790–791, pp. 414–419.

[5] Rónaföldi, A., Kovács, J., Roósz, A. (2007). Investigation and visualization of melt flow under rotating magnetic field. *Transactions of the Indian Institute of Metals*, Vols. 2–3, pp. 213–218.

[6] Fredriksson, H., Åkerlind, U. (2012). *Solidification and Crystallization Processing in Metals*. Chichester, John Wiley & Sons Ltd.

[7] Stefanescu, D. (2002). *Science and Engineering of Casting Solidification*. New York, Kluwer Academic/Plenum Publishers.

[8] Jackson, K., Hunt, J. (1966). Trans. Met. Soc. *AIME*, Vol. 236, p. 1129.

[9] Fisher, D., Kurz, W. (1980). A theory of branching limited growth of irregular eutectics. *Acta Metallurgica*, Vol. 28, No. 6, pp. 777–794.

[10] Magnin, P., Kurz, W. (1987). An analytical model of irregular eutectic growth and its application to Fe-C. *Acta Metallurgica*, Vol. 35, No. 5, pp. 1119–1128.

[11] Magnin, P., Mason, J. T., Trivedi, R. (1991). Growth of irregular eutectics and the A1-Si system. *Acta Metallurgica et Materialia*, Vol. 39, No. 4, pp. 469–480.

[12] Steen, H. A. H., Hellawell, A. (1975). The growth of eutectic silicon – contribution to undercooling. *Acta Metallurgica*, Vol. 23, pp. 529–535.

[13] Timpel, M., Wanderka, N., Kumar, G. V., Banhart, J. (2011). Microstructural investigation of Sr-modified Al-15 wt%Sialloys in the range from micrometer to atomic scale. *Ultramicroscopy*, Vol. 111, pp. 695–700.

[14] Gündüz, M., Kaya, H., Çadırlı, E., Özmen, A. (2004). Interflake spacings and undercoolings in Al-Si irregular eutectic alloy. *Material Science and Engineering*, Vol. A3690, pp. 215–229.

[15] Clapham, L., Smith, R. W. (1989). Partial modification in unidirectionally solidified Al-Si eutectic alloys. *Acta Metall.*, Vol. 37, No. 1, pp. 303–311.

[16] Flood, S., Hunt, J. (1981). Modification of Al-Si eutectic alloys with Na. *Metal Science*, Vol. 15, No. 7, pp. 287–294.

[17] Hogan, L., Song, H. (1987). Interparticle Spacings and Undercoolings in Al-Si Eutectic Microstructures. *Metallurgical Transactions A*, Vol. 18A, pp. 707–713.

[18] Glenister, S. M. D., Elliott, R. (1981). Strontium modification of AI-12.7wt-%Si alloys. *Metal Science*, Vol. 15, No. 4, pp. 181–184.

[19] Kobayashi, K. F., Hogan, L. M. (1985). The crystal growth of silicon in Al-Si alloys. *Journal of Materials Science*, Vol. 20, pp. 1961–1975.

[20] Yasuda, H., Nakatsuka, N., Nagira, T., Sugiyama, A., Yoshiya, M., Uesugi, K.et al. (2009). X-ray imaging study on grain refinement due to dendrite fragmentation. In: *EPM 2009, 6th International Conference on Electromagnetic Processing of Materials*, Dresden, Germany.

[21] Sugiura, K., Iwai, K. (2005). Refining mechanism of solidified structure of alloy by electromagnetic refining process. *ISIJ international*, Vol. 45, No. 7, pp. 962–966.

[22] Jie, D., Jianzhong, C., Wenjiang, D. (2006). Theoretical discussion of the effect of a low-frequency electromagnetic vibrating field on the as-cast microstructures of DC Al–Zn–Mg–Cu–Zr ingots. *Cryst Growth*, Vol. 2, No. 295, pp. 179–187.

[23] Hernandez, F. R., Sokolowski, J. (2006). Comparison among chemical and electromagnetic stirring and vibration melt treatments for Al–Si hypereutectic alloys. *Journal of alloys and compounds*, Vols. 1–2, No. 426, pp. 205–212.

[24] Jackson, K., Hunt, J. (1966). Lamellar and rod eutectic growth. *Transactions of the Metallurgical Society of AIME*, Vol. 236 (8), p. 1129.

[25] Kurz, W., Giovanola, B., Trivedi, R. (1986). Theory of microstructural development during rapid solidification. *Acta Metallurgica*, Vol. 34, No. 5, pp. 823–830.

Materials Science and Engineering, Volume 45, No. 1 (2020), pp. 182–190.
DOI: 10.32974.mse.2020.018

PREPARATION OF CALCIUM OXIDE BY A PRECIPITATION METHOD

EI EI KHINE[1] – PÉTER BAUMLI[2] − GEORGE KAPTAY[3]

Abstract: CaO nanoparticles were prepared using precipitation method. Different concentration of $CaCl_2$ and NaOH were used as starting raw materials. The structure and microstructure of the prepared CaO powders were examined using several characterization techniques including X-ray diffraction (XRD), Scanning electron microscope (SEM) and energy dispersive spectroscopy (EDS). Different crystallite sizes of nano and sub micro CaO were obtained based on the concentration of the reactants. Using precursors with low concentration leads to formation of product with small crystallite size.

Keywords: precipitation method, CaO particles

INTRODUCTION

Calcium oxide (CaO) is an important inorganic compound which is used in a wide range of applications, being of continuous interest in the field of materials research. It can be used as a catalyst, toxic-waste remediation agent, or as an additive in refractory and paint industries [1]. CaO nanoparticles can be used as an antimicrobial agent, a drug delivery agent as well as in various other biomedical applications [2]. Moreover, CaO is an attractive CO_2 absorber, due to its good kinetics and high capture capacity, even under low CO_2 partial pressure condition [3]. Calcium oxide has been regarded as one of the most promising candidates for carbon capture due to its high capturing efficiency, low running cost, and high abundance in the Earth's crust. Several different methods can be used for the preparation of CaO nanoparticles. Varying these methods, all physical and chemical properties of nano-CaO can be changed. The morphology, surface area and capturing efficiency can be carefully controlled under specific synthesis conditions [4].

Capturing CO_2 by using CaO based adsorbents has been attracted industrial sectors due to the high theoretical capacity of CO_2 capture, low cost, and potential use in large scale. The development of CaO-based adsorbents decreases over a number

[1] Department of Physical Metallurgy, Metal Forming and Nanotechnology, University of Miskolc
H-3515 Miskolc-Egyetemváros, Hungary
eieikhine5511@gmail.com
[2] Department of Physical Metallurgy, Metal Forming and Nanotechnology, University of Miskolc
H-3515 Miskolc-Egyetemváros, Hungary
baumlipeter@gmail.com
[3] Department of Physical Metallurgy, Metal Forming and Nanotechnology, University of Miskolc
H-3515 Miskolc-Egyetemváros, Hungary
kaptay@hotmail.com

of cycles of CaO carbonation/calcination. To improve the sintering-resistant properties of CaO-based adsorbents, many factors should be considered such as decreasing the particle size and increasing the surface area, dispersing CaO on an inert support, as well as surface modification [5]. The aim of this research work is to produce CaO nanoparticles through precipitation method by manipulating the concentrations of the precursors, the stirring speed and the calcination temperature and time. Various characterization techniques will be carried out including XRD, SEM and EDX to investigate the structure, the morphological feature and the elemental composition.

1. MATERIALS AND METHODS

Calcium oxide (CaO) powder was produced according to the following reactions:

$$CaCl_{2\,(aq)} + 2\,NaOH_{(aq)} \longrightarrow Ca(OH)_{2(s)} + 2\,NaCl_{(aq)} \quad (1)$$

$$Ca(OH)_{2(s)} \xrightarrow{650^{o}C\ /1hr} CaO_{(s)} + H_2O_{(g)}. \quad (2)$$

$CaCl_2.xH_2O$ and NaOH with different concentrations (1, 0.5, 0.1 M) of $CaCl_2$ and (2, 1, 0.2 M) of NaOH were used as initial reagents for the synthesis of $Ca(OH)_2$ powder, using stoichiometric Ca^{+2} : OH^{-} = 2 : 1 mole ratio. The concentrations of both aqueous solutions are shown in *Table 1*. First, both aqueous solutions ($CaCl_2$ and NaOH) were heated up to 80 °C. At this fixed temperature, a given NaOH solution was added dropwise to a given $CaCl_2$ solution under stirring (1,300 rpm) by magnetic stirrer for 30 minutes. During this process, white precipitates formed. After that, each mixture was filtered and washed five times with distilled water then dried overnight at room temperature to obtain dry $Ca(OH)_2$ powder. The obtained powders were calcined at 650 °C under argon gas environment for one hour to produce a CaO powder. The experimental reagent is given in *Table 1*.

Table 1

Composition and concentration of the reactants in aqueous solutions

Sample No	$CaCl_2$ (mol/L)	NaOH (mol/L)
1	0.1	0.2
2	0.5	1
3	1	2

2. RESULT AND DISCUSSIONS

2.1. SEM and EDX characterizations of the samples

The samples were examined by scanning electron microscopy using a Carl Zeiss EVO MA10 equipment at 20 kV using a Bruker microprobe. The pictures are taken under BSD-SE mode. The measurement of the particle size was done by ImageJ. Characteristic results of the SEM and EDX investigation are shown in *Figures 1–3* and *Table 2*.

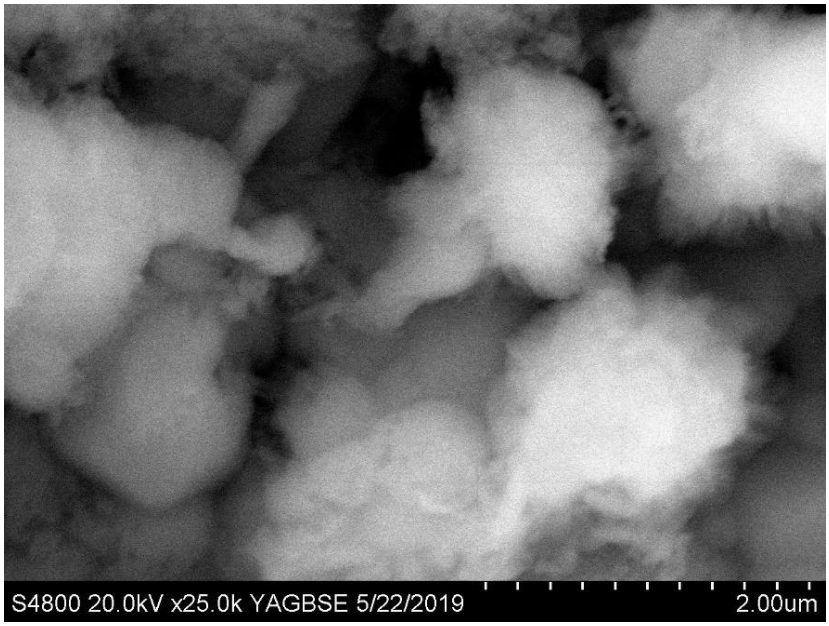

Figure 1
SEM image of CaO produced from Sample 1 (0.1M $CaCl_2$ + 0.2M NaOH)

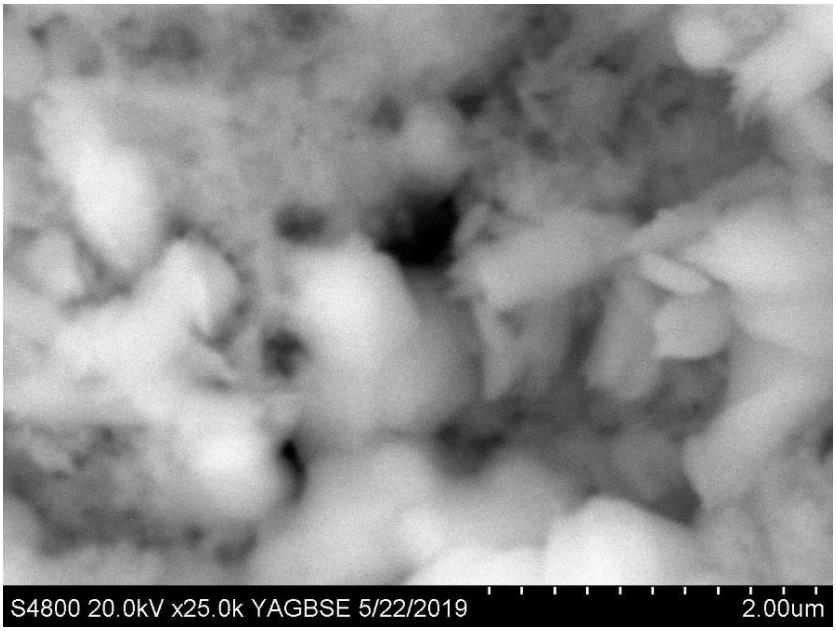

Figure 2
SEM image of CaO produced from Sample 2 (0.5M $CaCl_2$ + 1M NaOH)

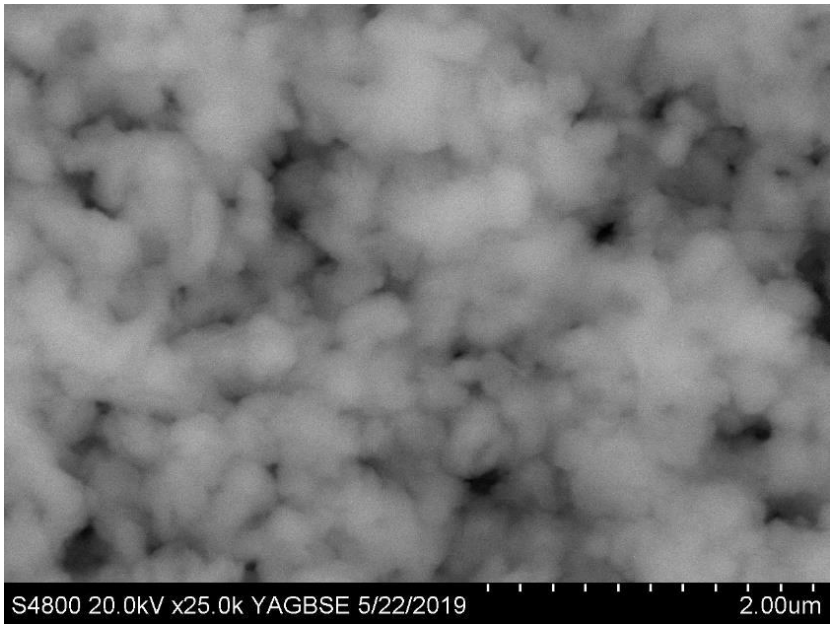

Figure 3
SEM image of CaO produced from Sample 3 (1M $CaCl_2$ + 2M NaOH)

According to EDX result shown in *Table 2*, using moderate concentration (0.5M) of $CaCl_2$ reactant leads to the formation of high amount of Ca and low amount of C and Cl, while using low concentration (0.1M) or high concentration (1M) of $CaCl_2$ resulted in production of high C content and low amount of Ca.

Table 2
The weight percentage and atomic percentage of the elements in the deposit of the product according to the EDX investigation

Elements	Weight percentage			Atomic percentage		
	Sample1	Sample2	Sample3	Sample1	Sample2	Sample3
C	8	5	7.3	15.6	10	14.2
O	39.5	35.5	35	55.4	54	52
Ca	52	59.3	57.5	28.7	35.9	33.7
Cl	0.5	0.2	0.2	0.3	0.1	0.1
Total	100	100	100	100	100	100

2.2. XRD investigation of the samples

The samples were measured by Bruker D8 Advance, Cu K-alpha radiation, 40 kV and 40 mA generator settings, parallel beam with Göbel mirror, Vantec-1 position

sensitive detector with 1° opening, scanning rate 0.007° (2Th)/24 sec. In the investigation of three different preparation ratios as shown in *Figures 4–6*, the highest percentage of CaO powder was found to be 84.8% with a small amount of calcium carbonate and calcium hydroxide.

The results of XRD investigations are shown in *Figures 4–6*.

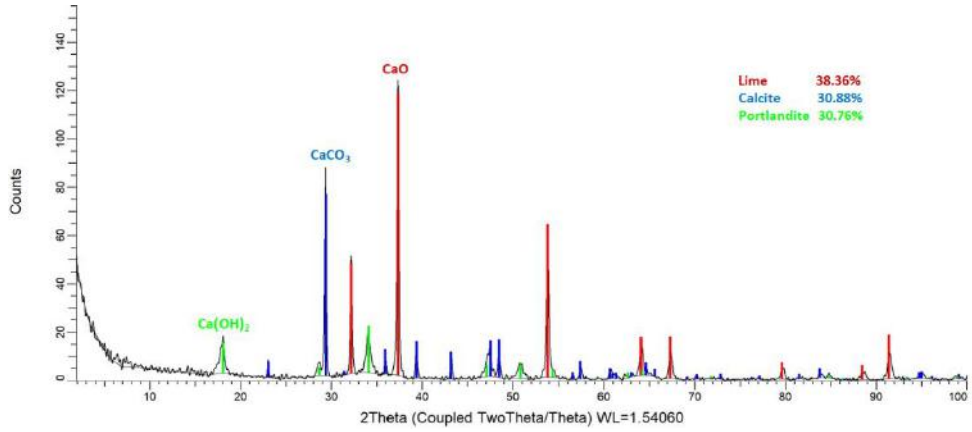

Figure 4
XRD diffractogram with the matched peaks of the calcined powder (Sample 1 with 0.1M $CaCl_2$ + 0.2M NaOH)

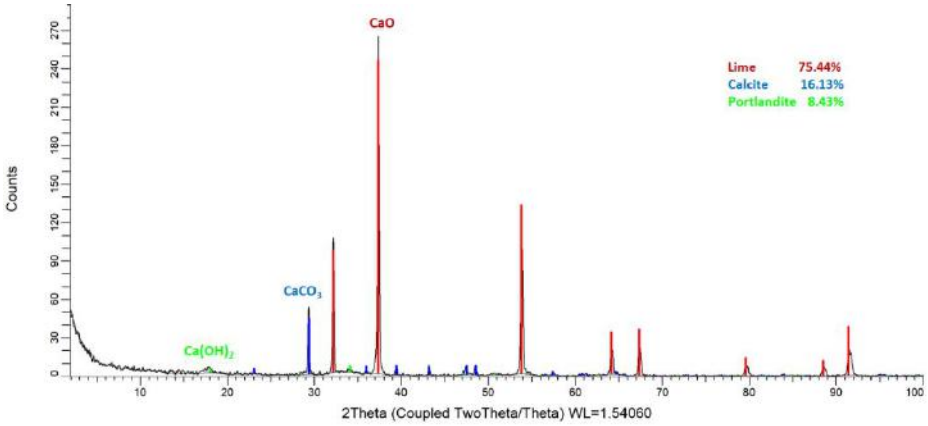

Figure 5
XRD diffractogram with the matched peaks of the calcined powder (Sample 2 with 0.5M $CaCl_2$ + 1M NaOH)

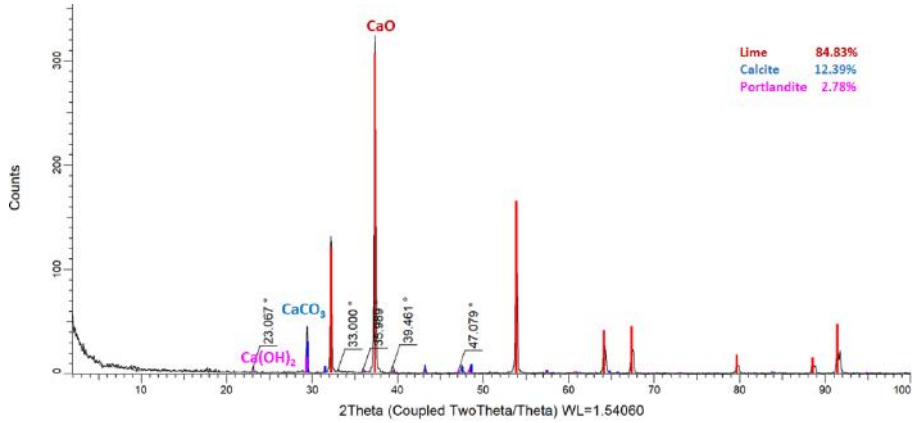

Figure 6

XRD diffractogram with the matched peaks for the calcined powder (Sample 3 with 1M $CaCl_2$ + 2M NaOH)

2.3. The correlation between the weight percentage, crystallite size and the concentrations of the reactants

Figure 7 shows the relationship between the concentrations of reactants and crystallite size of the produced CaO (see also *Table 1*). As follows from *Figure 7*, there is an approximately linear concentration dependence of the crystal size. It is in qualitative agreement with other experimental results obtained by precipitation techniques [6–16]. It is because the lower concentration of reagents leads to the smaller amount of matter attached to the nuclei in the growth phase. However, the line does not seem to pass through the origin (0; 0) – see *Figure 7*.

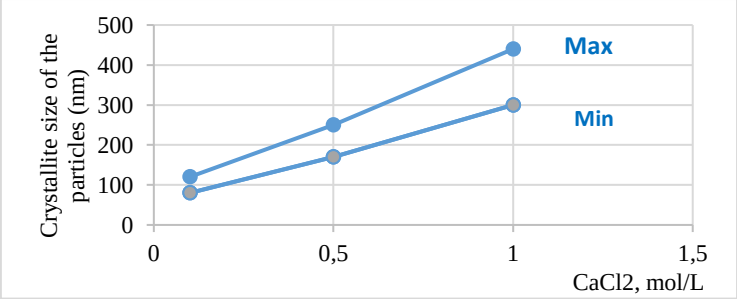

Figure 7

Crystallite sizes of the CaO as function of solution concentration

The connection between the concentrations of reactants and the composition of the final product is shown in *Figure 8*. One can see that the CaO content increases with the increase of the reactant concentrations. It is probably connected with *Figure 7*:

the increase in particle size decreases the specific surface area and does spontaneous capture of CO_2 or H_2O from the environment is decreased.

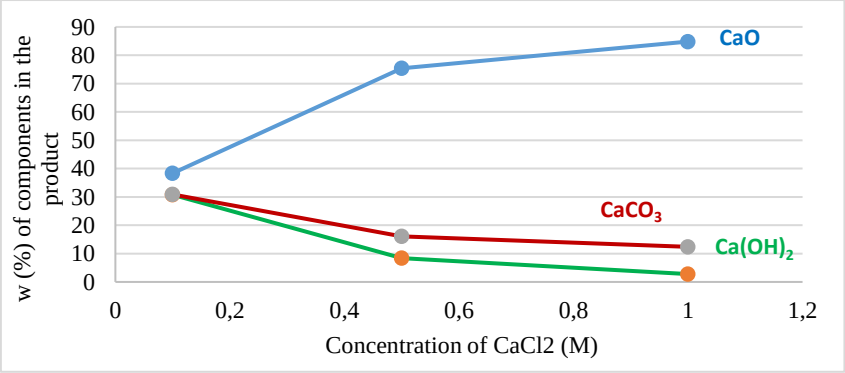

Figure 8

Composition of the final product vs the composition of the initial solution

CONCLUSION

Calcium oxide nano- and sub-micron particles were prepared by calcination of the product of chemical reaction between $CaCl_2$ and NaOH aqueous solutions. It is shown that about nano-range can be obtained only if a low concentration of the reactants is applied in the aqueous solution. The final product mostly contains CaO, although it is contaminated by $CaCO_3$ and Ca $(OH)_2$. This contamination decreases with decreasing the specific surface area of the particles, i.e. by increasing their size. Thus, the decrease in particle size and increasing at the same time the purity of the final CaO particles seems to be a challenge.

ACKNOWLEDGEMENTS

The authors are grateful to dr. Kristaly Ference of the University of Miskolc for his supporting in XRD analysis and discussions. We also thank to dr. Anna Sycheva and dr. Daniel Koncz-Horvath of the University of Miskolc for their helping in the investigation of SEM, EDX measurements and discussions in this research work.

REFERENCES

[1] Arul, E. et al. (2018). Bio-Directed Synthesis of Calcium Oxide (CaO) Nanoparticles Extracted from Limestone Using Honey. *J. Nanosci. Nanotechnol.*, Vol. 18, pp. 5790–5793.

[2] Abraham, Suja, Sarathy, V. P. (2018). Biomedical Applications of Calcium Oxide Nanoparticles – A Spectroscopic Study. *Int. J. Pharm. Sci. Rev. Res.*, Vol. 49, pp. 121–125.

[3] Butt, A. R., Ejaz, S., Baron, J. C., Ikram, M., Ali, S (2015). CaO Nanoparticles as a Potential Drug Delivery Agent for Biomedical Applications. *Digest Journal of Nanomaterials & Biostructures (DJNB)*, Vol. 10, 3, pp. 799–809, July 2015.

[4] Kulkarni, Deepak, Wachs, Israel E. (2002). Isopropanol oxidation by pure metal oxide catalysts: number of active surface sites and turnover frequencies. *Applied Catalysis A: General*, Vol. 237, pp. 121–137, May 2002.

[5] Sun, H. et al. (2018). Progress in the development and application of CaO-based adsorbents for CO2 capture – a review. *Materials Today Sustainability*, 1, pp. 1–27.

[6] López, José Manuel, Grasa, Gemma, Murillo, Ramon (2018). Evaluation of the effect of inert support on the carbonation reaction of synthetic CaO-based CO_2 sorbents. *Chemical Engineering Journal*, Vol. 350, pp. 559–572, May 2018.

[7] Mirghiasi, Zahra et al. (2014). Preparation and characterization of CaO nanoparticles from $Ca(OH)_2$ by direct thermal decomposition method. *Journal of Industrial and Engineering Chemistry*, Vol. 20, pp. 113–117.

[8] Ramli, M., Rossani, R. B., Nadia, Y., Darmawan, T., Saiful, Semarang, Febriani, Y. Ismail (2018). Nanoparticle fabrication of calcium oxide (CaO) mediated by the extract of red dragon fruit peels (Hylocereus Polyrhizus) and its application as inorganic–anti-microorganism materials. In: *IOP Conference Series: Materials Science and Engineering: Proceedings of the 13th Joint International Conference On Chemistry, JCC 2018*, Semarang, Indonesia, September 7–8, 2018, IOP, 2018. pp. 012090.

[9] Mohadi, Risfidian, et al. (2016). Preparation Calcium Oxide From Chicken Eggshells. *Sriwijaya Journal of Environment*, Vol. 1, 2, pp. 32–35.

[10] El-Dafrawy, Sh. M. et al. (2015). Synthesis of Nano-CaO Particles and Its Application for the Removal of Copper (II), Lead (II), Cadmium (II) and Iron (III) from Aqueous Solutions. *Egyptian Journal of Chemistry*, Vol. 58, 6, pp. 579–589.

[11] Tang, Zhen-Xing et al. (2013). Sonication-assisted preparation of CaO nanoparticles for antibacterial agents. *Química Nova*, Vol. 36, 7, pp. 933–936.

[12] Meysam, Sadeghi, Husseini, Mir Hassan (2013). A novel method for the synthesis of CaO nanoparticle for the decomposition of sulfurous pollutant. *Journal of Applied Chemical Research*, Vol. 7, 4, pp. 39–49.

[13] Tang, Zhen-Xing et al. (2008). Preparation of nano-CaO using thermal-decomposition method. *Materials Letters*, Vol. 62, 14, pp. 2096–2098.

[14] Szalai, Adrienn J., Manivannan, Nithyapriya, Kaptay, George (2019). Superparamagnetic magnetite nanoparticles obtained by different synthesis and separation methods stabilized by biocompatible coatings. *Colloids and Surfaces*

A: Physicochemical and Engineering Aspects, Vol. 568, pp. 113–122, May 2019.

[15] Habte, Lulit et al. Synthesis of nano-calcium oxide from waste eggshell by sol-gel method. *Sustainability*, Vol. 11, pp. 3196, June 2019.

[16] Aseel, M. A., Itab, F. H., Ahmed, F. M. (2018). Producing high purity of metal oxide Nano structural using simple chemical method. *Journal of Physics: Conference Series*, Vol. 1032, No. 1, IOP Publishing.

Materials Science and Engineering, Volume 45, No. 1 (2020), pp. 191–197.
DOI: 10.32974.mse.2020.019

THE EFFECT OF THE APPLIED PLASTER/WATER RATIO ON THE TECHNOLOGICAL PROPERTIES OF GYPSUM MOLD

EMESE KUROVICS[1] – LEA KÓSA[2] – LÁSZLÓ A. GÖMZE[3]

Abstract: In this research the properties of plaster samples were investigated. The samples were made from two different types of gypsum used in porcelain production. The plaster samples were made with the following 3 plaster/water ratios: 1.35, 1.51 and 1.75. The dimensions of the plaster samples were 20 × 20 × 100 mm. In this research, the water absorption, the flexural strength and the microstructure of the samples were investigated. Samples with a lower P/W ratio have higher water absorption rate, which can be beneficial when making porcelain products.

Keywords: gypsum, plaster/water ration, porcelain, strength, water absorption

INTRODUCTION

The raw material for making plasters is gypsum, which is a naturally occurring rock. Gypsum production and gypsum molds generate a large amount of waste, but the researchers seek to recycle gypsum waste [1], [2], [3]. Gypsum plays an important role in the ceramic industry, both in product design, forming and shaping operations such as slip casting [4], [5], [6], [7]. Gypsum or plaster molds are also used in the production of traditional ceramics (e.g. porcelain) and technical ceramics (e.g. alumina ceramics) by slip casting [8], [9], [10]. The slip casting is one of the most common industrial methods of ceramic casting. Slip casting begins with pouring the ceramic suspension (slurry) into a gypsum mold. The pores of the capillary system of the gypsum are smaller than the ceramic particles in the slurry. Therefore, due to capillary suction, the water content of the slurry penetrates the gypsum mold, while the ceramic particles retain on the inner wall of the gypsum mold. The retained particles are forming a continuously thickening layer. The quality of ceramic products and wall formation can be influenced by several factors, including the quality and properties of the gypsum used during the shaping [11], [12], [13], [14], [15].

During the slip casting operation, the wall formation mechanism of porcelain products *(Figure 1)* can be described by the following equation [16].

[1] Institute of Ceramics and Polymer Engineering, University of Miskolc
H-3515 Miskolc-Egyetemváros, Hungary
fememese@uni-miskolc.hu
[2] Institute of Ceramics and Polymer Engineering, University of Miskolc
H-3515 Miskolc-Egyetemváros, Hungary
[3] Institute of Ceramics and Polymer Engineering, University of Miskolc
H-3515 Miskolc-Egyetemváros, Hungary
femgomze@uni-miskolc.hu

$$x = \sqrt{\frac{2D(w_1 - w_2)}{k\rho}}\sqrt{t} \quad (1)$$

where: D the process-specific diffusion constant, $1/k$ proportionality factor, w_1, w_2 water content on the gypsum mold or slurry side, ρ density of the wall formed, t suction time.

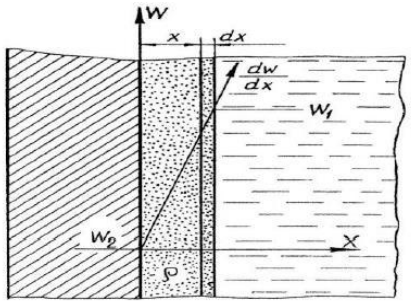

Figure 1
A semantic model of wall formation (taken from Gömze, L. A. [16])

Equation (1) illustrates that the wall thickness of the product is highly dependent on the suction time and the diffusion coefficient of the gypsum mold. The degree of diffusion is determined by the capillary system of the gypsum. It can be seen that it is important to characterize the properties of gypsum molds [17], [18], [19], [20], [21], which also depends on the method of production, including the type of gypsum used and the P/W ratio.

In the present research, the authors examined and compared the properties of plaster samples which made of two different gypsum types with 3 different P/W ratios.

1. MATERIALS AND METHODS

In this research plaster samples were with the use of different plaster/water ratio. First, were used the P/W ratio which was recommended by the manufacturer and after that, they chose a ratio below and above the recommended one *(Table 1)*. The recommended P/W ratio for both gypsum types was 1.51.

Table 1
The used plaster mixtures

No.	Water [ml]	Gypsum [kg]	P/W ratio
1.	482	0.65	1.35
2. (recommended by the manufacturer)	464	0.70	1.51
3.	429	0.75	1.75

After the addition of the appropriate gypsum-water ratio, followed by a soaking time of a few minutes the mass was homogenized by mixing then it was poured into the form. For gypsum specimens, the various gypsums were cast into a casting frame made of wood and separated by plate sheets *(Figure 2)*.

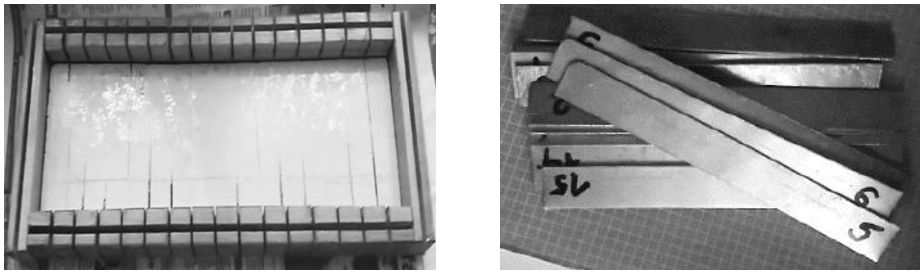

a) b)

Figure 2
The used wood form (a) and plate sheets (b) for making plaster samples

The dimensions of the rectangular specimens are nearly the same, 20 × 20 × 100 mm. The form was disassembled after the completion of the chemical reaction. The removed plaster samples were deburred. The samples were placed in a drying chamber at 60 °C for 48 h. The dried products were suitable for the tests.

The samples water absorption was examined by letting the samples in a bowl filled to the height of about 2 cm with water. Then the specimens were placed in a standing position *(Figure 3a)* in the bowl.

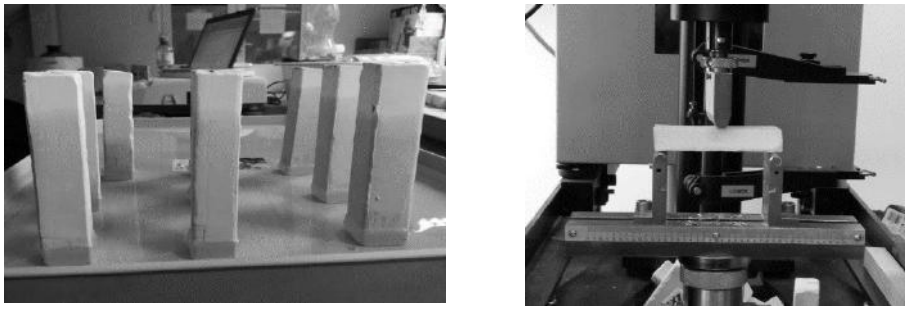

a) b)

Figure 3
The plaster samples during the water absorption (a) and the flexural strength test (b)

The mass of the specimens was measured at given time intervals. In this way were recorded the amount of absorbed water. The first measurement at 1 minute after the start of the study was performed. Then the water uptake was measured at every 5 and 10 minutes. To determining the flexural strength, the specimens were subjected to uniformly increasing stress until the specimens ruptured. In this work the strength

was measured by 3-point bending test using an INSTRON 5566 universal material testing equipment. The plaster samples were investigated in three different conditions (dry, half wet and wet). After the strength test, some fracture samples were taken. The microstructure of the fracture surface of samples were examined by Hitachi TM-1000 scanning electron microscopy.

2. RESULTS AND DISCUSSION

The results of the water absorption test are summarized in *Figure 4*.

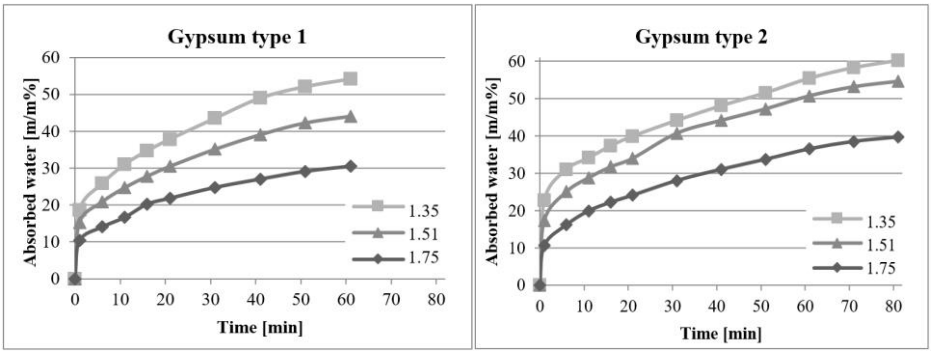

Figure 4

The absorbed water of two different types of gypsum using three P/W ratios

It worth mentioning that, in porcelain production, it is very important to know how much water the gypsum molds can absorb after a given time due to their capillary system, as this affects the quality of formation of porcelain wall. It can be seen from the experiment that as the plaster/water ratio increases, the water absorption capacity of the gypsum decreases. Gypsum mass with higher water content will be more porous after drying, therefore it can absorb more water within a given time.

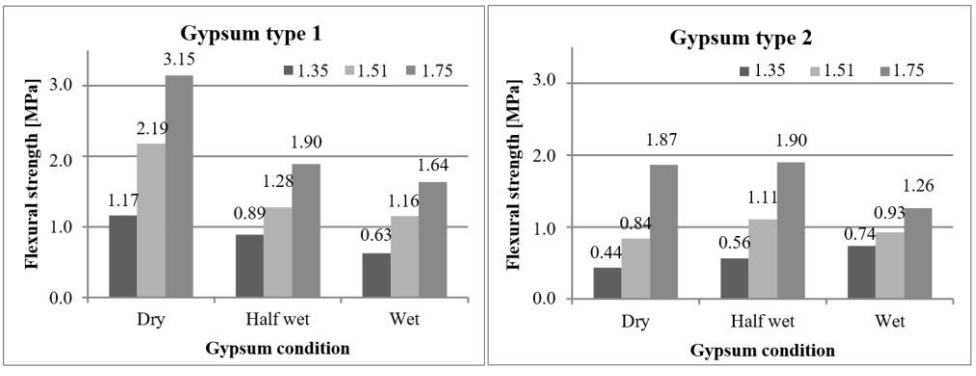

Figure 5

The flexural strength of two different types of gypsum using three P/W ratios

The P/W ratio has a significant effect on the strength of the gypsum samples. In general, wetting of the gypsum continuously reduces the strength value of the samples, which is worth considering for gypsum molds when used several times a day. For type 2, a slight increase in strength can be seen in the semi-wet state *(Figure 5)*.

No significant difference was observed in the microstructure of the fracture surface of the plaster samples made from the two gypsum types *(Figure 6)*. When examining samples made at different plaster/water ratios, it was observed that as the P/W ratio increased, the degree of porosity decreased, and the grain structure became more and more refined.

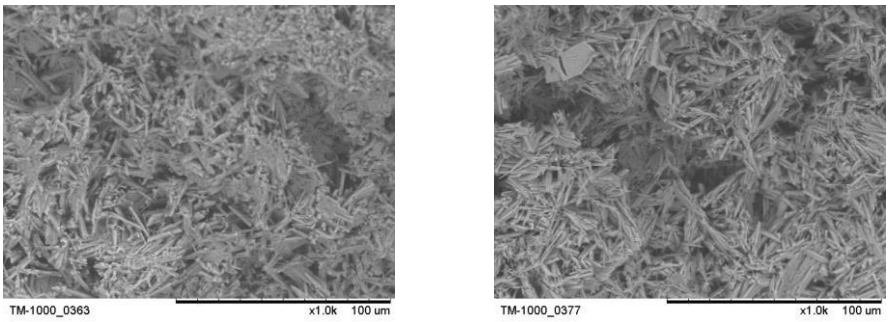

Type 1 Type 2

Figure 6
The fracture surface of the plaster samples (P/W = 1.75)

CONCLUSION

Gypsum mass with higher water content (lower P/W ratio) will be more porous after drying, so it can absorb water faster, which can be beneficial when making porcelain products. However, an increase in porosity results in a deterioration in strength. Therefore, it is important to use the optimal gypsum type and plaster/water ratio in the preparation of gypsum molds.

ACKNOWLEDGEMENTS

The described article was carried out as part of the EFOP-3.6.1-16-00011 *Younger and Renewing University – Innovative Knowledge City – institutional development of the University of Miskolc aiming at intelligent specialisation* project implemented in the framework of the Szechenyi 2020 program. The realization of this project is supported by the European Union, co-financed by the European Social Fund.

REFERENCES

[1] Binici, H., Resatoglu, R., Aksogan, O. (2018). Effect of egg white, perlite, gypsum and fly ash in environment friendly insulation materials, *Facta Universitatis Architecture and civil engineering*, Vol. 16, No. 3, pp. 329–342.

[Online]. Available: http://casopisi.junis.ni.ac.rs/index.php/FUArchCivEng/article/view/3018.

[2] Geraldo, R. H., Souza, J. D., Campos, S. C., Fernandes, L. F. R., Camarini, G. (2018). Pressured recycled gypsum plaster and wastes: Characteristics of eco-friendly building components. *Construction and Building Materials*, Vol. 191, pp. 136–144. [Online]. Available: https://doi.org/10.1016/j.conbuildmat.2018.09.193.

[3] Cipriano, P. B., Galdino, T., Sá, C., Ferraz, A. (2020). *Study of phases formed during sintering at different temperatures in ceramic composites containing gypsum waste*. [Online]. Available: https://dx.doi.org/10.21203/rs.3.rs-21149/v1preprint.

[4] Wiss, J. E., Camp, T. P., Ladoo, R. B. (1930). Gypsum plaster in the ceramic industries. *Journal of the American Ceramic Society*, Vol. 13, No. 5, pp. 287–314., 1930. [Online]. Available: https://doi.org/10.1111/j.1151-2916.1930.tb16271.x.

[5] Li, L., Arakawa, M. (1991). The Relationship between the Pore Characteristics and the Suctionability of a Gypsum Mold. *Journal of the Society of Powder Technology*, Vol. 28, No. 11, pp. 684–688. [Online]. Available: https://doi.org/10.4164/sptj.28.684.

[6] Kryuchkov, Y. N., Neklyudova, T. L. (2015). Structure of Gypsum and Polymer Molds for Slip Casting. *Glass Ceram.*, Vol. 71, pp. 324–326. [Online]. Available: https://doi.org/10.1007/s10717-015-9679-5.

[7] Neklyudova, T. L., Kryuchkov, Y. N. (2017). Effect of Pigments on the Properties of Colored Slips for Porcelain Production. *Glass Ceram*., Vol. 74, pp. 240–242. [Online]. Available: https://doi.org/10.1007/s10717-017-9971-7.

[8] Hotta, Y., Banno, T., Sano, S., Tsuzuki, A., Oda, K. (2000). Translucent Alumina Produced by Slip-Casting Using a Gypsum Mold. *Journal of the Ceramic Society of Japan*, Vol. 108, Issue 1263, pp. 1030–1033. [Online]. Available: https://doi.org/10.2109/jcersj.108.1263-1030.

[9] Schilling, C. H. (2001). Colloid Casting. *Encyclopedia of Materials: Science and Technology*. (2nd ed.), pp. 1314–1319. [Online]. Available: https://doi.org/10.1016/B0-08-043152-6/00248-5.

[10] Gholami, M., Khakpour, Z. (2019). Manufacturing of new potential plaster molds for slip casting of alumina nanoparticles. *Journal of the Australian Ceramic Society*, Vol. 55, pp. 633–637. [Online]. Available: https://doi.org/10.1007/s41779-018-0272-6.

[11] Adcock, D. S., McDowall, I. C. (1957). The Mechanism of Filter Pressing and Slip Casting. *Journal of the American Ceramic Society*, Vol. 40, Issue 10. [Online]. Available: https://doi.org/10.1111/j.1151-2916.1957.tb12552.x.

[12] Gömze, L. A., Liszátzné Helvei, Á., Simonné Odler, A., Szabó, M. (2001). *Ceramic yearbook I. 2001*. Budapest, ÉTK–MÉASZ, pp. 30–85., ISBN 963 512 774 X.

[13] Orosz, V., Gömze, L. A. (2008). Analysis of casting faults in producing of silicon carbide products. *Global Roadmap for Ceramics – ICC2 Proceedings*, Verona, June 29–July 4, 2008.

[14] Nagy, K. G., Gömze, L. A. (2013). Investigation of porcelain slip casting. *10th International Conference Preparation of Ceramic Materials*, Herľany, Slovakia, June 18–20, 2013, pp. 90–91. [Online]. Available: http://web.tuke.sk/seminar_PKM/TEXT/2013/P%20%201%20Nagy.pdf.

[15] Gömze L. A. (2005). *Agyagásványok aprításának és kerámiák alakadásának matematikai modellezése*. Miskolc, 2005. 05. 11., pp. 37–38. [Online]. Available: https://www.researchgate.net/publication/341510744_Agyagasvanyok _apritasanak_es_keramiak_alakadasanak_matematikai_modellezese.

[16] Wahab, N. H. A., Saad, N. H., Sahab, A. R. M., Nasir, N., Rashid, A. A. (2017). The effect of water/plaster ratio variation on absorption properties and flexurel strength of gypsum plaster for ceramic slip rotary moulding. *Sci. Int. (Lahore)*, Vol. 29, No. 4, pp. 843–846., ISSN 1013-5316; CODEN: SINTE 8, [Online]. Available: http://www.sci-int.com/pdf/636359665904844313.pdf.

[17] Moghadam, H. A., Masir, M. J., Torshaki, Z. B., Dehghan, A. (2019). Effect of Mixing Rate of Plaster with Water on Properties of Gypsum Plaster. *Advanced Recearches in Civil Engineering*, Vol. 1, Issue 1, pp. 42–48. [Online]. Available: https://dx.doi.org/10.30469/arce.2019.82738.

[18] Singh, M., Garg, M. (1996). Relationship between mechanical properties and porosity of water-resistant gypsum binder. *Cement and Concrete Research*, Vol. 26, Issue 3, pp. 449–456. [Online]. Available: https://doi.org/10.1016/S0008-8846(96)85032-0.

[19] Soroka, P. J. S. (1968). Interrelation of Hardness, Modulus of Elasticity, and Porosity in Various Gypsum Systems. *Journal of the American Ceramic Society*, Vol. 51, Issue 6. [Online]. Available: https://doi.org/10.1111/j.1151-2916.1968.tb15949.x.

[20] Borselli, L., Carnicelli, S., Ferrari, G. A., Pagliai, M., Lucamante, G. (1996). Effects of gypsum on hydrological, mechanical and porosity properties of a kaolinitic crusting soil. *Soil Technology*, Vol. 9, Issues 1–2, pp. 39–54. [Online]. Available: https://doi.org/10.1016/0933-3630(95)00034-8.

Materials Science and Engineering, Volume 45, No. 1 (2020), pp. 198–206.
DOI: 10.32974.mse.2020.020

PHASE CHANGE COMPOSITES WITH MILLED CARBON FIBER

HAMID LAHMAIDI[1] – PÉTER BAUMLI[2]

Abstract: The use of phase change materials (PCMs) in latent heat storage attracts more and more attention in recent years, but their low thermal conductivity is one of main issues that should be resolved. In order to overcome this problem, the dispersion of solid-liquid PCMs into carbon based materials has been investigated in many studies. In the present study, the pressing method was used for the preparation a PCM composite. $NaNO_3$ and $CsNO_3$ will be chosen as the PCMs and the milled carbon nanofiber (MCF) as the high thermal conductive filler. Several studies have been developing new types of PCMs by introducing high thermal conductive filler such as carbon additives or metal foams. Carbon materials are so far the best fillers to increase the effective thermal conductivity of PCM since only small volume fraction is needed and they have high thermal conductivity and low density.

Keywords: PCMs, carbon Additives, thermal conductivity

INTRODUCTION

Recently the higher demand of fossil fuels and increasing attention of risks related to environmental issues have contributed to find other renewable sources of energy [1, 2, 3]. Due to the different industrial and daily domestic activities, the energy consumption changes significantly between peak and off peak period. Among various forms of energy that can lead to a better power management and improve the performance of thermal systems is thermal energy which is remarkably available in nature as solar radiations and geothermal energy and building applications.

Thermal energy aims to heat a material until the phase change is realized which can be from solid to solid, solid to liquid or from liquid [4, 5]. In the aim of making this transformation happens; a large amount of heat is absorbed by the material. Phase change materials (PCMs) are mostly used to store such thermal energy. As a matter of fact, most of the PCMs have low effective thermal conductivity which requires the development of high thermal conductive materials [6, 7, 8].

The necessity of increasing the thermal conductivity of PCMs is evident due to its low charging/discharging rates which is important during thermal cycling. Several studies have been developing new type of PCMs by introducing high thermal conductive filler such as carbon additives or metal foams. Carbon materials are so far the best fillers to increase the effective thermal conductivity of PCM since only

[1] Institute of Physical Metallurgy, Metalforming and Nanotechnology, University of Miskolc H-3515 Miskolc-Egyetemváros, Hungary
[2] Institute of Physical Metallurgy, Metalforming and Nanotechnology, University of Miskolc H-3515 Miskolc-Egyetemváros, Hungary
baumlipeter@gmail.com

small volume fraction is needed and they have high thermal conductivity and low density. The thermal conductivity enhancement using carbon material is the point of focus of this work.

Many studies have been done on improving the heat transfer of PCMs. In general, the studies are divided into several categories depending on the types of thermal conductivity enhancers:

Expanded graphite

Xu et al. [9] prepared $LiNO_3 - KCl - NaNO_3/EG$ composite PCM using the capillary method with 5 wt%, 10 wt%, 15 wt%, 20 wt%, and 25 wt% EG. At 25 wt% mass fraction of EG, they found out that no leakage was observed. Using the SEM images, it has been proven that $LiNO_3 - KCl - NaNO_3$ composites were intensely absorbed by EG. In their experiments, the thermal conductivity and the compress density show a strong linear relationship. However, the thermal conductivity of the eutectic salt under a compress density of 1.482 g/cm^3 was 1.608 W/mK. When the compress density of the composite PCM varies from 0.9 to 2 g/cm^3; the thermal conductivity varies from 18.57 to 31.53 W/mK which was 11.5–19.6 higher than that of the pure salt. Song et al. [10] use also EG as a high thermal conductivity enhancer and $MgCl_2.6H_2O$ as PCM. It has low thermal conductivity, liquid leakage, high supercooling and poor thermal reliability after numerous thermal cycles. To overcome those issue, EG with different mass fraction (9 wt%, 13 wt%, 16.67 wt%, and 20 wt%) was mixed with $MgCl_2.6H_2O$. The thermal conductivity data of composite PCMs with 9 wt%, 13 wt%, 16.67 wt%, and 20 wt% of EG was respectively measured to be 0.942 W/mK, 1.053 W/mK, 1.354 W/mK and 1.658 W/mK. Also, DSC analysis showed that the addition of EG decreased the degree of supercooling by 29.4 °C. Zhong et al [11] prepared three kinds of porous composite change materials using three types of binary salts ($LiNO_3 - KCl$, $LiNO_3 - NaNO_3$ and $LiNO_3 - NaCl$) as the phase change materials and expanded graphite as the high thermal conductive additive. The thermal conductivity was significantly increased. It is analyzed that, after impregnation with the EG, the thermal conductivity of $LiNO_3 - KCl$ is intensified by 5.0 times; $LiNO_3 - NaNO_3$, 6.9 times; and $LiNO_3 - NaCl$, 4.9 times. Many studies combined EG with various PCMs, and the obtained results that the thermal conductivity of the composites have been significantly increased [12, 13, 14, 15].

Carbon nanotubes

Qian et al. [16] reported the preparation of a new polyethylene glycol (PEG)/diatomite form-stable phase change composite (fs-PCC) with single-walled carbon nanotubes (SWCNs) as nano-additive. The obtained results showed that the thermal conductivity of the PCC has been increased from 0.24 W/mK in case of pure PEG to 0.87 W/mK with a small fraction off SWCNTS (2 wt%). Zhang et al. [17] studied the effect of the introduction of CNTs as a additive for improving the thermal conductivity of paraffin-carbon nanotubes/expanded perlite form-stable composite phase change materials (PA-CNTs/EP FS-CPCMs). The vacuum impregnation

method was used to prepare the composite with different mass fraction of CNT. The thermal conductivity of PA-CNTs/EP FSCPCMs5.27 (0.516 Wm−1 K−1) was 4.82 times that of PA-CNTs/EP FS-CPCMs0. The thermal storage and release properties of PA-CNTs/EP FS-CPCMs were significantly improved as compared with those of PACNTs/EP FS-CPCMs0. Feng et al. [18] prepared a new composite where t MWCNTs was chosen as the high thermal conductivity enhancer, Na_2CO_3 was used as phase change material and MgO as a supporting material. With the increase of MWCNTS amount and temperature of use, the thermal conductivity has been significantly increased. Tao et al. [19] found out that the single walled carbon nanotubes are more efficient to enhance the thermal conductivity. The thermal conductivity increased up to 56.98%.

Carbon fiber

There have been several studies reporting the preparation of phase change materials composites using carbon fiber [20, 21]. Zhao et al. [22] used graphite fiber to prepare Carbon bonded carbon fiber (CBCF) monoliths. The CBCF were filled with paraffin wax to for the PCM composite. The in-plane thermal conductivity of the PCM composite was significantly increased up to 57 times over the pure wax, while the out-of-plane thermal conductivity was also increased by 3.7 to 5.5 times. In addition, the improvements in thermal conductivity showed almost linear relationship with the volume fraction of carbon fibers in the PCM composites.

Takahiro et al. [23] developed a new phase change material composite with a percolating network of Carbon Fiber using two types of methods: The conventional melting dispersion method (MD) and a novel hot press method (HP). Erythritol with low thermal conductivity (0.73 W/mK) was chosen as the phase change material and carbon fiber as the high thermal conductive filler (900 W/mK). The results showed that the percolating network can be easily formed by HP method. The thermal conductivity of the PCC prepared by both methods increased with the increase of CF. moreover, the thermal conductivity of the PCC prepared by HP method increased exponentially and was much high than those fabricated by MD.

In order to develop a high thermal conductive composite material, a new type PCM composite (dispersion of milled carbon fiber in $NaNO_3$ and $CsNO_3$ molten salts), was prepared pressing method (PM) in the present work. The composites of $NaNO_3$/MCF and $CsNO_3$/MCF with varying volume fraction were prepared. SEM analysis experimentally studied.

1. EXPERIMENTAL

1.1. Objective

The main goal of this research is the fabrication of a new phase change material (PCM) for medium temperature thermal energy storage. We selected Sodium nitrate and cesium nitrate as the phase change materials (PCMs) and the milled carbon fiber (MCF) as the high thermal conductive filler. In general, those PCMs have a low

thermal conductivity ($K_{NaNO_3} \cong 0.565$ W/mK, $K_{CsNO_3} \cong 0.31$ W/mK). This leads to a slow charging and discharging. To address this issue, the milled carbon fiber (MCF) will be included as a thermal conductivity enhancement material. *Table 1* lists the specification of the MCF. It has a length of 150 μm and a carbon content of >95. Firstly, the distribution of the PCMs and The MCF in the composite will be investigated, then the thermal conductivity and thermal stability of the composite will be investigated.

Table 1

Specifications of carbon fiber as the high thermal conductivity filler

	Density (g/cm^3)	**Fiber diameter (μm)**	**Fiber length (μm)**	**λ_{MCF} (W/mK)**
MCF	1.81	7.2	150	600–900

1.2. Fabrication of phase change material composites

Sodium nitrate, cesium nitrates and milled carbon fiber were in solid form at the ambient temperature. The fabrication process involves weighing the material particles, followed by grinding the salts at ambient temperature, then trough mixing and compressing to produce samples in the shape of discs. The compressing (tableting) will be done at a pressure of 800 tones, and the resulting tablets will have a mass of 5 g and 10 mm in diameter. The pellets will be dried at 120 °C for 2 h. In latent heat storage application, The gaseous heat transfer will be used to transfer heat trough the compressed pellets (Molten salts/Milled carbon fiber); while the liquid flow (water, oil...) cannot be used, because the salts will be dissolved in this liquid.

Table 2

Volume fractions of MCFs

Sample No.	S1	S2	S3	S4
MCF (vol%)	1	2	5	10

Four PCC samples, with different volume ratio (vol%) of CF will be prepared as *Table 2* shows. It has been concluded that the concentration of the MCF in the composite would influence the thermal conductivity of the composite.

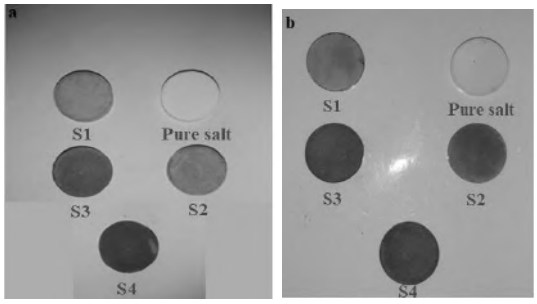

Figure 1

Photos of samples: (a) Sodium nitrate/MCF (b) Cesium nitrate/MCF

2. RESULTS AND DISCUSSION

2.1. Microscopy images of $NaNO_3$/MCF and $CsNO_3$/MCF composites

Figure 2 and *Figure 3* show the SEM images of the composite material with 1 vol% and 5 vol% of milled carbon fiber. The morphologies of the composite materials with low amount of MCF are similar to that containing 1 vol% of MCF while that with higher amount of MCF are similar to that containing 5 vol% of MCF. As a consequence, only two of the SEM images are shown and discussed.

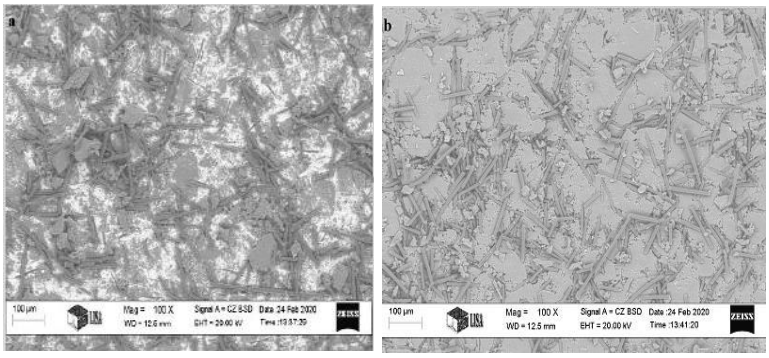

Figure 2
SEM images of sodium nitrate/MCF composite at (a) 1 vol% and (b) 5 vol% of MCF in the composite

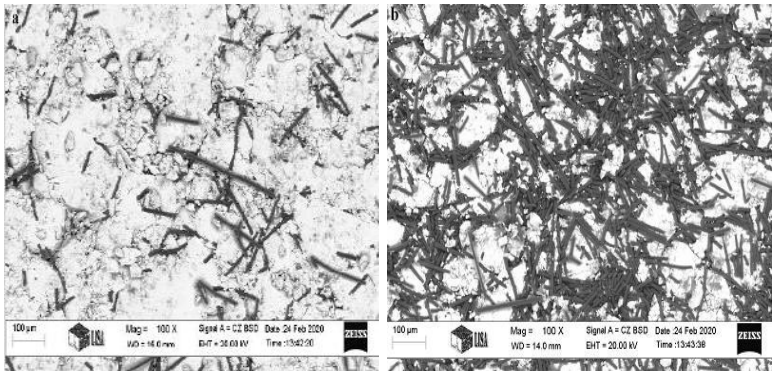

Figure 3
SEM images of Cesium nitrate/MCF composite at (a) 1 vol% and (b) 5 vol% of MCF in the composite

Comparing the different MCF distribution in the PCC prepared by Pressing method, significant differences were observed. The network of MCF was observed in the PCC with low amount of MCF, while the network of MCF can clearly observed in the PCC containing higher amount of MCF *(Figures 2, 3)*. This was the main reason that the thermal conductivity of the PCC increased significantly (see *Figure 4*). On

the other hand, for the samples containing high amount of MCF; the thermal conductivity increased infinitesimally, which proves that small amount of MCF is enough to enhance the thermal conductivity.

As shown in *Figure 2* and *Figure 3*, in the samples containing low amount of MCF. the MCF was randomly located around the PCM particles. This was because the PCM particles were in solid form during the pressing procedure. We assume that the network of MCF and PCM was easily formed in this condition since, initially, the PCM particles were in contact with each other, and the void of PCM particles were filled by the MCF.

2.2. Thermal conductivity enhancement of PCMs using carbon materials: A comparison

Phase change materials are mostly used to store such thermal energy. However, their low thermal conductivity presents one of the issues that should be resolved. Higher thermal conductivity could be achieved by using some additives in the aim of increasing the energy charge/discharging rates. Many studies have been done on the preparation of new phase change material composites using different carbon additives. The comparison between those studies is given in the table below.

The comparison of the thermal conductivity enhancement using different types of carbon additives are listed in *Table 1*. The conclusions can be drawn:

- The thermal conductivity is significantly increased in case of high aspect ratio of carbon additive.
- The addition of small amount of CNTs can contribute to the enhancement of thermal conductivity.
- The EG and graphite powder are promising additive to enhance the thermal conductivity.

Table 3

Comparison of the thermal conductivity enhancement with some types of carbon additives

Carbon additive	PCM	K_{PCM} (W/m.K)	Fraction	K_{PCC} (W/m.K)	Increase (%)
Expanded Graphite	Eutectic $LiNO_3/KCl$ [19]	1.749	30 wt%	11.63	665
	Ternary eutectic chloride [24]	1.174	5 wt%	2.084	178
	Form stable PCM [25]	0.43	20 wt%	4.59	1,067
Carbon fiber	Erythritol [23]	0.733	25 vol%	≈30	4,000
Grafted CNTs	Paraffin [26]	0.2312	4 wt%	0.7903	342
Short SWCNT	Water [27]	0.580	0.48 vol%	0.604	104
Long SWCNT	Water [27]	0.580	0.48 vol%	0.627	108
MWCNT	Water [27]	0.580	0.48 vol%	0.598	103

CONCLUSIONS

This work describes the preparation of high thermal conductive PCC by pressing method. The relationship between the thermal conductivity of the PCC and the distribution of the PCC and MCF was investigated. The main conclusions are provided below:

1. The pressing method (PM) was used to prepare a high thermal conductive PCM composite. It is an effective method for preparing high thermal conductivity PCC using anisotropic, high thermal conductivity fillers, such as MCF.
2. Using $CsNO_3$ and $NaNO_3$ as the PCMs and MCF as the filler, a network of MCF was found with a smaller amount of MCF in the composite.
3. However, the selection of any additive is based on the stability of both components (PCM and additive) in the composite, the economic costs and environmental impact etc.

ACKNOWLEDGEMENTS

The authors would like to express their appreciation to the Institute of Physical Metallurgy, Metal Forming and Nanotechnology, University of Miskolc in the person of dr. Dániel Koncz Horváth, for their support in order to accomplish the experiments (SEM analysis) in the best conditions.

REFERENCES

[1] Foster, E., Contestabile, M., Blazquez, J., Manzano, B., Workman, M., Shah, N. (2017). The unstudied barriers to widespread renewable energy deployment: Fossil fuel price responses. *Energy Policy*, Vol. 103, pp. 258–264.

[2] Rennkamp, B., Haunss, S., Wongsa, K., Ortega, A., Casamadrid, E. (2017). Competing coalitions: The politics of renewable energy and fossil fuels in Mexico, South Africa and Thailand. *Energy Research & Social Science*, Vol. 34, pp. 214–223.

[3] Letcher, T. M. (ed.) (2020). *Future energy: improved, sustainable and clean options for our planet*. Elsevier, Amsterdam, Netherlands, ISBN: 978-0-08-102886-5.

[4] Steinmann, W. D., Tamme, R. (2008). Latent heat storage for solar steam systems. *Journal of solar energy engineering*, Vol. 130 (1), pp. 1–5.

[5] Regin, A. F., Solanki, S. C., Saini, J. S.(2008). Heat transfer characteristics of thermal energy storage system using PCM capsules: a review. *Renewable and Sustainable Energy Reviews*, Vol. 12 (9), pp. 2438–2458.

[6] Lin, Y., Jia, Y., Alva, G., Fang, G. (2018). Review on thermal conductivity enhancement, thermal properties and applications of phase change materials

in thermal energy storage. *Renewable and sustainable energy reviews*, Vol. 82, pp. 2730–2742.

[7] Zou, D., Ma, X., Liu, X., Zheng, P., Hu, Y. (2018). Thermal performance enhancement of composite phase change materials (PCM) using graphene and carbon nanotubes as additives for the potential application in lithium-ion power battery. *International Journal of Heat and Mass Transfer*, Vol. 120, pp. 33–41.

[8] Ramakrishnan, S., Wang, X., Sanjayan, J. (2019). Effects of various carbon additives on the thermal storage performance of form-stable PCM integrated cementitious composites. *Applied Thermal Engineering*, Vol. 148, pp. 491–501.

[9] Xu, T., Li, Y., Chen, J., Liu, J. (2017). Preparation and thermal energy storage properties of LiNO3-KCl-NaNO3/expanded graphite composite phase change material. *Solar Energy Materials and Solar Cells*, Vol. 169, pp. 215–221.

[10] Song, Z., Deng, Y., Li, J., Nian, H. (2018). Expanded graphite for thermal conductivity and reliability enhancement and supercooling decrease of MgCl2· 6H2O phase change material. *Materials Research Bulletin*, Vol. 102, pp. 203–208.

[11] Zhong, L., Zhang, X., Luan, Y., Wang, G., Feng, Y., Feng, D. (2014). Preparation and thermal properties of porous heterogeneous composite phase change materials based on molten salts/expanded graphite. *Solar Energy*, Vol. 107, pp. 63–73.

[12] Wu, Y., Wang, T. (2015). Hydrated salts/expanded graphite composite with high thermal conductivity as a shape-stabilized phase change material for thermal energy storage. *Energy conversion and management*, Vol. 101, pp. 164–171.

[13] Tian, H., Wang, W., Ding, J., Wei, X., Huang, C. (2016). Preparation of binary eutectic chloride/expanded graphite as high-temperature thermal energy storage materials. *Solar Energy Materials and Solar Cells*, Vol. 149, pp. 187–194.

[14] Huang, Z., Gao, X., Xu, T., Fang, Y., Zhang, Z. (2014). Thermal property measurement and heat storage analysis of LiNO3/KCl–expanded graphite composite phase change material. *Applied Energy*, Vol. 115, pp. 265–271.

[15] Xiao, J., Huang, J., Zhu, P.., Wang, C., Li, X. (2014). Preparation, characterization and thermal properties of binary nitrate salts/expanded graphite as composite phase change material. *Thermochimica Acta*, Vol. 587, pp. 52–58.

[16] Qian, T., Li, J., Feng, W. (2017). Enhanced thermal conductivity of form-stable phase change composite with single-walled carbon nanotubes for thermal energy storage. *Scientific Reports*, Vol. 7, p. 44710.

[17] Zhang, X., Wen, R., Huang, Z., Tang, C., Huang, Y., Liu, Y., Xu, Y. (2017). Enhancement of thermal conductivity by the introduction of carbon nanotubes as a filler in paraffin/expanded perlite form-stable phase-change materials. *Energy and Buildings*, Vol. 149, pp. 463–470.

[18] Ye, F., Ge, Z., Ding, Y., Yang, J. (2014). Multi-walled carbon nanotubes added to Na2CO3/MgO composites for thermal energy storage. *Particuology*, Vol. 15, pp. 56–60.

[19] Tao, Y. B., Lin, C. H., He, Y. L. (2015). Preparation and thermal properties characterization of carbonate salt/carbon nanomaterial composite phase change material. *Energy Conversion and Management*, Vol. 97, pp. 103–110.

[20] Elgafy, A., Lafdi, K. (2005). Effect of carbon nanofiber additives on thermal behavior of phase change materials. *Carbon*, Vol. 43 (15), pp. 3067–3074.

[21] Fukai, J., Hamada, Y., Morozumi, Y., Miyatake, O. (2002). Effect of carbon-fiber brushes on conductive heat transfer in phase change materials. *International Journal of Heat and Mass Transfer*, Vol. 45 (24), pp. 4781–4792.

[22] Jiang, Z., Ouyang, T., Yang, Y., Chen, L., Fan, X., Chen, Y., Fei, Y. (2018). Thermal conductivity enhancement of phase change materials with form-stable carbon bonded carbon fiber network. *Materials & Design*, Vol. 143, pp. 177–184.

[23] Nomura, T., Tabuchi, K., Zhu, C., Sheng, N., Wang, S., Akiyama, T. (2015). High thermal conductivity phase change composite with percolating carbon fiber network. *Applied Energy*, Vol. 154, pp. 678–685.

[24] Tian, H., Wang, W., Ding, J., Wei, X., Song, M., Yang, J. (2015). Thermal conductivities and characteristics of ternary eutectic chloride/expanded graphite thermal energy storage composites. *Applied Energy*, Vol. 148, pp. 87–92.

[25] Wang, X., Guo, Q., Wang, J., Zhong, Y., Wang, L., Wei, X., Liu, L. (2013). Thermal conductivity enhancement of form-stable phase-change composites by milling of expanded graphite, micro-capsules and polyethylene. *Renewable Energy*, Vol. 60, pp. 506–509.

[26] Li, M., Chen, M., Wu, Z., Liu, J. (2014). Carbon nanotube grafted with polyalcohol and its influence on the thermal conductivity of phase change material. *Energy Conversion and Management*, Vol. 83, pp. 325–329.

[27] Xing, M., Yu, J., Wang, R. (2015). Experimental study on the thermal conductivity enhancement of water based nanofluids using different types of carbon nanotubes. *International Journal of Heat and Mass Transfer*, Vol. 88, pp. 609–616.

Materials Science and Engineering, Volume 45, No. 1 (2020), pp. 207–216.
DOI: 10.32974.mse.2020.021

EFFECT OF CHANGE IN TEMPERATURE ON THE CONCENTRATION OF FLUE GAS COMPONENTS FROM WOOD COMBUSTION

DÓRA MENTES[1] – CSABA PÓLISKA[2]

Abstract: Knowledge of the mechanism of formation of flue gas components from residential solid fuels is essential for the reduction of gaseous substances which causes climate change and are harmful to the environment.

The complexity of formation of the flue gas components was simplified during laboratory experiments. The homogeneity and mass of the sample affecting the firing was constant, and volume flow of the continuously flowing combustion air was 140 dm^3/h. The temperature of the combustion chamber was changed, it was heated to 600 °C, 700 °C and 800 °C. It was obtained an answer to how increasing the temperature of the combustion chamber affects the amount of CO, CO_2, O_2, and NO_x components formed in the flue gas as a function of time as a result.

The CO formation can be divided into two stages during combustion: the inflammatory stage and the combustion stage. During the inflammatory phase the amount of CO is affected by oxygen involved in the combustion and the amount of the excess air, while in the combustion phase it is primary influenced by temperature.

Keywords: effect of change in furnace chamber's temperature, biomass combustion, amounts of flue gas components

INTRODUCTION

One of the biggest challenges of the Anthropocene era is the crisis of air pollution, which poses a potential risk to human's health and economy growth [1]. The assessment and improvement of air quality, and the complexity and importance of the consequences of air pollution have attracted much attention among researchers. According to the source of air pollution, it can be distinguished between anthropogenic (man-made) and natural sources. The atmosphere is thus a complex chemical system in which emissions of urban pollutants are mixed with emissions from the natural environment [2]. Although many pollutants from natural activities (volcanic eruptions and scrub and forest fires in the Mediterranean countries, California and Australia, etc. [3], [4], [5]) releases in the atmosphere, anthropogenic activities are the main causes of ambient air pollution [6].

[1] Department of Combustion Technology and Thermal Energy, University of Miskolc
H-3515 Miskolc-Egyetemváros, Hungary
tuzdora@uni-miskolc.hu

[2] Department of Combustion Technology and Thermal Energy, University of Miskolc
H-3515 Miskolc-Egyetemváros, Hungary
tuzcsaba@uni-miskolc.hu

Emissions of the most important air pollutants in Europe decreased between 2002 and 2011, resulting in improved air quality in the region in case of some pollutants. Despite these results, not all countries and economic sectors have made satisfactory development and progress in reducing emissions [7]. However continuous progress has been observed in other sectors (such as industry), emissions from agriculture and residential solid fuel combustion have either decreased slightly (for agriculture) or not at all in the last decade (for household fuel combustion) [7].

Emission of benzo-a-pyrene (BaP), which is considered as a marker of imperfect combustion and as a representative of polycyclic aromatic compounds, increased by 11% in the EU-27 between 2002 and 2011, due to a 24% increase in emissions from residential solid fuels. BaP pollution is a growing problem in Europe, especially in areas where residential solid combustion (like coal and wood) is common [7].

Considering to the emission of particulate matter, 47.3% of total emission in Europe comes from households. This share increased by more than 6% compared to data of 2006 [8]. Poland has the highest concentration limits for particulate matter in ambient air in the EU. The PM10 is 200 $\mu g/m^3$ and the PM2.5 is 300 $\mu g/m^3$. These quantities are eight and six times higher, respectively, than the given limits found in the World Health Organization (WHO) guidelines [8].

It can be declared that biomass combustion has become one of the biggest sources of air pollution [9]. Since the wood burning is much more affordable and reachable for the households in energy poverty than for example using of solar power for heating. It is also considered a climate-friendly energy source because it is renewable and carbon-neutral [7].

The aim of the laboratory experiments is to examine how the changing of the temperature of the combustion chamber effects to concentration of flue gas components. The experiments presented in the work are preliminary experiments. Another direction of the research is to study the evolution of the amounts of flue gas components from waste combustion.

1. MATERIALS AND METHODS

1.1. Materials

In the laboratory-sized experiments, the oak sample was in an air-dry state. The sample was grounded to homogeneous in order to ensure that the heterogeneity did not affect the results of the measurements. The homogeneous sample was compressed into a puck-shape using the apparatus shown in *Figure 1*.

A sufficiently large surface area of puck-shaped fuel had got in contact the combustion air during the firing, which resulted the reduction of the emission of CO. This could be explained by increased specific surface area. If the specific surface area of the fuel was not large enough during the combustion, the air-fuel mixing quality was poor, which resulted the formation of CO [11].

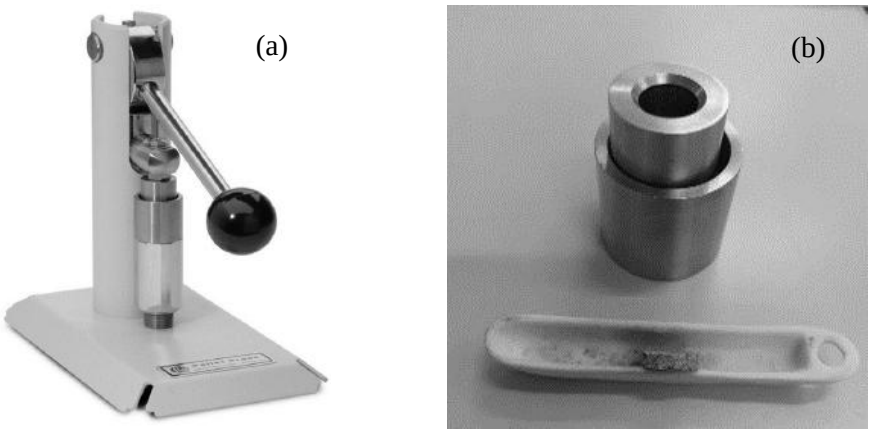

Figure 1
Picture of a pressing machine forming the shape of the sample (a) [10], *image of the sample in the boat (b)*

1.2. Measurement process of the laboratory experiment

The combustion process was tested in a Hőker Cső 350/900 type electric resistance tube furnace, which had a horizontal working chamber and a programmable temperature of the furnace temperature controller, thus allowing the temperature set at a given time to be maintained. The analysis of the concentration of the gases from the combustion process (CO_2, O_2, CO, NO_x) was performed with a Horiba PG 250 gas analyzer. The air flow rate was regulated by the compressed air tank, rotameter, and valve. The experimental setup is schematically illustrated in *Figure 2*.

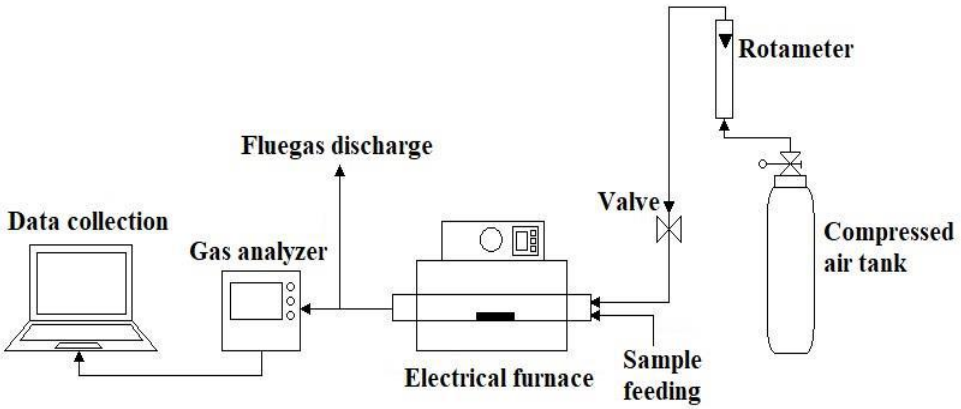

Figure 2
Measuring system

The actual combustion air flow rate was set at the beginning of the experiment. The sample in the quartz boat was pushed into the combustion zone, after the tube furnace reached the predetermined temperature of the furnace chamber. Combustion started immediately in the combustion zone, along with the recording of emission values. The experiment time lasted longer at lower temperatures than at higher temperatures.

Investigation of the combustion process happened at a combustion air volume flow of 140 dm^3/h and at a temperature of 600 °C, 700 °C, 800 °C. Three experiments were performed in each settings. The data shown in the figures are the averages of the experimental results.

A similar measuring system could be found in the literature, however the set combustion parameters and the tested fuels were different. For example Peng et al. [12] investigated emission characteristics of PAHs during MSW/coal co-combustion. Wielgosiński et. al. [13] examined the emission of CO, NOx and TOC from biomass combustion in comparison to hard coal in 5 different temperatures and at 3 different air flow rates excess air.

2. RESULTS

2.1. Evolution of the amount of flue gas components during combustion

Thermal degradation of the wood, and in particular decomposition of carbohydrates, is a complex process and it includes many different reactions occurring simultaneously, e.g. dehydration, depolymerization, fragmentation, rearrangement, repolymerization, condensation and carbonization [14].

Combustion processes are strongly influenced by the elemental and chemical composition of the fuel and the combustion parameters. The chemical composition of the wood cannot be defined precisely for a given tree species or even for a given tree. Chemical composition varies with tree part (root, stem, or branch), type of wood (i. e., normal, tension, or compression) geographic location, climate, and soil conditions [15]. Biomass is a complex material, mainly composed of hemicellulose, cellulose and lignin in addition to extractives (tannins, fatty acids, resins) and inorganic salts. Cellulose is the most important element in biomass due to its large proportion [16]. Cellulose, hemicellulose and lignin of oak proportions are 41%, 26.35% and 25.71% in general based on the literature data's [17].

All combustion processes can be considered as emission sources, during which not only CO_2 and H_2O are produced, but as well many other components released from the perfect (SO_2) and imperfect (CO) combustion. Many formation pathways of the end products are known during combustion. Every biomass combustion start with the pyrolysis of the cellulose *(Figure 3)*.

In addition the inorganic components of the biomass react with the cellulose which leads to a wide range of reactivities, from enhancement to total inhibition of the smouldering combustion by variation in the rates of production of CO and CO_2 and the corresponding rates of heat release [19].

So knowledge of the formation mechanisms and pathways allows the so-called the use of primary methods to reduce emissions [20].

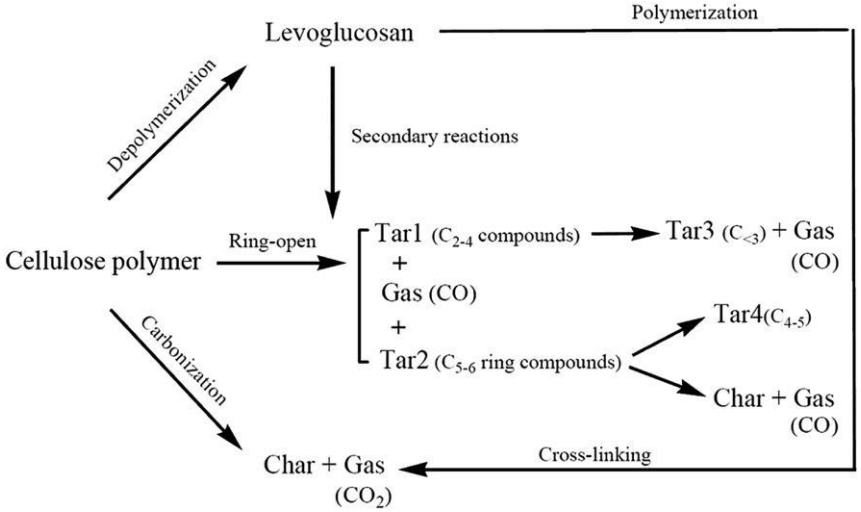

Figure 3

Kinetic scheme proposed by Shen et al. [18] *for fast pyrolysis of cellulose*

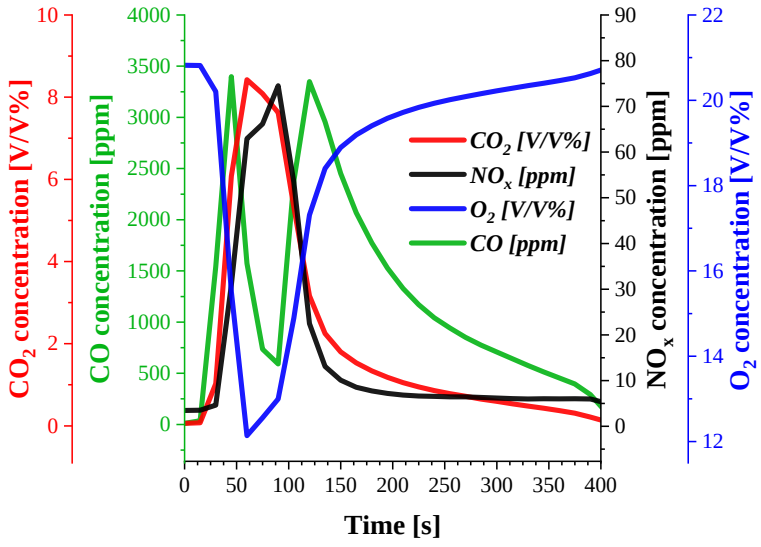

Figure 4

Evolution of the amount of flue gas components during combustion (140 dm^3/h, 600 °C)

Cereceda-Balic et al. [21] obtained similar curve in experiments with two hardwood and one softwood compared to the *Figure 4*.

In the case of CO concentration, two peaks can be observed:

- up to the first peak, the inflammatory stage is visible, where volatile substances leave the biomass,
- the rest of the curve indicates combustion stage.

Firstly, during the primary attack by oxygen on hydrocarbons, CO is formed by a fast reaction mechanism shown in simplified *Equation (1)*. The subsequent reaction of CO to CO_2 in simplified *Equation (2)* is slow and requires adequate residence time to achieve completion. Thus, in a poorly designed or overloaded stove, it is possible to produce significant CO emissions even in the presence of large amounts of excess air [22]:

$$C_{(s)} + 0{,}5\ 0_{2\,(g)} \leftrightarrow CO_{(g)} \tag{1}$$

$$CO_{(g)} + 0{,}5\ O_{2\,(g)} \leftrightarrow CO_{2\,(g)} \tag{2}$$

During the intensive combustion stage, the concentration of carbon dioxide increases, and then decreases as the amount of carbon monoxide in the flue gas begins to increase. It can be argued that the production of carbon monoxide (CO) decreases with increasing temperature at the expense of higher production of carbon dioxide (CO_2) [23]. The minimum of the O_2 curve and the maximum of the CO_2 curve indicate the phase of intense combustion.

2.2. Effect of the furnace chamber's temperature on the flue gas components

Figure 5 shows that in the inflammatory phase, the concentration maximum of the CO component decreases to a certain optimum with increasing temperature of the combustion chamber (700 °C) and then begins to increase again after the optimum is reached. CO is generated in two ways in the inflammatory phase:

- when the oxygen is less than the theoretical amount of oxygen required for complete combustion supplied,
- or when there is too much excess air in the combustion process, which decreases the temperature of the combustion chamber.

In the combustion phase, the CO concentration maximum decreases with increasing temperature, which means that the reaction between CO and O_2 is promoted by the temperature of the combustion chamber.

NO is a product of high-temperature combustion processes that is further oxidized to NO_2 at temperatures below 650 °C [24]. Since the temperature of the combustion chamber was set to less than 1,300 °C during the experiments, only NO formation from the nitrogen content of the fuel should be taken into account [25], [26]. In general, all the factors that increase the temperature of the flame increase the amount of NO formed too [27].

The concentration of carbon dioxide reaches a maximum when concentration of oxygen is zero. Increasing the temperature of the combustion chamber promotes the formation of CO_2 formed during the reaction according to *Equation (2) (Figure 5)*.

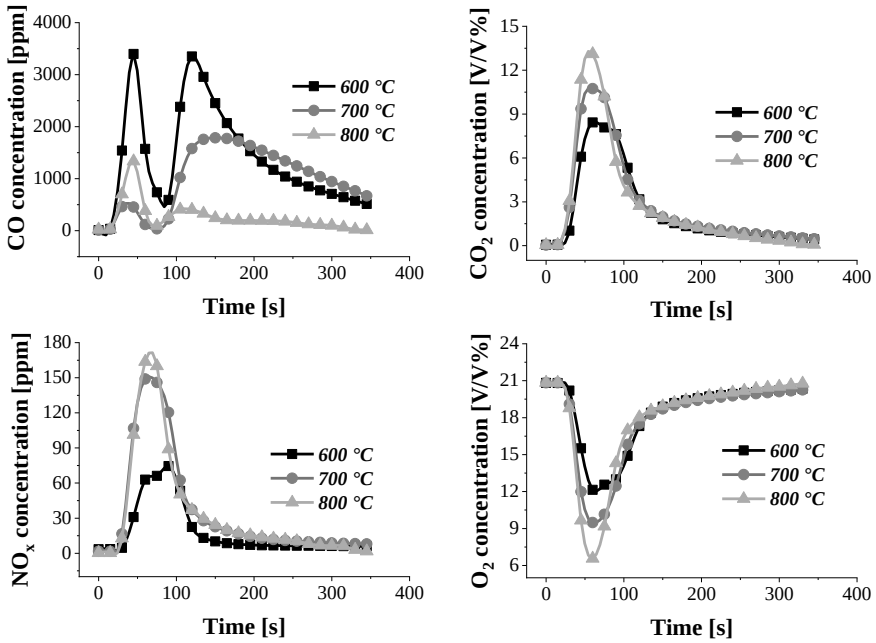

Figure 5
Effect of furnace chamber's temperature change on concentration of the flue gas components

CONCLUSION

One of the aims of this research was to reduce the CO emissions of a newly purchased residential solid fuel boiler below the emission limit values set out in Regulation 2015/1185 issued by the European Commission. The results and experience gained from laboratory-scale experiments would help to reduce the concentration of CO mentioned above.

Based on the results, it could be clearly concluded that the evolution of CO concentration could be divided into two stages. The first stage was the inflammatory stage. The minimum of the CO concentration could be reached at the optimum combustion temperature of the furnace chamber.

When the oxygen was less than the theoretical amount of oxygen required for complete combustion supplied, CO was a final product of the reaction. Otherwise too much excess air led to lower temperature of combustion chamber. This could be explained by the fact that the oxygen and nitrogen – that were not involved in the combustion – absorbed usable heat and carried it out of the chamber. This process promoted the formation of CO. The second stage was characterized by the temperature of the furnace chamber. The reaction between CO and O_2 is promoted by the temperature.

The concentration of NO_x and CO_2 components increased with increasing temperature of the combustion chamber, while the concentration of O_2 decreased. These results indicated that more O_2 was involved in combustion reactions at higher temperatures.

ACKNOWLEDGMENTS

The research was carried out at the University of Miskolc, within the framework of the Thematic Excellence Program funded by the Ministry of Innovation and Technology of Hungary. (Grant Contract reg. nr.: NKFIH-846-8/2019).

REFERENCES

[1] Tilt, B. (2019). China's air pollution crisis: Science and policy perspectives. *Environ. Sci. Policy*, Vol. 92, pp. 275–280., Feb. 2019.

[2] Robinson, E., Robbins, R. C. (1970). Gaseous Atmospheric Pollutants from Urban and Natural Sources. In: *Global Effects of Environmental Pollution*. (Ed. Singer, S. F.) Dordrecht, Holland: D. reidel Publishing Company, pp. 50–64.

[3] Matteo, B., Luca, M., Federica, P., Daniele, C. B., Marina, C. (2019). Urban air pollution, climate change and wildfires: The case study of an extended forest fire episode in northern Italy favoured by drought and warm weather conditions. *6th International Conference on Energy and Environment Research*, ICEER 2019, 22–25 July, University of Aveiro, Portugal.

[4] De Vos, A. J. B. M., Reisen, F., Cook, A., Devine, B., Weinstein, P. (2009). Respiratory irritants in australian bushfire smoke: Air toxics sampling in a smoke chamber and during prescribed burns. *Arch. Environ. Contam. Toxicol.*, Vol. 56, No. 3, pp. 380–388., Apr. 2009.

[5] Sim, M. (2002). Bushfires: are we doing enough to reduce the human impact? *Occup Env. Med.*, Vol. 59, pp. 215–216.

[6] Kampa, M., Castanas, E. (2008). Human health effects of air pollution. *Environmental Pollution*, Vol. 151, No. 2. pp. 362–367., Jan-2008.

[7] Guerreiro, C. B. B., Foltescu, V., de Leeuw, F. (2014). Air quality status and trends in Europe. *Atmos. Environ.*, Vol. 98, pp. 376–384., Dec. 2014.

[8] Brodny, J., Tutak, M. (2019). Analysis of the diversity in emissions of selected gaseous and particulate pollutants in the European Union countries. *J. Environ. Manage.*, Vol. 231, pp. 582–595., Feb. 2019.

[9] Saffari, A. et al. (2013). Increased biomass burning due to the economic crisis in Greece and its adverse impact on wintertime air quality in Thessaloniki. *Environ. Sci. Technol.*, Vol. 47, No. 23, pp. 13313–13320., Dec. 2013.

[10] *Parr pressing machine*. [Online]. Available: https://www.parrinst.com/products/oxygen-bomb-calorimeters/options-accessories/ [Accessed: 07-Apr-2020].

[11] Roy, M., Dutta, A., Corscadden, K. (2013). An experimental study of combustion and emissions of biomass pellets in a prototype pellet furnace. *Appl. Energy*, Vol. 108, pp. 298–307., Aug. 2013.

[12] Peng, N., Li, Y., Liu, Z., Liu, T., Gai, C. (2016). Emission, distribution and toxicity of polycyclic aromatic hydrocarbons (PAHs) during municipal solid waste (MSW) and coal co-combustion. *Sci. Total Environ.*, Vol. 565, pp. 1201–1207., Sep. 2016.

[13] Wielgosiński, G., Łechtańska, P., Namiecińska, O. (2017). Emission of some pollutants from biomass combustion in comparison to hard coal combustion. *J. Energy Inst.*, Vol. 90, No. 5, pp. 787–796., Oct. 2017.

[14] Werner, K., Pommer,L., Broström, M. (2014). Thermal decomposition of hemicelluloses. *J. Anal. Appl. Pyrolysis*, Vol. 110, No. 1, pp. 130–137., Nov. 2014.

[15] Pettersen, R. C. (1984). The Chemical Compostition of Wood; Chapter 2. In: *THE chemistry of solid wood*. (Ed. Rowell, R.) Washington D.C.: American Chemical Society, pp. 57–125.

[16] Shen, D. K., Gu, S. (2009). The mechanism for thermal decomposition of cellulose and its main products. *Bioresour. Technol.*, Vol. 100, No. 24, pp. 6496–6504., Dec. 2009.

[17] Le Floch, A., Jourdes, M., Teissedre, P. L. (2015). Polysaccharides and lignin from oak wood used in cooperage: Composition, interest, assays: A review. *Carbohydrate Research*, Vol. 417, Elsevier Ltd, pp. 94–102., 19-Nov-2015.

[18] Shen, D. K., Gu, S. (2010). Pyrolytic behaviour of cellulose in a fluidized bed reactor. *Cellul. Chem. Technol.*, Vol. 44, No. 3, pp. 79–87.

[19] Shafizadeh, F. (1984). The Chemistry of Pyrolysis and Combustion; Chapet 13. In: *The chemistry of solid wood*. (Ed. Rowell, R.) Washington D.C.: American Chemical Society, pp. 489–529.

[20] Wielgosiński, G. (2012). Pollutant Formation in Combustion Processes. In: *Advances in Chemical Engineering*. (Eds. Nawaz. Z., Naveed, S.) Rijeka, Croatia: InTech, pp. 295–324.

[21] Cereceda-Balic, F. et al. (2017). Emission factors for PM2.5, CO, CO2, NOx, SO2 and particle size distributions from the combustion of wood species using a new controlled combustion chamber 3CE. *Sci. Total Environ.*, Vol. 584–585, pp. 901–910., Apr. 2017.

[22] Ndiema, C. K. W., Mpendazoe, F. M., Williams, A. (1998). Emission of pollutants from a biomass stove. *Energy Convers. Manag.*, Vol. 39, No. 13, pp. 1357–1367., Sep. 1998.

[23] Nosek, R., Holubiík, M., Papuiík, Š. (2014). Emission Controls Using Different Temperatures of Combustion Air. *The Scientific World Journal through*. [Online]. Available: https://www.hindawi.com/journals/tswj/2014/487549/ [Accessed: 07-Apr-2020].

[24] Szűcs István, Woperáné Serédi Ágnes (2001). *Levegőtisztítás*. Miskolc, Miskolci Egyetemi Kiadó.

[25] Mitchell, E. J. S., Lea-Langton, A. R., Jones, J. M., Williams, A., Layden, P., Johnson, R. (2016). The impact of fuel properties on the emissions from the combustion of biomass and other solid fuels in a fixed bed domestic stove. *Fuel Process. Technol.*, Vol. 142, pp. 115–123., Feb. 2016.

[26] Monedero, E., Portero, H., Lapuerta, M. (2018). Combustion of Poplar and Pine Pellet Blends in a 50 kW Domestic Boiler: Emissions and Combustion Efficiency. *Energies*, Vol. 11, No. 6, p. 1580., Jun. 2018.

[27] Szemmelveisz Tamásné et al. (2011). *Hevítéstechnológia energiagazdálkodási és környezetvédelmi vonatkozásai*. Budapest, Nemzeti Tankönyvkiadó.

Materials Science and Engineering, Volume 45, No. 1 (2020), pp. 217–226.
DOI: 10.32974.mse.2020.022

REVERSE ENGINEERING OF A BRONZE AGE SOCKETED AXE

DÁNIEL MOLNÁR[1] – PÉTER BARKÓCZY[2] – BÉLA TÖRÖK[3] –
JÁNOS GÁBOR TARBAY[4]

Abstract: The details of the production technology of an artefact is always a question. Based on the technological knowledge of the given age, the results of archaeology and archeometallurgy a feasible production technology can be determined. This feasible production technology can be examined using computer simulation tools to find answers to open technological questions.

In this project, the casting technology of the Bronze Age is examined, based on the artefacts of the Hungarian National Museum, using archaeology, technology and theoretical tools. The multifunctional socketed axe tool is examined, the casting defects are analysed and the production technology is reproduced.

Keywords: artefact, reverse engineering, gravity casting technology, simulation

1. THE HISTORY OF AXES

The axe is one of the oldest tools used by mankind and the oldest axes were known as hand axes. The hand axe was a pear-shaped and roughly chipped stone tool brought to an even point, with a broad handle. Later, the axe was given a wooden handle, several different types of axes were developed, which may be divided into two main groups: Non-shaft-hole axes and shaft-hole axes.

The non-shaft-hole axes had no hole for the handle and were generally made from flint, greenstone or slate and in time had an evolution such as core axe, flake axe, thin-butted axe, round stone axe and hollow-edged axe.

The shaft-hole axes were made using various stones, although not flint, and were more likely to be status weapons or ceremonial objects. Types are the polygonal axe, double-headed battle-axe and the boat axe. [1, 2]

[1] Institute of Casting, University of Miskolc
H-3515 Miskolc-Egyetemváros, Hungary
daniel.molnar@uni-miskolc.hu

[2] Institute of Physical Metallurgy, Metalforming and Nanotechnology, University of Miskolc
H-3515 Miskolc-Egyetemváros, Hungary
peter.barkoczy@gmail.com

[3] Institute of Metallurgy, University of Miskolc
H-3515 Miskolc-Egyetemváros, Hungary
bela.torok@uni-miskolc.hu

[4] Hungarian National Museum
H-1088 Budapest, Múzeum krt. 14–16, Hungary
tarbay.gabor@mnm.hu

1.1. The Socketed Axe

During the Bronze Age, stone axes began giving way to axes with a head made of mould cast copper or bronze, which initially were often pure copies of stone axes.

One type of Bronze Age axe is the socketed axe a wedge-shaped axe head with no shaft hole. The handle is instead fixed into a socket at the end part. Since the axe is made hollow and the handle is inserted into the head, a perfectly functional working axe can be made with minimal materials.

Socketed axes are widespread multi-functional tools of the Bronze Age world. Their stylistic appearance might differ from each other in certain areas of the continent but their main casting techniques show great similarities. In the archaeological material, the socketed axes are the ones which show the most characteristic casting defect types. Some of them have intensively porous inner structure, shifted parts, incomplete loops or amorphous patterns. Typical socketed axe geometry with handle reproduction can be seen in *Figure 1* [3].

Figure 1
Copper alloy socketed axe with modern handle, 1000–700 BC

2. THE SIMULATION PROCEDURE

A socketed axe is a metal object, where the production method was gravity casting. In this research computer-based simulation methods are used for the technology reconstruction of the casting process. Many modelling and simulation methods can be employed for gravity casting, including physical modelling and numerical methods. Most of the current modelling and simulation work is done using numerical methods that can be used to solve the appropriate partial differential equations for heat and fluid flow, using numerical algorithms. The following requirements are considered as essential parts of a casting simulation:

- correct geometric description of the domain,
- accurate thermodynamic phase data,
- accurate boundary conditions,
- proper material properties,
- a set of solvable equations describing the physical phenomena,
- experimental and numerical validation.

Generally, models solve equations for the temperatures and the fluid flow. To describe the complex phenomena correctly, good insight into the physics of liquid, semi-solid, and solid constitutive behaviour at high temperatures is required to decide which partial differential equations are best suited to describing the physical phenomena of interest. The parameters of these models should be realistic and physical. This implies very close interaction between controlled experiments of solidification or stress measurements of the high-temperature plasticity behaviour and process physics formulation. Accurate boundary condition and property data are essential if model results are to be representative.

The physical phenomena behind a technological problem should be identified and a mathematical model must be written. This mathematical model must be solved using an analytical or a numerical solution and the physical interpretation of this mathematical solution should be done for the technological solution. Especially in manufacturing processes such as casting, the misinterpretation of otherwise correct mathematical results could lead to wrong conclusions, and hence to no solution of the originating problem [4, 5].

In this research paper, the commercial software NovaFlow&Solid is used to solve the material- and heat transport processes. The method of simulation experiments can be seen in *Figure 2*.

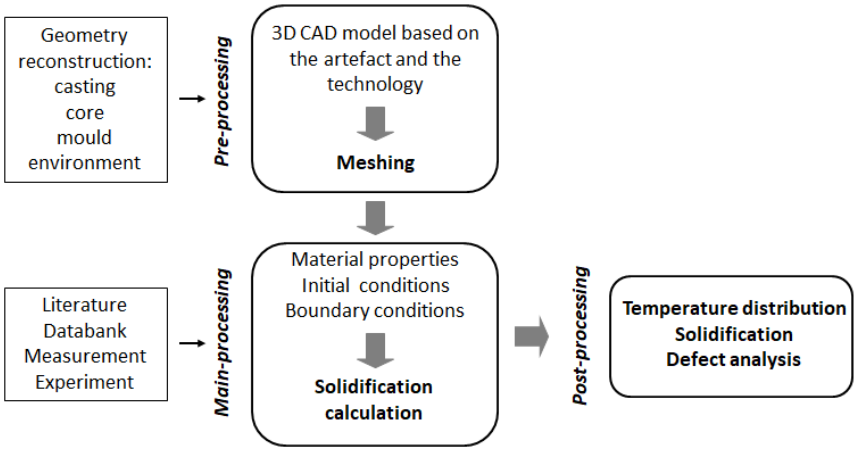

Figure 2
Concept of the simulation experiments

In Pre-processing the first step is to define the geometry of the casting system into a discrete number of segmented volume elements for the subsequent calculations.

Before the equations that govern the filling and solidification processes can be solved, the necessary thermophysical material data must be available. Apart from the material data themselves, other relevant process parameters have to be defined. Initial conditions for the unknown quantities and boundary conditions for the unknowns

must be defined. Other relevant information also needs to be input, so that all the factors that affect the filling and solidification of the casting can be accounted for.

Main-processing is the most demanding part of the numerical simulation follows in respect of both the algorithmic development and the requirements for computer capacity, solution of the governing equations. The most usual approach here is to solve all the basic equations, this being a prerequisite for simulating all relevant casting problems of a technical nature. It is clear that these calculations, in which primitive fields such as temperatures, displacements, stresses, velocities, pressure, etc. are determined, require the solution of the governing differential equations.

Post-processing is the presentation of the results. After the computations, the resulting basic fields (temperatures, velocities, pressure, displacements, stresses, etc.) should be presented appropriately.

3. THE EXAMINED ARTEFACT

The examined artefact is a socketed axe geometry (Ha B1-B2/3) from Isaszeg, Hungary. The chemical composition of the axe is 83 wt% copper (Cu), 11 wt% tin (Sn) and 6 wt% antimony (Sb). The chemical composition is analysed using prompt-gamma activation analysis, which is a nuclear analytical technique for non-destructive determination of elemental and isotopic compositions.

The artefact was analysed by neutron radiography where the overall amount of porosity is determined as 3.06%. The artefact geometry and the resulting figures of the neutron radiography can be seen in *Figure 3*.

Figure 3
Geometry of the artefact and results of the neutron radiography

Based on the artefact a virtual model is created in 3D, using Computer-Aided Design. For the technology analysis, the 3D model must consist of the axe, the core, the gating system, the mould and the environment. Based on the neutron radiography analysis a simplified axe geometry is created (43 cm^3), without gating system, while the core and the mould are created using Boolean features.

Based on a literature survey and trial experiments a gating system is created which can fill the cavity on a realistic way without significant turbulence. The result of the mould filling analysis [6] is not presented in this paper. Only the mould filling

defects will be presented to understand the simulation results. The geometry of the casting with the gating system and the 3D cut of the calculation domain can be seen in *Figure 4*.

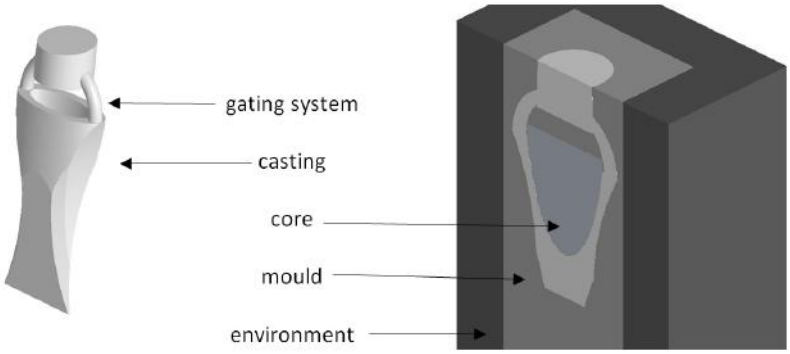

Figure 4
Examined geometries

4. SOLIDIFICATION ANALYSIS

Based on the archaeological excavation and literature survey [7, 8] the 3D CAD model of the simplified axe geometry with the gating system and the core is prepared. The pending question is the material of the mould, therefore two cases were examined simultaneously:

A. The alloy was poured into a sand mould. It supposes a so-called expendable mould where the mould is used only once.
B. The alloy was poured into a stone mould. It supposes a so-called permanent mould where the mould is used several times. Before pouring the stone mould was surrounded by sand which is symbolized by the environment, see *Figure 4*.

The Design of Experiments (DoE) can be seen in *Table 1*, where the chemical composition of the alloy was composed based on the artefact. The pouring temperature was examined in several steps, where the steps were defined based on the possible maximum temperatures of the ancient melting techniques.

Table 1
Design of experiments

Expendable mould	**A1**	**A2**	**A3**	**A4**	**A5**	**A6**
Alloy temperature	1,015 °C	1,025 °C	1,035 °C	1,050 °C	1,070 °C	1,100 °C
Mould	sand (20 °C)					
Environment	sand (20 °C)					
Permanent mould	**B1**	**B2**	**B3**	**B4**	**B5**	**B6**
Alloy temperature	1,015 °C	1,025 °C	1,035 °C	1,050 °C	1,070 °C	1,100 °C
Mould	stone (20 °C)					
Environment	sand (20 °C)					

The solidification of the Project A1 can be seen in *Figure 5*, where the scale is liquid phase: 5–95%.

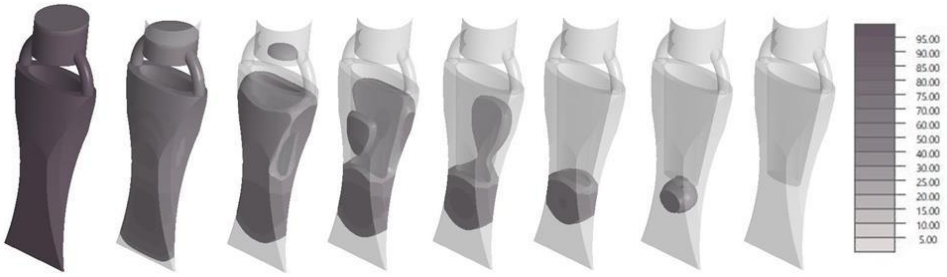

Figure 5
Solidification process

4.1. Result analysis

Although the mould filling analysis is not presented in this paper, but some results of it must be explained. During filling the air inside the cavity must leave. This can be done by venting or by the diffusion of air through the mould, which is called gas permeability. Based on the filling analysis it can be determined that melt blocks the gates, so the air cannot leaves through the gating system. Without venting the air cannot leave the cavity. The gas permeability of the mould depends on the moulding material. The expandable sand mould has good gas permeability, while the permanent stone mould has nearly zero. By the result analysis, these effects must be investigated.

During solidification the alloy shrinks which causes shrinkage cavities and porosities. The casting solidifies without a riser, although the metal in the gating system can feed the casting for a limited time. The rest of the metal in the cavity solidifies without feeding.

These effects will result in empty places inside the geometry, which locations can be calculated based on the solidification calculation.

According to the DoE, 6 different melt temperatures were examined in both moulding methods. The question was the amount and the distribution of shrinkages, to be able to compare these values with the analysed results of the artefact, where the value of the overall porosity is 3.06%. The results can be seen in *Table 2*.

Based on the neutron radiography porosity analysis of the artefact the overall amount of porosity (3.06%) can be compared with the simulation results. The measured value is analogous to the following simulation results:

- Expendable sand mould with 1,070 °C pouring temperature.
- Permanent stone mould with 1,015 °C pouring temperature.

To decide which moulding method and which pouring temperature is more feasible the technology of the Bronze Age must be investigated. By the early furnace- and melting technology to reach a higher metal temperature was limited. Based on the investigation of the residual slags and the reproduction experiments it is clear

that the lowest pouring temperature must be applied, the liquidus temperature of the alloy is 1,013 °C.

Table 2
Calculated results

Expendable mould	**A1**	**A2**	**A3**	**A4**	**A5**	**A6**
Alloy temperature	1,015 °C	1,025 °C	1,035 °C	1,050 °C	1,070 °C	1,100 °C
Solidification time	56.88 s	57.98 s	59.15 s	61.35 s	61.63 s	67.47 s
Shrinkage	2.92%	2.977%	3.035%	3.04%	3.069%	3.161%
Permanent mould	**B1**	**B2**	**B3**	**B4**	**B5**	**B6**
Alloy temperature	1,015 °C	1,025 °C	1,035 °C	1,050 °C	1,070 °C	1,100 °C
Solidification time	25.03 s	25.51 s	25.03 s	26.91 s	27.85 s	29.26 s
Shrinkage	3.071%	3.128%	3.184%	3.135%	3.244%	3.253%

If the moulding method is examined there are several pieces of evidence which prove, that at the Bronze Age permanent mould were applied since unused and burned out mould fragments are excavated in a lot of places, see *Figure 6* [9].

Figure 6
Permanent mould from the Early Bronze Age

Based on these statements, the B1 Project is examined in details, where the mould is permanent stone mould and the pouring temperature is 1,015 °C. The amount of shrinkages is 3.071%.

The shrinkages of the geometry in 3D sections along the X-axis can be seen in *Figure 7*, where the scale is shrinkage 1–90%.

The 3D view of the shrinkages in *Figure 7* is not a detailed representation of the calculation results. To do this, the 3D geometry must be cut in 2D sections, that can be compared to the neutron radiography results. In this paper, only the middle cut of the geometry is presented, while the analysis of the geometry was complete.

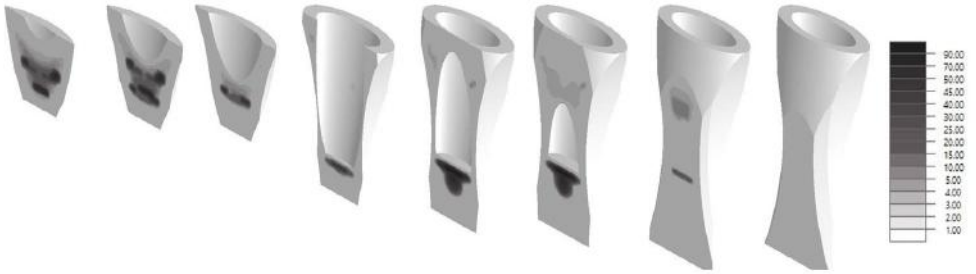

Figure 7
3D sections of the shrinkages

The question is how the simulation software represents the shrinkage results. By using a scale the feasibility of shrinkages can be displayed, which means that in the different areas how many amounts of shrinkages occur.

Next question is the gas entrapment during solidification. The gas bubbles can be seen on the 2D cut as smooth-surfaced round empty places. In the simulation, only the theoretical distribution of the bubbles can be seen.

In *Figure 8*, the calculated shrinkages can be seen on the right side, where the 10% and 50% values are rounded with iso-lines. These lines are copied to the left side of the figure, where the same 2D cut can be seen of the artefact geometry, where both shrinkages and air entrapments are visible. Shrinkage scale: 1–90%.

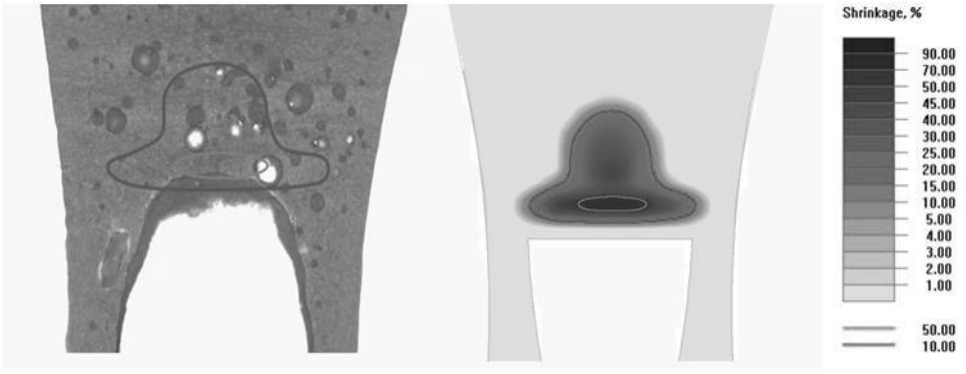

Figure 8
2D cut of the axe and the calculated shrinkages

In *Figure 9* the calculated shrinkages and the distribution of gas bubbles can be seen on the right side, where the 10% and 50% values are rounded with iso-lines. The circles highlight the aggregation of the gas bubbles. This line is copied to the left side of the figure, where the same 2D cut can be seen of the axe geometry. Shrinkage scale: 1–90%.

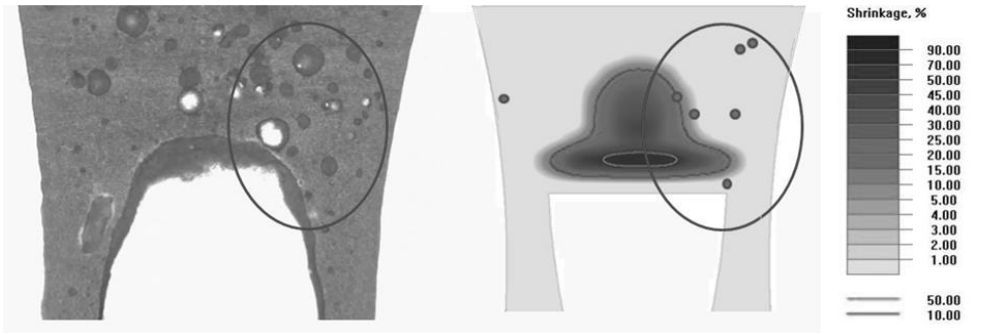

Figure 9
2D cut of the axe and the calculated shrinkages and gas bubbles

In both cases, it is clear that the distribution of shrinkages and gas bubbles are homologous in case of simulation and neutron radiography results. These distributions need further analysis e.g. image analysis to be able to run a quantitative analysis.

SUMMARY

In this paper, a socketed axe geometry is examined with computer simulation, where the details of the production technology are analysed. In this case, reverse engineering of an artefact means the reconstruction of the casting technology by computer simulation.

A socketed axe geometry from the Bronze Age is examined from middle Hungary, where the geometry is analysed with neutron radiography.

Based on the artefact a simplified 3D CAD geometry is created where the possible gating system designs were tested and analysed.

12 possible solidification experiments were run, where the effect of the mould material and the pouring temperature was examined on the shrinkages.

The shrinkages were compared with the figures of the neutron radiography and the results are interpreted.

The future goal is to create a method by the help of which the graphical values can be translated into numerical ones.

ACKNOWLEDGEMENT

The described article was carried out as part of the EFOP-3.6.1-16-2016-00011 *Younger and Renewing University – Innovative Knowledge City – institutional*

development of the University of Miskolc aiming at intelligent specialisation project implemented in the framework of the Szechenyi 2020 program. The realization of this project is supported by the European Union, co-financed by the European Social Fund.

Thank you for the support of the NovaCast Systems AB for the NovaFlow&Solid simulation software.

REFERENCES

[1] Simpson, Bruce L. (1969). *History of the Metalcasting Industry*. AFS, Chicago, USA.

[2] www.gransforsbruk.com/en/axe-knowledge/the-history-of-the-axe, 2020. 05.

[3] www.museumoflondonprints.com/image/65134/copper-alloy-socketed-axe head-late-bronze-age, 2020.05.

[4] Hattel, Jesper (2005). *Fundamentals of Numerical modelling of Casting Processes*. Polyteknisk, Lyngby, Denmark.

[5] *NovaFlow&Solid User Guide* (2019). Novacast Systems AB.

[6] Molnár, Dániel et al. (2019). The Application of Computer Simulation on Reverse Engineering of Artefacts. *5th International Conference Archaeometallurgy in Europe*, (19–21 June 2019), Miskolc.

[7] Gruszka, D. et al. (2018). *The use of experimental and computer aided methods in reconstruction of metal artefacts from the bronze age*, 73rd WFC.

[8] Garbacz-Klempka, Aldona et al. (2016). Badania i wizualizacja technologii, Metalurdzy znad Kaczawy. In: *Metalurdzy znad Kaczawy cmentarzysko ciałopalne z epoki brązu odkryte w Legnicy przy ul*. Spokojnej. Publisher: Muzeum Miedzi w Legnicy. Editors: Kamil Nowak, Tomasz Stolarczyk. Legnica, Poland.

[9] Lene Melheim (2015). Late Bronze Age axe traffic from Volga-Kamato Scandinavia? The riddle of the KAM axes revisited. In: *Proceedings of the 3rd International Conference, Deutsches Bergbau-Museum*. Publisher: Montanhistorische Zeitschrif. Editors: Andreas Hauptmann, Diana Modarressi-Tehran. Bochum, Germany.

Materials Science and Engineering, Volume 45, No. 1 (2020), pp. 227–232.
DOI: 10.32974.mse.2020.023

THE COMPARISON OF AA1060 AND AA3003 ALUMINIUM ALLOYS BY THEIR CRYSTALLOGRAPHIC TEXTURE

DÁNIEL PETHŐ[1] – ADRIENN HLAVÁCS[2] – MÁRTON BENKE[3]

Abstract: In this research the AA1060 and AA3003 alloys were compared by their crystallographic texture, hardness and earing. Both alloy sheets were rolled, and heat treated by the same manufacturing route. The cold rolled samples had the strain of 1.94, then the subsequent heat treatment was carried out between 190 °C and 380 °C. The annealing temperatures were chosen in respect to the industrial annealing temperatures. After the experiments XRD evaluation was carried out to determine the crystallographic texture of the sheets. The XRD results were compared with the industry-known earing test's and hardness test's results. The results can be applied in the industry for the optimization of a given technology.

Keywords: AA1060, AA3003, crystallographic texture, earing

INTRODUCTION

In most cases the aluminium sheets are semi-products, meaning that after the rolling and annealing steps, these sheets are deep drawn. In order to define the deep-drawability of the sheets prior to the operation, crystallographic texture needs to be defined. The crystallographic texture describes the degree of anisotropy by defining the crystallographic orientation of all grains within the material [1]. In most industrial environments, the deep-drawability is described by the hardness of the sheet, but that does not give an adequate answer to the deep-drawability.

The two alloys studied are the AA1060 and the AA3003. The AA1060 is low on alloying elements, but the AA3003 alloy's main alloying component is manganese [2]. Manganese in aluminium alloys, depending on the temperature, could dissolve from the solid solution and form compounds [3]. These compounds influence the recrystallization of the AA3003 alloy [4]. The aim of this research is to compare the recrystallization kinetics of the two alloys based on crystallographic texture, earing and hardness.

[1] Institute of Physical Metallurgy, Metalforming and Nanotechnology, University of Miskolc
H-3515 Miskolc-Egyetemváros, Hungary
femdani@uni-miskolc.hu
[2] Institute of Physical Metallurgy, Metalforming and Nanotechnology, University of Miskolc
H-3515 Miskolc-Egyetemváros, Hungary
[3] Institute of Physical Metallurgy, Metalforming and Nanotechnology, University of Miskolc
H-3515 Miskolc-Egyetemváros, Hungary

1. MATERIALS AND METHODS

1.1. Experimental route

During the examinations the as-received hot rolled 7 mm thick sheet was cold rolled to 1 mm thickness. Subsequently the heat treatments were carried out at 190 °C, 280 °C and 380 °C for 1, 2, 3, 4 and 5 hours. On *Figure 1* the experimental route is displayed. The heat treatments were done in an air furnace, and the samples were inserted when the furnace was heated to the annealing temperature. The samples cooled down in air. The earing examination was carried out by ARCONIC-Köfém Kft. The interpretation of the earing values is as it follows: positive values refer to 0/90° earing of the deep-drawn sheets, which is defined positive (recrystallized); negative values refer to the 45° earing of the sheets, which is defined as negative (rolled) [5]. The hardness tests were carried out with the Tukon 2100B.

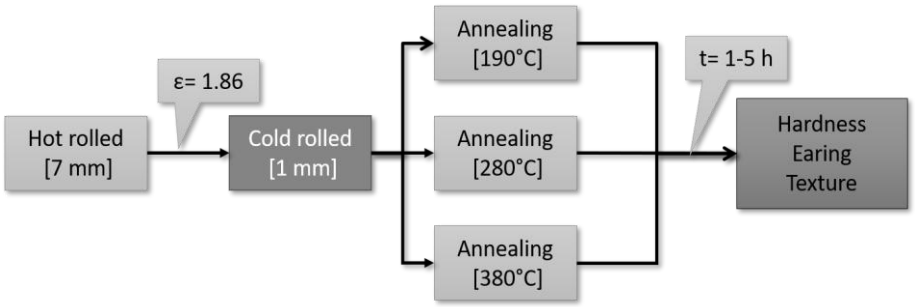

Figure 1
Route of the examinations

1.2. XRD measurements

The texture examinations were carried out with the Bruker D8 Advance X-ray diffractometer equipped with a Eulerian cradle. The measurement parameters: 40 mA, 40 kV, CoKα. The {111}, {200}, {220} lattice planes were measured, with the corresponding pole figures recorded. The pole figures were recalculated, then used for Orientation Distribution Function (ODF) synthesis. ODF cuts were made at 5° steps of the φ_2 values. The texture components are defined by the three Eulerian angles and were measured from the ODF. The texture components are specific Eulerian angle triplets which are characteristic of the manufacturing steps or physical processes (rolling, recrystallization…etc.).

2. RESULTS

2.1. Hardness results

The hardness test results can be seen on *Figure 2*. The 0-hour sample (not annealed, just rolled) is shown on the left. It can be seen that both alloys exhibit the same behaviour. The samples annealed at 190 °C did not change their hardness significantly due

to annealing. At 280 °C the first 2 hours show rapid decrease in hardness, but after 3 to 5 hours, the decrease has already reached its plateau. That is backed up by the fact that after the 380 °C annealing, all samples have around the same hardness value.

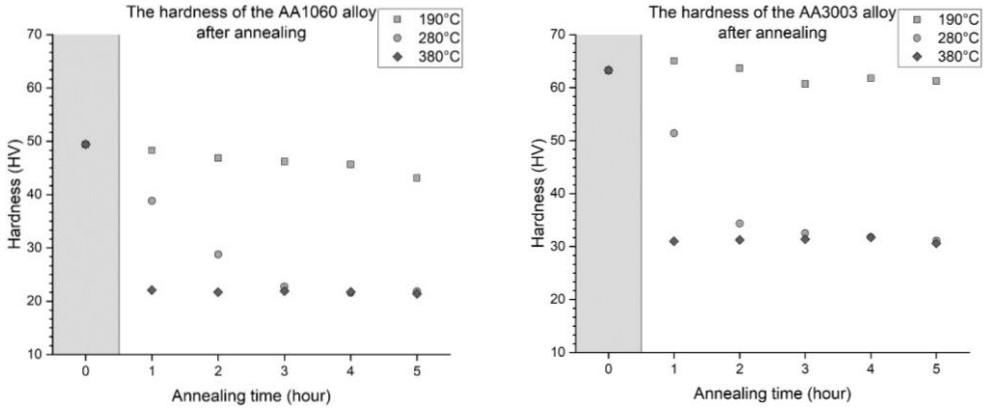

a) b)

Figure 2

Hardness of the alloys after annealing: a) AA1060; b) AA3003

2.2. Earing results

The results of the earing tests can be seen on *Figure 3*. As in the case of hardness, the earing values seem to follow a similar trend for both alloys (in the opposite direction). The 190 °C annealing did not change the earing notably. The annealing at 280 °C between 1–3 hours increased the earing value sharply. The highest annealing temperature, 390 °C, shows increased earing values even after the 1-hour heat treatment. Through the trends are the same for both alloys, the AA1060 has more optimal earing values than AA3003 (closer to 0).

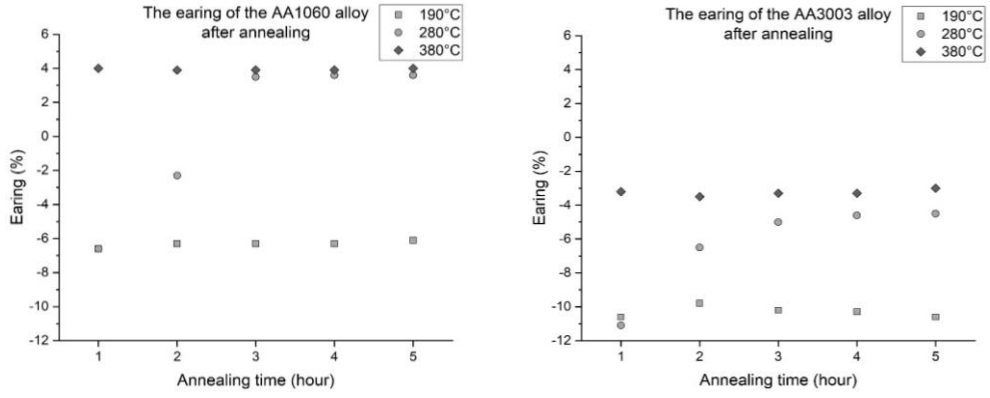

a) b)

Figure 3

Earing of the alloys after annealing: a) AA1060; b) AA3003

2.3. Texture results

The texture components and their volume percentage can be seen on *Figure 4.*

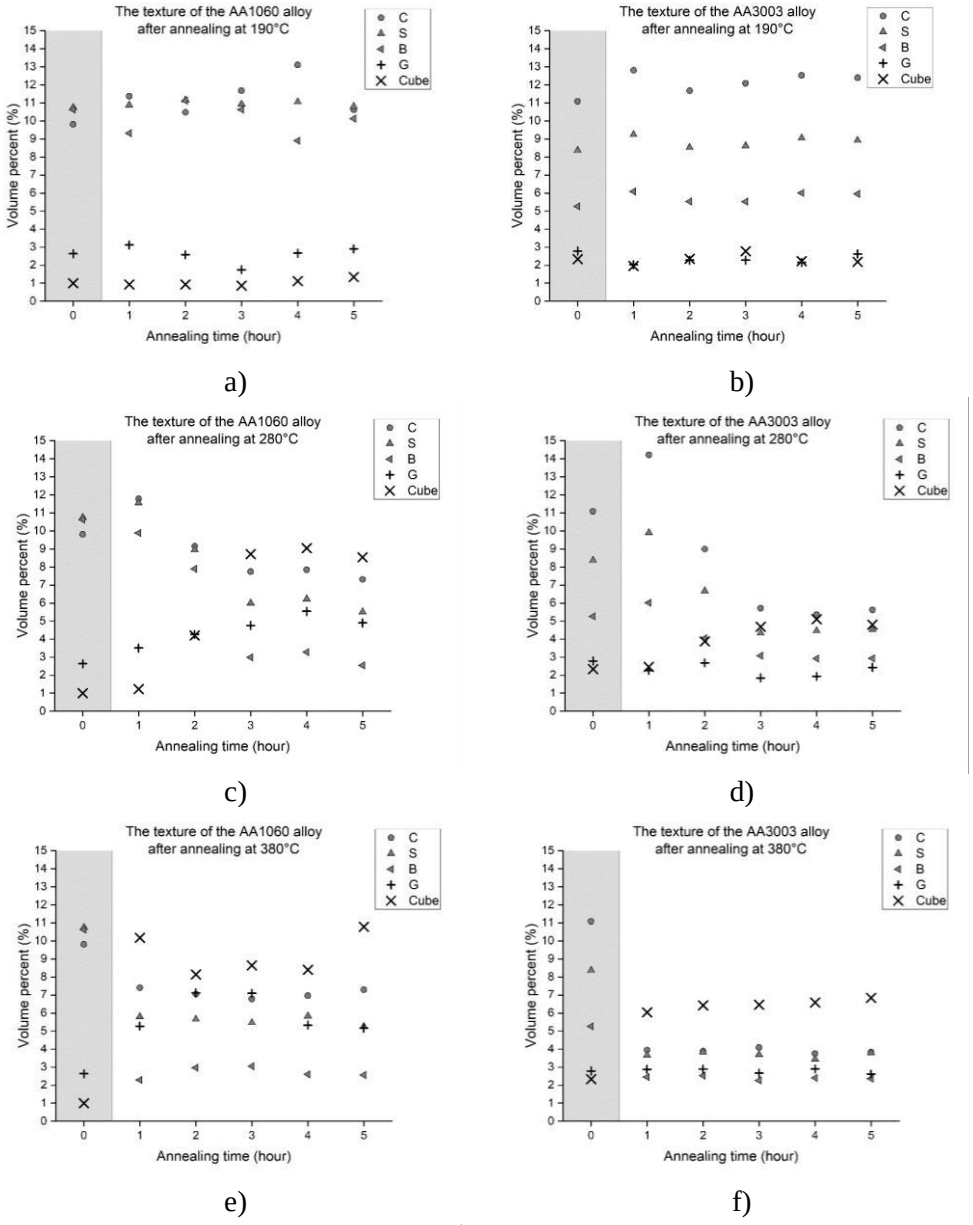

Figure 4

Texture of the alloys after annealing: a) AA1060-190 °C; b) AA3003-190 °C; c) AA1060-280 °C; d) AA3003-280 °C; e) AA1060-380 °C; f) AA3003-380 °C

Both alloys are paired up by their annealing temperature for easier comparison. In all cases the 0-hour state (cold rolled) is displayed in grey. The texture components representing plastic formation (rolling) are displayed with grey markings (C, S, B) and the texture components representing the recrystallization and its processes (G, Cube) are displayed line-based markings.

The texture results after annealing at 190 °C can be seen on *Figure 4a)* and *b)*. Basically, no change in the texture can be seen. The C, S, B components are much higher than the annealing components and the annealing time had no effect on the crystallographic texture. The AA3003 alloy has its C, S, B components more scattered by volume percent, but it is due to the 0-hour sample's state.

After annealing on 280 °C several effects can be seen (*Figure 4c)* and *d)*). In the case of both alloys, after 1 hour of heat treatment, recovery occurs, which increases the texture components referring to rolling. This is due to the fact that during recovery, only the subgrains are ordered, but no grain boundary movement occurs, therefore there will be more volume within the sheet with the same orientation than before annealing [6]. Between 2 and 3 hours of annealing the recrystallization texture components increase and the rolling components decrease. Between 3–5 hours the AA1060 alloy recrystallizes. Due to the fact that the Cube component has the highest values, it refers to recrystallization, but after the Cube, the rolling components are the highest. This indicates that a mixed recrystallization took place, both the classic high angle boundary movement related recrystallization, and the particle stimulated nucleation (PSN). In the case of the AA3003 alloy between 1 and 3 hours of annealing, all things written above are the same, but between 3 and 5 hours entirely PSN recrystallization takes place. This is backed up by the almost equal values of both the rolling and recrystallization components and the fact that the AA3003 is filled with precipitations containing Mn.

AT 380 °C IN THE CASE OF BOTH ALLOYS CLASSICAL RECRYSTALLIZATION OCCURRED, THIS CAN CLEARLY BE SEEN ON THE *FIGURE 4E)* AND *F)*. THE CUBE COMPONENT IS THE HIGHEST IN ALL STATES. THIS MEANS THAT THERE IS NO POINT IN ANNEALING FOR MORE THAN 1 HOUR AT THIS TEMPERATURE.

CONCLUSIONS

In this research the comparison of aluminium sheets with different composition and same processing parameters were carried out. The comparison is based on hardness, earing and texture results. The following can be concluded:

a) In both alloys the earing and hardness results indicate that at 190 °C no significant change occurred, at 280 °C between 1 and 3 hours of annealing there is a considerable drop in hardness, and a notable increase of earing, indicating that recrystallization took place.
b) The texture results are in good agreement with the hardness and earing results; however, they are more precise when describing the recrystallization process. The data reveals that at 280 °C mixed recrystallization took place in AA1060 and PSN-type recrystallization took place in AA3003.

c) The experiments clearly outline the optimal parameters for the studied alloys. In the case of AA1060, at 280 °C the optimal annealing time between 2 and 3 hours could result in 0% earing.

ACKNOWLEDGEMENT

The described article was carried out as part of the EFOP-3.6.1-16-2016-00011 *Younger and Renewing University – Innovative Knowledge City – institutional development of the University of Miskolc aiming at intelligent specialisation* project implemented in the framework of the Szechenyi 2020 program. The realization of this project is supported by the European Union, co-financed by the European Social Fund. This research was supported by the NKFI 119566K project.

REFERENCES

[1] Suwas, S., Bay, R. K. (2014). *Crystallographic texture of materials*. (Enginee ring materials and processes), London, Springer.

[2] The Aluminium Association. *International Alloy Designations and Chemical Composition Limits for Wrought Aluminum and Wrought Aluminum Alloys*. [Online]. Available: https://www.aluminum.org/sites/default/files/Teal%20 Sheets.pdf [Accessed March 02, 2020].

[3] Dehmas, M., Aeby-Gautier, E., Archambault, P., Serriére, M. (2012). Interaction Between Eutectic Intermetallic Particles and Dispersoids in the 3003 Aluminum Alloy During Homogenization Treatments. *Metallurgical and Materials Transactions A*, 44, pp. 1059–1073.

[4] Merchant, H. D., Morris, J. G., Hodgson, D. S. (1990). Characterization of Intermetallics inAluminum Alloy 3004. *Materials Characterization*, 25, pp 339–373.

[5] Engler, O., Hirsch, J. (2006). Polycrystal-plasticity simulation of six and eight in deep drawn aluminium cups. *Materals Science and Engineering A*, 452–453, pp. 640–651.

[6] Humpreys, F. J., Hatherly, M. (2004). Recrystallization and Related Annealing Phenomena. Oxford, Elsevier.

Materials Science and Engineering, Volume 45, No. 1 (2020), pp. 233–240.
DOI: 10.32974.mse.2020.024

PREPARATION AND CHARACTERIZATION OF SELENIUM NANOPARTICLES

ÁDÁM PREKOB[1] – VIKTÓRIA HAJDU[2] – LÁSZLÓ VANYOREK[3]

Abstract: Selenium nanoparticles were prepared with reduction method from sodium-selenite. To stabilize the nanoparticles, two different stabilizers were used. The prepared nanoparticles were characterized with transmission electron microscopy (TEM), with the use of the images the diameters of the nanoparticles were measured which were 70.9 nm in average in case of gum arabics as stabilizer, and 21.7 nm with guar gum. To evidence the presence of the stabilizer layers, Fourier transformation infra-red spectroscopy (FTIR) was used. Applying X-ray diffraction (XRD), the states of the nanoparticles were determined. As a mixture of organic and inorganic selenium compounds, these nanoparticles could provide both fast and slow, long-term uptake for edible plants which could make up the missing amount of Se for human body.

Keywords: Selenium nanoparticles, TEM, XRD, FTIR

INTRODUCTION

Selenium is considered to be an important trace element of the human body [1]. The proper level of selenium has many advantageous effects like protection of immune system, thyroid, and homeostasis [2], furthermore keeping up the ideal amount is a good way to prevent serious illnesses like cancer [3] or Alzheimer [4]. The main cause of these illnesses is the oxidative stress (caused by the free radicals like reactive oxygen and nitrogen species) which is usually neutralized by the glutathione peroxidase protein. For this mechanism, selenium is an important component [5]–[10]. The main source of selenium in everyday life is different edible plants which can uptake the different forms of selenium from the soil [11]. According to The American Recommended Dietary Allowance (RDA), the necessary amount is 70 microgram for men and 55 for women per day [12]. However, in many countries (mainly in Europe) the soils are poor in selenium so there is a high chance for the formation of deficit in human

[1] Institute of Chemistry, University of Miskolc
H-3515 Miskolc-Egyetemváros, Hungary
prekob.a@gmail.com
[2] Institute of Chemistry, University of Miskolc
H-3515 Miskolc-Egyetemváros, Hungary
kemviki@uni-miskolc.hu
[3] Institute of Chemistry, University of Miskolc
H-3515 Miskolc-Egyetemváros, Hungary
kemvanyi@uni-miskolc.hu

body. The selenium deficit already effects about 3 billion people worldwide, meanwhile researchers predict further selenium loss from soils due to the climate change which will further increase their number [13].

Due to the chemical similarity of selenium and sulphur, plants take up the selenium via sulphur transporters [14]. Selenite, selenate, and organic selenium are ideals forms of selenium to uptake for plans. However, selenides and elemental selenium ensure a slow, and lasting uptake because microbials in soil first have to transform them to other forms which can be taken up [15]. Nano selenium seems to be the least toxic selenium form, furthermore unlike to the common used selenite and selenate, metallic nano selenium do not inhibits the growing process of the plants, instead it can stimulate the root regeneration [16].

In this paper, selenium nanoparticles were prepared both with organic and elemental selenium content which could ensure both fast and lasting selenium uptake. This could be a lasting solution to increase the selenium amount in the soils and make up the missing amount in the human body through edible plants. The nanoparticles were stabilized with two different non-toxic stabilizers.

1. MATERIALS AND METHODS

1.1. Materials

For the Se nanoparticle preparation cysteine ($C_3H_7NO_2S$) and sodium-selenite (Na_2SeO_3) were purchased from *Reanal*. As a solvent, distilled water was used. Two different stabilizers were used during our experiments, guar gum *(Donauchem)* and gum-arabic *(Reanal)*.

1.2. Characterization methods

Transmission electron microscopy (TEM) was used to characterize the nanoparticles. For the examination a FEI Tecnai G2 20 X-Twin instrument was used with 200 kV voltage. The sample was dropped on copper grid from water/ethanol suspension. Using the images, the size of the particles was measured by image analysing software (ImageJ).

Fourier transformation infra-red spectroscopy (FTIR) was used to evidence the presence of the stabilizers. For the measurement, a Bruker Vertex 70 instrument was used with 4 cm^{-1} resolution and 16 s^{-1} scanning velocity.

X-ray diffraction (XRD) was used to detect the different states of Se nanoparticles. For this measurement, a Bruker D8 Advance type instrument was used.

1.3. Preparation of stabilized Se nanoparticles

In the first step, 0.4 g cysteine was solved in 20 ml distilled water and 5 g stabilizer in 250 ml distilled water *(Figure 1.1)*. The two solution was mixed and homogenized with ultrasonic homogeniser (340 W, 19.42 kHz) for 10 minutes *(Figure 1.2)*. For the next step, 0.11 g sodium-selenite was solved in 10 ml distilled water and added to the solution in drops during continuous mixing *(Figure 1.3)*. After mixing, the

solvent was removed by vacuum-evaporation on 60 °C then the sample was dried on 80 °C overnight *(Figure 1.4)*. As a result, stabilized Se nanoparticles were prepared.

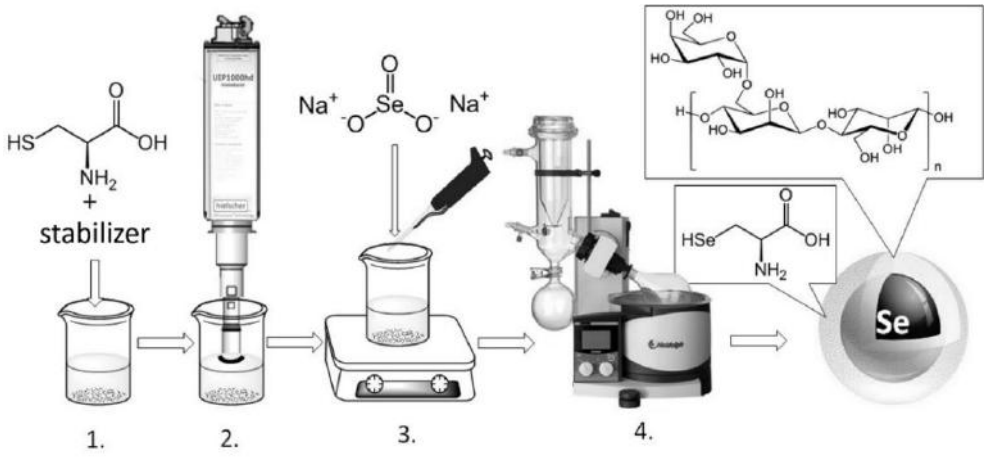

Figure 1
Preparation process of stabilized Se nanoparticles

2. RESULTS AND DISCUSSION

2.1. TEM examinations

TEM was used to characterize the Se nanoparticles shape and size. The gum arabic stabilized nanoparticles had spherical shape *(Figure 2)*. The particles were between 20–80 nm diameter with an average of 70.9 nm diameter. The stabilizer layer can be seen around the particles.

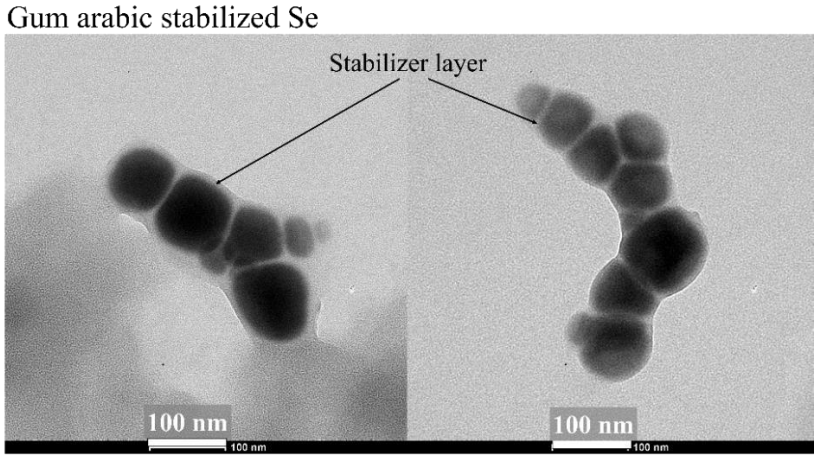

Figure 2
SEM image of stabilized Se nanoparticles with gum arabic

The guar gum stabilized nanoparticles did not have a well-defined shape but they had a significantly lower diameter (average of 21.7 nm) *(Figure 3)*. The vast majority of the particles (80%) were under 24 nm, some particles were bigger with a maximum of 55 nm.

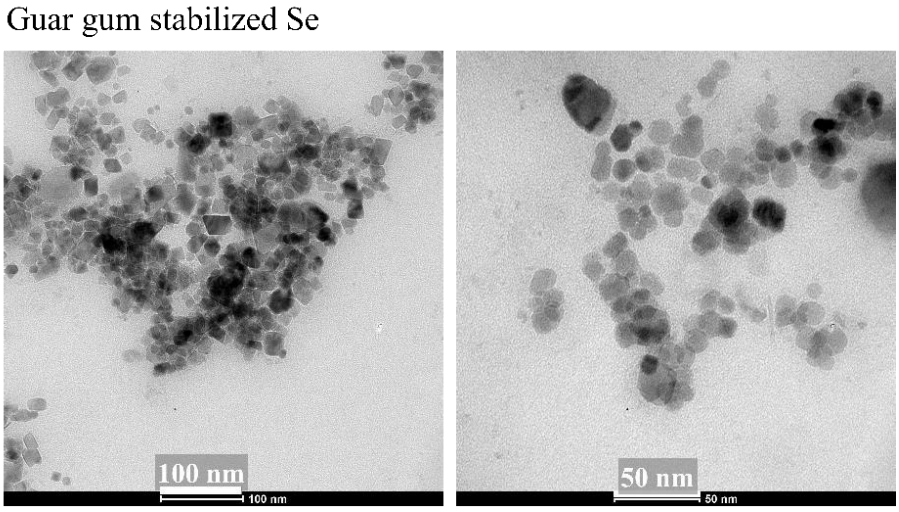

Figure 3
SEM image of stabilized Se nanoparticles with guar gum

2.2. XRD measurements

XRD measurements were used to evidence the success of elemental Se preparation *(Figure 4)*.

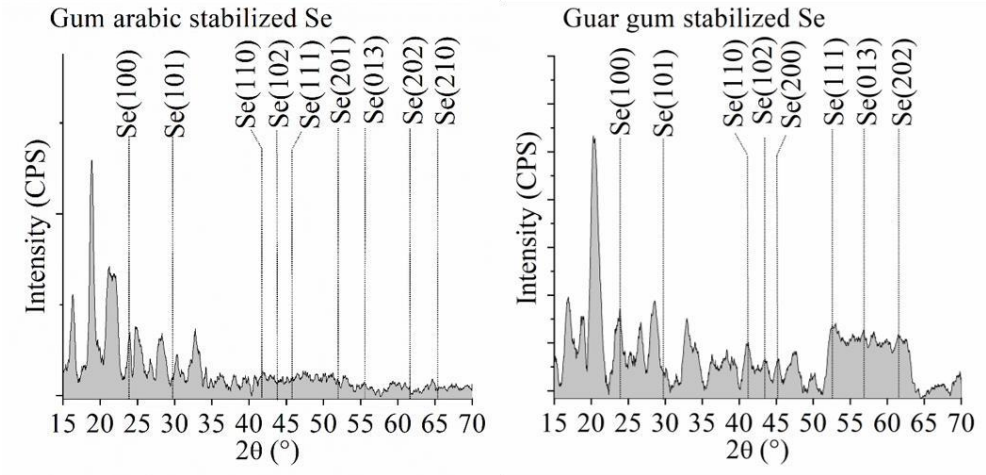

Figure 4
XRD measurements of Se nanoparticles with gum arabic and guar gum stabilizers

Selenium have many crystal planes which appear on the XRD images: (100) at 23.9°, (101) at 29.8°, (110) at 41.7°, (102) at 43.7°, (111) at 45.8°, (201) at 51.9°, (013) at 55.6°, (202) at 61.5°, and (210) at 65.3° 2Θ degrees. The presence of crystal planes evidences the metallic form of selenium so the success of the reduction. The crystal planes appeared in case of all the samples.

2.3. FTIR measurements

FTIR measurements were used to evidence the presence of the stabilizers on the samples *(Figure 5).* Comparing the spectrum of the Se containing sample with the spectrum of the components, small shifts have been detected caused by the interactions between the Se and the stabilizer or the cysteine.

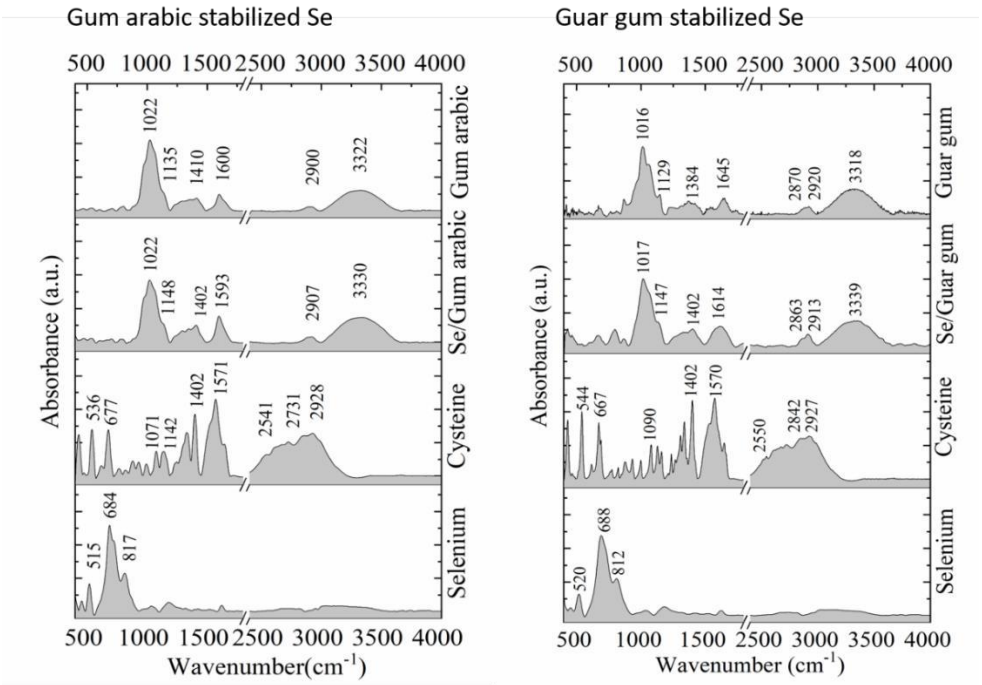

Figure 5

FTIR measurements of Se nanoparticles with gum arabic and guar gum

On the FTIR spectrum of gum arabic stabilized Se nanoparticles the peak of C-O-C bonds was detected at 1,022 cm^{-1} in case of both the gum arabic and the selenium contained sample. The νC-O(H) bond appears at 1,135 cm^{-1} in the stabilizer, but in case of the sample it shows a small shift (1,148 cm^{-1}). The peak of βOH shifts from 1,410 cm^{-1} to 1,402 cm^{-1}, meanwhile the νOH shifts from 3,326 cm^{-1} to 3,332 cm^{-1}. These shifts show strong interactions between the Se nanoparticles and the polymer which help the nanoparticle stabilization. The specific peaks of the reducing agent

(cysteine) are not detectable on the spectrum of the sample due to the low quantity. The peaks of selenium are also not visible in the sample because the nanoparticles are coated with the stabilizer.

In case of the guar gum stabilized sample the C-O-C bond appears at 1,016–1,017 cm^{-1}, while the νC-O bond of alcoholic and glyosidic hydroxyl groups shift from 1,129 cm^{-1} to 1,147 cm^{-1}. The absorbance of βOH groups shifted from 1,384 cm^{-1} to 1,402 cm^{-1}. This shift also means the interact between the Se particles and the stabilizer, and the selenium-cysteine complex formation. The νOH groups appeared at 3,318 cm^{-1} in case of the guar gum, meanwhile in thee selenium contained sample it shifted to 3,339 cm^{-1}. The specific peaks of cysteine and selenium are not visible due to the low quantity.

CONCLUSION

In this paper selenium nanoparticles were prepared with two different non-toxic stabilizers in order to prepare a Se source which ensures both fast and lasting uptake for plants. For this purpose, selenium contained samples were prepared with both elemental and organic content. The nanoparticles were examined by transmission electron microscopy to characterize their shape and size. The gum arabic stabilized sample had an average 70.9 nm diameter and well-defined spherical-like shape, meanwhile the guar gum stabilized sample had an average of 21.7 nm diameter with irregular shape. X-ray diffraction was used to evidence the success of the reduction step and to determine the crystal planes of Se. The measurement showed the presence of elemental (metallic) Se. Fourier transformation infra-red spectroscopy was used to identify the functional groups, to evidence the presence of the stabilizers, and to characterize the interactions between the nanoparticles and the stabilizer. In both cases the measurement evidenced the presence of the stabilizers, meanwhile the peak shifts mean that there is an interaction between the nanoparticles and the stabilizer mainly by OH groups.

In further experiments we would like to do biological tests to examine the uptake of the nanoparticles by plants and determine the composition of the samples.

ACKNOWLEDGEMENT

P. Á.: Supported by the ÚNKP-19-3 new national excellence program of the ministry for innovation and technology.

REFERENCES

[1] Hartikainen, H. (2005). Biogeochemistry of selenium and its impact on food chain quality and human health. *Journal of Trace Elements in Medicine and Biology*, Vol. 18, No. 4, pp. 309–318., DOI: 10.1016/j.jtemb.2005.02.009.

[2] Duntas, L. H., Benvenga, S. (2015). Selenium: an element for life. *Endocrine*, Vol. 48, No. 3, Humana Press Inc., pp. 756–775., 01-Apr-2015, DOI: 10.1007 /s12020-014-0477-6.

[3] Vinceti, M. et al. (2018). Selenium for preventing cancer. *Cochrane Database Syst. Rev.*, Vol. 2018, No. 1, Jan. 2018, DOI: 10.1002/14651858.CD005195. pub4.

[4] Loef, M., Schrauzer, G. N., Walach, H. (2011). Selenium and alzheimer's disease: A systematic review. *Journal of Alzheimer's Disease*, Vol. 26, No. 1, IOS Press, pp. 81–104., 2011, DOI: 10.3233/JAD-2011-110414.

[5] Tinggi, U. (2008). Selenium: Its role as antioxidant in human health. *Environmental Health and Preventive Medicine*, Vol. 13, No. 2, pp. 102–108., DOI: 10.1007/s12199-007-0019-4.

[6] Brenneisen, P., Steinbrenner, H., Sies, H. (2005). Selenium, oxidative stress, and health aspects. *Molecular Aspects of Medicine*, Vol. 26, No. 4–5, SPEC. ISS. Pergamon, pp. 256–267., 01-Aug-2005, DOI: 10.1016/j.mam.2005.07.004.

[7] Mroczek-Zdyrska, M., Wójcik, M. (2012). The influence of selenium on root growth and oxidative stress induced by lead in Vicia faba L. minor plants. *Biol. Trace Elem. Res.*, Vol. 147, No. 1–3, pp. 320–328., Jun. 2012, DOI: 10.10 07/s12011-011-9292-6.

[8] Wang, Y. et al. (2013). The protective effects of selenium on cadmium-induced oxidative stress and apoptosis via mitochondria pathway in mice kidney. *Food Chem. Toxicol.*, Vol. 58, pp. 61–67., Aug. 2013, DOI: 10.1016/ j.fct.2013.04.013.

[9] Richie, J. P. et al. (2014). Comparative effects of two different forms of selenium on oxidative stress biomarkers in healthy men: A randomized clinical trial. *Cancer Prev. Res.*, Vol. 7, No. 8, pp. 796–804., Aug. 2014, DOI: 10.1158/1940-6207.CAPR-14-0042.

[10] Hoffman, D. J., Heinz, G. H. (1998). Effects of mercury and selenium on glutathione metabolism and oxidative stress in mallard ducks. *Environ. Toxicol. Chem.*, Vol. 17, No. 2, pp. 161–166., Feb. 1998, DOI: 10.1002/etc. 5620170204.

[11] Gupta, M., Gupta, S. (2017). An overview of selenium uptake, metabolism, and toxicity in plants. *Front. Plant Sci.*, Vol. 7, Jan. 2017, DOI: 10.3389/fpls. 2016.02074.

[12] Kipp, A. P. et al. (2015). Revised reference values for selenium intake. *Journal of Trace Elements in Medicine and Biology*, Vol. 32. Elsevier GmbH, pp. 195–199., 01-Oct-2015, DOI: 10.1016/j.jtemb.2015.07.005.

[13] Jones, G. D. et al. (2017). Selenium deficiency risk predicted to increase under future climate change. *Proc. Natl. Acad. Sci. U. S. A.*, Vol. 114, No. 11, pp. 2848–2853., Mar. 2017, DOI: 10.1073/pnas.1611576114.

[14] Sors, T. G. et al. (2005). Analysis of sulfur and selenium assimilation in Astragalus plants with varying capacities to accumulate selenium. *Plant J.*, Vol. 42, No. 6, pp. 785–797., Jun. 2005, DOI: 10.1111/j.1365-313X.2005. 02413.x.

[15] Woodbury, P. B., McCune, D. C., Weinstein, L. H. (1999). A Review of Selenium Uptake, Transformation, and Accumulation by Plants with Particular Reference to Coal Fly Ash Landfills. In: *Biogeochemistry of Trace Elements in Coal and Coal Combustion Byproducts* (Eds. Sajwan et al.). Boston, MA, Springer US, pp. 309–338.

[16] D. Szabolcsy, Éva (2011). *Biological effect and fortification possibilities of inorganic selenium forms in higher plants*. Debrecen, University of Debrecen.

Materials Science and Engineering, Volume 45, No. 1 (2020), pp. 241–251.
DOI: 10.32974.mse.2020.025

VIRTUAL AND PHYSICAL SIMULATION OF MULTI-AXIAL FORGING PROCESSES

JÓZSEF B. RENKÓ[1] – PÉTER BERECZKI[2] – GYÖRGY KRÁLLICS[3]

Abstract: On a Gleeble 3800 thermo-physical simulator, multi-axial forging of high-purity copper workpieces were performed. The strain rate during the simulation process was 0.1 s^{-1}. The force response and the geometric changes of the workpiece as a function of time were continuously recorded. For a deeper understanding of the multi-axial forging process, a finite element model was created in Qform3D, analysing the changes in the deformation history. In the virtual model, tool movements were controlled using the recorded data of physical simulations. The force-displacement curves of the physical and finite element simulation were compared. The measured and simulated temperature and force values were used to verify the finite element model.

Keywords: multi-axial forging, simulation, finite element, Gleeble, modelling

INTRODUCTION

The technology of severe plastic deformation (SPD) has undergone significant development over the last 25 years. Various methods have been invented, such as equal channel angular pressing (ECAP) [1–4], high-pressure torsion [4, 5], cyclic extrusion-compression processes [6, 7], cyclic closed die forging [8], or multi-axial forging [9–12]. Due to its easy setup, multi-axial forging is one of the easiest to implement severe plastic deformation technology. Another advantage of multi-axial forging is the possibility to forge workpieces of even up to the size of 50–100 mm.

For the physical realisation of multi-axial forging, a Gleeble 3800 thermo-physical simulator equipped with a MaxStrain unit was used. In a Gleeble system, multiple parameters can be controlled with high precision during the entire forming process, like tool movements, forming speeds, forming forces and temperatures. An additional camera was built into the system to track the deformed geometry.

For a deeper understanding of the process, the performed physical simulations were also created in a finite element simulation. The simulations were created with

[1] Budapest University of Technology and Economics, Department of Materials Science and Engineering, H-1111 Budapest, Hungary
renko.jozsef@edu.bme.hu
[2] Institute of Engineering Sciences, University of Dunaújváros
H-2401 Dunaújváros, Hungary
bereczkip@uniduna.hu
[3] Institute of Physical Metallurgy, Metal Forming and Nanotechnology, University of Miskolc
H-3515 Miskolc-Egyetemváros, Hungary
femkgy@uni-miskolc.hu

QForm3D. The proper use of the finite element simulation could allow studying the whole forging process at any moment. With a well-prepared virtual model, real conditions can be simulated with high accuracy [13–15]. Using finite element simulations before production or physical testing, defects and failed locations could be eliminated almost without exception, even during the design phase [16, 17].

We aimed to reproduce the non-monotonous deformation history of multi-axial forging in a finite element simulation and then to evaluate its reliability. Different characteristic curves of the physical and finite element simulation were compared using the data recorded during both processes.

1. MATERIALS AND METHODS

1.1. Material

The chosen material was an industrial-grade, pure copper. The composition of the material was within the prescribed limits. The chemical composition of the substance is shown in *Table 1*.

Table 1

Chemical composition of the studied CuE material

Element	Cu	Fe	Pb	S	Zn	Ni	Sn
Conc. (atomic%)	99.978	0.005	0.004	0.004	0.004	0.002	0.002

The chosen material must be suitable for cold forming, in which deformation was not held back by precipitations. CuE is a high-purity industrial copper with a minimum ratio of alloys and contaminants, making it ideal for the selected tests.

1.2. Programming of Gleeble thermo-physical simulator

Multi-axial forging was performed on the MaxStrain unit of the Gleeble 3800 thermo-physical simulator. The workpiece was to be forged in ten steps. The equivalent plastic strain achieved in each forming step was 0.4. Thus, the cumulative strain at the end of the process was 4. During the simulation, the middle, 12 × 12 × 12 mm size part of the square cross-sectional volume was forged with flat-faced, 10 mm wide tools. The workpiece was secured with clamps, connected to a manipulator, allowing the workpiece to be rotated along its longitudinal axis. The multidirectional cyclic deformation is thus carried out by the same tool, with the manipulator rotating 90° on the workpiece between each forming step *(Figure 1)*.

The simulator continuously records tool movements, force and temperature according to the previously set 100 Hz measurement frequency. By programming the simulator, the dimensions of the workpiece between the forging steps can also be recorded. To accurately determine the dimensions of the workpiece, preforming is necessary at a rate of 0.1 s^{-1} before each forging steps. The equivalent plastic strain of the preforming was set to 0.1. This is necessary because the free surfaces of the workpiece start barrelling during forging. At the beginning of each step, the contact

surface between the workpiece and the tool would be irregular, causing also irregular force. The phenomenon could be corrected by suppressing the barrelled surfaces of the workpiece with the small plastic deformation described previously between the main forming steps.

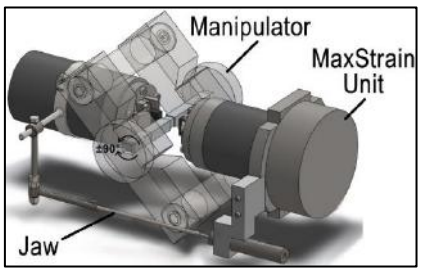

Figure 1
Conceptual setup of MaxStrain unit and the workpiece rotating manipulator

The system has been augmented with an integrated camera that allows the geometry of the workpiece to be captured in snapshots before and after each forming steps. The pictures recorded during the shaping steps are shown in *Figure 2*.

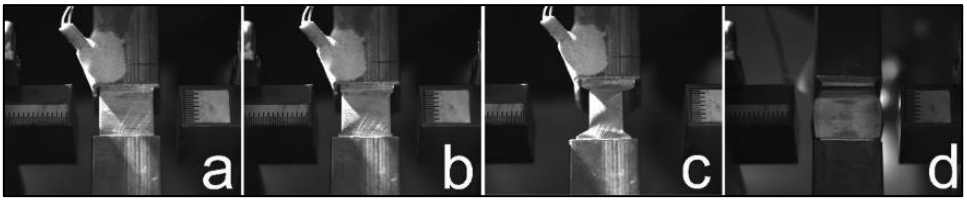

Figure 2
Pictures recorded by the camera between steps: before pre-forming (a), after pre-forming (b), after main forming (c), rotated with 90° after main forming (d)

To record the changes of the temperature, a thermocouple was fixed into the workpiece as shown in the top left corner in *Figure 2*. The binder used to secure the thermocouple had to be heated up to 100 °C. Due to the excellent thermal conductivity of copper, the entire workpiece was heated, so it must be cooled before the experiments. The forging experiments were thus started at 30 °C.

2. FINITE ELEMENT SIMULATION

Finite element simulations of the process were performed with QForm3D 9.0.8. software. The CAD model of the workpiece, tools and fixing clamps were previously created to support the simulation. To reduce the computational time, a half-model was used. Further simplification of the workpiece, possibly a quarter or eighth model was not applicable due to the design of the mounting clamps *(Figure 3)*.

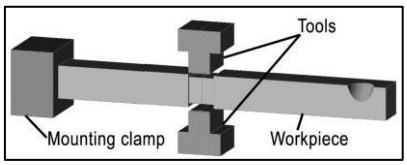

Figure 3
Workpiece clamping and tool placement

2.1. Determination of tool movements

In the virtual simulation, the rotation of the workpiece was simplified by defining two additional tools. While one of the tool pairs performed the active forming step, the other tool pair waited in the rear end position. After forging, the active tools returned to their rear end position. The active and passive tools were then interchanged, and the next forming step has begun.

Using the time-displacement value pairs recorded during multi-axial forging, tool-paths in different directions were created. Jaw recorded the relative displacement of the two tools from each other since the measurement started *(Figure 4)*. Positive values indicate the convergence of the tools, while negative values indicate the distancing. In the Gleeble simulator, at the rear end position of the tools, the Jaw was set to –21 mm. This is due to the need to maintain sufficient distance between the tools and the workpiece during rotations, thus protecting the machine from collisions. Examining the displacement curve, the ten shaping steps have a total of thirty characteristic peaks. For each forming step, the first of the three vertices is the preforming, the second is a thickness measured perpendicular to the direction of the current forming step, and the third one is the main forming.

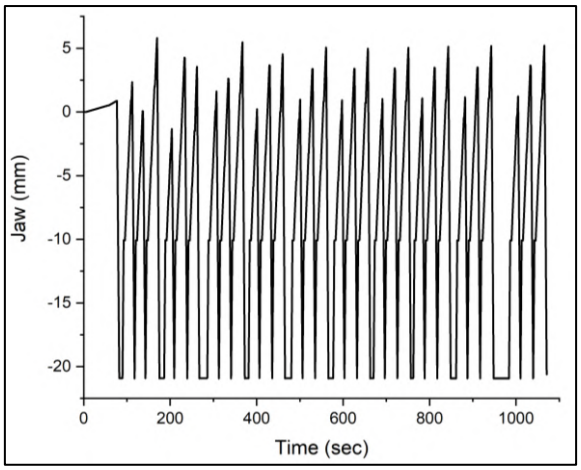

Figure 4
Relative tool distance recorded by Jaw

The tool-paths have been modified so that in their rear end position, the tools do not reach the deforming workpiece, nor do they move unnecessarily far. Based on the data recorded by the Gleeble simulator, the optimal rear end position was determined to be at –2.5 mm from the surface of the unformed workpiece. The dead time thus released was also removed from the tool movements. Pre-positioning tool movements, preforming, and measuring movements were also neglected. The curve describing the relative displacement of the tools is shifted along the y-axis so that at point 0 the surface of the tool and the unformed workpiece touch each other. Finally, the resulting curve was divided into two parts and its value was halved depending on the direction from which the forming is taking place. The resulting tool-paths are shown in *Figure 5*. The curves thus obtained were used to describe the tool movements over time.

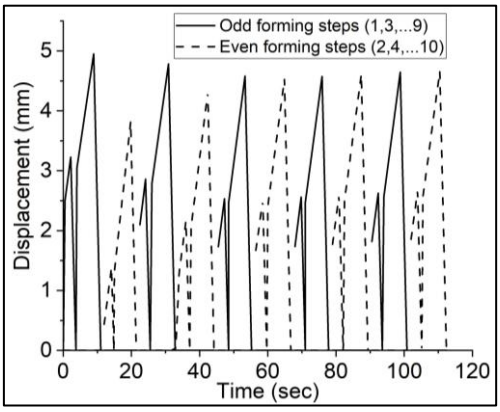

Figure 5
Tool movements as a function of time

2.2. Additional settings

The meshing of the bodies was created automatically by the QForm3D system using the previously set boundary conditions. The mesh density was set to finer in the environment of the clamp and the deformation area, while coarser in the stem of the workpiece. Using this mesh, the planned measurement accuracy was achieved, while the computation time did not increase significantly *(Figure 6)*. The re-meshing during the simulation was continuous and automatic, preserving the boundary conditions, as well as further increasing the mesh density in the plastic deformation zone. The number of initial nodes was thus 6,049, while the number of initial elements was 32,213. The number of elements and nodes has been constantly changing with re-meshing. The maximum number of elements was 80,373 and the maximum number of nodes was 14,448.

As previously described, we aimed to study the reliability of the material model used in general. The material model used in the simulations was CuE, available from the software database. In the adjusted elastic-plastic material model, the flow stress was the function of strain, strain rate and temperature. Thus, thermo-physical aspects

were also considered during the simulation. The initial temperature was set to 30 °C according to the actual measurement conditions.

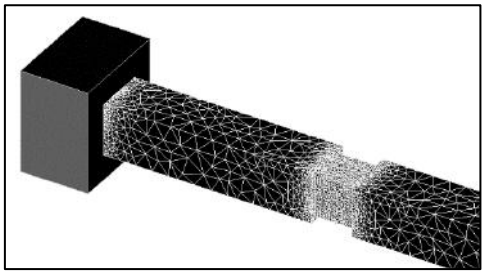

Figure 6
The initial meshing of the workpiece

3. RESULTS AND DISCUSSION

3.1. Force and displacement

Using the force-time-displacement values recorded by the Gleeble simulator, we decomposed the measurement data into ten forming cycles. The force-displacement values experienced during the physical simulation are shown in *Figure 7.a.* The force required for the odd forming steps was significantly higher at the beginning than for the even shaping steps. The dislocation structure formed in the first forming step was less resistant to stress from other directions [18, 19]. The dislocation structure formed in the previous forming step was rearranged depending on the new direction of load. As the forging steps progress, the grain structure of the copper refines, and the curves get closer and closer to each other. The phenomenon is similar to that observed for aluminium alloys studied by Bereczki et al. [18–20].

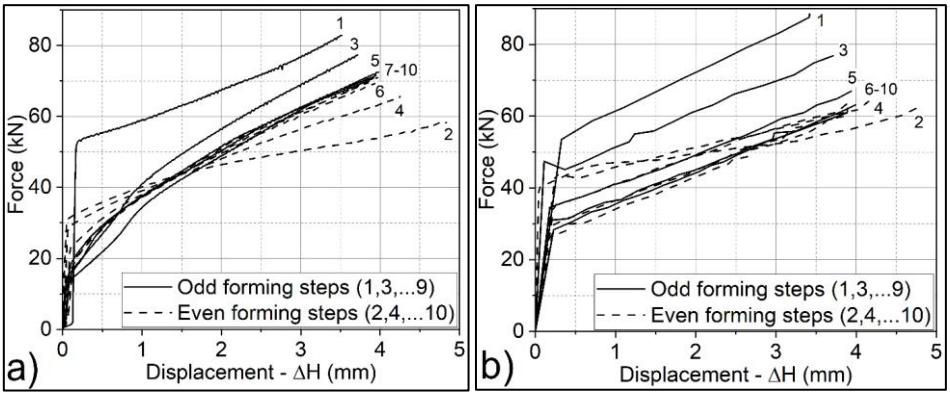

Figure 7
The force as a function of the displacement during physical (a) and finite element (b) simulation

Evaluating the results of the finite element simulation, force-displacement values were recorded *(Figure 7.b)*. The curves showed similar characteristic to the force-displacement curves of the physical simulation. However, fitting the curves of the two simulations to each other, the difference emerges *(Figure 8)*.

During the first and second forging steps, the finite element simulation assigned higher force values for the same displacements than the physical simulation. During the third and fourth forging steps, the two simulations converged to the same force values, while from the fifth step, the previously observed trend was reversed. The physical simulation required a force approximately 5 kN higher than the finite element simulation.

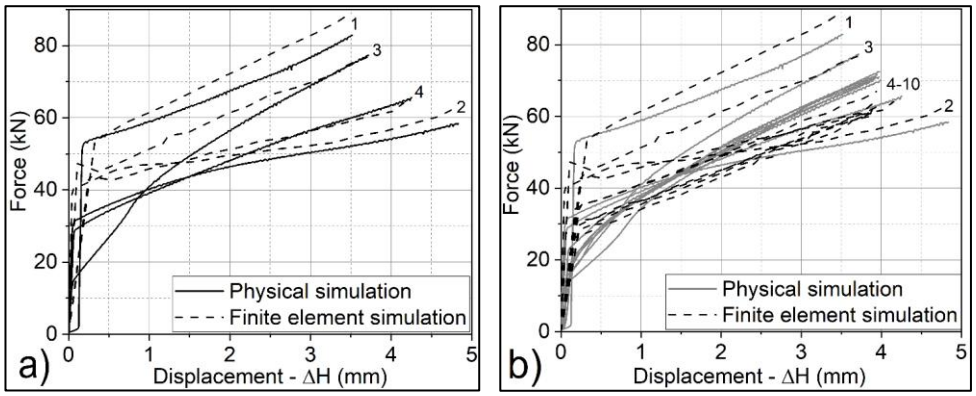

Figure 8
Force-displacement curves recorded during the first four forging steps (a) and during the whole (b) physical and finite element simulation

The reversal of the force curves' trend could be caused by the processes changing the microstructure. Under real conditions, by increasing the cumulative plastic strain, significant grain refining takes place in the forged volume. As a result of the grain refinement, the resistance of the material against deformation increased. Consequently, the force requirement also increased. However, the finite element model did not calculate with such changes in the microstructure, therefore, it couldn't apply its effects.

3.2. Temperature

The temperature change was recorded in both simulations. During the physical simulation, the temperature was measured with a thermocouple. It was embedded into a hole drilled adjacent to the deformation zone. During the finite element simulation, the temperature change was retrieved at the same position as the end of the thermocouple *(Figure 9)*.

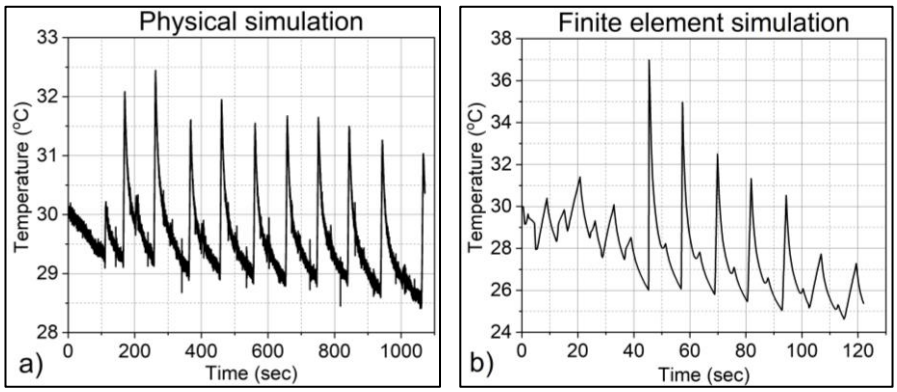

Figure 9
Temperature change recorded during physical (a) and finite element (b) simulations

Although the temperature curves are very similar, the heat released during forging is much larger in the virtual simulation. This is due to the difference in running time. The finite element simulation ran in 122 seconds, while the physical simulation required nearly 1,100 seconds. With significantly larger tool movements, rotations and measurements, the workpiece have time to transfer heat to its surroundings, so the temperature increase during the physical simulation is less intense.

3.3. Deformed shapes

Copper showed an interesting deformation during multi-axial forging. The usual barrelling in uniaxial compression tests was only observed during the first step. From the second forming step, the thickness of the formed volume continuously decreased inward *(Figure 10)*.

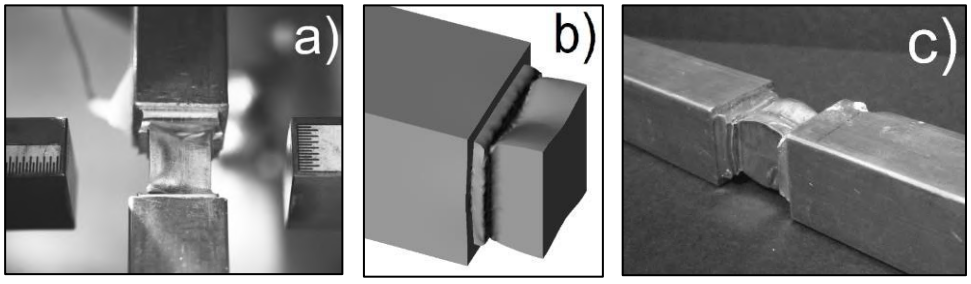

Figure 10
The geometry of the workpiece in the physical simulation (a) and in the finite element simulation (b) after the second forging step. The geometry of the workpiece after the whole multi-axial forging process (c)

The phenomenon became less and less characteristic as the forming progressed, the material in the middle became more and more resistant to the deformation as the accumulated plastic strain increased. The phenomenon was visible even after the whole forging process *(Figure 10.c)*. In contrast to the physical simulations, the previously presented mode of deformation in the finite element simulation was maintained throughout. It did not deviate significantly from the shape shown in *Figure 10.b* even after the tenth step.

CONCLUSION

To summarise the results of the study, the implemented finite element simulation was able to reproduce the physical simulation's results with a good approximation. The temperature change, during both processes, moved within a narrow range, so its effect did not cause any significant differences. The force-displacement curves showed a similar nature in both cases. Compared to the first forging step, the second forging step required significantly less force. After the second forging step, the curves run in the region bounded by the first and second curves, getting closer and closer to each other. Assuming the existence of the force-displacement curve of the theoretical, infinite forging cycle, from the third forging step the odd-numbered force-displacement curves approach that from above, and the even-numbered curves approach that from below.

When comparing the force-displacement values, the curves recorded in the virtual simulation showed higher force necessity during the first couple of forging steps. However, with increasing cumulative plastic strain, the trend was reversed and showed lower force values at the same displacement than the physical simulation. The differences between the force curves could be traced back to the applied material model. As the cumulative plastic strain increased, the geometry of the finite element model also differed more and more from that observed in the physical simulator. The used material model was presumably unable to trace the refinement of the grain structure and the increase in strength associated with the dislocation structure arranging in different directions.

Most of the parameters set in the finite element simulation could be suitable for studying the process of multi-axial forging. To do this, however, critical elements, such as the material model need to be redesigned specifically for multi-axial forging. By setting up a material model suitable to describe the changes during multi-axial forging, we could gain a more in-depth insight into the processes using virtual simulations.

ACKNOWLEDGEMENT

This study was supported by the Hungarian Scientific Research Fund, OTKA, Grant No. K-119566. The results presented in this paper are part of a research work, which is also supported by the EFOP-3.6.1-16-2016-00003 project of Hungarian Government, called *The long term collaboration of the R&D processes* at University of Dunaújváros.

REFERENCES

[1] Segal, V. M., Reznikov, V. I., Drobyshevkij, A. E., Kopylov, V. I. (1981). *Russian Metallurgy.* 1, p. 115.

[2] Segal, V. M. (1995). Materials processing by simple shear. *Mater. Sci. Eng. A*, 197, pp. 157–164.

[3] Segal, V. M. (2004). The development of essentials of material processing by severy plastic deformation. *Metally*, 1, pp. 5–14.

[4] Valiev, R. Z., Islamgaliev, R. K., Alexandrov, I. V. (2000). Bulk nanostructured materials from severe plastic deformation. *Progress in Mater. Sci.*, 45, pp. 103–189.

[5] Popov, A. A., Pyshmintsev, I. Y., Demakov, S. I., Illarionov, A. G., Lowe, T. C., Valiev, R. Z. (1997). Structural and mechanical properties of nanocrystalline titanium processed by severe plastic deformation processing. *Scr. Mater*., 37, pp. 1089–1094.

[6] Korbel, A., Richert, M., Richert, J. (1981). The effects of very high cumulative deformation on structure and mechanical properties of aluminium In: *Proc. 2nd Riso Int. Symp. on Metallurgy and Material Science*, Roskilde, Denmark, September 14–18, pp. 445–450.

[7] Zrnik, J., Dobatkin, S. V., Mamuzi, I. (2008). Processing of metals by severe plastic deformation (SPD) – structure and mechanical properties respond. *Metalurgija*, 47 (3), pp. 211–216.

[8] Magalhães, D., Pratti, A., Kliauga, A., Rubert, J., Ferrante, M., Sordi, V. (2018). Numerical simulation of cryogenic cyclic closed-die forging of Cu: Hardness distribution, strain maps and microstructural stability. *Journal of Materials Research and Technology*, 8 (1), pp. 333–343.

[9] Szabó, P. J., Bereczki, P., Verő, B. (2011). The Effect of Multiaxial Forging on the Grain Refinement of Low Alloyed Steel. *Periodica Polytechnica Mechanical Engineering*, 55 (1), pp. 63–66.

[10] Naser, T. S. B., Krállics, G. (2012). The effect of multiple forging and cold rolling on bending and tensile behavior of Al 7075 alloy. *Mater. Sci. Forum*, 729, pp. 464–469.

[11] Tikhonova, M., Dudko, V., Belyakov, A., Kaibyshev, R. (2010). The Formation of Submicrometer Scale Grains in a Super304H Steel during Multiple Compressions at 700 °C. *Materials Science Forum*, 667–669, pp. 565–570.

[12] Ringeval, S., Driver, J. H. (2006). A Comparison of Flow Stress and Microstructure Development of Al Alloys in Plane Strain Compression and Multiple Forging. *Materials Science Forum*, 519–521, pp. 979–984.

[13] Li, J., Wu, F. (2017). Finite Element Analysis on the Precision Forging of the Semimonocoque. *International Conference on Smart Grid and Electrical Automation (ICSGEA)*, Changsha, pp. 355–357.

[14] Roque, C. M. O. L., Button, S. T. (2000). Application of the finite element method in cold forging processes. *Journal of the Brazilian Society of Mechanical Sciences*, 22 (2), pp. 189–202.

[15] Renkó, J. B., Kemény, D., Nyirő, J., Kovács, D. (2019). Comparison of cooling simulations of injection moulding tools created with cutting machining and additive manufacturing. *Materials Today: Proceedings*, 12, pp. 462–469.

[16] Wangchaichune, S., Suranuntchai, S. (2018). Finite Element Simulation of Hot Forging Process for KVBM Gear. *Applied Mechanics and Materials*, 875, pp. 30–35.

[17] Behrens, B.-A. (2008). Finite element analysis of die wear in hot forging processes. *Cirp Annals-manufacturing Technology*, 57, pp. 305–308.

[18] Bereczki, P., Szombathelyi, V., Krállics, G. (2014). Determination of flow curve at large cyclic plastic strain by multiaxial forging on MaxStrain System. *International Journal of Mechanical Sciences*, 84, pp. 182–188.

[19] Bereczki, P., Szombathelyi, V., Krallics, G. (2014). Production of ultrafine-grained aluminum by cyclic severe plastic deformation at ambient temperature. *IOP Conf. Series: Materials Science and Engineering*, 63 (012140).

[20] Bereczki, P., Krallics, G., Renkó, J. B. (2019). The effect of strain rate under multiple forging on the mechanical and microstructural properties. *Procedia Manufacturing*, 37, pp. 253–260.

Materials Science and Engineering, Volume 45, No. 1 (2020), pp. 252–260.
DOI: 10.32974.mse.2020.026

CO-GASIFICATION OF REFUSE DERIVED FUEL CHAR WITH HUNGARIAN BROWN COAL

EMESE SEBE[1] – GÁBOR NAGY[2] – ANDRÁS ARNOLD KÁLLAY[3]

Abstract: Pyrolysis is a promising process for the thermal treatment of residual municipal solid wastes. In this process the final products are composed of synthesis gas (syngas) and pyrolysis char. The char generally has high carbon content thereby it is suitable for further syngas production by gasification. Nowadays syngas is mainly derived from fossil fuels. In this study gasification characteristics of Hungarian brown coal and Refuse Derived Fuel (RDF) char blend were determined in a laboratory bench scale equipment at 900 °C using steam as gasification agent. SEM tests were also carried out in order to determine the surface morphology of the blending materials. The results showed that during co-gasification of brown coal and RDF pyrolysis char the tar formation decreased while the H_2 content of the syngas increased compared to the gasification of the individual materials. The EDS spectrums revealed the presence of alkali and alkaline earth metals, which can have catalytic effect on the gasification.

Keywords: pyrolysis, gasification, refuse derived fuel

INTRODUCTION

Due to the continuous growth of the population, we have to face several challenges these days. According to the World Bank the global waste generation – including municipal solid waste – is expected to increase significantly in the next years [1]. Based on the 2008/98/EC directive, in the European Union the following waste hierarchy should be applied: prevention, reuse, recycling, energy recovery and disposal [2]. Nevertheless, in Hungary approximately half of the generated municipal solid wastes (MSW) ends up on landfills [3]. In order to meet the expectations, it is important to reduce landfilling. One of the possible routes to this is to further utilize the energy content of the wastes that cannot be economically reused or recycled. Pyrolysis is a promising alternative for energy recovery by providing an opportunity to convert wastes into value added products like char or syngas [4]. Due to their high

[1] Institute of Energy and Quality, University of Miskolc
H-3515 Miskolc-Egyetemváros, Hungary
sebe.emese@uni-miskolc.hu
[2] Institute of Energy and Quality, University of Miskolc
H-3515 Miskolc-Egyetemváros, Hungary
nagy.gabi@uni-miskolc.hu
[3] Institute of Energy and Quality, University of Miskolc
H-3515 Miskolc-Egyetemváros, Hungary
tuzaak@uni-miskolc.hu

carbon content, pyrolysis chars can be suitable for high quality syngas generation by steam gasification.

Even these days syngas is mainly produced from fossil fuels [5]. However, the growing concerns about environmental issues like greenhouse gas (GHG) emissions and the depletion of fossil fuels, accelerated the spread of renewable energy and cleaner technologies. There are more and more studies about co-gasification of coal with other solid fuels [6], [7]. The use of biomasses as a blending material has the advantages that these are available in large quantities and the alkali and alkaline earth metal (AAEM) species present in these materials can have catalytic effect during the thermal decomposition. The presence of AAEMs may result the reduction of tar formation or CO_2 concentration of the syngas [8], [9]. Although biomasses usually have lower energy density and can be widely dispersed what increases the transportation costs and further increases the environmental impact [10]. Furthermore, during biomass gasification particulate matter and tar formation are usually higher compared to coal, but it also depends on the quality of the coal [11]. Another group of the potential blending materials includes different kind of wastes like waste tyres, plastics, sewage sludge or MSW [12], [13], [14], [15], [16]. By the co-gasification of coal and wastes it is possible to reduce the quantity of landfilled materials and the consumption of fossil fuels as well. Furthermore, earlier studies [8] showed that besides AAEMs, other metal-oxides, such as SiO_2 and Fe_2O_3 present in coal also have catalytic effect on gasification. According to Loy et al. [8] it can increase the H_2 and CO concentration in the syngas, which is an important parameter in terms of the further utilization. This study focuses on the co-gasification of Hungarian brown coal and RDF (Refuse Derived Fuel) char.

1. MATERIALS AND METHODS

1.1. Samples

Three samples were investigated, including Hungarian brown coal, RDF char and a blend (50 : 50 m/m%) of these. The brown coal was crushed below 5 mm before the experiments. The RDF samples were prepared in a mechanical-physical processing plant from non-selectively collected residual MSW [17]. The RDF was pyrolyzed at 700 °C in a 20–60 kg/h capacity pilot-scale plant. Based on the laboratory sample analysis [18] the remaining char still has 38 m/m% carbon content. The results of the gasification experiments with these two base materials were previously published [18]. This study is focusing on the investigation of the brown coal and RDF char co-gasification. The particle sizes of the materials were between 0.9–3.15 mm. For each experiment 30-30 g samples were used.

1.2. Experimental system

The gasification experiments were performed in a laboratory bench scale – 20–30 g capacity – system *(Figure 1)*, which contains two tube furnaces and a steel tube. The samples were placed into that part of the tube, which was heated by the left furnace.

In this study steam was used as gasification agent. The furnaces were heated up to 900 °C. First the samples were pyrolyzed at this temperature, the gasification started when the temperature of the furnaces reached 900 °C and there was no observable pyrolysis gas production. The gas flow was measured with rotameters. Samples were taken from the gaseous products and analysed with through gas chromatography (DANI 500). Furthermore, the coal and char samples were subjected to scanning electron microscopy (SEM) in order to determine the differences in the surface morphology of the blending materials.

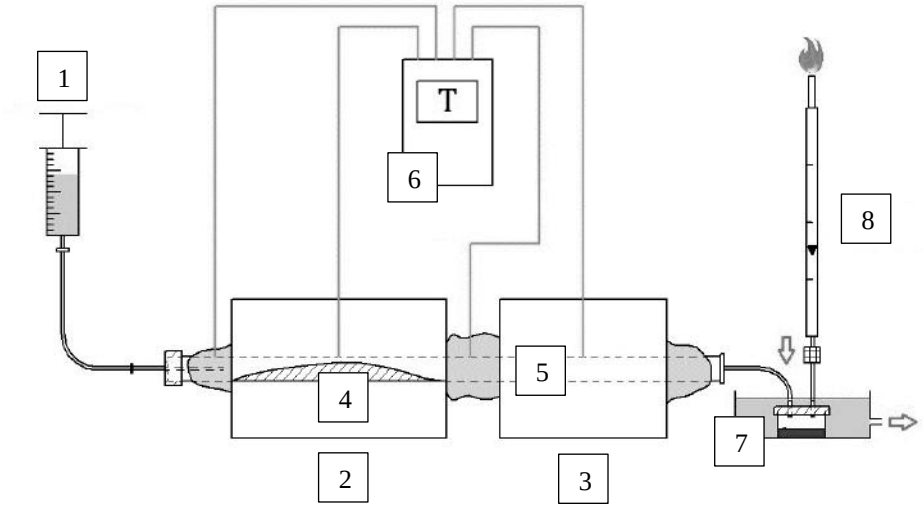

Figure 1
Laboratory scale experimental system (1. water supply, 2–3. tube furnaces, 4. feedstock material, 5. reactor tube, 6. temperature measuring device, 7. liquid collecting vessel with water cooling, 8. rotameter) [18]

2. RESULTS AND DISCUSSION

As shown in *Figure 2* the highest conversion rate occurred during the gasification of the Hungarian brown coal, in case of the RDF char the amount of the remaining solid material was significantly more. In this regard the blended material showed an intermediate value, although the tar formation was slightly lower compared to the base materials.

Based on our previous results [18] the initial ash content of the brown coal was lower compared to the RDF char. Probably this is the explanation for the higher conversion rate during the brown coal gasification. The results shown on *Figure 3* confirm the values described above. The highest gas formation was observed during the brown coal gasification.

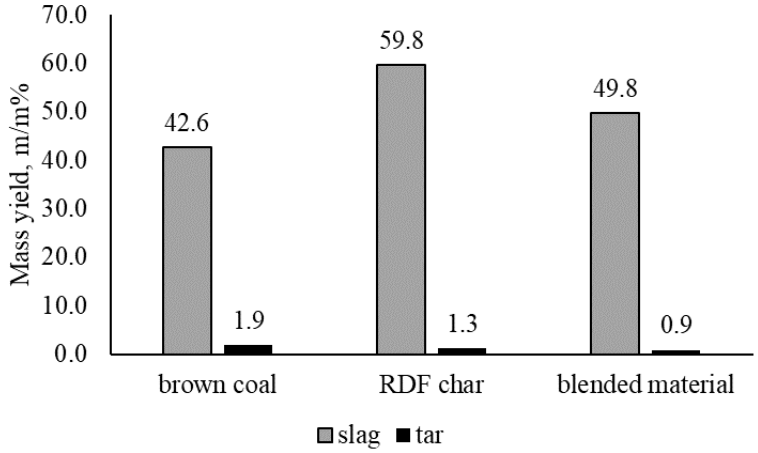

Figure 2
Mass yield of the remaining slag and tar on dry basis

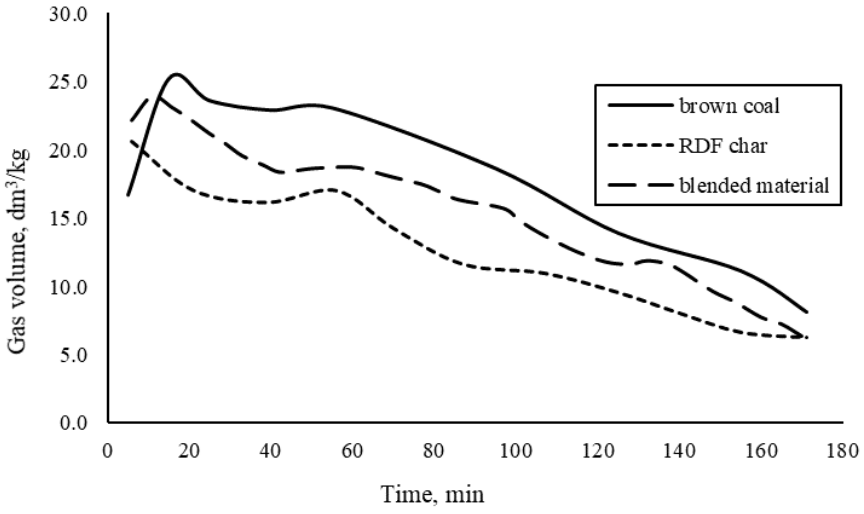

Figure 3
Comparison based on syngas production

Figure 4 shows the rate of the main components (CO_2, CO, H_2) in the syngas based on the results of gas chromatography (GC). In terms of the CO and CO_2 the syngas compositions were especially similar.

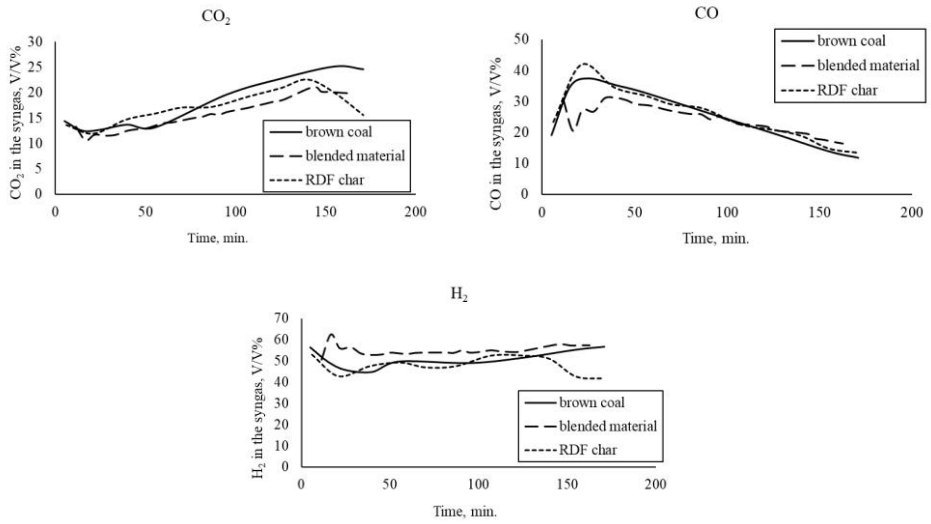

Figure 4
Results of the GC measurements about the main syngas components

Despite that, the H_2 shows a similar concentration for each starting material, only the blend derived syngas contained slightly larger concentration during the whole gasification process. This fact and the lower tar formation indicate that some components had catalytic effect on co-gasification reactivity.

During our previous gasification experiments with the blending materials [18], we found that the carbon conversion was greater in case of the examined RDF char compared to the coal samples. Several studies reported that the gasification reactivity is affected by the char morphology and specific surface area [19], [20]. According to Seo et al. [20] as the volatile matter releases during pyrolysis, the surfaces area of the material increases significantly, which can improve the gasification performance.

Figure 5 shows the microstructure of the brown coal and RDF char particles. The RDF char is a heterogenous material with several different components which have different gasification characteristics. Smooth and rough surfaces both can be found in case of the char sample. Some components have filamentous structure, which were probably derived from cellulosic materials.

As the composition of the MSW changes, the ratio of these components in the RDF and its char will also be different. By blending this with a material with less variable composition, we can reduce the fluctuations in the quality and quantity of the produced syngas. *Figure 6* shows the EDS (energy dispersive X-ray spectroscopy) spectrums of the brown coal and RDF char samples. The spectrums revealed the presence of AAEMs in both materials, like Na, Mg, K and Ca. The samples also contained Si, which could deactivate the AAEM catalyst [21]. Although to determine the exact concentration of these inorganic elements in the ashes further tests should be performed.

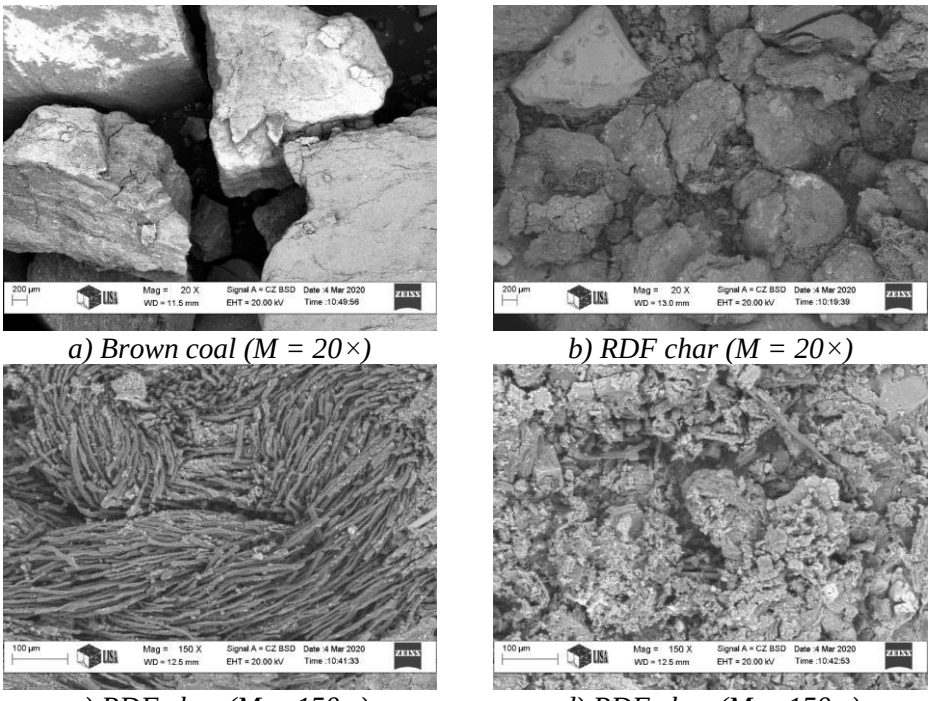

a) Brown coal (M = 20×) *b) RDF char (M = 20×)*

c) RDF char (M = 150×) *d) RDF char (M = 150×)*

Figure 5

SEM micrographs of the brown coal and RDF char samples

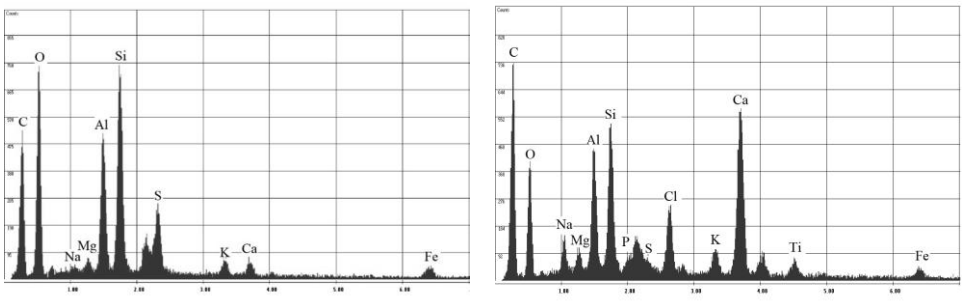

a) Brown coal b) RDF char

Figure 6

EDS spectrum of the brown coal and RDF char samples

CONCLUSION

The aim of this research was to study the co-gasification of Hungarian brown coal and RDF char. The results showed that the tar formation was lower and the H_2 concentration of the syngas was slightly higher compared to the gasification of the individual materials. One possible reason to this is the presence of AAEMs. although it would be useful in the future to perform experiments at different temperatures and with different heating rates in order to determine the catalytic effect under other conditions. Based on these results Hungarian brown coal and RDF char can be effectively used for syngas production by co-gasification with steam.

ACKNOWLEDGMENT

The authors are grateful to Árpád Kovács for the SEM analysis. This study is supported by the ÚNKP-19-3 New National Excellence Program of the Ministry for Innovation and Technology.

REFERENCES

[1] Kaza, S., Yao, L., Bhada-Tata, P. et al. (2018). "What a Waste 2.0" A Global Snapshot of Solid Waste Management to 2050. Washington, World Bank Group.

[2] *Waste Framework Directive* (2008/98/EC). https://ec.europa.eu/environment/waste accessed: 2020. 03. 12.

[3] STADAT 5.5.2. *Az egyes hulladékfajták mennyisége a kezelés módja szerint*. Available: https://www.ksh.hu/docs/hun/xstadat/xstadat_eves/i_ur006.html. Accessed: 2018. 07. 17.

[4] Tokmurzin, D., Kuspangaliyeva, B., Aimbetov, B., Abylkhani, B., Inglezakis, V., Anthony, E. J., Sarbassov, Y. (2020). Characterization of solid char produced from pyrolysis of the organic fraction of municipal solid waste, high volatile coal and their blends. *Energy*, 191, p. 116562.

[5] *The Global Syngas Technologies Council*. Available: https://www.globalsyngas.org/, accessed: 2020. 01. 09.

[6] Ren, L., Wei, R., Zhu, T. (2020). Co-gasification reactivity of petroleum coke with coal and coal liquefaction residue. *Journal of the Energy Institute*, 93, pp. 436–441.

[7] Xiao, Y., Xu, S., Liu, Y., Qiao, C. (2020). Catalytic steam co-gasification of biomass and coal in a dual loop gasification system with olivine catalysts. *Journal of the Energy Institute*, Vol. 93, pp. 1074–1082.

[8] Loy, A. C. M., Yusup, S., Lam, M. K., Chin, B. L. F., Shahbaz, M., Yamamoto, A., Acda, M. N. (2018). The effect of industrial waste coal bottom ash as catalyst in catalytic pyrolysis of rice husk for syngas production. *Energy Conversion and Management*, 165, pp. 541–554.

[9] Islam, M. W. (2020). A review of dolomite catalyst for biomass gasification tar removal. *Fuel*, Vol. 267, p. 117095.

[10] Inayat, M., Sulaiman, S. A., Kurnia, J. C., Shahbaz, M. (2019). Effect of various blended fuels on syngas quality and performance in catalytic co-gasification: A review. *Renewable and Sustainable Energy Reviews*, 105, pp. 252–267.

[11] Emami-Taba, L., Irfan, M. F., Daud, W. M. A. W., Chakrabarti, M. H. (2013). Fuel blending effects on the co-gasification of coal and biomass – A review. *Biomass and Bioenergy*, 57, pp. 249–263.

[12] Isaac, M., Dai, B., Zhang, L. (2019). Kinetics underpinning the C-CO2 gasification of waste tyre char and its interaction with coal char upon co-gasification. *Fuel*, 256, p. 115991.

[13] Hu, B., Huang, Q., Buekens, A., Chi, Y., Yana, J. (2017). Co-gasification of municipal solid waste with high alkali coal char in a three-stage gasifier. *Energy Conversion and Management*, Vol. 153, 1 December 2017, pp. 473–481.

[14] Ding, G., He, B. (2020). Process Simulation of Co-Gasification of Raw Municipal Solid Waste and Bituminous Coal in CO_2/O_2 Atmosphere. *Appl. Sci.*, 10, p. 1921.

[15] Zaccariello, L., Mastellone, M. L. (2015). Fluidized-Bed Gasification of Plastic Waste, Wood, and Their Blends with Coal. *Energies*, Vol. 8, pp. 8052–8068.

[16] Jeong. Y. S., Choi, Y. K., Park, K. B., Kim, J. S. (2019). Air co-gasification of coal and dried sewage sludge in a two-stage gasifier: Effect of blending ratio on the producer gas composition and tar removal. *Energy*, Vol. 185, 15 October 2019, pp. 708–716.

[17] Faitli, J., Csőke, B., Romenda, R., Nagy, Z., Németh, S. (2018). Developing the combined magnetic, electric and air flow (KLME) separator for RMSW processing. *Waste Management & Research*, Vol. 36, No. 9, pp. 779–787.

[18] Sebe E., Nagy G., Kállay A. A. (2019). RDF pirolíziséből származó koksz és bárnászén élgázosításának vizsgálata láborátóriumi körülmények között. *International Journal of Engineering and Management Sciences / Műszaki és Menedszment Tudományi Közlemények*, 4, pp. 188–193.

[19] Guizani, C., Jeguirim, M., Gadiou, R., Sanz, F. J. E., Salvador, S. (2016). Biomass char gasification by H_2O, CO_2 and their mixture: Evolution of chemical, textural and structural properties of the chars. *Energy*, 112, pp. 133–145.

[20] Seo, M. W., Kim, S. D., Lee, S. H., Lee, J. G. (2010). Pyrolysis characteristics of coal and RDF blends in non-isothermal and isothermal conditions. *Journal of Analytical and Applied Pyrolysis*, 88, pp. 160–167.

[21] Klinghoffer, N. B., Castaldi, M. J., Nzihou, A. (2015). Influence of char composition and inorganics on catalytic activity of char from biomass gasification. *Fuel*, 157, pp. 37–47.

Materials Science and Engineering, Volume 45, No. 1 (2020), pp. 261–270.
DOI: 10.32974.mse.2020.027

EFFECT OF THE FIRING TEMPERATURE ON THE PROPERTIES OF AL_2O_3/GLASS COMPOSITES

ANDREA SIMON[1] – GÁBOR MUCSI[2] – ISTVÁN KOCSERHA[3]

Abstract: Nowadays, ceramic materials having adequate strength and good electrical insulating properties, but also can be sintered at relatively low temperatures, play an increasingly important role. Ceramics providing this property combination are the glass-composite ceramics. The low-temperature sintering is ensured by the glass powder added to the base ceramic (which is usually alumina). Glass is typically a well-designed oxide frit that is sintered and melts/softens below 1,000 °C.

In this research work, the effect of firing temperature on the properties of glass/ceramic composite ceramics was studied. The samples were prepared by injection moulding technology. Density, porosity, flexural and compressive strength, thermal conductivity of the fired samples was measured. The morphology and the phases of the fired products were also analyzed.

Keywords: glass/ceramic composite, microstructure, injection moulding, sintering

INTRODUCTION

Glass-ceramic composites are increasingly being researched in the world of ceramics due to their well-controlled, individually adjustable properties [1–17]. In glass-ceramic composites, the main phase is a dielectric material having a high sintering temperature [8]. This crystalline phase provides the appropriate dielectric properties. The glass phase increases the dielectric loss but reduces the relative permittivity and the sintering temperature (depending on the composition of the glass) [8].

The shrinkage process of the composite is controlled by the viscous flow of the glass and the reactions taking place at the alumina/glass interface [1]. During sintering, the alumina dissolves in the glass and changes its composition. As a consequence, instead of cristoballite, other phases, e.g. anortite, albite are formed in the interfacial layer [1–3, 10, 13–14]. The formation of cristoballite limits the efficiency of the ceramic substrate when used on circuit boards [16]. An adequate amount (min. 10–20 V/V%) of Al_2O_3 and sintering at 900 °C at least is required to prevent the

[1] Institute of Ceramic and Polymer Engineering, University of Miskolc
H-3515 Miskolc-Egyetemváros, Hungary
simon.andrea@uni-miskolc.hu
[2] Cerlux Ltd.
H-5900 Orosháza, Csorvási 68., Hungary
gabor.mucsi@cerlux.hu
[3] Institute of Ceramic and Polymer Engineering, University of Miskolc
H-3515 Miskolc-Egyetemváros, Hungary
fempityu@uni-miskolc.hu

formation of cristoballite. The intensity of crystallization increases with temperature, however, firing at 1,100 °C increases the proportion of amorphous phase again [2–3]. When firing at a temperature of about 700 °C, partial dissolution of Al_2O_3 in the low viscosity glass phase begins and continues up to 800 °C. The anortite phase begins to crystallize from the glass phase at 875 °C on the surface of the Al_2O_3 particles. The weight fraction of anortite increases with the temperature until it stabilizes at 950 °C or higher [6]. The addition of Al_2O_3 prevents the formation of cristoballite, because during sintering Al3 + ions diffuse into the glass and a strong bond can develop between $Al3^+/Al_2O_3$ and the Na^+/K^+ ions of the glass, leading to changes in the structure and composition of the glass [7, 16–17].

Because the aluminum ion acts as a glass former, its dissolution in the glass reduces the amount of non-bridging oxygen ions, which significantly increases the viscosity of the glass. This phenomenon becomes more and more significant with the decrease in the particle size of alumina. It follows that the dissolution of alumina in glass slows the shrinkage of glass/alumina composites [1]. Shrinkage is also significantly influenced by the firing temperature, when examined between 900–1,100 °C, it initially increases with the sintering temperature, reaches a maximum value around 1,000 °C then decreases. During liquid-phase sintering, the viscosity of the glass melt decreases with increasing temperature, which in turn increases the densification due to rearrangement and changes in surface tension [4, 12]. Above 1,000 °C, the dissolution of alumina becomes more and more intense, as a result of which the viscosity of the glass melt increases, which slows down the grain rearrangement required for shrinkage [4, 18–20].

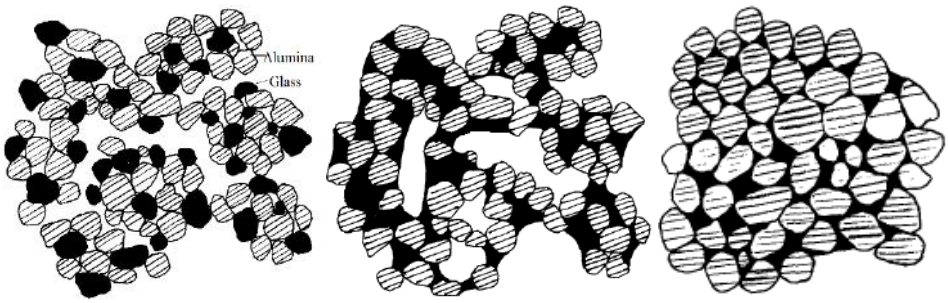

a) *b)* *c)*

Figure 1

Schematic representation of the sintering process: a) green (pressed) glass/alumina composite, b) less densified structure (partly due to early neck solidification), c) well-densified structure [4]

Early solidification of the neck results in the formation of a solid alumina network that slows densification at higher temperatures, as this structure is difficult to break up due to the very high viscosity of the alumina-rich, liquid glass phase *(Figure 1)* [4, 20]. The glass/ceramic composite begins to densify at the temperature where the viscosity of the glass phase decreases sufficiently, i.e. where the glass melt is formed,

since above this temperature the viscous flow promotes further sintering [6, 21–23]. According to other studies, maximum shrinkage can be achieved by sintering between 800–900 °C, and the density of the fired composites decreases by increasing the temperature further [9]. According to Kumar et al. [14], the sintering temperature should be below 1,050 °C to reduce the excess solubility of Al_2O_3 in the glass.

In summary, several aspects must be taken into account when determining the appropriate firing temperature. Firstly, the firing temperature of a material designed for LTCC (low temperature cofired ceramic) application should be below 950 °C in order not to exceed the melting point of the built-in metal parts (e.g. silver – 961 °C). Secondly, at least 800 °C is required for the complete removal of the organic components [8]. This temperature range also limits the composition of the adequate glasses. Glasses with low softening point (e.g. borosilicate) cannot be used, or at least not on themselves, only in combination with an other glass having a high softening point.

The optimal composition for the glass-ceramic composites was set in preliminary experiments. In this research work, the optimal firing temperature, which fulfil the main requirements for the glass-ceramic composites, was investigated. First, the temperature should be below 1,000 °C to avoid the excess solubility of Al_2O_3 in the glass. On the other hand, it has to ensure the appropriate physical and mechanical properties. To this end, scanning electron microscopy (SEM), X-ray diffraction (XRD), porosity (Archimedes method), thermal conductivity, compressive and flexural strength tests were performed on the fired samples.

1. MATERIALS AND METHODS

1.1. Sample preparation

Alumina (Elektrokorund, IMERYS), glass frit (FERROX Frits), paraffin and oleic acid were used to prepare the glass/ceramic composites. The powder mixture consisted of a 3 : 2 alumina and glass. The feedstock contained the base and the binding materials in 4 : 1 ratio. The injection mass was pre-heated in a direct mixer to 80 °C. Samples with different shapes and geometrical dimensions corresponding to the required tests were produced on Cerlux Ltd.'s self-developed, low-pressure injection moulding equipment. The pressure and the temperature of the injection moulding was 6 bar and 70 °C, respectively. Dimensions of the green, injection moulded samples are listed in *Table 1*.

Table 1

Dimensions of the green samples

Test sample	Diameter, mm	Height, mm	Width, mm	Length, mm
Compressive strength	10	11		
Flexural strength		6	6	100
Thermal conductivity	30	12		

Binder removal was accomplished at 650 °C in a 48-hour heat treatment cycle, in a natural gas furnace. The samples were fired at a maximum temperature of 850–900–950–1,000–1,050–1,100 °C in a Nabertherm HT 40/18 laboratory furnace, at a heating rate of 60 °C/hour.

1.2. Test methods

The particle size distribution of the alumina and glass frit was determined with a Horiba LA-950 laser granulometer. The phases of the raw materials and the fired specimens were identified by a Rigaku Miniflex II (Cu Kα, 2θ 3–90°) tabletop X-ray diffractometer, with a PDXL2 software to evaluate the results. The Rietveld complete profile fitting procedure was used to quantify the phases. The chemical composition and the surface morphology of the materials was measured using a ZEISS scanning electron microscope equipped with an EDAX detector. The specimens suitable for flexural and compressive strength tests were made in different geometries in an injection moulding tool. Columns were used for the former and cylindrical samples for the latter. Strength measurements were made with an Instron 5,560 universal tensile-pressing equipment. The porosity of the products was calculated from the water absorption test, in which the samples were boiled for 3 hours then soaked for 24 hours. All measurements requiring statistical evaluation were performed on at least 20 samples. Thermal conductivity tests were conducted on cylindrical samples with a polished surface and a diameter of 30 mm. C-Therm TCi thermal conductivity device operating on the principle of the Modified Transient Plane Source (MTPS) technique was used. Measurements were performed at room temperature.

2. RESULTS

2.1. Raw materials

Based on the X-ray examinations performed, the alumina consists mainly of corundum (Al_2O_3), with small amounts of diaoyudaoite ($NaAl_{11}O_{17}$) and hibonite ($CaAl_{12}O_{19}$), which are artificial minerals formed during corundum production. The frit is completely amorphous.

Table 2

Oxide composition and particle sizes of the raw materials

***Oxide composition*, wt%**								
	Na_2O	***MgO***	***Al_2O_3***	***SiO_2***	***ZrO_2***	***K_2O***	***CaO***	***ZnO***
Alumina	0.8		98.78				0.42	
Frit	2.47	2.69	6.21	58.28	8.78	2.78	11.10	7.70
Particle size, µm								
	D90	***D50***	***D10***	***Aver-age***	***Me-dian***			
Alumina	43.9	17.67	7.89	22.65	17.67			
Frit	22.54	10.52	4.34	12.33	10.50			

Table 2 shows the oxide composition and particle size distribution of the raw materials. *Figure 2* represents the initial morphology of the materials. Alumina and frit are characterized by polyhedral particle shapes, both in terms of coarse and finer fractions.

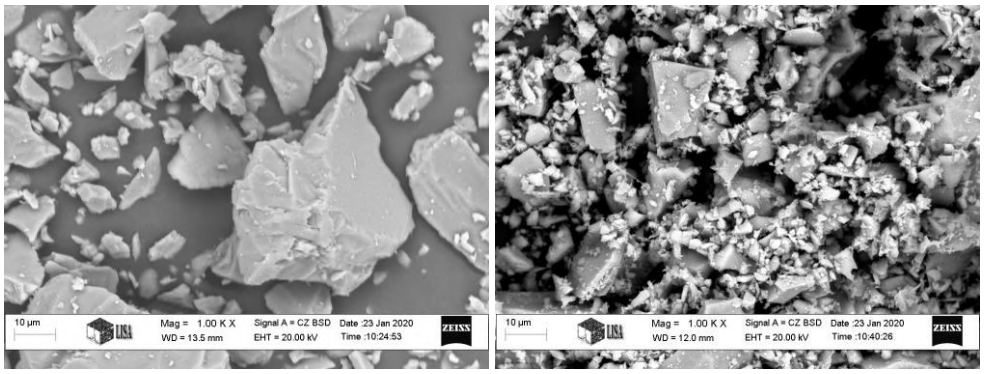

Figure 2
SEM micrographs of alumina and frit (M = 1,000×)

2.2. The effect of the firing temperature

Figure 3 shows the compressive and flexural strength of alumina/glass composites fired at 850–1,100 °C.

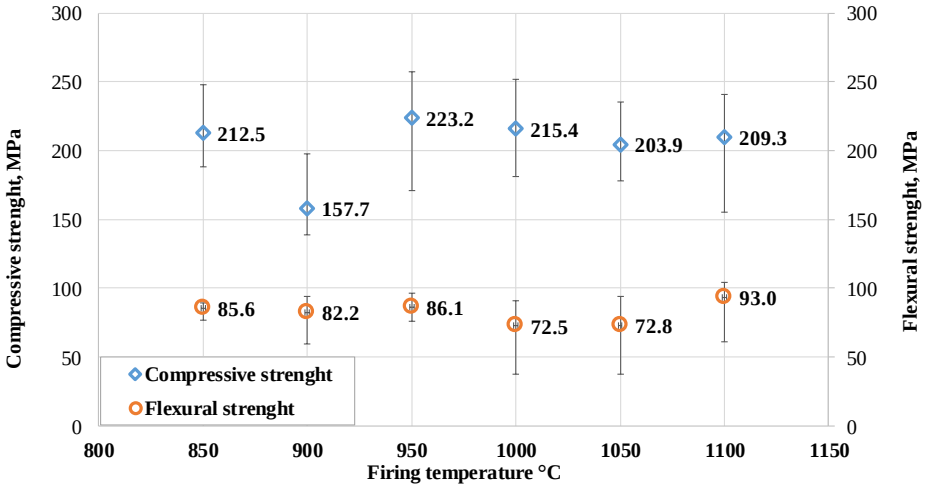

Figure 3
Compressive and flexural strength of the samples

The effect of the firing temperature is not clear as the standard deviation of the results is quite large. The samples fired at 950 °C had the best combination of flexural and compressive strength. The compressive strength slightly reduces by increasing the firing temperature, but

the smallest temperature produced similar results. The samples fired at 900 °C presented the lowest strength.

Table 3

Average values of shrinkage, water absorption and thermal conductivity of the fired samples

	Firing temperature					
	850 °C	*900 °C*	*950 °C*	*1000 °C*	*1050 °C*	*1100 °C*
Shrinkage in diameter, %	3.98	3.92	3.84	4.06	4.00	3.94
Shrinkage in length, %	5.42	4.08	5.41	5.37	5.20	5.05
Average shrinkage, %	4.61	4.00	4.62	4.71	4.60	4.49
Water absorption, %	11.00	10.8	10.7	11.00	11.4	11.20
Thermal conductivity, W/mK	1.86	2.00	2.01	1.95	1.87	2.11

Figure 4 and *Table 3* represents the results of the density, porosity and shrinkage, water absorption, thermal conductivity tests, respectively. The shrinkage in diameter did not change significantly, the difference between the sample sintered at 950 °C and 1,000 °C was only 5.5%. Along the height and length, samples sintered at 900 °C presented the lowest shrinkage. There is a similar trend in the values of water absorption and thermal conductivity. The density was not affected by temperature. The porosity value was the lowest at 950 °C, but it also differed only by 5.5% from the maximum value measured at 1,050 °C.

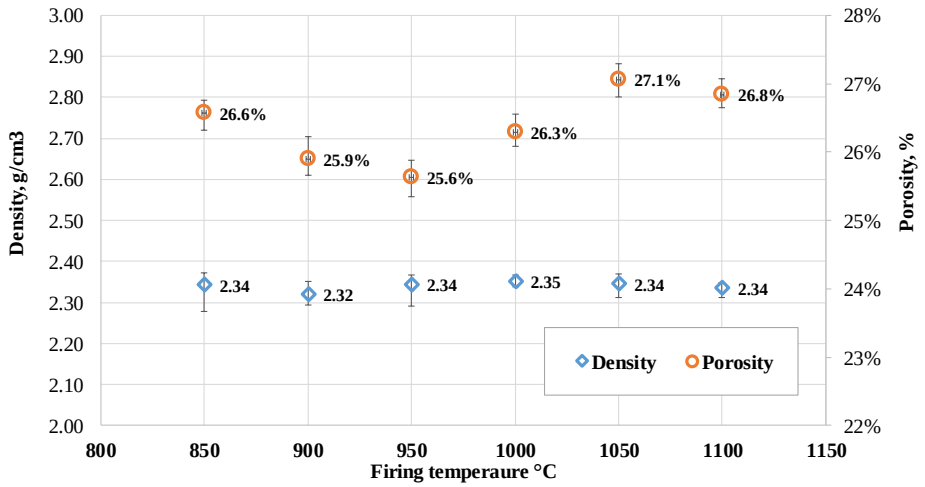

Figure 4

Density and porosity of the samples in the function of temperature

2.3. Morphology and phase analysis

Scanning electron micrographs of the fracture surface *(Figure 5)* show a pore system remained after the debinding. The pores, having a maximum size of a few 10 μm,

are inhomogeneously distributed. These micrographs underline the large variance in the strength data and the significant porosity values as well. Increasing the firing temperature did not change significantly the morphology of the fracture surfaces.

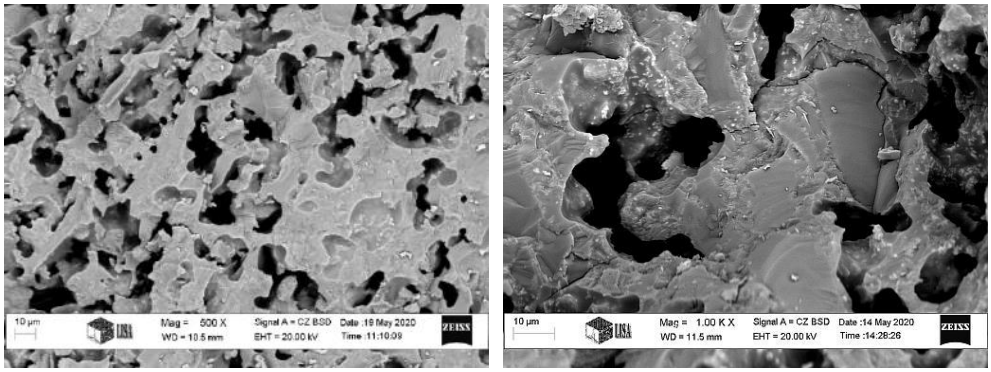

a) *b)*

Figure 5

Microstructure of the alumina/glass composites sintered at 850 °C and 1,100 °C

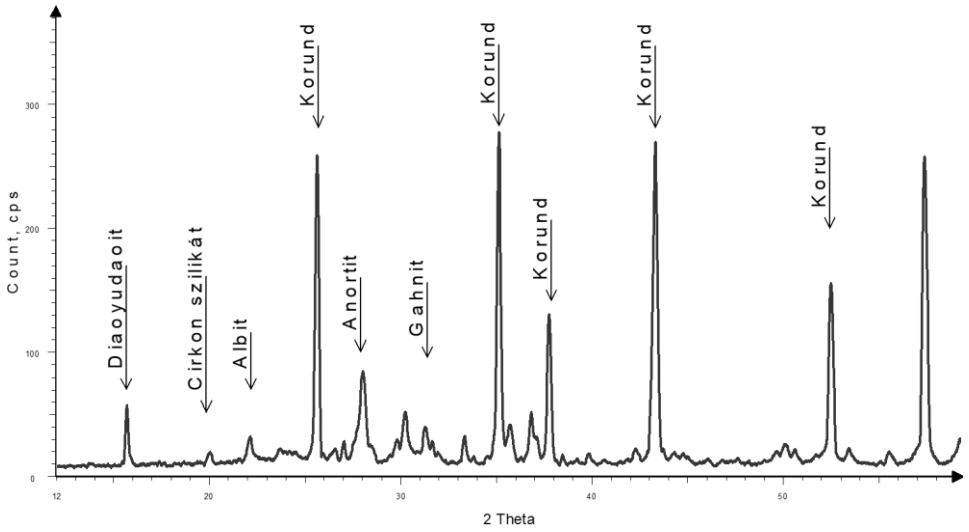

Figure 6

Phases of the samples fired at 850 °C

Based on the X-ray diffraction analysis, from the mixture of the starting crystalline corundum phase and the amorphous fritted glass phase, mainly crystalline phases are present in the sample fired at 850 °C, with an amorphous content of about 5%. The phases identified were corundum, albite, anortite, zirconium silicate, gahnite, and

diaoyudaoite *(Figure 6)*. These phases remain up to 1,100 °C, but their amount varies slightly. In the sample sintered at 900 °C, the frit already started to melt, which increases the amount of amorphous phase to 22 wt%. It decreases to 16 wt% at 950 °C, indicating an increase in the proportion of the crystalline phase.

CONCLUSIONS

In this research, the effect of firing temperature on the properties of alumina/glass composites was studied. The melting behaviour of the frit and the debinding process affect mostly the main (non-electrical) properties of the samples. In the sintering range of 850–1,100 °C, the tested characteristics did not change significantly. The samples sintered at 900 °C had the lowest compressive strength and shrinkage. Based on the above measurements, the tested material can be fired even at 850 °C, since the higher firing temperatures do not provide significantly better properties.

ACKNOWLEDGMENTS

This research work is co-financed by the European Social Fund and the Government of Hungary within the framework of the project GINOP-2.1.2-8-1-4-16-2017-00219. The authors thank Árpád Kovács (Institute of Physical Metallurgy, Metal Forming and Nanotechnology) for the SEM micrographs and EDAX analyzes, dr. Tamás Mikó (Institute of Physical Metallurgy, Metal Forming and Nanotechnology) for his help in the compressive strength tests, Nora Papne Halyag (Faculty Of Earth Science And Engineering) for the laser granulometry tests, Károly Gál for the water absorption measurements, and Ildikó Tasnádi for the help in the flexural strength tests.

REFERENCES

[1] Fang, Yu-Ching, Jean, Jau-Ho (2007). Effects of Alumina on Densification of a Low-Temperature Cofired Crystallizable Glass+Alumina System. *Japanese Journal of Applied Physics*, Vol. 46, No. 6A, pp. 3475–3480.

[2] Jean, Jau-Ho, Fang, Yu-Ching, Dai, Steve X., Wilcox, David L. (2003). Effects of Alumina on Devitrification Kinetics and Mechanism of K_2O–CaO–SrO–BaO–B_2O_3–SiO_2 Glass. *Jpn. J. Appl. Phys*., Vol. 42, Part 1, No. 7A, pp. 4438–4443., July 2003.

[3] Dursun, Gülsüm Meryem, Duran, Cihangir (2019). Glass alumina composites for functional and structural applications. *Ceramics International*, 45, pp. 12550–12557.

[4] Kumar, K. P., Ramesh, R., Seshan, K., Prasad, V. C. S. (1990). Liquid-phase sintering of lead borosilicate glass-alumina composite *Journal of Materials Science Letters*, 9, pp. 663–665.

[5] Makarovič, Kostja, Meden, Anton, Hrovat, Marko, Holc, Janez, Benčan, Andreja, Dakskobler, Aleš, Belavič, Darko, Kosec, Marija. *The Effect of the*

Firing Temperature on the Properties of LTCC. https://pdfs.semanticscholar.org/742a/ 32f8acadf54f52368387987f9f5f3584e38a.pdf, Accessed on 16/03/2020.

[6] Suprapedi, Muljadi, Ramlan (2018). Effect of Addition of Amorphous Glass (Soda Lime Glass) on Sintering Process and Properties of Alumina Ceramics. *IOP Conf. Series: Journal of Physics: Conf. Series*, 1120, p. 012038.

[7] Lima, M. M. R. A., Monteiro, R. C. C., Graça, M. P. F., Ferreira da Silva, M. G. (2012). Structural, electrical and thermal properties of borosilicate glass–alumina composites. *Journal of Alloys and Compounds*, 538, pp. 66–72.

[8] Lima, M. M. R. A., Monteiro, R. C. C. (2006). Shrinkage Behaviour of Borosilicate Glass-Al_2O_3 Composites during Isothermal Sintering. *Materials Science Forum*, Vol. 514–516, pp. 648–652.

[9] Li, Bo, Xu, Yang, Zhang, Shuren (2015). The Size-Effect of Al_2O_3 on the Sinterability, Microstructure and Properties of Glass-Alumina Composites. *Glass Physics and Chemistry*, Vol. 41, No. 5, pp. 503–508.

[10] Margarida, M., Lima, R. A., Monteiro, C. C. (2008). Viscous Sintering in a Glass-Alumina System. *Materials Science Forum*, Vol. 587–588, pp. 143–147.

[11] Higby, I., Shelby, James E. (1983). Properties of Glass/Alumina Composites. *Communications of the American Ceramic Society*, December 1983, C-229.

[12] Zhu, Qingshan, de With, Gijsbertus, Dortmans, Leonardus J. M. G., Feenstra, Frits (2005). Near net-shape fabrication of alumina glass composites. *Journal of the European Ceramic Society*, 25, pp. 633–638.

[13] Xia, Qin, Zhong, Chao-Wei, Luo, Jian (2014). Low temperature sintering and characteristics of K_2O–B_2O_3–SiO_2–Al_2O_3 glass/ceramic composites for LTCC applications. *J. Mater. Sci: Mater. Electron.*, 25, pp. 4187–4192.

[14] Kumar, K. P., Prasad, V. C. S., Mukherjee, P. S., Mukunda, P. G. (1989). Behaviour of Lead Borosilicate Glass/Alumina Composite in the Temperature Range 900–1100 °C. *Materials Science and Engineering*, B5, pp. 1–4.

[15] SebastianM. T., Jantunen, H. (2008). Low loss dielectric materials for LTCC applications: a review. *International Materials Reviews*, Vol. 53, No. 2, pp. 57–90.

[16] El-Kheshen, A. A. (2003). Effect of alumina addition on properties of glass/ ceramic composite. *British Ceramic Transactions*, Vol. 102, No. 5, pp. 205–209.

[17] Jean, Jau-Ho, Chang, Chia-Ruey, Chang, Ruey-Ling, Kuan, Tong-Hua (1995). Effect of alumina particle size on prevention of crystal growth in low-k silica dielectric composite. *Materials Chemistry and Physics*, 40, pp. 50–55.

[18] Monteiro, R. C. C., Lima, M. M. R. A. (2003). Effect of compaction on the sintering of borosilicate glass/alumina composites. *Journal of the European Ceramic Society*, 23, pp. 1813–1818.

[19] Palanisamy, P., Sarma, D. H. R., West, R. W. (1985). Liquid-Phase Sintering in Thick-Film Resistor Processing. *J. Am. Ceram. Soc*., 68, 1, C215–216.

[20] Shiou, B. I., Hsu, W.-Y., Duh, J.-G. (1988). Fabrication and electrical behavior of liquid phase sintered zirconia. Ceramics International.*Ceram. Int.*, 14, p. 7.

[21] Kemethmüller, S., Hagymasi, M., Stiegelschmitt, A., Roosen, A. (2007). Viscous Flow as the Driving Force for the Densification of Low-Temperature Co-Fired Ceramics. *Journal of the American Ceramic Society*, 90 (1), pp. 64–70.

[22] Cole, S., Wellfair, G. (1974). High temperature viscosity control in multilayer glasses – a new concept. *Proceedings of the ISHM Symposium*, Boston, Massachusetts, pp. 25–34.

[23] Simon, A., Lipusz, D., Györffy, B., Kristály, F., Gácsi, Z. (2013). Properties of Al2O3-glass composites. In: Meo, M. (ed.). *9th International Conference on composite science and technology*, DEStech Publications, pp. 702–711.

Materials Science and Engineering, Volume 45, No. 1 (2020), pp. 271–283.
DOI: 10.32974.mse.2020.028

COMPARISON OF SIMPLIFIED AND FINITE ELEMENT ANALYSIS ON COLD FLAT ROLLING

MÁTÉ SZŰCS[1] – KRISTÓF BOBOR[2] – GÁBOR SZABÓ[3] – GYÖRGY KRÁLLICS[4] – SÁNDOR KOVÁCS[5]

Abstract: A simplified calculation method was developed to evaluate experimental rolling processes in order to determine the characteristic parameters of velocity and deformation field of cold-rolled material. The calculation allows us to make an analysis of 3D material flow as well when a significant widening of material occurs during the forming process. Based on the measured data (rolling force and rolling torque) the coefficient of friction and the neutral angle for the deformation zone was determined. Using these parameters, the mechanical fields with a higher accuracy can be determined. Experimental rolling was analyzed by finite element calculation similarly. After comparing the two models, we found that the mechanical fields differ slightly. The simplified calculation procedure is also suitable for testing multi-pass rolling. The method also provides input data of the texture calculation (velocity gradient tensor of a selected material point) as a function of time that significantly expands the application possibilities.

Keywords: cold flat rolling, numerical analysis, deformation field

Table 1
Nomenclature

F_{roll}	rolling force	R	radius of the roll
F_f	force at the exit	F_0	force at the entry
M_{roll}	torque	R'	radius of the deformed roll
μ	coefficient of friction	α	rolling angle
S_f	forward slip	α_0	bite angle
$\bar{\sigma}$	mean flow stress of material	α_n	neutral angle

[1] Institute of Physical Metallurgy, Metal Forming and Nanotechnology, University of Miskolc
H-3515 Miskolc-Egyetemváros, Hungary
femszmat@uni-miskolc.hu

[2] Department of Materials Science and Engineering, Budapest University of Technology and Economics, H-1111 Budapest, XI. Bertalan L. u. 7. Build. MT
bobor@eik.bme.hu

[3] Institute of Metallurgy, University of Miskolc
H-3515 Miskolc-Egyetemváros, Hungary
szabogabor@uni-miskolc.hu

[4] Institute of Physical Metallurgy, Metal forming and Nanotechnology
H-3515 Miskolc-Egyetemváros, Hungary
femkgy@uni-miskolc.hu

[5] Institute of Physical Metallurgy, Metal Forming and Nanotechnology, University of Miskolc
H-3515 Miskolc-Egyetemváros, Hungary
femkovac@uni-miskolc.hu

b	strip width	l_d	arc of length
h	strip thickness	v_1	horizontal speed of the material
h_0	initial thickness of the strip	v_0	entry speed of the material
h_f	final thickness of the strip	v_f	speed at the exit
h_n	thickness at the neutral plane	v_{1n}	horizontal speed at the neutral plane
Δh	thickness reduction	v_{roll}	roll speed
r	reduction, $(h_{entry}-h_{exit})/h_{entry}$	x_{1n}	horizontal coo. of the neutral point
E	Modulus of elasticity (roll)	σ_{11}	normal stress in the horizontal dir.
ν	Poisson's ratio (roll)	p	pressure
u_n	Components of material point displacement, $n = 1…3$	X_n	Initial coordinates of material point, $n = 1…3$

INTRODUCTION

There are several numerical methods to simulate the rolling process and the calculational results obtained under the condition of plane strain mechanically is a precise approximation for the rolling of wide strip. Probably, the most commonly used calculation techniques are the slab method [1], [2], the upper bound method [3], [4], and the finite element analysis [5], [6]. Each of them provides good numerical results, but the latter one is very useful even to solve three dimensional and other complex problems. The friction between rolls and sheet is defined usually by the Coulomb's [7] or Kudo's shear friction model [8] and the mostly used formula for roll flattening was proposed by Hitchcock [9].

In the literature the rolled sheet is considered mostly as an isotropic material [10], [11]. But a relatively few articles deal with the modeling of anisotropic behavior [12].

The cold-rolled product is generally defined as a rigid-plastic [13] or elastic-plastic material [14]. In many solutions the roll is treated as a rigid type contact body [24] but examples calculating with elastic roll [15] can be found as well. More complex three-dimensional solutions are also used to study the rolling gap and deformation zone within. In such a complex study, the local variables of rolling are analyzed in detail not only in longitudinal- but the transverse direction as well [16].

In present work, we compared the quantities of deformation zone. The flow of material passing through the rolling gap was described by two numerical method.

1. EXPERIMENTAL ROLLING

The experimental rolling of aluminum alloy was performed by using a VonRoll rolling mill equipped with two work rolls. *Table 2* shows the chemical composition of alloy. The roll diameter and width were 220 mm and 200 mm respectively, the

rolling speed was set to 15 or 28 m/min according to the specification of experimental plan.

Table 2

The chemical composition of aluminium alloy (wt%)

Cr	0.009
Cu	0.042
Fe	1.09
Mg	0.028
Mn	0.40
Si	0.16
Ti	0.008
Zn	0.043
Al	rest

Initial width and thickness of the hot rolled narrow strip material are respectively, b_0 = 100 mm and h_0 = 6.80 mm respectively, the initial temperature of cold rolling was 20 °C. A mineral oil based Cyndolube type mixture was applied which is commonly used in cold strip- and sheet rolling. The rolling force and torque were measured by sensors connected to an HBM PMX data acquisition system. The parameters of passes are detailed in *Table 3*, where the h_0 and h_f are the initial- and final thickness of material, the measured force and torque are designated by F_{roll} and M_{roll} respectively, while the $F_{roll,c}$ and $M_{roll,c}$ are the calculated data obtained after the finite element analysis of rolling.

Table 3

Reduction per pass and rolling parameters

Pass number	h_0 **(mm)**	h_f **(mm)**	F_{roll} **(kN)**	M_{roll} **(Nm)**	$F_{roll,c}$ **(kN)**	$M_{roll,c}$ **(Nm)**	v_{roll} **(m/min)**
1	6.80	5.23	243.43	2,736	310	2,350	15
2	5.23	3.80	293.18	3,250	340	1,950	15
3	3.80	2.74	292.85	2,760	310	1,600	28

The strain-, strain rate- and temperature dependent flow stress of the material is obtained by the JMatpro software, based on the chemical composition and the average grain size of material in its current state. The calculated data of flow stress was validated by the measured data of upsetting test of cylindrical specimen at room temperature and low strain rate.

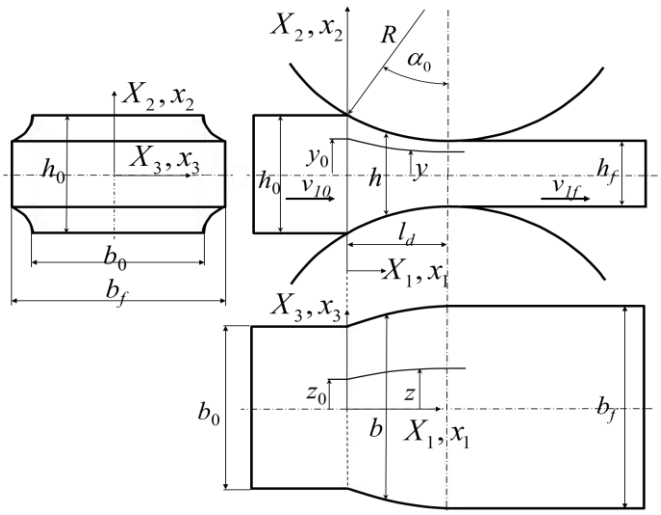

Figure 1
Schematic picture of rolling process

2. MODELLING OF ROLLING

2.1. Simplified mechanical analysis of cold rolling

The schema of rolling process illustrated by *Figure 1*. In the deformation zone the sheet material completely fills the gap between the rigid rolls and its size is expressed on the x_1, x_2 plane by the following equation:

$$h = 2R(1-\cos\alpha)+h_f \tag{1}$$

The arc length of rolling is:

$$l_d = \sqrt{R\Delta h+(\Delta h/2)^2},\ \Delta h = h_0 - h_f \tag{2}$$

Next equation describes the widening of the sheet

$$\Delta b = 2\frac{x_1}{l_d}(b_f - b_0) - \left(\frac{x_1}{l_d}\right)^2 (b_f - b_0),\ b = b_0 + \Delta b\,, \tag{3}$$

The quantity of $\Delta b_f = b_f - b_0$ is measured directly after the rolling pass or we can calculate with the following relationship:

$$\Delta b_f = \left(1+\frac{\Delta h}{h_0}\right)\mu\left(l_d - \frac{\Delta h}{2\mu}\right)\frac{\Delta h}{h_0} \tag{4}$$

where μ – Coulomb's coefficient of friction. The above equation doesn't consider the effect of front- and back tension on the material. Any material points on the sur-

face have an initial coordinate of $X_2 = \pm h_0 / 2$. The same material points' displacement along the vertical direction is given by $u_2 = \pm \Delta h /2 = (h_0 - h_f)/2$. The other coordinate of initial position on the edge is $X_3 = \pm b_0 / 2$. Due to the widening of material, the third component of displacement is $u_3 = \pm \Delta b /2 = (b_0 - b_f)/2$. Assuming a simplified mechanical schema:

a) u_2, u_3 displacement depends linearly on the x_2, x_3 coordinates
b) u_1 displacement only depends on x_1 coordinates (the cross-sectional planes perpendicular to the longitudinal axis remain planes even after the deformation)
c) the widening of sheet is homogeneous through the whole thickness, u_3, x_2 while u_2 is independent of x_3.

Based on the above mentioned, the components of displacement are the followings:

$$u_1 = u_1(x_1),\ u_2(x_1, x_2) = 0.5(h - h_0)\frac{2x_2}{h},\ u_3(x_1, x_3) = 0.5(b - b_0)\frac{2x_3}{b} \tag{5}$$

One of the main characteristics of the rolling is the neutral angle α_n besides the bite angle α_0. The approximate solution without using any tension is expressed by the next formula [17]:

$$\alpha_n = \arcsin\left(0.5\sin\alpha_0 - \frac{1-\cos\alpha_0}{2\mu}\right) \tag{6}$$

The bite angle is determined by

$$\alpha_0 = \arccos\left(1 - \frac{h_0 - h_f}{2R}\right) \tag{7}$$

The roll velocity, v_{roll} is a known parameter, but we don't know velocity of the material at entry v_0. The relationship between them is as follows:

$$v_0 = v_{roll}\frac{\cos\alpha_n}{h_0}h_n,\ h_n = h_f + (1 - \cos\alpha_n)2\mathrm{R} \tag{8}$$

Using the relationship between inverse deformation – and displacement gradient

$$\frac{\partial \mathbf{X}}{\partial \mathbf{x}} = \mathbf{I} - \frac{\partial \mathbf{u}}{\partial \mathbf{x}},\ \frac{\partial X_i}{\partial x_k} = \delta_{ik} - \frac{\partial u_i}{\partial x_k} \tag{9}$$

Based on the displacement field, the calculated form of the inverse deformation – and displacement gradient tensors are the followings

$$\mathbf{F}^{-1} = \frac{\partial \mathbf{X}}{\partial \mathbf{x}} = \begin{bmatrix} \frac{hb}{h_0 b_0} & 0 & 0 \\ -\frac{h' h_0}{h^2}x_2 & \frac{h_0}{h} & 0 \\ -\frac{b' b_0}{b^2}x_3 & 0 & \frac{b_0}{b} \end{bmatrix},\ \mathbf{F} = \frac{\partial \mathbf{x}}{\partial \mathbf{X}} = \begin{bmatrix} \frac{h_0 b_0}{hb} & 0 & 0 \\ \frac{h_0 b_0 h'}{h^2 b}x_2 & \frac{h}{h_0} & 0 \\ \frac{h_0 b_0 b'}{hb^2}x_3 & 0 & \frac{b}{b_0} \end{bmatrix},\ h' = \frac{dh}{dx_1},\ b' = \frac{db}{dx_1} \tag{10}$$

For the mechanical evaluation of rolling process, it is necessary to know the strain variables. In the field of forming technologies, the Hencky's logarithmic strain tensors are commonly used. To get these quantities, the next steps are required to perform. After the expression the square of the right-side deviator tensor, **C** by the deformation gradient, we get the formula of $\mathbf{U}^2 = \mathbf{F}^T \cdot \mathbf{F} = \mathbf{C}$. Then the logarithmic strain tensor described by the next equation.

$$\mathbf{H} = \mathbf{R} \quad ln(\mathbf{U})\mathbf{R}^T \tag{11}$$

where $\boldsymbol{R}$ – is the rotation tensor, $\mathbf{U}$ – is right stretch tensor. Beside the strains the components of velocity field must also be known. In the present problem, we assume that the rolling is in a steady state. Then, the relationship between the Euler's velocity field and the derivatives of the inverse mapping function in general and in the simplified model is as follows:

$$\begin{aligned}
v_1 &= v_0\left(\frac{\partial X_2}{\partial x_2}\frac{\partial X_3}{\partial x_3} - \frac{\partial X_2}{\partial x_3}\frac{\partial X_3}{\partial x_2}\right), \quad v_1 = v_0\left(\frac{\partial X_2}{\partial x_2}\frac{\partial X_3}{\partial x_3}\right) = v_1(x_1) \\
v_2 &= v_0\left(\frac{\partial X_3}{\partial x_1}\frac{\partial X_2}{\partial x_3} - \frac{\partial X_2}{\partial x_1}\frac{\partial X_3}{\partial x_3}\right), \quad v_2 = v_0\left(-\frac{\partial X_2}{\partial x_1}\frac{\partial X_3}{\partial x_3}\right) = v_2(x_1, x_2) \\
v_3 &= v_0\left(\frac{\partial X_2}{\partial x_1}\frac{\partial X_3}{\partial x_2} - \frac{\partial X_2}{\partial x_2}\frac{\partial X_3}{\partial x_1}\right), \quad v_3 = v_0\left(-\frac{\partial X_2}{\partial x_2}\frac{\partial X_3}{\partial x_1}\right) = v_3(x_1, x_3)
\end{aligned} \tag{12}$$

Knowing the velocity field, the velocity gradient tensor is the following:

$$\mathbf{L} = \frac{\partial \mathbf{v}}{\partial \mathbf{x}} = \begin{bmatrix} \frac{\partial v_1}{\partial x_1} & \frac{\partial v_1}{\partial x_2} & \frac{\partial v_1}{\partial x_3} \\ \frac{\partial v_2}{\partial x_1} & \frac{\partial v_2}{\partial x_2} & \frac{\partial v_2}{\partial x_2} \\ \frac{\partial v_3}{\partial x_2} & \frac{\partial v_3}{\partial x_2} & \frac{\partial v_3}{\partial x_2} \end{bmatrix} = \begin{bmatrix} \frac{\partial v_1}{\partial x_1} & 0 & 0 \\ \frac{\partial v_2}{\partial x_1} & \frac{\partial v_2}{\partial x_2} & 0 \\ \frac{\partial v_3}{\partial x_1} & 0 & \frac{\partial v_3}{\partial x_3} \end{bmatrix}, \tag{13}$$

The velocity gradient tensor's symmetrical part is the strain rate tensor, while the asymmetrical part is the spin tensor.

$$\boldsymbol{\xi} = \frac{1}{2}\left(\mathbf{L} + \mathbf{L}^T\right) = \begin{bmatrix} \frac{\partial v_1}{\partial x_1} & \frac{1}{2}\frac{\partial v_2}{\partial x_1} & \frac{1}{2}\frac{\partial v_3}{\partial x_1} \\ \frac{1}{2}\frac{\partial v_2}{\partial x_1} & \frac{\partial v_2}{\partial x_2} & 0 \\ \frac{1}{2}\frac{\partial v_3}{\partial x_1} & 0 & \frac{\partial v_3}{\partial x_3} \end{bmatrix}, \tag{14}$$

The total accumulated strain is:

$$\bar{\varepsilon} = \int_0^t \xi_{eq}\, dt = \int_0^{x_1} \frac{\xi_{eq}}{v_1}\, dx_1 + \Delta\bar{\varepsilon}_\Gamma + \bar{\varepsilon}_{prev} \tag{15}$$

where $\Delta\bar{\varepsilon}_\Gamma$ – the strain resulted by velocity discontinuity on boundary, at the entry $\bar{\varepsilon}_{prev}$ – equivalent strain in previous pass. The integration must be solved along the trajectory of the selected material point (**r**).

$$\mathbf{r}^T = \begin{bmatrix} x_1 & \frac{y_0}{h_0} h(x_1) & \frac{z_0}{b_0} b(x_1) \end{bmatrix} \tag{16}$$

The strain on boundary of discontinuity is described by the next relationship:

$$\Delta\bar{\varepsilon}_\Gamma = \left. \frac{\sqrt{v_2^2 + v_3^2}}{v_0\sqrt{3}} \right|_{\text{entry-cross section}} \tag{17}$$

In the above calculations, we assumed that the roll is a rigid body. But under the real conditions of rolling, the rolls deformed elastically and change its sizes due to the force acting on the surface. According to Hitchcock [18] the loaded radius of roll *R'* can be expressed by the following formula:

$$R' = R\left[1 + \frac{16\left(1-\nu^2\right)}{\pi E} \cdot \frac{F_{roll}}{b_{ave}\Delta h}\right] \tag{18}$$

Since we know the force F_{roll}, the reduction in height Δh, the average width of material b_{ave} and the elastic properties of roll in any pass, then the loaded roll radius is predictable.

The coefficient of friction is an input parameter of mechanical model that is calculated on the basis of measured rolling force and torque [19].

$$\mu = \frac{\frac{F_{roll}}{\bar{\sigma}\sqrt{R'\Delta h}} - 1.08 + 1.2\left(1 - \frac{h_f}{h_0}\right)}{1.79\left(1 - \frac{h_f}{h_0}\right)\sqrt{\frac{R'}{h_0}}} \tag{19}$$

To use the relationship above, it is necessary to know the flow stress equation of the given material. So, the coefficient of friction can be calculated. In addition, the neutral angle is also an important parameter that we can determine by using the *Equation (6)*.

Based on the JMatpro material database the flow stress is available in a wide range of strain, strain rate and temperature. For the cold rolling problem, we made a simplified material model by using the Johnson-Cook equation [20] that describes the flow stress in a smaller range of parameters.

$$\sigma_y = \left(A + B\bar{\varepsilon}^n\right)\left(1 + C\ln\dot{\varepsilon}^*\right)\left(1 - T^{*m}\right) \tag{20}$$

where $\dot{\varepsilon}^* = \dot{\varepsilon} / \dot{\varepsilon}_{ref}$, $T^* = \frac{T - T_{ref}}{T_m - T_{ref}}$, $\dot{\varepsilon}_{ref}, T_f, T_m$ –respectively the reference strain rate, the reference temperature, the melting point of material, *A*, *B*, *n*, *C* and *m* are the

material parameters that were determined by a technique detailed in [21]. The parameters are valid in the range of $0 \le \bar{\varepsilon} \le 4,\ 0.1 \le \dot{\varepsilon} \le 100/s,\ 20+273 \le T \le 140+273K$ The parameter values of *Equation (22)* are the followings *A = 27.25, B = 176.20, n = 0.317, C = 0.0114, m = 1.173*.

2.2. Finite element model

The rolling process was defined as a two-dimensional problem since we observed a minimal widening of material after experimental rolling. The friction condition and velocity are the same on both contact surface between roll and sheet, so the rolling process has a symmetry in thickness direction.

The deformable body of sheet included approximately 4,000 finite elements, and the average element size was 0.2 mm. The element type was four node, quadrilateral with linear interpolation. For the calculations we used the MSC.Marc software that simulated the process with constant time steps applying multifrontal spars solver algorithm with updated Lagrange description. The model included a rigid roll and the strip defined as a linear elastic-nonlinear plastic body. The elastic, plastic and the thermal properties of aluminium alloy were given by JMatPro software which considers the chemical composition and the microstructure of material as initial conditions. For the numerical simulation, the material was substituted with 50 mm long segment of the real specimen. This length is proper to get a steady state of rolling and at the same the calculational time is also acceptable. The initial geometry of finite element model is illustrated in *Figure 2*.

The initial temperature of specimen was 20 °C and it assumed that the temperature rise is low during the forming process and it influences the flow stress material only a small extent. In addition, we assumed that the material cools down to 20 °C after each pass of rolling. The Coulomb model was applied for the calculation of friction between contact bodies. The coefficient of friction was set to μ = 0.2 for the first three passes that average value was determined by the simplified model. The technological data of the passes and calculation results are listed previously in *Table 3*.

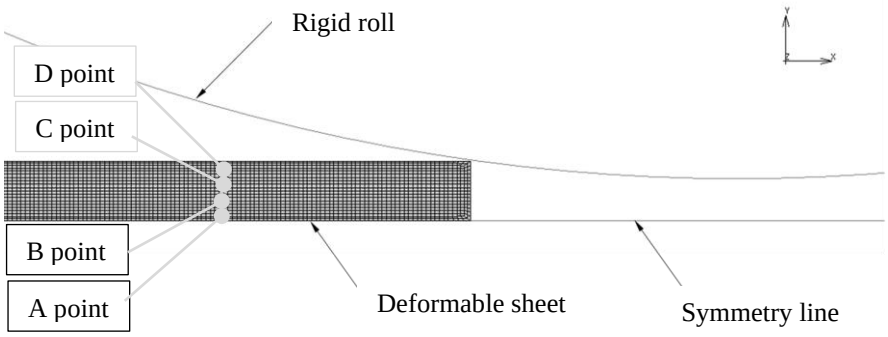

Figure 2
Initial geometry and finite element model of the first pass, and analysed material points through the half-thickness of material

The strain variables were analysed through the motion of four different material points *(Figure 2)*, the initial y coordinate of point A is zero from the symmetry line, the point B, C and D coordinates are 0.94, 1.90 and 3.15 mm respectively from the symmetry line.

3. CALCULATION RESULTS

Numerical calculations were performed for three consecutive passes, and in all three steps we plotted the deformation gradient components, the equivalent logarithmic deformation, and the cumulative total equivalent plastic strain in the investigated material points (A, B, C and D) along the arc length. The value of total equivalent plastic strain is the integral of stepwise increments of plastic deformation for the forming time, as it is expressed by *Equation (15)*, while the equivalent logarithmic strain characterizes the mechanical state of the material at a moment of rolling.

The results of the simplified and finite element calculations are summarized in the following diagrams. The components of the deformation gradient calculated for the first pass are shown in *Figures 3* and *4*, the curves refer to material points A and D, the arc length is indicated on the horizontal axis.

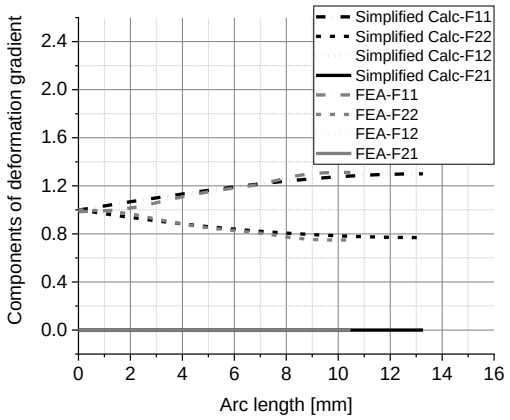

Figure 3
Deformation gradient components as a function of arc length (first pass, point A)

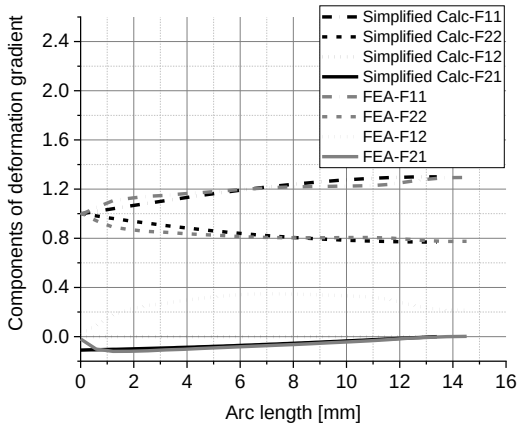

Figure 4
Deformation gradient components as a function of arc length (first pass, point D)

The *Figures 5* and *6* show the curves of equivalent logarithmic strain and the cumulative plastic strain as a function of arc length for the first and third passes of rolling.

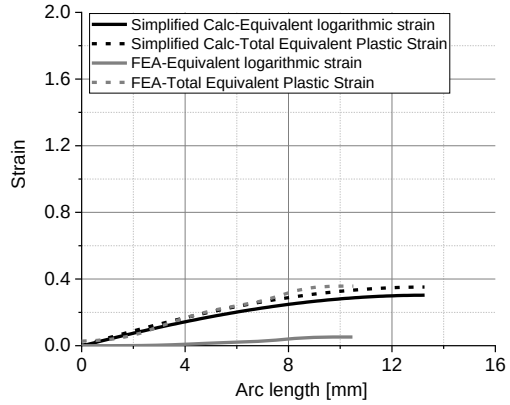

Figure 5
Equivalent logarithmic and total plastic strain (first pass, point A)

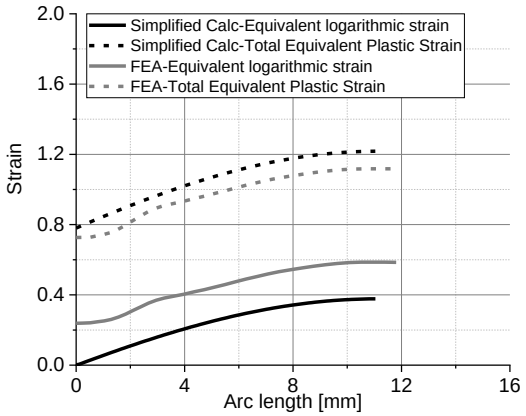

Figure 6
Equivalent logarithmic and total plastic strain (third pass, point A)

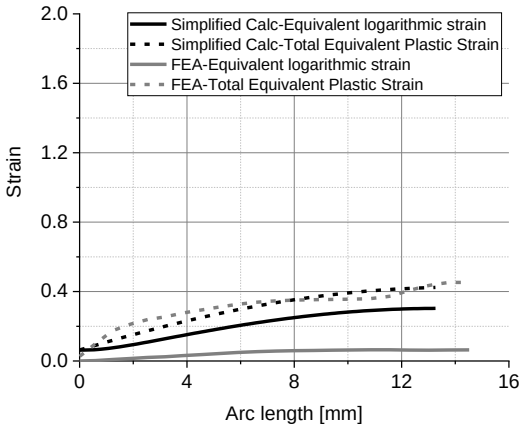

Figure 7
Equivalent logarithmic and total plastic strain (first pass, point D)

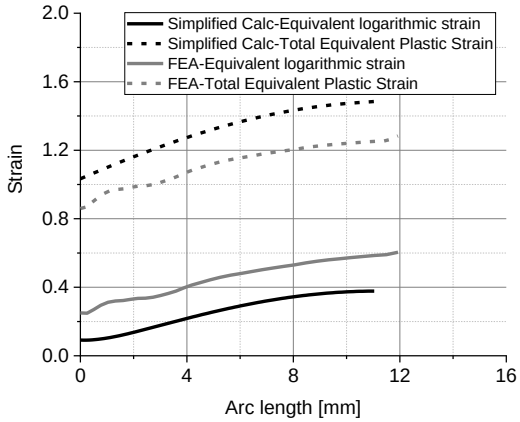

Figure 8
Equivalent logarithmic and total plastic strain (third pass, point D)

CONCLUSION

The simplified mechanical model describes well the field of deformation during rolling. The finite element calculation results support this. The coefficient of friction was obtained by the simplified calculation and it was an input data of finite element simulation. Both models were suitable for calculating the local velocity gradient required for texture calculation.

ACKNOWLEDGEMENTS

The described study was carried out as part of the EFOP-3.6.1-16-2016-00011 *Younger and Renewing University – Innovative Knowledge City – institutional development of the University of Miskolc aiming at intelligent specialisation* project implemented in the framework of the Széchenyi 2020 program. The realization of this project is supported by the European Union, co-financed by the European Social Fund. The present paper was supported through the National Research, Development and Innovation Office – NKFIH K119566 project and the new national excellence program of the Ministry of Human Capacities

REFERENCES

[1] Cawthorn, Christopher J., Loukaides, Evripides G., Allwood, Julian M. (2014). Comparison of analytical models for sheet rolling. *Procedia Engineering*, 81, pp. 2451–2456.

[2] Wang, H. Y., Li, X., Sun, J., Wang, Z. H., Zhao, D. W., Zhang, D. H. (2016). Analysis of sandwich rolling with two different thicknesses outer layers based on slab method. *International Journal of Mechanical Sciences*, 106, pp. 194–208.

[3] Shivpuri, R., Chou, P. C. (1989). Comparative study of slab, upper bound and finite element methods for predicting force and torque in cold rolling. *Int. J. Mach. Manufact*., Vol. 29, No. 3. pp. 305–322.

[4] Haghighat, Heshmatollah, Saadati, Pedram (2015). An upper bound analysis of rolling process of non-bonded sandwich sheets. *Trans. Nonferrous Met. Soc. China*, 25, pp. 1605−1613.

[5] Liu, Xiang-hua, Shi, Xu, Li, Shan-qing, Xu, Jian-yong, Wang, Guo-dong (2007). FEM analysis of rolling pressure along strip width in cold rolling process. *Journal of Iron and Steel Research, International*, 14 (5), pp. 22–26.

[6] Jiang, Z. Y., Tieu, A. K., Zhang, X. M., Lu, C., Sun, W. H. (2003). Finite element simulation of cold rolling of thin strip. *Journal of Materials Processing Technology*, 140, pp. 542–547.

[7] Gudur, P. P., Salunkhe, M. A., Dixit, U. S. (2008). A theoretical study on the application of asymmetric rolling for the estimation of friction. *International Journal of Mechanical Sciences*, 50, pp. 315–327.

[8] Hwang, Yeong-Maw, Tzou, Gow-Yi (1996). An analytical approach to asymmetrical cold- and hot-rolling of clad sheet using the slab method. *Journal of Materials Processing Technology*, 62, pp. 249–259.

[9] Hitchcock, J. H. (1935). *Roll Neck Bearings.* App. I. New York, ASME.

[10] Dixit, U. S., Dixit, P. M. (1996). A finite element analysis of flat rolling and application of fuzzy set theory. *Int. J. Math. Tools Mar~faet*., Vol. 36, No. 8, pp. 947–969.

[11] Abo-Elkhier, M. (1997). Elasto-plastic finite element modelling of strip cold rolling using Eulerian fixed mesh technique. *Finite Elements in Analysis and Design*, 27, pp. 323–334.

[12] Dixit, U. S., Dixit, P. M. (1997). Finite-element analysis of flat rolling with inclusion of anisotropy. *Int. J. Mech. Sci*., Vol. 39, No. 11, pp. 1237–1255.

[13] Jiang, Z. Y., Tieu, A. K., Zhang, X. M. (2004). Finite element modelling of mixed film lubrication in cold strip rolling. *Journal of Materials Processing Technology*, 151, pp. 242–247.

[14] Gudur, P. P., Dixit, U. S., A neural network-assisted finite element analysis of cold flat rolling. *Engineering Applications of Artificial Intelligence*, 21, pp. 43–52.

[15] Shangwu, Xiong, Rodrigues, J. M. C., Martins, P. A. F. (1999). Simulation of plane strain rolling through a combined Finite element boundary element approach. *Journal of Materials Processing Technology*, 96, pp. 173–181.

[16] Liu, Xiang-hua, Shi, Xu, Li, Shan-qing, Xu, Jian-yong, Wang, Guo-dong (2007). FEM analysis of rolling pressure along strip width in cold rolling process. *Journal of iron and steel research, International*, 14, pp. 22–26.

[17] Celikov, A. I., Nikitin, G. S., Rokotjan, S. E. (1980). *Teorija prodol'noj prokatki*. M., Metallurgija, 320 s.

[18] Hitchcock, J. H. (1935). *Roll neck bearings*. App. I. New York, ASME.

[19] McConnell, Cambell, Lenard, J. G. (2000). Friction in cold rolling of a low carbon steel with lubricants. *Journal of Materials Processing Technology*, 99, pp. 86–93.

[20] Johnson, G. R., Cook, W. H. (1983). A constitutive model and data for metals subjected to large strains, high strain rates and high temperatures. *Proceedings, 7th International Symposium on Ballistics*, Hague, pp. 541–547.

[21] Murugesan, M., Jung, Dong Won (2019). Johnson Cook Material and Failure Model Parameters Mohanraj Estimation of AISI-1045 Medium Carbon Steel for Metal Forming Applications. *Materials*, 12, p. 609.

Materials Science and Engineering, Volume 45, No. 1 (2020), pp. 284–294.
DOI: 10.32974.mse.2020.029

INVESTIGATION OF TRIBOLOGICAL CONDITIONS FOR COLD ROLLING OF ALUMINUM

MÁTÉ SZŰCS[1] – GÁBOR SZABÓ[2] – GYÖRGY KRÁLLICS[3] – PÉTER BERECZKI[4] – CSABA PUSKÁS[5] – MOCHAMMAD GHULAM ISAQ KHAN[6]

Abstract: A test method was developed for the qualification of lubricants by cold rolling. Gradually changing tribological conditions were produced during rolling, up to the onset of the herringbone phenomenon. The force and torque requirements of the rolling were measured continuously. By evaluating the model of rolling, the friction factor of the process and other parameters characterizing the tribological conditions were determined. Using the test and evaluation method to compare different lubricants, a significant difference could be found in the technological applicability of the materials.

Keywords: cold strip rolling, lubrication, numerical calculation

INTRODUCTION

Tribology phenomena have many involved parameters, and the physical interaction affects the cold rolling process. The most important parameters are reduction, speed, temperature, and surface roughness. Although the subject of tribology is much wider than a friction study, friction does have a leading role in the performance of many mechanical systems. In some cases, low friction is desirable and even essential because it is beneficial for kinetic energy, transfer torque and efficiency [1]. The general theory of friction is approached by adhesion theory, based on the investigation

[1] Institute of Physical Metallurgy, Metal forming and Nanotechnology,University of Miskolc
H-3515 Miskolc-Egyetemváros, Hungary
femszmat@uni-miskolc.hu
[2] Institute Metallurgy, University of Miskolc
H-3515 Miskolc-Egyetemváros, Hungary
szabogabor@uni-miskolc.hu
[3] Institute of Physical Metallurgy, Metal forming and Nanotechnology, University of Miskolc
H-3515 Miskolc-Egyetemváros, Hungary
femkgy@uni-miskolc.hu
[4] Institute of Engineering Sciences, University of Dunaújváros
H-2400, Táncsics M. str.1/A, Dunaújváros, Hungary
berczkip@uniduna.hu
[5] Institute of Physical Metallurgy, Metal forming and Nanotechnology, University of Miskolc
H-3515 Miskolc-Egyetemváros, Hungary
fempcs@uni-miskolc.hu
[6] Institute of Physical Metallurgy, Metal forming and Nanotechnology, University of Miskolc
H-3515 Miskolc-Egyetemváros, Hungary
ghulamisaqkhan@gmail.com

that two clean and dry surfaces contact each other at only a fraction of the plain area. The normal stresses at the asperities of the contacting surfaces are high: this causes plastic deformation at the junctions. The contact creates an adhesive bond – or micro welds. The sliding motion between two bodies with an interface will be appear, only if the tangential force is applied. The friction force (F) is required to shear the junctions or plow through the softer material, and the ratio F/N is the coefficient of friction [2], where N is the normal force.

There are several friction models that can be used in the metal forming analysis from simple to complex. Coulomb's model expresses the proportionality of the frictional shear stress τ to the contact pressure p and a constant friction coefficient $0 \leq \mu \leq 1/\sqrt{3}$. This law is correct at small contact pressure, but it is less appropriate at high contact pressure [3]. Due to the higher contact pressure, the frictional shear stress is overestimated when the material shear strength k is exceeded. Constant shear stress has been widely used in simulations of bulk metal forming due to the theoretical simplicity and numerical rigidity [4]. However, experiments show that the friction at the interface cannot exceed the shear strength of material. A constant friction model has been developed to remedy this deficit, which correlates the frictional shear stress to the product of the shear yield strength k of the deformed material through a constant friction factor ($0 \leq m \leq 1$) [5]. The Levanov-type friction model integrates the effect of the previous two models, i.e. it considers the pressure on the contact surfaces and the yield stress of the deformable material [6].

In the cold rolling process, oil is used as lubricant and coolant to reduce the friction and temperature in the rolling gap. The common lubrication regime for metal forming is mixed lubrication. In this regime, friction is caused by viscous shear in the lubricant film and shear between the touching asperities [7]. With increasing reduction, the total force and the roll pressure increase as well. The asperities are flattened, and the real area of contact approaches the apparent area. The adhesive bonding increases and the bonding strength will depend on the two materials. The mixed lubrication regime is attained when the hydrodynamic pockets are interspersed with boundary lubricated zones. This is important for rolling efficiency and especially for the surface finish. In aluminum cold rolling, the most common lubricants are mineral oil with low viscosity, where the oil film is strengthened by boundary additives [8].

Minimum friction must be achieved to minimize the drive torque, although there must be enough friction to ensure acceptance of the strip by the roll gap and to ensure freedom from excessive slip. Continuous slip makes the rolling process difficult to control and results in system instability [9]. In general, the coefficient of friction decreases as the reduction increases. This is confirmed by the rolling of low carbon steel strips. However, this phenomenon and behavior of the friction factor is not lawful and general because it changes for softer metals such as aluminum alloys. In this case the coefficient of friction increases with the reduction, showing the faster rate of asperity flattening of the softer metals, leading to a higher rate of increase of the real area of contact [10]. The coefficient of friction drops as the velocity grows in the boundary and mixed lubrication regimes. The mechanisms that affect the velocity dependence of frictional resistance are the increase of the resistance of the material

as the rate of straining is increased, and the availability of less time for adhesion of the contacting asperities [11]. Increasing the velocity will drop the coefficient of friction. This is supported by two phenomena: the increased amount of lubricant being drawn into the contact zone and the time dependent nature of the formation of adhesive bonds.

The extreme higher reduction during the rolling process leads to visible failure on the surface called the herring-bone structure *(Figure 1)*.

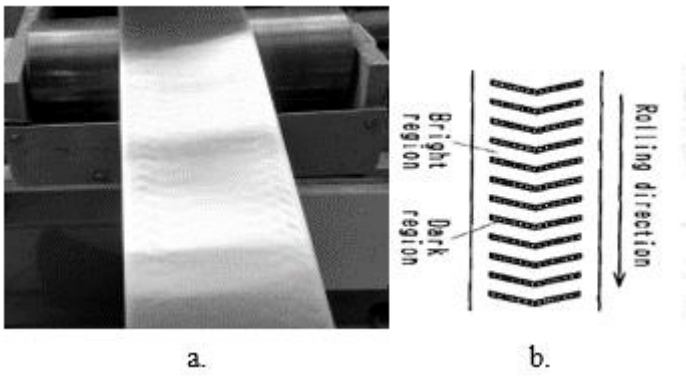

Figure 1
Herring-bone structure (a) real case (b) schematic [12]

The lubrication process directly affects the failure. Bad lubrication conditions could lead to an intense increase of the friction coefficient. The surface defects are inclined to disappear for low reduction of height, rich addition of rolling oil, and for low rolling temperature. The frictional and lubricant conditions of the regions of bright gloss differ from that of dark gloss. The distance between two neighboring lines coincides with the length of the projected material-roll contact arc in certain rolling conditions [12].

The main objective of this research is to analyze the tribological conditions of cold rolling aluminum strips, based on measured data from physical experiments, and the results of numerical calculations developed to simulate the forming process. Another aim of this work is to rank the lubricants used in the experiments in order to provide recommendations for the rolling process.

1. EXPERIMENTS

The equipment used in the experiments is a Von-Roll two-high rolling mill with a diameter and width of 220 mm and 220 mm respectively, shown in *Figure 2*. A specific lubricating system was developed to provide enough lubricant on the metal surface, spreading with a quasi-homogeneous thickness on both sides of the strip (150 mm width). The strips were front- and back tensioned constantly with the same value of force, 4,000 N, and two different rolling speeds were set, 10 m/min and 100

m/min. During the process, the workpiece was rolled with different reduction in each pass. The rolling force and torque were measured continuously by load cells and a torque sensor connected to a data acquisition system. Each rolling was finished once the herring-bone failure surface defect appeared on the surface. The initial temperature of the strips is 23 °C. In order to get the proper surface temperature, one piece of strip coil was first rolled to heat the rolls up to 62 °C.

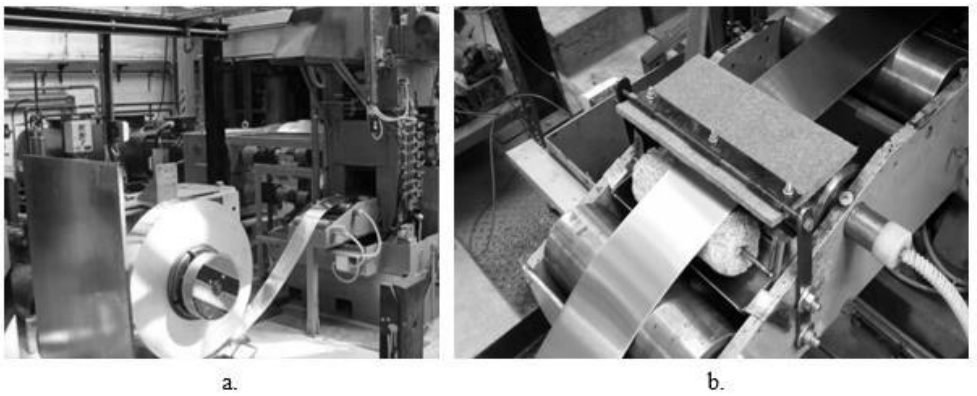

a. b.

Figure 2
Rolling mill equipped with (a) decoiler and strip, and (b) lubricating system at the entry

1.1. Material and lubricants

The rolled material used was AA5754 aluminum alloy. The fully annealed alloy was obtained in the form of a coiled strip prepared for cold rolling, with a width of 150 mm and a thickness of 2.02 mm. The initial surface roughness of the samples was approximately Ra = 0.3μm. During cold rolling, material hardening is expected and it is represented through the flow stress. The temperature and strain rate dependent stress-strain curves were obtained from the JMatPro database. For the rolling task, we developed a simplified material model in a narrower parameter range.

$$k_f = (A + B\bar{\varepsilon}^n)\left(1 + C\, ln\dot{\varepsilon}^*\right)(1 - T^{*m}) \tag{1}$$

where $\dot{\varepsilon}^* = \frac{\dot{\varepsilon}}{\dot{\varepsilon}_{ref}}$, $T^* = \frac{T - T_{ref}}{T_m - T_{ref}}$, $\dot{\varepsilon}_{ref}$, T_{ref}, T_m are the reference strain rate, reference temperature, and melting point respectively, and A, B, n, C, and m are material parameters. In our case $\dot{\varepsilon}_{ref} = 1\frac{1}{s}$, $T_{ref} = 293\ K$, $T_m = 913\ K$. The examined parameter range $0 \leq \bar{\varepsilon} \leq 4$, $0.1 \leq \dot{\varepsilon} \leq 100/s$, $293\ K \leq T \leq 413K$. The parameters of *Equation (1)* are A = 72.025, B = 281.43, n = 0.323, C = 0.0167, m = 2.1012.

Lubrilam S31L paraffinic mineral oil was mixed with two different types of additives, the boundary additive and lauril- and miristril alcohol, to obtain A and B

lubricant mixtures *(Table 1)*. The specific mixing ratio and properties of the oil, such as kinematic viscosity and temperature- and pressure-viscosity parameters were unknown, but earlier work with these lubricants indicated that at a high range of rolling speeds, sufficient amounts of oil were entrained and were able to cause decreasing loads on the rolling mill.

Table 1

The oil mixture, Additives

Type	Oil Mixture + Additive
A	93% Lubrilam S31L + 7% Palmerol 1298 NF (KLK Oleo) – 100% lauril alcohol
B	93% Lubrilam S31L + 7% Cindolube ARC 775 (Houghton) – 70% lauril alcohol + 30% miristril alcohol

2. THE MATHEMATICAL MODEL OF ROLLING

The objectives of the model include simplicity, short calculation time and the avoidance of the finite element approach. Simplified velocities and states of stresses were included in the formulation. Since the formulas do not consider the effect of temperature, we did not do so for the model. A detailed description of the model and analysis can be found in an earlier work [16].

Using the slab method, the force balance in the deformation zone in the horizontal and vertical direction leads to the differential *Equation (2)* where the (+) symbol indicates that the strip velocity is higher than the roll surface velocity and the (–) symbol indicates the opposite. The roll is assumed to be rigid and the rolled strip is taken to be rigid-plastic and hardening. In the numerical solution, Maple 16 computer algebra systems was used, considering the material flow stress and the frictional stress

$$\frac{d\sigma_{11}}{dx_1} + \frac{k_f}{\sqrt{3}}\left(2 \pm m(tan\,\alpha + cot\,\alpha)\right)\frac{\partial h}{\partial x_1}\frac{1}{h} = 0 \tag{2}$$

where x_1 is the variable into the rolling axis σ_{11} is the stress in the rolling direction, α is the angle in the roll gap, h is the actual thickness of the workpiece, m is the friction factor and k_f is the flow stress.

The simplified model is suitable to obtain the local parameters on the arc of contact relatively fast compared to using the finite element method. *Figure 2* illustrates the properties distribution for a rolling process (h_{entry} = 2.02 mm, h_{exit} = 1.70 mm, and m = 0.19).

In an inverse method, all data is processed to get the values of the average friction factor for the experimental rolling passes depending on the different cases of roll velocities and reductions. In the inverse process, the aim was to minimize the differences between the measured and computed force and torque data.

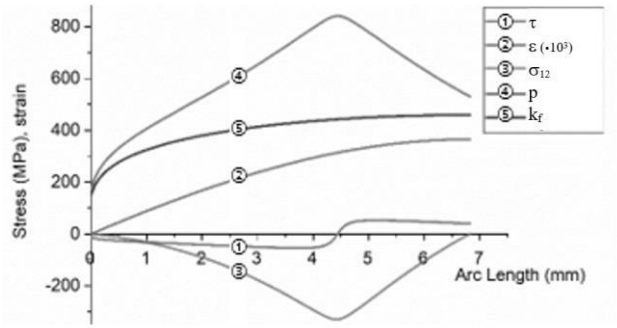

Figure 3
The distribution of calculated local parameters along the contact length (h_{entry} = 2.02 mm, h_{exit} = 1.70 mm, and m = 0.19)

3. RESULTS AND DISCUSSION

3.1. Measured data of rolling experiments

The rolling experiments first involved a rolling pass, with dimensions listed in *Table 2*. Due to the elastic deformation of the mill, the actual size of the strip is differed from this. These data were also recorded.

Table 2
Roll pass data for 10 and 100 m/min rolling speed

pass n.	1	2	3	4	5	6	7	8	9	10
$h_{exit}(mm)$	1.78	1.584	1.41	1.255	1.117	0.994	0.885	0.787	0.701	
$h_{exit}(mm)$	1.8	1.604	1.43	1.273	1.134	1.011	0.901	0.803	0.715	0.637

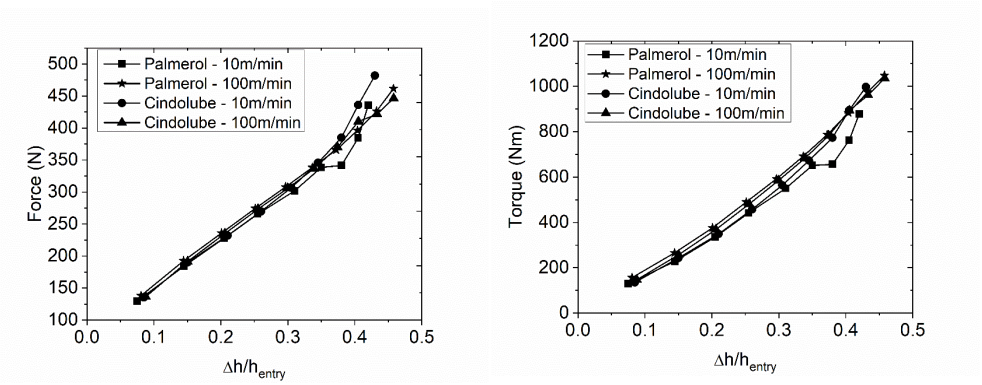

a. b.

Figure 4
The relationship between the measured roll force (a) and roll torque (b) as a function of the reduction

The primary measured data of laboratory rolling are the force and torque; these are used for further analysis. The relationship between the reduction and roll separating forces are shown in *Figure 4*. The roll forces and torque increase with the increase of reduction. The higher reduction leads the development of frictional resistance so that it needs more pressure to realize the rolling process. The force and torque value of two types lubricants and velocities are relatively close especially until 35% reduction. For the higher reduction, the Cindolube "B" lubricant has the higher value than Palmerol "A" lubricant. This condition is predicted as the effect of the lubricants on the roll separating forces that is more pronounced and observable with higher reduction [13].

Considering the effect of roll velocity toward the roll force and torque, on the Cindolube "B" lubricant lubricant, the higher roll velocity produces the lower roll force and torque and the Palmerol "A" lubricant lubricant shows an inconsistent trend. The roll forces and torques decrease as the speed is increased. This is due to the time-dependent nature of the frictional resistance and the effect of increasing of lubricant volume in the deformation zone. Both the torque and forces are typically similar in the trend toward the degree of reduction.

3.2. Mathematical Analysis

The pressure distribution occurring on the contact surface can be obtained from the numerical analysis calculation, thus the average pressure and maximum pressure are also known. Both values are particularly important for the technological process and materials limit for the deformation. The average pressure is the pressure needed to get a certain reduction, and the higher reduction needs a higher average pressure. The maximum pressure is defined as the pressure that can be applied to the workpiece without suffering failure. The value of average and maximum pressure in the certain reduction for two different lubricants is shown in *Figure 5*.

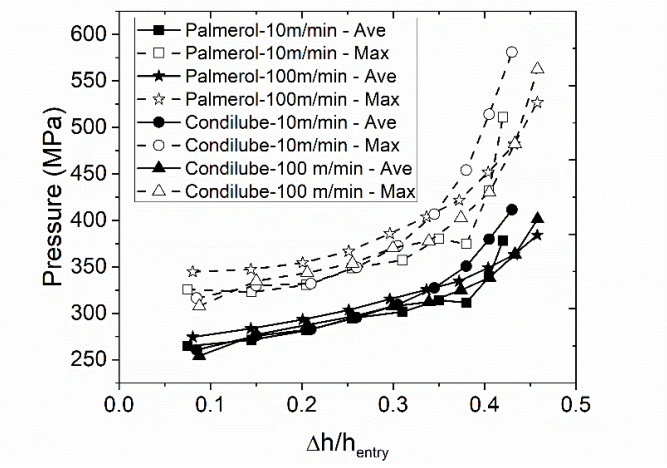

Figure 5

The relationship between the roll pressure and reduction

Both force and pressure have the same increasing trend toward the reduction, however, the pressure trend is started with the slight increase until around 35% reduction and followed by the significant increasing trend. From the graph, we could also investigate the effect of roll velocity on the pressure. In Cindolube "B" lubricant, from 10% to 30% reduction, the lower roll velocity produces a lower maximum and average pressure, and for higher reduction (30–45%), the lower roll velocity has the higher pressure. Thus, for Palmerol "A" lubricant, mostly the higher roll velocity has the higher value in maximum and average pressure, except for the reduction over 43%. In the ideal case, this condition has to be similar to the behavior of roll velocity to the force, and both properties have the reverse characteristic.

The friction coefficient is the value that represents the frictional condition between the strip and the roll. In the rolling process practice, the lubricant is inserted between the two contact bodies so that the friction force will be affected, and the friction coefficient will change as well. Different lubricants have different effects on the friction phenomena. To analyze this deeper, we need to consider more complex tribology, surface, and chemical aspects. Instead of considering the direct tribological conditions of rolling, a simplified lubricant effect is investigated through the friction phenomena, especially using the friction coefficient. *Figure 6* shows the calculated friction factors as a function of reductions for different lubricants and rolling velocities.

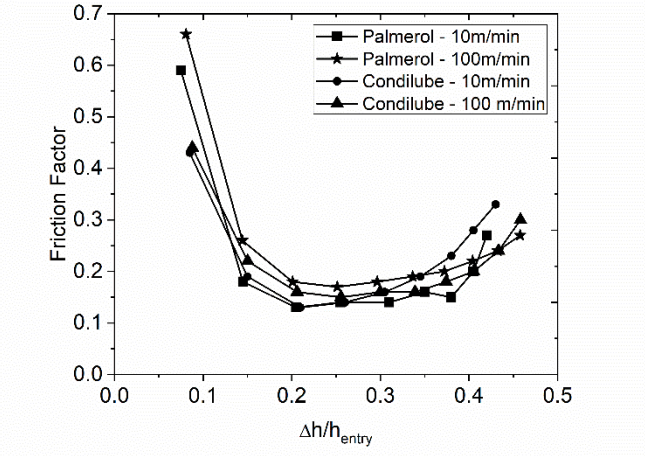

Figure 6
The trend of Kudo's friction coefficient factor (m) for different lubricants and roll velocity

Considering the trend of the friction coefficient, there is a drop in initial reduction range (<15%), then it increases slightly. To analyze these phenomena, the lubrication process must be considered. Initially, the high friction coefficient shows that the process is still in the dry or semi-dry condition and the reduction can be realized with a lower pressure, but the area of contact covered by lubricant is relatively small. From the range around 15–30% of reduction, the friction coefficient is in the lower and

stable value over the process. This shows that the lubricant has been spread through the contact uniformly well and all the surfaces were covered completely. In this stage, it is assumed that mixed lubrication has occurred. For reduction above 30%, higher pressure occurs and the material stress limit is theoretically approached, so the friction coefficient increases. Furthermore, the higher reduction leads to the development of frictional resistance so that the pressure will increase to finish the rolling process with success.

Further investigating the effect of roll velocity on the friction coefficient, it is shown that the two lubricants have different trends. For the Cindolube "B" lubricant, for small reduction (<30%) the higher roll velocity has the bigger friction coefficient and the reverse relation is found for higher reduction (>30%). Whereas for the Palmerol "A" lubricant, a higher roll velocity produces a higher friction coefficient value in every case. In other research, the frictional resistance decreases with increasing rolling speeds and increasing reduction. The phenomenon of increasing friction with reduction occurs because of the ease with which aluminum oxides adhere to the roll surfaces during the process in the addition to asperity [5]. Furthermore, the Cindolube "B" lubricant results in a lower friction coefficient value in a larger part of the whole reduction range, so generally it can be stated that the Cindolube "B" lubricant is better than the Palmerol "A" lubricant.

3.3. Rank of Lubricants

On the basis of the friction factor and pressure analysis, it can be concluded that the Cindolube "B" lubricant produces less friction and maximum pressure in realizing the rolling process compared with the Palmerol "A" lubricant.

CONCLUSIONS

In the aluminum rolling process, the data from laboratory rolling was processed with a simplified modelling method (Maple calculation) in order to get further properties such as friction factor, pressure and velocity distribution, and to analyze the tribological conditions of the process. In the range the lower reduction, semi-dry lubrication is formed, and the friction factor is higher. For higher reduction, the lubrication becomes mixed lubrication and more stable, so the friction factor will decrease. At a certain reduction that is close to the material limit, the lubrication effect is less dominant compared to the material and process factor. The frictional resistance will increase (friction factor increases) and the maximum pressure will increase, to realize the rolling process due to too high reduction and surface conditions. The limit of materials to be rolled is shown, and indicated by the failure on the surface, the herring bone structure.

ACKNOWLEDGEMENTS

This research was supported by the *ALUFORM GINOP 2.2.1-15-2016-00018* project. The described article/presentation/study was carried out as part of the EFOP-

3.6.1-16-2016-00011 *Younger and Renewing University – Innovative Knowledge City – institutional development of the University of Miskolc aiming at intelligent specialisation* project implemented in the framework of the Szechenyi 2020 program. The realization of this project is supported by the European Union, co-financed by the European Social Fund.

REFERENCES

[1] Hutchings, I., Shipway, P. (2017). *Tribology – Friction and Wear of Engineering Materials*. 2nd edition, Oxford, Elsevier, pp. 78–80.

[2] Kalpakjian, S., Schmid, S. R. (2009). *Manufacturing Engineering and Technology*. 6th edition, New York, Prentice Hall, pp. 316–972.

[3] Behrens, B. A., Bouguecha, A. (2011). Advanced friction modeling for bulk metal forming processes. *Prod. Eng. Res. Devel*., 5, pp. 621–627.

[4] Joun, M. S., Moon, H. G., Choi, I. S., Lee, M. C., Jun, B. Y. (2009). Effects of friction laws on metal forming processes. *Tribology International*, 42, pp. 311–319.

[5] Altan, T., Tekkaya, A. E. (2012). *Sheet Metal Forming — Fundamentals*. Ohio, ASM International, pp. 89–98.

[6] Levanov, A. N. (1997). Improvement of metal forming processes by means of useful effects of plastic friction. *Journal of Materials Processing Technology*, 72, pp. 314–316.

[7] Lugt, P. M., Wernekamp, A. W., ten Napel, W. E. (1993). Lubrication in cold rolling: elasto-plasto-hydrodynamic lubricrant of smoot surfaces. *Wear*, 166, pp. 203–214.

[8] Totten, G. E., MacKenzzie, D. S. (2003). *Handbook of Aluminum*. Volume 1, New York, Marcel Dekker, Inc.

[9] Lin, J. F., Huang, T. K., Hsu, C. T. (1991). Evaluation of lubricants for cold strip rolling. *Wear*, 147, pp. 79–91.

[10] Ghosh, S., Li, M., Gardiner, D. (2004). A Computational and Experimental Study of Cold Rolling of Aluminum Alloys with Edge Cracking. *Journal of Manufacturing Science and Engineering-transactions of The Asme*, pp. 74-82.

[11] Lenard, J. G. (2000). Tribology in Metal Rolling. Keynote Presentation, *CIRP* Annals, Volume 49, Issue 2, pp. 567–590.

[12] Komori, K. (1996). Analysis of herring-bone mechanism in sheet rolling. *Journal of Materials Processing Technology*, Volume 60, pp. 377–380.

[13] McConnell, C., Lenard, J. G. (2000). Friction in cold rolling of a low carbon steel with lubricants. *Journal of Materials Processing Technology*, 99, pp. 86–93.

[14] Chen, S., Li, W., Liu, X. (2014). Calculation of rolling pressure distribution and force based on improved Karman equation for hot strip mill. *International Journal of Mechanical Sciences*, 89, pp. 256–263.

[15] Valberg, H. S. (2010). *Applied Metal Forming*. Cambridge, Cambridge University Press.

[16] Szűcs, M., Krallics, G., Lenard, J. G. (2003). A study of the coefficient of friction. Under publication. *Issues of Informatics and ICT*, July 22–26, 2002, Dortmund, Germany. Boston: Kluwer Academic.

Materials Science and Engineering, Volume 45, No. 1 (2020), pp. 295–306.
DOI: 10.32974.mse.2020.030

HOT ROLL BONDING OF ALUMINIUM ALLOYS

MÁTÉ SZŰCS[1] – GÁBOR SZABÓ[2] – GYÖRGY KRÁLLICS[3] –
TAMÁS MIKÓ[4] – ÁRPÁD KOVÁCS[5] – ZHENG WENQIANG[6]

Abstract: This research presents an experimental investigation of roll bonding of aluminium alloys, prepared using various surface preparation methods. The effects of surface preparation and rolling velocity on the quality of the bond are examined. Rolling experiments are performed to produce sandwich structures with different thickness layers for hot rolling of a given material pair. The bond strengths of the rolled materials and the factors affecting them are examined. The influence of the rolling process parameters on thickness reduction and rolling speed in hot rolled samples is also analysed.

Keywords: roll bonding, two layered sheet, material properties

INTRODUCTION

Roll bonding is a solid-state welding process used to combine similar and dissimilar metals. It is widely used in manufacturing. Bonding includes hot rolling or cold rolling methods. Hot rolling is a method of combining the component materials by using high temperatures that are generally above the recrystallization temperature. The main mechanism of roll bonding of metals under normal pressure and temperature is the fracture of the brittle surface oxide layer. The virgin materials are extruded through the cracks and create the bond. The temperature and the loading time determine the quality of the bond.

Several theories of the bonding mechanism were proposed previously in the literature, such as recrystallization theory [1], metallic bonds theory [2], energy theory [3], diffusion theory [4], dislocation theory [5], and film theory [6]. All of the above-

[1] Institute of Physical Metallurgy, Metal forming and Nanotechnology, University of Miskolc
H-3515 Miskolc-Egyetemváros, Hungary
femszmat@uni-miskolc.hu
[2] Institute Metallurgy, University of Miskolc
H-3515 Miskolc-Egyetemváros, Hungary
szabogabor@uni-miskolc.hu
[3] Institute of Physical Metallurgy, Metal forming and Nanotechnology, University of Miskolc
H-3515 Miskolc-Egyetemváros, Hungary
femkgy@uni-miskolc.hu
[4] Institute of Physical Metallurgy, Metal forming and Nanotechnology, University of Miskolc
H-3515 Miskolc-Egyetemváros, Hungary
femmiko@uni-miskolc.hu
[5] Institute of Physical Metallurgy, Metal forming and Nanotechnology, University of Miskolc
H-3515 Miskolc-Egyetemváros, Hungary
femkov@uni-miskolc.hu
[6] Institute of Physical Metallurgy, Metal forming and Nanotechnology, University of Miskolc
H-3515 Miskolc-Egyetemváros, Hungary

mentioned composite mechanisms reveal to some extent the law of metal bonding and they are not mutually exclusive but complement each other. It can be said that understanding of the bimetallic solid-phase compounding mechanism is still continuing. Until now, multiple types of metals and alloys have been successfully bonded by the roll bonding process. For example, aluminium, copper, steel, silver, nickel and zinc were bonded by continuously rolling processes [7], [8], [9]. During the process, the surface layer or the thin film of oxides and contaminants breaks up due to expansion of the surfaces in contact. Then, the normal pressure is sufficient to extrude the virgin material through these surface cracks and brings it to within atomic distances, thus resulting in bonding [10]. Bonding always occurs only after a certain threshold deformation has been reached [10]. The threshold deformation for a given metal combination appears to be dependent upon the type of the process [11], for example the temperature during the roll bonding.

Surface preparation is one of the most important steps which can affect the final bonding strength. Before the roll bonding process, surface treatment is always applied to improve the bonding strength. Scratch brushing has been reported to be an effective method, widely applied for surface preparation during cold welding processes [12]. This process not only removes the surface contaminants, but it also forms a hard and brittle cover layer on the surface by work hardening it and behaving as a single layer. Therefore, the virgin metals are easier to be squeezed out and joined. In addition, the surface roughness also has an influence on the bonding strength. Jiantao Liu et al. found that micro-surface engineering yielded better bonding quality than macro-surface engineering. The critical surface roughness of the core was about 0.58 μm below which bonding quality in terms of area contact and bonding energy can be significantly improved [13]. It was studied the effect of metal surface oxides on bonding strength [14]. They found that bonding strength was decreased by providing Al_2O_3 oxide film on the strips. Based on the experiment, Bay considered the surface of metals consisting of the brittle cover layer formed by scratch-brushing and the contaminant film of oxides and water vapour. They proposed a theoretical model for the strength of the weld [15], [16], [17], [18]. There are many other parameters that may affect the strength of the bond. These include the surface expansion, type of material, the velocity of rolls, the strength and the hardness of the starting material, normal pressure, crystal structure of the bonding materials, and the temperature and time of roll bonding prior to the process [19]. In general, higher thickness reduction and temperature cause increasing bonding strength. For Al/Al bimetal strips, it also shows that the threshold is around 21% of reduction. Under this value only minimal effect is observed [20]. The effect of annealing after the cold rolling process on bonding strength was also investigated [21]. In this study the relationship between shear strength and rolling speed at the entry temperature of 280 °C was analysed. The shear strength was observed to decrease sharply as the speed increased, caused by the shorter time of contact. The effect of the reduction was also observed. At higher reductions the bond strength was higher, caused by the longer contact time. Increasing rolling speed resulted in sharply lower bond strength. The results indicated that time is more important than the temperature.

Mechanical tests are commonly used to obtain the bonding property of clad metals. Among these is the peel test [22], [23], [24]. In these cases, the plastic dissipation plays an important role for the total peeling work. Therefore, the apparent peel strength measured in the peel test does not accurately identify the true peel strength. Other measurements, such as the shear test by pressing is extensively used to examine the bonding property of clad steel plates for boilers and pressure vessels [25] and is also preferred to evaluate the bonding property of clad bars and tubes. The shear test by tension loading is also used to measure the roll bonding strength between aluminium and steel sheets [26]. According to ASTM standards [27], [28], the reported shear strength of adhesives is considered as the apparent shear strength due to the edge effect [29]. Mechanical analysis of a tensile shearing test is required to determine the accurate shear strength of the bond. The weaker metal sheet breaks easier before the bond fails. Despite the drawbacks, the tensile shearing test is usually preferred for the evaluation of the bonding quality.

In this study, the effects of rolling conditions – the rolling thickness reduction, the surface condition and the rolling speed – on the bond strength are discussed.

1. EXPERIMENTS

1.1. Equipment and preparation

a)

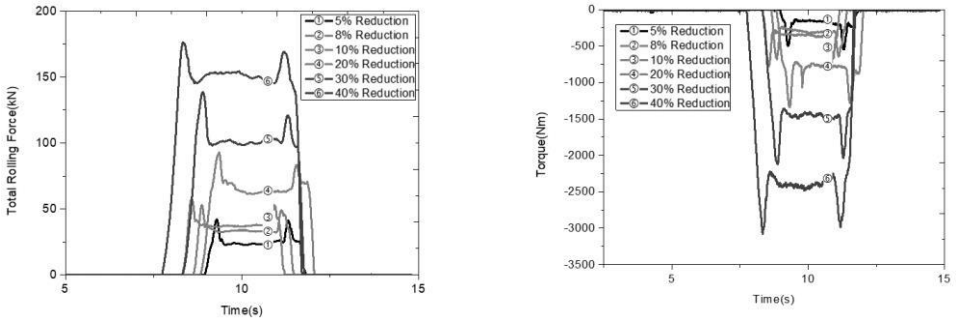

b) c)

Figure 1

a) Two-high rolling mill b) rolling force – time diagram
c) rolling torque – time diagram

Two layers of metal specimens are bonded by hot rolling *(Figure 1.a)*. All experiments were conducted on a Von Roll two-high rolling mill, providing rolling speeds up to 300 m/min surface velocity. The tool steel rolls have 200 mm diameter and 220 mm face width. The force and torque are recorded *(Figure 1.b, c)* by two force transducers and a torque transducer connected to a data acquisition system.

Load cells are placed over the bearing blocks of the top work roll. A torque transducer is mounted between the gear box and drive shaft. Unlubricated condition was provided to avoid lubricant entering the contact between layers.

1.2. Material and the samples

Two alloys were rolled together; the upper layer is AlMn1Cu0.5 (0336), and the lower layer is AlSi10 (4045). The chemical compositions of the materials are given in *Table 1*. The thickness is 5.2 ± 0.2 mm and the length and width of the work pieces are respectively 200 mm and 63 mm. After cutting the raw materials the specimens were wire brushed to get rough surfaces to be bonded. The materials were stacked and fixed at their ends by using steel wires to avoid any separation at the entry of the roll gap. *Figure 2* shows an example of the prepared two layered work piece.

Table 1

Chemical composition of the rolled alloys

Alloy	Code	Si	Fe	Cu	Mn	Mg	Cr	Zn	Ti	Be	Ni
AlMn1Cu0.5	38 C37P	0.1	0.3	0.6	1.1	0.1	0.1	0	0.1	1ppm	0.1
AlSi10	91 C78P	10	0.3	0	0.1	0	0.1	0.1	0	1ppm	0

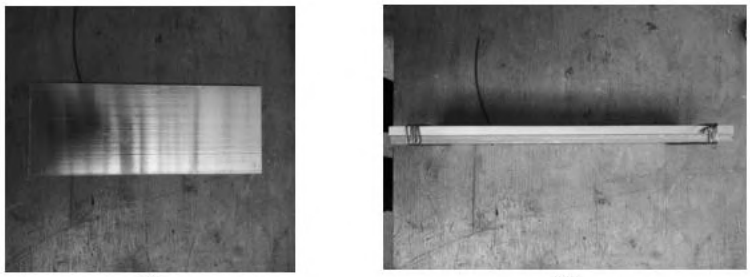

Figure 2

a) Sample after cutting b) Tied two-layered specimen before rolling

Figure 3 shows the flow chart of the roll bonding process. Before heating up the work pieces, the material surface is prepared to produce a satisfactory metallurgical bond. It is essential to remove contaminants from the surfaces of the strips to be joined. These layers are composed of greases, oxides, adsorbed ions and dust particles. The strips were degreased in acetone bath at first. After the surface treatment process two different types of surfaces were obtained. One type is a brushed surface,

another one is not brushed. After the preparation the materials are preheated for 30 minutes to 500 °C in a furnace. The roll temperature and the ambient temperature are 23 °C.

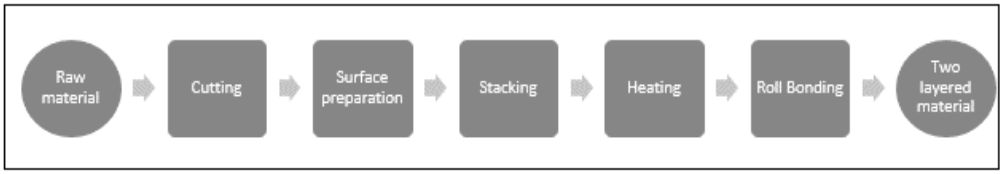

Figure 3
Flow chart of the roll bonding process

Before entry into the roll gap the surface temperature of the samples varied in a relatively small range between 450 °C and 500 °C. The exit surface temperature was between 380 °C and 420 °C. At the end of the process, the samples cooled in air.

Table 2
Experimental results of bonding process

ID	Reduction	△h	Surface condition	velocity	result
1	5%	0.52mm	unbrushed	5m/min	failure
2	5%	0.52mm	brushed	5m/min	failure
3	5%	0.52mm	unbrushed	50m/min	failure
4	5%	0.52mm	brushed	50m/min	failure
5	8%	0.832mm	unbrushed	5m/min	failure
6	8%	0.832mm	brushed	5m/min	failure
7	8%	0.832mm	unbrushed	50m/min	failure
8	8%	0.832mm	brushed	50m/min	failure
9	10%	1.04mm	unbrushed	5m/min	min. joint
10	10%	1.04mm	brushed	5m/min	min. joint
11	10%	1.04mm	unbrushed	50m/min	failure
12	10%	1.04mm	brushed	50m/min	failure
13	20%	2.08mm	unbrushed	5m/min	success
14	20%	2.08mm	brushed	5m/min	success
15	20%	2.08mm	unbrushed	50m/min	success
16	20%	2.08mm	brushed	50m/min	success
17	30%	3.12mm	unbrushed	5m/min	success
18	30%	3.12mm	brushed	5m/min	success
19	30%	3.12mm	unbrushed	50m/min	success
20	30%	3.12mm	brushed	50m/min	success
21	40%	4.16mm	unbrushed	5m/min	success
22	40%	4.16mm	brushed	5m/min	success
23	40%	4.16mm	unbrushed	50m/min	success
24	40%	4.16mm	brushed	50m/min	success

Acetone was used to clean the work rolls before each experiment. After each pass the sample's thickness was measured. Among the roll bonding conditions, the thickness reduction, surface condition and the rolling speed are the variables. For this metal combination, a series of rolling experiments were carried out using rolling reductions between 5%, 8%, 10%, 20%, 30% and 40%. In order to study the effect of rolling speed and surface condition on the bond strength between layers, the tests were carried out at two different rolling speeds (5 m/min, 50 m/min) and two different surface conditions (brushed and unbrushed). A total of 24 tests were conducted. The experimental parameters are summarized in *Table 2*.

2. DEBONDING TEST AND BONDING CHARACTERIZATION

2.1. Shear test

After the rolling process, the well bonded, two-layered work pieces were machined to make them suitable for the shear tests. *Figure 4* shows the dimensions and shapes of the specimens after machining. The groove distances were measured optically using a Zeiss AxioVision microscopy, illustrated by *Figure 5*.

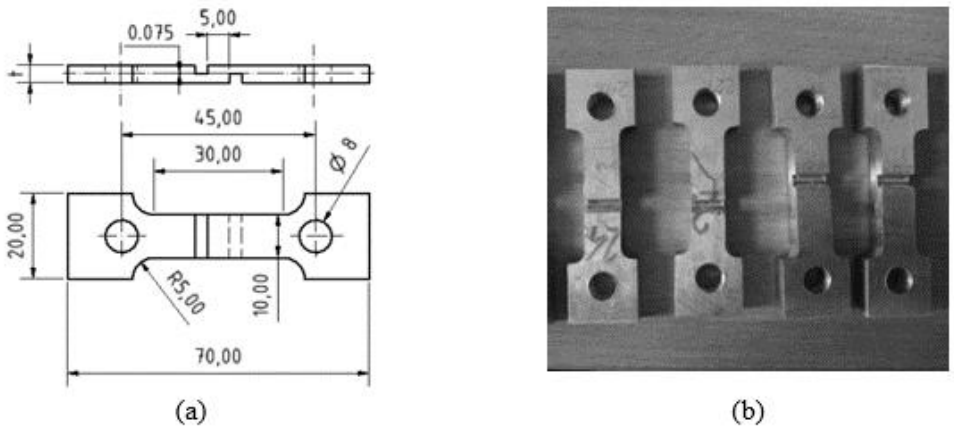

Figure 4
Geometry of the shear test specimen, (b) machined samples

The shear tests were performed at room temperatures and at an elevated temperature, at 450 °C (same as the rolling temperature) using an Instron type universal material tester machine equipped with a three-zone resistance wire wound furnace. The specimen temperature is controlled by measuring the furnace temperature at the heating zone. The tensile speed was set to 3 mm/min for the tests performed at room temperature.

The shear test data lead to an estimate of the shear strength of the bond for different rolling conditions. Although the given test is more quantitative than others, it still suffers from a few drawbacks. For instance, the sample preparation is very challenging as precise slots are to be machined on thin samples. Considerable bending and unbending

occur during the test and consequently the calculated shear stress is not the pure shear stress, but a shear stress component and it is assumed that the other stress components are considerably smaller. In addition, it should be noted that the bond strength is reduced by the mechanical forces exerted during sample preparation.

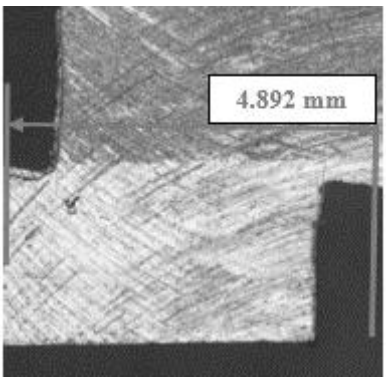

Figure 5
Measurement of groove distance after machining

2.2. Shear test results

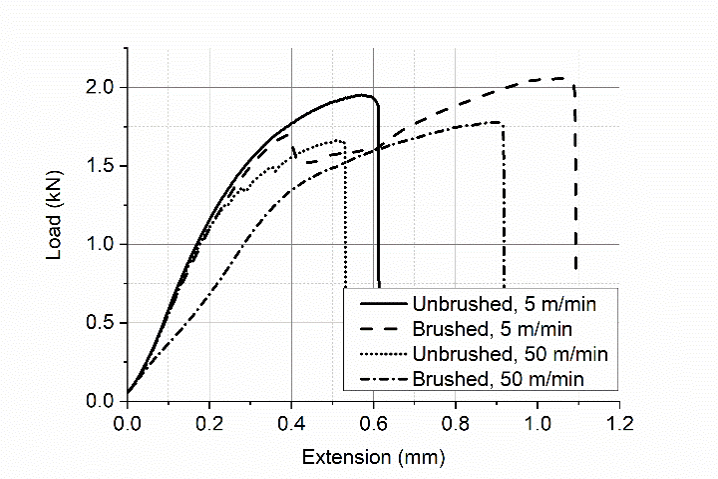

Figure 6
Displacement and force diagram (reduction per rolling pass: 20%)

The shear strength was calculated from the maximal force and the bonding area. The latter one is defined by the measured data of groove distance and specimen width. *Figure 6* shows the force – extension curves of specimens rolled under different speeds and different initial surface conditions.

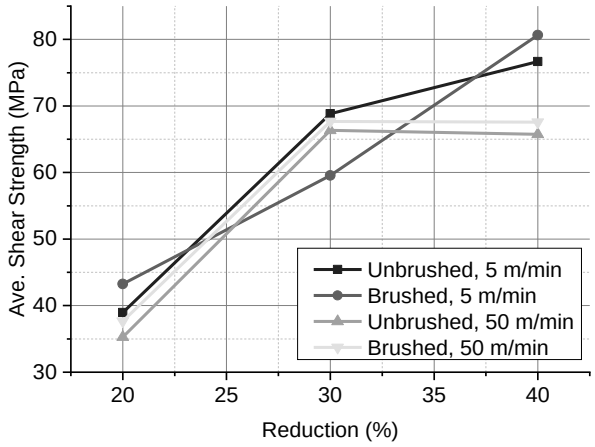

Figure 7
Relationship between reduction and shear stress at room temperature

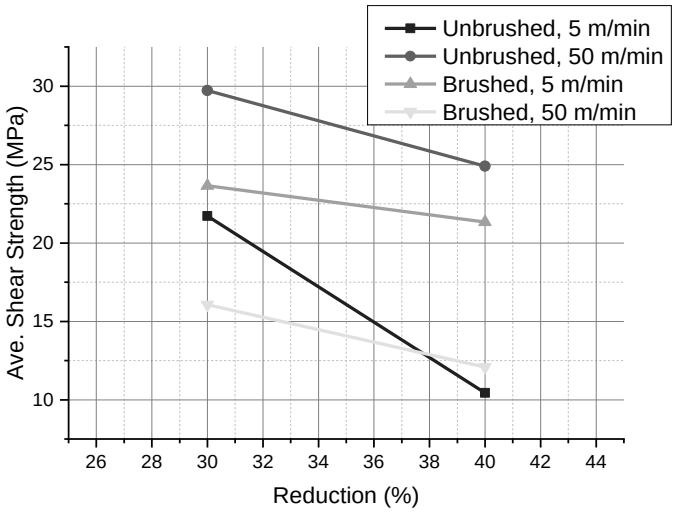

Figure 8
Relationship between reduction and shear strength at rolling temperature (450 °C)

It was confirmed that the thickness reduction has a significant effect on the bond strength. At lower rolling speeds the shear strength increases as a function of the reduction. At higher speeds and above reductions of 30% the shear strength decreases. The larger reduction causes more pure metal to be extruded into the cracks of the oxide layers, so the probability of the solid metallurgical bond's formation is greater. The experimental results indicate that the rolling speed is another significant

contributor to the strength, above a specific reduction. Increasing the rolling speed and the reduction, the strain rate and the flow stress on the contact surface increase, causing increasing resistance for the material to enter the cracks. While the higher speed and the reduction cause the temperature to rise, the rate of strain has a more significant effect on bond creation. The quality of roll bonding depends also on the initial surface of the materials. Two types of surface conditions were studied – brushed and unbrushed. At 20% reduction the brushed samples showed better bonding strength at both speeds. *Figure 8* shows the shear strength of the bond as a function of the reduction. As the reduction is increased, the bond strength dropped in all instances.

2.3. SEM test characterization

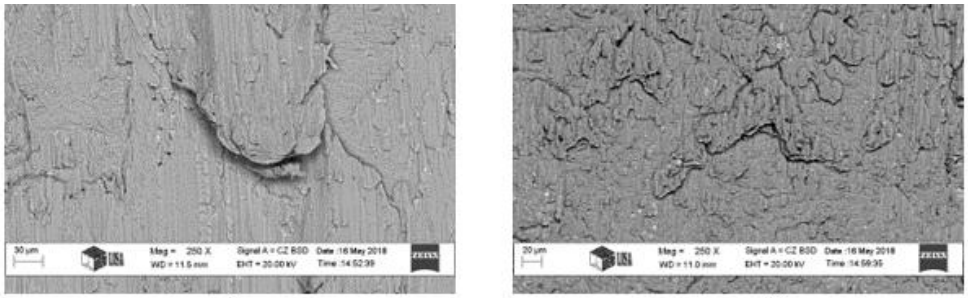

Figure 9

SEM Micrograph shows the surface condition of 0336 aluminium alloys previously a) brushed/rolled and b) unbrushed/rolled after shear test

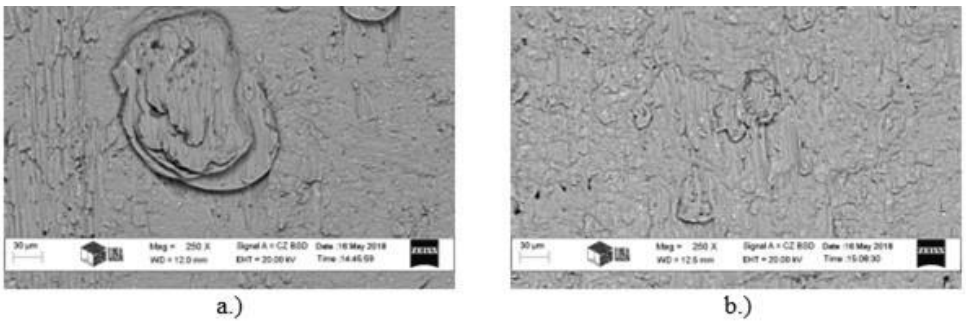

Figure 10

SEM Micrograph shows the surface condition of 4045 aluminium alloys previously a) brushed/rolled and b) unbrushed/rolled after shear test

After the cold shear test, scanning electron microscopy was used to investigate the sheared zones and debonded surfaces.

The micrographs of the surfaces under different rolling conditions are illustrated in *Figure 9* and *Figure 10*. Qualitative analysis confirmed that the initial rolling condition has got a strong effect on surface morphology. For initially brushed samples larger bonding area is detected. This is one of the key factors to improve the shear strength of the bond created by hot rolling.

CONCLUSIONS

The hot roll bonding process and a series of tests on the samples were performed. In the hot rolling experiments the total force and torque data were obtained, which provided data support for the further simulation work. Through the shear experiments, the influence of various factors on the shear strength was analysed. Among them, the shear strength increases as the thickness decreases. The shear strength decreases as the hot rolling speed increases. The brushed surface is more conducive to bonding.

ACKNOWLEDGEMENTS

The described study was carried out as part of the EFOP-3.6.1-16-2016-00011 *Younger and Renewing University – Innovative Knowledge City – institutional development of the University of Miskolc aiming at intelligent specialisation* project implemented in the framework of the Széchenyi 2020 program. The realization of this project is supported by the European Union, co-financed by the European Social Fund.

REFERENCES

[1] Parks, J. M. (1953). Recrystallization in welding. *Weld J*., 32, pp. 209–21.

[2] Daw, Murray S., Foiles, Stephen M., Baskes, Michael I. The embedded-atom method: a review of theory and applications. *Materials Science Reports*, 9 (7–8), pp. 251–310.

[3] Semenov, A. P. (1961). The phenomenon of seizure and its investigation. *Wear*, 4, 1, pp. 1–9.

[4] Mitani, Y., Vargas, R., Zavala, M. (1984). Deformation and diffusion bonding of aluminidecoated steels. *Thin Solid Films*, 111, 37, pp. 34–42.

[5] Taylor, G. I. (1934). The Mechanism of Plastic Deformation of Crystals. Part I. Theoretical. *Proceedings of the Royal Society of London*, Series A, 145 (855), pp. 362–87.

[6] Mohamed, H. A., Washburn, J. (1975). Mechanism of solid state pressure welding. *Weld J*, 55, 302s–10s.

[7] Wu, H. Y., Lee, S., Wang, J. Y. (1998). Solid state bonding of iron-base alloy, steel-brass and aluminium alloy. *J. Mater. Process. Technol.*, 75, pp. 173–179.

[8] Ulam, J. B. (1978). *US Patent: 4,103,076, Clad Metal Product of Cu, Al and Stainless Steel*. Clad Metals, Inc. Canonsburg, PA.

[9] Ulam, J. B., Camp, W. C. (1967). *US patent: 3,350,772, Methods of Cladding Stainless Steel to Aluminium*. Composite Metal Products, Inc. Canonsburg, PA.

[10] Bay. N. (1986). Cold welding. Part 1: characteristics, bonding, mechanisms, bonding strength. *Metal Construction*, 18, p. 369.

[11] Tylecote, R. F. (1968). *The solid phase welding of metals*. London, Edward Arnold.

[12] Zhang, W., Bay, N. (1997). Cold welding-experimental investigation of the surface preparation methods. *Welding Journal*, 76, pp. 326–330.

[13] Liu, Jiantao, Li, Ming, Sheu, Simon, Karabin, M. E., Schultz, R. W. (2008). Macro- and micro-surface engineering to improve hot roll bonding of aluminium plate and sheet. *Materials Science and Engineering A*, 479, pp. 45–57.

[14] Bay, N. (1983). Mechanisms Producing Metallic Bonds in Cold Welding. *Welding Research Supplement*, 62 (5), pp. 137–142.

[15] Bay, N. (1986). Cold Welding, Part 2 Process Variants and Applications. *Metal Construction*, 18 (8), pp. 486–490.

[16] Bay, N. (1986). Cold Welding, Part 3 Influence of Surface Preparation on Bond Strength. *Metal Construction*, 18 (10), pp. 625–629.

[17] Zhang, W., Bay, N. (1992). Influence of Hydrostatic Pressure in Cold-Pressure Welding. *Annals of the CIRP*, 41 (1), pp. 293–297.

[18] Bay, N., Clemensen, C., Juelstorp, O., Wanheima, T. (1985). Bond Strength in Cold Roll Bonding. *Materials and design*, 34 (1), pp. 221–224.

[19] Eizadjou, M., Danesh-Manesh, H. K. (2009). Janghorban: Mechanism of warm and cold roll bonding of aluminium alloy strips. *Materials and Design*, 30, pp. 4156–4161.

[20] Yan Hong-zhi (2016). Key factors for warm rolled bond of 6111-aluminium strip. *Transactions of Nonferrous Metals Society of China*, 16, pp. 84–90.

[21] ASTM D903 (2004). *Standard test method for peel or stripping strength of adhesive bonds*.

[22] ASTM D3167 (2004). *Standard Test Method for Floating Roller Peel Resistance of Adhesives*.

[23] ASTM D1781 (2004). *Standard Test Method for Climbing Drum Peel for Adhesives.*

[24] ASTM B898 (2005). *Standard Specification for Reactive and Refractory Metal Clad Plate*.

[25] Buchner, M., Buchner, B., Buchmayr, B., Kilian, H., Riemelmoser, F. (2008). Investigation of Different Parameters on Roll Bonding Quality of Aluminium and Steel Sheets. *11th ESAFORM2008 Conference on Material Forming*, April 23–25 2008.

[26] ASTM D1002 (2005). *Standard Test Method for Apparent Shear Strength of Single-Lap-Joint Adhesively Bonded Metal Specimens by Tension Loading (Metal-to-Metal)*.

[27] ASTM D2339 (2004). *Standard Test Method for Strength Properties of Adhesives in Two-Ply Wood Construction in Shear by Tension Loading*.

[28] ASTM D3983 (2004). *Standard Test Method for Measuring Strength and Shear Modulus of Non-rigid Adhesives by the Thick-Adherend Tensile-Lap Specimen.*

[29] Sitterle, V. B., Sun, W., Levenston, M. E. (2008). A Modified Lap Test to More Accurately Estimate Interfacial Shear Strength for Bonded Tissues. *Journal of Biomechanics*, 41, pp. 3260–3264.

Materials Science and Engineering, Volume 45, No. 1 (2020), pp. 307–315.
DOI: 10.32974.mse.2020.031

THE ISSUE OF PROTECTION FROM AN ENGINEERING PERSPECTIVE

CSENGE EMESE TÓTH[1] – KINGA TAMÁSI[1, 2] –
ESZTER BORSODI[3] – KÁLMÁN MAROSSY[4]

Abstract: Our goal in recent research was to compare the materials science of latex-based condoms of various brands. To do this, we had different types of condoms that were subjected to mechanical testing before and after soaking in different solvents for a specified period. Our solutions were: Simulated Body fluid, lactic acid, in which the products were swollen for 30 days. In the solvent studies, weight changes were examined, and samples were dried for 24 hours after swelling. Subsequently, tensile strength and surface tests (FT-IR) were performed. The purpose of these studies was to compare the mechanical and surface properties of commercially available condoms.

Keywords: latex, FT-IR, SBF, lactic acid, mechanical properties

INTRODUCTION

One of the major problems nowadays is proper sexual control. It is as essential for the protection from sexually transmitted diseases as it is for controlling the number of pregnancies. The primary problem of condoms is the occurrence of allergic reactions and a possible rupture. Several factors can lead to the latter, such as the use of sharp nails, improper lubricant, improper storage or use. The purpose of our studies is that keeping in mid the allergic risks inherent in latex-based condoms, to study them with different material testing methods, and to find a link between the possible mechanical and chemical degradation processes caused by test solutions (Simulated Body Fluid and lactic acid solutions), suggesting alternative substances, differentiating between different types of condoms.

The uniform, international dimensioning of condoms is dealt with by Condom Amsterdam Standard (CAS).

[1] Institute of Ceramics and Polymer Engineering, University of Miskolc
H-3515 Miskolc-Egyetemváros, Hungary
tothcsengeemese@gmail.com
[2] Institute of Ceramics and Polymer Engineering, University of Miskolc
H-3515 Miskolc-Egyetemváros, Hungary
polkinga@uni-miskolc.hu
[3] Institute of Ceramics and Polymer Engineering, University of Miskolc
H-3515 Miskolc-Egyetemváros, Hungary
eszter.borsodii@gmail.com
[4] Institute of Ceramics and Polymer Engineering, University of Miskolc
H-3515 Miskolc-Egyetemváros, Hungary
polkal01@uni-miskolc.com

1. MATERIALS AND METHODS

1.1. Materials used

1.1.1. Latex based condoms

Latex is a colloidal system in which the disperse phase is a 1,4-cis-polyisoprene polymer, also known as Natural Rubber (NR), where the dispersion medium is water. Natural Rubber is a milky liquid obtained by splitting the bark of the *Hevea Brasiliensis* tree [1]. One of the most used ingredients in condoms is latex. Condom making is a relatively simple process using a dip technology in which a mold is dipped into the colloidal solution. Subsequently it is coagulated (hardened), since later the product is fabricated from the colloidal system. In order for the latex to be transported, it must be preserved, which usually involves ammonia gas or thickening it by reducing the water content. The final technological process is the crosslinking using S_2Cl_2. Products from 4 different manufacturers were used for the tests. The labeled data of the latex products from the box is presented in the table below. The products are identified by the letters A, B, C, D and are referred to hereinafter.

Table 1

Condoms used in the test with specifications

	A	**B**	**C**	**D**
Diameter [mm]	53.00	52.00	54.00	56.00
Lubricant type	water-based	water-based	water-based	water-based
Appearance	cylindrical, with tip	cylindrical, with tip	cylindrical, with tip	cylindrical, with tip

All condoms tested were lubricated. Of course, the quality of a condom depends not only on the properties of the raw material or lubricant, but also on its packaging. Currently, all condoms commercially available are put in a distinctive square aluminum packaging. In 2016, Gerofi et al. (2017) conducted a very thoughtful series of experiments to investigate the effect of packaging of six different branded condoms on the mechanical properties (leaks, blowouts, tensile strengths) [2]. They conducted their tests in accordance with ISO 4074:2014 and has found that the shape of the condom in the package (folded ring) did indeed greatly affect the properties of latex. What provided a starting point for us was the tensile strength parameters for my later investigations.

1.1.2. Lactic acid (LA)

A solution of pharmaceutical grade lactic acid (also known as 2-hydroxypropanoic acid) was used, which simulates the lactic acid solution produced by the Lactobacillus present in the vagina. This is responsible for normal vaginal pH and provides protection against possible infections. The molecule is a α-hydroxy acid containing

one carboxyl and one –OH group. In solution, it releases a proton from the carboxyl group, the resulting ion is called lactate ion.

$$CH_3CH\ (OH)\ COO^-$$

It is readily miscible with water and ethanol [2]. Lactic acid is a chiral molecule with two stereo isomers. One is called L-(+)-lactic acid or (S)-lactic acid, while its mirror image is called D-(–)-lactic acid or (R)-actic acid. L-(+)-lactic acid is the isomer with higher biological importance.

1.1.3. Simulated body fluid (SBF)

The other soaking medium we used was Simulated Body Fluid (SBF). This solution is in fact an electrolyte solution used to simulate human blood plasma in medical technology [3–9] for the development of various bones, metal foams or implants. The ionic composition of human plasma and SBF, shown in *Table 2*, was prepared according to the literature.

Table 2

Literature composition of SBF solution [10]

Name of compound	**Amount required for 1 liter SBF** [g]
NaCl	8.000
Na_2CO_3	0.350
KCl	0.224
K_2HPO_4	0.228
$MgCl_2 \cdot 6\ H_2O$	0.305
1 mol HCl	38.000
$CaCl_2 \cdot 2\ H_2O$	0.368
$Na_2SO_4 \cdot 10\ H_2O$	0.178
Tris (hydroxymethyl) aminomethane	6.057

1.2. Applied methods

Our starting hypothesis is that our simulation solutions can negatively affect the mechanical and surface properties of condoms, following the test methods used in the literature, which will be supported by the following tests: swelling, FT-IR, tensile strength test.

1.2.1. Swelling

In the course of our investigations, the effects of SBF and lactic acid solution on the degradation of the substances were examined. The swelling experiments were not carried out in a prestressed state, but in the original (rolled up) or unrolled state taken out of the packaging in the different soaking media. Observation of swelling processes associated with weight changes took place for a total of 720 hours. Testing of the specimens began with a preparatory step of testing the solvent uptake of rubber

condom samples (labeled A-B-C-D in SBF and lactic acid solution) at constant temperature (T = 20 °C) and normal atmospheric pressure.

During the soaking, our aim was to simulate a realistic internal human environment during the act. Our assumption is that prolonged exposure might contribute to the degradation of the material and lead to its earlier loss of integrity. According to the literature, it would have been worthwhile to weigh in the first 30 minutes, at 5-minute intervals, but our options were limited in time, so 0 (or pre-soak mass, m0); on days 1, 5, 10, 15, 20, 25 and 30 we repeated the measurement of the weight and pH of the samples in 30 ml of solvent, 720 hours.

1.2.2. Fourier-transform infrared spectroscopy (FT-IR)

The application of Fourier transform infrared (FTIR) spectroscopic techniques to assess polymer interaction has been conducted for many years. FTIR spectroscopy has been proven as a powerful tool in characterizing the detailed structure and interaction of polymer solids with nondestructive and fast measurement. The changes of interaction behavior can be characterized through the identification of the IR spectral features in intensity, bandwidth, and position. It is a method for identifying the structure of a given compound, tracking sub-processes and checking the purity of the finished product. This analytical spectroscopic method examines the interactions between matter and electromagnetic radiation, providing information on the quantitative and qualitative composition of a substance. The samples were analyzed before and after soaking and the results compared by BRUKER Tensor 27 type Fourier Transformed Infrared Spectrometer in reflection mode, a diamond ATR was used. The infrared absorbance spectra of samples were recorded for 400–4,000 cm^{-1}.

1.2.3. Tensile strength test

Mechanical properties are one of the most important properties of polymers and this is particularly emphasized in condoms as they are subjected to mechanical stress in virtually every application. After the swelling experiments, the specimens were cleaned off of the soaking medium and then cut into 100 × 20 mm ribbon shape specimens. The test series was carried out using an Instron 5566 tensile tester with a crosshead speed of 250 mm/min.

2. RESULTS

2.1. Swelling

The swelling tests were followed for a total of 30 days, during which time changes in sample weight and pH were recorded. During the examinations we found that the lubricants were probably dissolved both in SBF and in lactic acid solutions, which caused an about 1 to 3 pH fluctuation. Similarly, samples B, C, D were discolored in the SBF solution after 21 days.

The highest swelling was observed in the samples soaked in the lactic acid solution without exception, the largestuptake was measuredt in the case of *sample B*,

and the lowest in the SBF solutions in the case of *sample A*. Condoms soaked in SBF were unwound, while the condoms in the lactic acid solutions were kept folded. This explains the separation of the two solution types in *Figure 1*. The samples initially exhibited a sudden increase in weight, but after some of the lubricants on them had diffused into the solution, a kind of decrease was observable for all samples.

Due to the nature of the solutions, in addition to the change in weight of the samples, a change in the pH of the solutions was also recorded on these days. As pH changes, it is observed that at the beginning of the measurement it decreased in all solutions and then started to increase between day 20 and day 25, until on day 30 all solutions reached pH 3, which corresponds to an acidic medium.

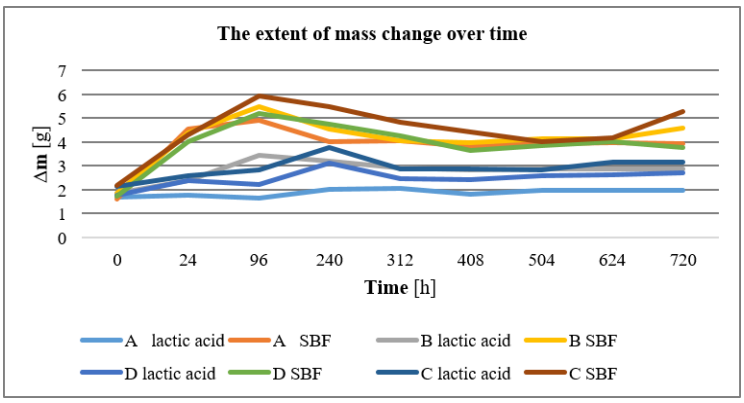

Figure 1
Mass change over soaking time

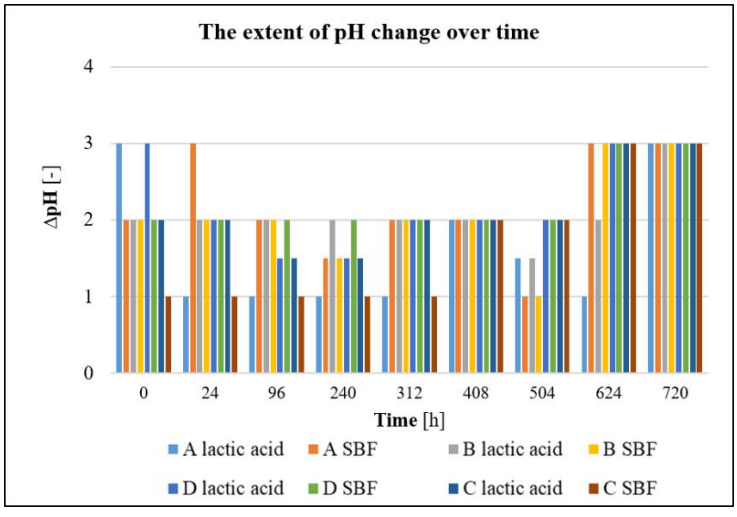

Figure 2
pH changes as a function of soaking time

As shown in *Figure 2*, the pH values fluctuated continuously, only stagnating around 3 during the last soaking hours. The pH measurement in this form did not give adequate results, perhaps a more radical change at elevated temperatures could be observed. Another hypothesis is that the lubricant on the surface of the condom interacts with the surrounding medium – we weren't able to measure the total pH of the lubricant.

2.2. Fourier-transform infrared spectroscopy (FT-IR)

According to literature, certain lubricants may contain glycerol (water-based), and traces thereof have been detected using the FT-IR apparatus at a wave number of 3,500–3,000 cm^{-1}. Comparing the spectra, it was found that rubber condoms are made up of the similar materials, except for differences in the intensity of the peaks of the constituent components.

Figure 3 shows a comparative spectrum of condoms labeled A, three nearly identical diagrams. According to the published FT-IR spectra of lubricants we found glycerol and its aqueous solution were presumed to be present in the system, and also in its aqueous solution. A peak appeared indicating the presence of an aromatic compound. The other two types show no peaks there, but appear at 2345 cm^{-1}, which refers to amines, 1484 cm^{-1}, which refers to aromatic hydrocarbons, 839 cm^{-1} to nitrate, or terminal epoxy group fatty acid derivatives. Further, at 822cm^{-1}, which may indicate the presence of 1,4-disubstituted or 1,2,4,5-tetrasubstituted aromatic compounds.

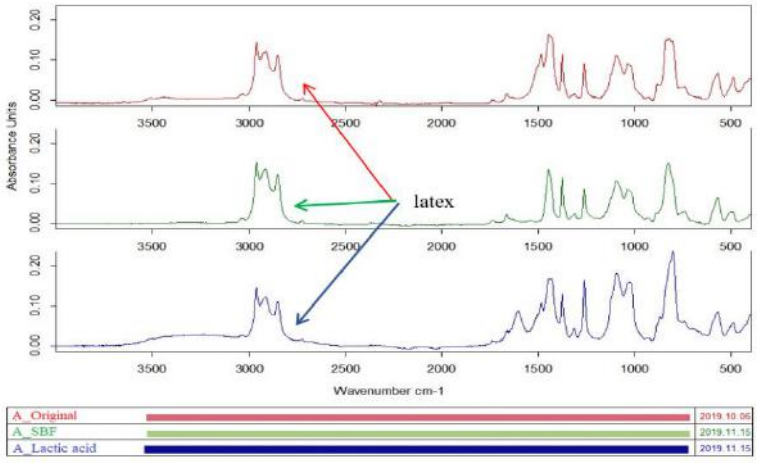

Figure 3
*Comparative FT-IR spectra of sample **A** before and after soaking*

2.3. Tensile strength test

Our hypotheses regarding the damage processes were supported by the tensile tests, which were performed on strip-shaped specimens from samples. The deformation rate was 500 mm/min, under 50% relative humidity and room temperature (T = 20 °C).

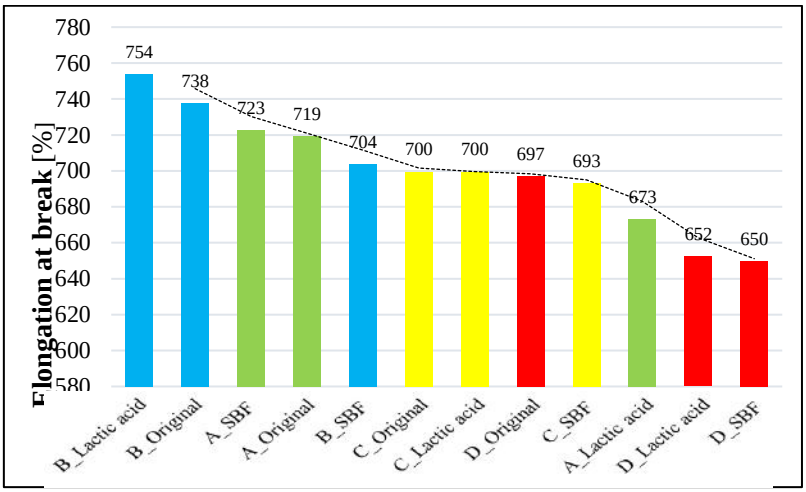

Figure 4
Elongation at brake

We found that -sample B soaked in lactic acid had the highest elongation at break (753.67%), while the lowest value was in the SBF treated D sample (649.91%). However, it is not possible to make a clear distinction between the samples soaked in the two reference solutions. With this series of experiment it was possible to prove that the simulated human body fluids have a negative effect on the mechanical properties of the condom, although in our case the test was carried out under extreme conditions (30-day swelling interval).

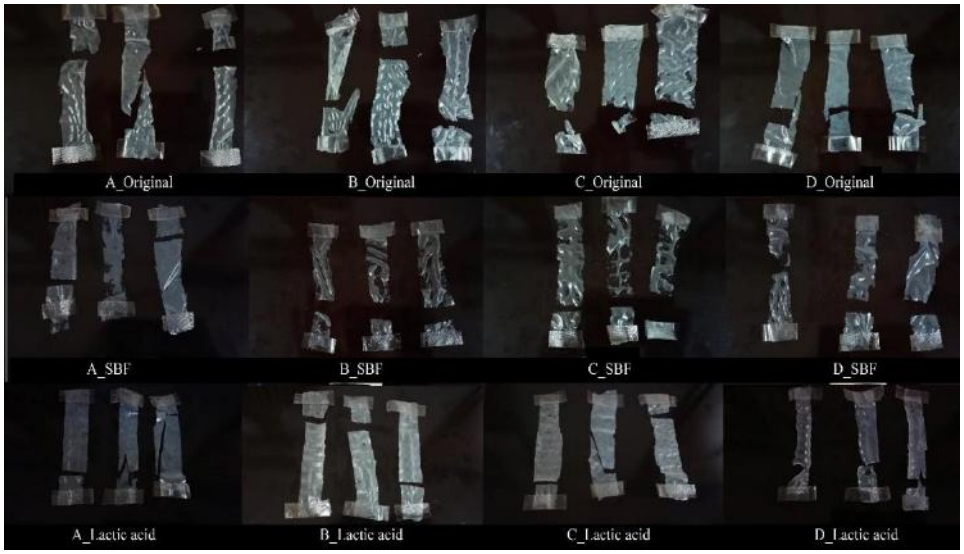

Figure 5
The torn test specimens

CONCLUSION

A total of four latex-based rubber condoms of different brands (A, B, C, D) were tested in two different liquids simulating human body fluids (SBF and lactic acid solution) to analyze the possible material damaging processes caused by the solutions. First, solvent uptake was investigated, then the specimens were subjected to FT-IR spectroscopy and tensile strength analysis. The swelling tests were carried out for a total of 30 days, during which time changes in sample weight of the condoms and pH of solution were recorded.

During the examinations we found that the lubricants were probably dissolved in the SBF and lactic acid solutions, which probably caused the pH fluctuation of (1–3Ph units). Similarly, samples B, C, D were stained in SBF solutions after 21 days. The highest swelling was observed in the samples soaked in lactic acid solution without exception, the most solvent was absorbed in the case of sample B, and the least in case of SBF solutions for sample A.

Number of 3,500–3,000 cm^{-1}. Comparing the spectra, it was found that rubber condoms are made up of the similar materials, except for differences in the intensity of the peaks of the constituent components.

Our hypotheses regarding the possible damage processes were partially supported by tensile strength tests, which were performed on strip-shaped specimens. The crosshead speed was 500 mm/min, under 50% relative humidity and room temperature. We found that sample B soaked in lactic acid had the highest elongation (753.67%), while the lowest value was for the SBF treated sample D (649.91%). However, it is not possible to make a clear distinction between the samples soaked in the two reference solutions. With this series of experiments it was proven that the simulated human body fluids could have a negative effect on the mechanical properties of the condom, although in our case the test was carried out under extreme conditions (30-day treatmen). The mechanism of action of lubricants on the condom material and on the human body remains an open question for us; in the future we would like to carry out a series of tests that are also related to human health (diseases, fungi, etc.). The starting point for this was the specimens treate with SBF.

ACKNOWLEDGEMENT

The described article/presentation/study was carried out as part of the EFOP-3.6.1-16-2016-00011 *Younger and Renewing University – Innovative Knowledge City – institutional development of the University of Miskolc aiming at intelligent specialisation* project implemented in the framework of the Szechenyi 2020 program. The realization of this project is supported by the European Union, co-financed by the European Social Fund.

REFERENCES

[1] Morlin, B. (2018). *Természetes polimer szerkezeti anyagok*. BME Polimertechnikai Tanszék, [Online, Accessed: 2019. 11. 01.]

[2] Gerofi, J., Sorensen, M. (2017). Comparison of condom deterioration in different pack shapes. *Polymer Testing*, Vol. 59, pp. 38–45., DOI: 10.1016/j.polymertesting.2017.01.005.

[3] Favre, H. A., Powell, W. H. (2014). *Nomenclature of Organic Chemistry: IUPAC Recommendations and Preferred Names 2013*. Cambridge, England, p. 748., ISBN: 978-0-85404-182-4.

[4] Lee, T. C., Koshy, P., Abdullah, H. Z., Idris, M. I. (2016). Precipitation of bone-like apatite on anodise titanium in simulated body fluid under UV irradiation. *Surface and Coatings Technology*, Vol. 301, pp. 20–28., DOI: 10.1016/j.surfcoat.2015.11.010.

[5] Lu, X., Leng, Y. (2005). Theoretical analysis of calcium phosphate precipitation in simulated body fluid. *Biomaterials*, Vol. 26, pp. 1097–1108., DOI: 10.1016/j.biomaterials.2004.05.034.

[6] Mutlu, I. E. O. (2013). Characterization of 17-4 PH stainless steel foam for biomedical applications in simulated body fluid and artificial saliva environments. *Materials Science and Engineering*, Vol. 33, No. 3, pp. 1125–1131., DOI: 10.1016/j.msec.2012.12.004.

[7] Wang, X. X., Hayakawa, W., Tsuru, S., Osaka, K. (2003). Apatite deposition on thermally and anodically oxidized titanium surfaces in a simulated body fluid. *Biomaterials*, Vol. 24, No. 25, pp. 4631–4337., DOI: 10.1016/S0142-9612(03)00357-0.

[8] Zhao, W., Bowen, L. J. (2017). A comparative study of simulated body fluids in the presence of proteins. *Acta Biomaterialia*, Volume 53, pp. 506–514., DOI: 10.1016/j.actbio.2017.02.006.

[9] Macaluso, M., Lawson, L., Akers, R., Valappil, T., Hammond, K., Blackwell, R., Hortin, G (1999). Prostate-Specific Antigen in Vaginal Fluid as a Biologic Marker of Condom Failure. *Contraception*, Vol. 59, No. 3, pp. 195–201., DOI: 10.1016/s0010-7824(99)00013-x.

[10] Marques, M. R. C., Loebenberg, R. Almukainzi, M. (2011). Simulated Biological Fluids with Possible Application in Dissolution Testing. *Dissolution Technologies*, Vol. 8, p. 16., DOI: 10.14227/DT180311P15.

Materials Science and Engineering, Volume 45, No. 1 (2020), pp. 316–322.
DOI: 10.32974.mse.2020.032

POSSIBILITIES OF UTILIZATION GROUND REED IN CEMENT FOAM

BELLA UDVARDI[1] – ALEXANDRA HAMZA[2] –
FLÓRA FEHÉR[3] – ISTVÁN KOCSERHA[4]

Abstract: Nowadays, due to overpopulation heating energy consumptions constantly increasing, however this could be reduced by suitable insulation materials. Thermal insulation products play a significant role in building materials. In the construction and building industry reed is known as an ecological insulation material. Using reed energy-saving production process can be created and with this natural material, environmentally friendly material use can be achieved. For this reason the present study has a dual goal: partly integration of ground reed into cement foam as a space filler and insulation material, on the other part making an insulating panel using reed particles. During the experiment, the reed fibres were cut and then mixed with cement paste. In this research work the compressive strength of the samples (at 7, 17 and 28 days), density and finally the thermal conductivity of the samples were measured.

Keywords: reed, cement foam, insulting materials

INTRODUCTION

Today, there is a rapid growth in the construction industry worldwide. Due to rapid urbanization, total energy consumption and a significant portion of greenhouse gas emissions is attributed to construction industry. All over the world one third of the total energy is used to heat or cool buildings. In order to save the energy consumption of concrete buildings, there is a large demand for the development of structural cement based materials with low thermal conductivity and eligible compressive strength [1, 2].

Several agricultural waste materials have already been used as alternatives to cement-based products [3, 4].

[1] Institute of Ceramics and Polymer Engineering, University of Miskolc
H-3515 Miskolc-Egyetemváros, Hungary
fembella@uni-miskolc.hu
[2] FIEK, University of Miskolc
H-3515 Miskolc-Egyetemváros, Hungary
femhamza@uni-miskolc.hu
[3] FIEK, University of Miskolc
H-3515 Miskolc-Egyetemváros, Hungary
femflora@uni-miskolc.hu
[4] Institute of Ceramic and Polymer Engineering, University of Miskolc
H-3515 Miskolc-Egyetemváros, Hungary
istvan.kocserha@uni-miskolc.hu

Benmansour et al. [5] had main goal is to assess the potential of a new natural material (palm fibres, DPF) as a building materials. In their experiment, several mixtures were made with palm fibres added in different amounts (0 to 30 wt%). According to their measurement results that the incorporation of palm fibres into the mortar along with the weight of sample reduces the thermal conductivity and compressive strength of composite. By their study, the use of palm wood fibres in 5–15 wt% suits the thermal and mechanical requirements of building materials.

Remesar et al. [6] investigated the effect of a combination of three different materials, namely coarse expanded clay (CEC), fine expanded clay (FEC) and fly ash. Experimental results show that the use of FEC results in lower thermal conductivity and lower compressive strength than the use of CEC. The reason for this was explained by the finer pore size distribution and the smaller pore size. Of the three materials, fly ash has the least effect on thermal and mechanical properties, while combination of the three materials shows that the thermal conductivity decreases, as well as the compressive strength is within acceptable limits.

Bołtryk and Pawluczuk [7] aimed to establish the properties of lightweight cement composites with natural fillers, such as reed and conifer sawdust. The compressive strength, density and porosity of the samples were measured.

These research works inspired us to add ground reed in to the cement paste. The aim of research was to reduce the amount of primary materials used in the production of cement foams. As the reed has a thermal conductivity of 0.05 W/mK, so it has excellent thermal insulation properties, which can further improve the energy performance of cement-based lightweight concrete products. In addition to these properties, it is important to know the effect of the additive on the strength values. Therefore, in this research work compressive strength tests were measured.

1. MATERIALS AND METHODS

In the research work the first step was the grinding of 2 m long reeds, which was done by an AL-KO, Power Slider 2500 R type blade shredder. In the shredder the knives make a rotating motion as a result of which the reed fibres are cut. As a result of this shredding mechanism, ground reeds of different fractions were obtained, which were used in different ways.

Figure 1
Ground reed

After grinding, cement foams were made using these reeds in the range of 5–40 mm. In this case, the reed particles were used as filler. During the research work DDC CEM II/ B-M (V-LL) 32,5 R type cement was applied to prepare the cement foam to which 30 wt% concentration H_2O_2 solution in amount of 4 wt%, proportionally to the weight of the cement, as a foaming additive and 10 wt% ground reed were added at a factor of 0.488 w/c.

During the experiment the ground reed was added to the cement paste then the cement mass was cast into 75 × 75 × 75 mm moulds. Specimens were removed from the moulds at one day of age and those were stored in a steam chamber until the day of compressive strength test. The temperature of the steam chamber was 22 °C and the relative humidity was ~ 90%. A total of 27 specimens were prepared on which compressive strength of 7, 14 and 28 days were measured.

Figure 2
Cement foams made from ground reeds

During the experiments it was found that after mixing the ground reed with cement paste the water was absorbed from the cement paste and as a result the samples had a hard time to dry. The next step is the mineralization, known from the production of wood wool boards, i.e. utilizing the hygroscopic capacity of reeds, so a mineral was injected into its structure. In the production of wood wool boards the mineralization of wood raw materials is carried out with an aqueous solution of calcium chloride ($CaCl_2$), occasionally using magnesium chloride ($MgCl_2$) or water glass (Na_2SiO_3).

For all these reasons the ground reeds were fractionated using a sieve with 5 mm opening size, then cylindrical seeds were prepared from the sieved reeds. During the reed seed preparation, 100 g of reeds were mixed with 160 g of water glass, (Na_2SiO_3) and then it was compressed into a PVC pipe with 25 mm in diameter and 150 mm in length. As a result of compression, the water glass glued the reeds particles together. After one day it could be easily removed from the pipe, without being fractured. The reed seeds were made to size proportionally to the mould and fixed in the 150 × 150 × 150 mm mould. The 6 reed seeds were fixed by the clamping force of the mould *(Figure 3)*, and foamed around with cement paste.

Figure 3
The reed seeds in the mould

During the foaming of the reed seeds, CRH CEM II/B-S 42.5 N type Portland cement was used. In this case, too H_2O_2 was used in an amount of 4 wt% as foaming agent with w/c factor of 0.553.

After that, a pressed insulating panel was made using ground reeds in the range of 5–40 mm. For this DDC CEM I 52.5 N type cement and 16 wt% reed were used to obtain a more stable panel as a final product. The insulating panel made using ground reed is based on similar concept for commercially available Heraklith® wood wool insulation boards [8]. During the production of the insulating panel, ground reeds were added to a relatively dilute (0.46 w/c) cement paste with gradual mixing. After mixing, the cement-reed paste was casted into the 300 × 300 × 50 mm mould of size, and then the top was located on crest of the mould. Following this the sample was pressed by a pneumatic cylinder, where a pressure load of 2 bar was applied to the sample for one hour. Affected by this the cemented reed mixture was compressed, resulting in a pressed reed panel which is similar to wood wool insulation boards.

Figure 4
The process of pressing a reed panel

2. RESULTS AND DISCUSSION

Compressive strength testing was performed on cement foams at 7, 14 and 28 days of age. The test was made with an INSTRON electromechanical tensile and compression testing apparatus. The measurement results of the compressive strength of cement foam can be seen in *Figure 5*. The mean of the compressive strength results measured at 7 and 28 days of age was 0.85 MPa, while the mean values for the 14 day results were 0.64 MPa.

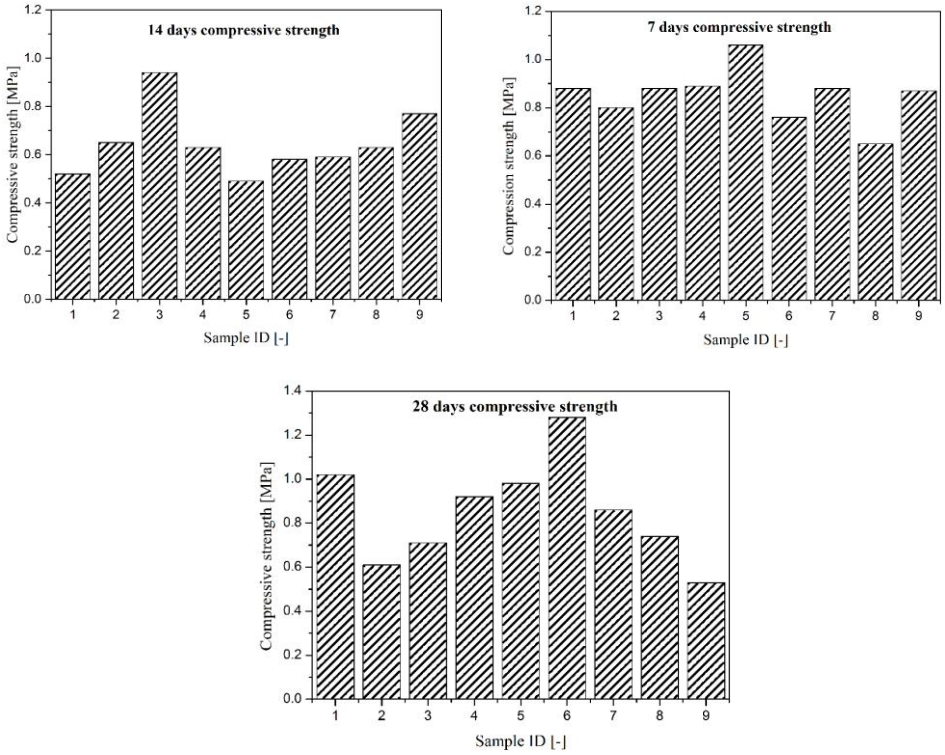

Figure 5
Compressive strength of cement foams

The specimen density of the cement foams was determined from their geometric data. The highest density was in the 7 days samples, this values was 643 kg/m^3. The lowest density was shown by dried and measured cement foams after 14 day of age with average values of 623 kg/m^3. The average densities of the samples aged for 28 days were 640 kg/m^3.

It can be stated that the reeds do not absorb water from the cement paste when the reeds are treated with the mineralizing material. It is important that the reeds treated with water glass glued together. Due to foaming of the sample, its volume increases and this is the reason why some reed seeds broke or moved out of place.

After curing time the pressed reed panel was dried to constant weight and then its thermal conductivity was measured. The test was carried out with the RAPID K type instrument, which work on the principle of heat flux measurement. According to the examination a favourable thermal conductivity value (0.0738 W/mK) was measured, as it is in the set value range (0.07–0.08 W/mK).

Figure 6
Thermal insulation reed panel

It can be seen in *Figure 6* that the insulating panel was very stable and solid after it was removed from the mould. In the research work only the thermal conductivity was determined as a qualifying test, because it was the primary aim. Further qualification tests are also planned for the future.

CONCLUSION

Based on the experiments, it can be stated that reed particles can be used in different forms to produce cement foams. During the mixing of the reed particles into the cement foam by the reed gradually adding, a sufficiently homogeneous cement paste can be prepared, which is suitable for foaming with hydrogen peroxide. By this method some of primary materials applied can be replaced, thus a more environmentally friendly product can be produced. Using a combination of 4 wt% hydrogen peroxide and 10 wt% reed particles proportionally to the weight of cement, test specimens with a specimen density of 620–650 kg/m^3 were prepared. It is 28 days compressive strength showed a value of around 1 MPa.

It was proved to be possible to prepare reed seeds with fine reed particles ($d < 5$ mm) and water glass, however the foaming cement damaged the reed seeds fixed into the mould. Thus, further investigation are needed for such apply.

During the production of the thermal insulation panel, the DDC CEM I 52.5 N type cement is suitable, so a stable thermal insulation board can be prepared.

ACKNOWLEDGEMENTS

This research was supported by the European Union ant the Hungarian State, co-financed by the European Regional Development Fund in the framework of the GINOP – 2.3.4.-15-2016-00004 project, aimed to promote the cooperation between the higher education and the industry.

REFERENCES

[1] Al-Homoud, M. S. (2005). Performance characteristics and practical applications of common building thermal insulation materials. *Building and Environment*, Vol. 40, No. 13, p. 353, March 2005, https://doi.org/10.1016/j.buildenv.2004.05.013.

[2] Gupta, P., Maji, P. K. (2019). Characterization of Wood, Cork and Their Composites for Building Insulation. *Applied Sciences*, Vol, 2, No. 15, p. 44, January 2020, https:// doi.org/10.1016/B978-0-12-803581-8.10591-0.

[3] Zawawi, M. N. A. A., Muthusamy, K., Majeed, A. P. P. A., Musa, R. M., Budiea, A. M. A. (2020). Mechanical properties of oil palm waste lightweight aggregate concrete with fly ash as fine aggregate replacement. *Journal of Building Engineering*, Vol. 27, No. 20, p. 100924, June 2020, https://doi.org/10.1016/j.jobe.2019.100924.

[4] Prusty, J. K., Patro, S. K., Basarkar, S. S. (2016). Concrete using agro-waste as fine aggregate for sustainable built environment – A review. *International Journal of Sustainable Built Environment*, Vol. 5, No. 21, p. 312, December 2016, http://dx. doi.org/ 10.1016/j.ijsbe.2016.06.003.

[5] Benmansour, N., Agoudjil, B., Gherabli, A., Kareche, A., Boudenne, A. (2014). Thermal and mechanical performance of natural mortar reinforced-with date palm fibers for use as insulating materials in building. *Energy and Buildings*, Vol. 81, No. 6, p. 98, October 2014, http://dx.doi.org/10.1016/j.enbuild.2014.05.032.

[6] Remesar, J. C., Simon, F., Vera, S., Lopez, M. (2020). Improved balance between compressive strength and thermal conductivity of insulating and structural lightweight concretes for low rise construction. *Construction and Building Materials*, Vol. 247, No. 12, p. 118448, June 2020, https://doi.org/10.1016/j.conbuildmat.2020.118448.

[7] Bołtryk, M., Pawluczuk, E. (2014). Properties of a lightweight cement composite with an ecological organic filler. *Construction and Building Materials*, Vol. 51, No. 8, p. 97, January 2014, http://dx.doi.org/10.1016/j.conbuildmat.2013.10.065.

[8] HERAKLITH. *Basic Panel*. [Online]. Available: https://www.heraklith.hu/bemutatjuk-heraklithr-termekcsaladunkat [Accessed May 11, 2020].

Materials Science and Engineering, Volume 45, No. 1 (2020), pp. 323–331.
DOI: 10.32974.mse.2020.033

WETTING AND GRAIN BOUNDARY PENETRATION OF 42CRMO4 STEEL BY COPPER

DHEERAJ VARANASI[1] – PÉTER BAUMLI[2]

Abstract: Process like brazing and soldering are used in electronic packaging of integrated circuits, fabrication of heat exchangers for both commercial and aerospace applications. They are also used in manufacturing of high-performance sturdy equipment. Wetting plays a major role in these processes as it determines the efficiency and efficacy of the joints. The present study is focussed on understanding the wettability of low alloyed steels like 42CrMo4 (1.2 w% Cr, 0.75 w% Mn, 0.3 w% Mo) by molten copper. The experiments were conducted at 1,100 °C under vacuum. The sessile drop technique is used and a good wetting is observed by copper on the surface of the steel. The wetting is almost spontaneous agreeing with the widely known phenomenon of excellent metal/metal wetting. Scanning Electron Microscopy (SEM-BSD) analysis showed excellent grain boundary wetting and corresponding groove formation at the steel/Cu interface. These grooves formed at the interface further leads to formation of copper channels which will result in grain boundary penetration of steel by copper.

Keywords: steels, wetting, grain boundary penetration, low alloyed steels

INTRODUCTION

Wetting as a precursor to brazing processes is well known in the scientific field as can be seen in studies on brazing [1–2]. Since copper is the most widely used braze filler and steels are the most commonly used industrial equipment, there is a general interest in the interactions of copper-steel/iron. Interactions of copper as liquid metal on iron/steel surfaces was studied extensively since the second half of last century [3–7].

Perhaps, the most comprehensive literature in the interaction of iron/Cu with regards to grain boundary wetting and grain boundary penetration was discussed by [8]. They investigated the copper penetration into iron grain boundaries. Their investigation resulted in formulation that during melting of copper and subsequent interaction with iron grain boundaries, the grains of iron separate and vacancies would be formed on the surface. These vacancies would then create a channel which would be filled by liquid copper. The driving force is the surface/interface free energy. The surface of iron experiences liquid metal embrittlement and the grain boundary cracks

[1] Institute of Physical Metallurgy, Metalforming and Nanotechnology, University of Miskolc
H-3515 Miskolc-Egyetemváros, Hungary
djvaranasi@gmail.com
[2] Institute of Physical Metallurgy, Metalforming and Nanotechnology, University of Miskolc
H-3515 Miskolc-Egyetemváros, Hungary
baumlipeter@gmail.com

encouraging further penetration. Copper interaction with medium carbon steels was reported by [9–10] and observed both wetting and grain boundary penetration. The grain boundary penetration observed grew exponentially with time.

Grain boundary penetration is also of prime focus in the wetting studies [11–12] focussed on the non-wetting/wetting transition of the grain boundaries in alloys. Wetting also includes phenomenon of spreading and studies mentioned in [13–14] deal with spread characteristics of wetting in metal/ceramic systems. Investigations into the wetting factors were discussed by [15] from perspective of wetting liquids. Just as wetting is in focus in the field of joining, dewetting/non wetting studies are also on rise to understand the reasons for spallation of joints attributed by the behaviour of various materials and their interface. These were reported in the studies [16–18].

The present study focusses solely on the grain boundary wetting and grain boundary penetration of Cr-Mo low alloyed steel by copper.

1. EXPERIMENTAL

The composition of the steels used in the study is tabulated below *Table 1*.

Table 1

Composition of steels used in the study

Steel	Fe w%	C w%	Cr w%	S w%	Mn w%	Mo w%	Source
42CrMo4	rest	0.40	1.3	0.030	0.75	0.30	XRF

Wetting as a precursor for brazing was conducted by copper on steel surface. The steel is cut to size 10*7*5 mm, ground and polished prior to experimentation. A small piece of copper foil is (99.99% pure) of 70 micron thickness and is cut and subjected to ultrasonication in an acetone bath. The piece of copper is placed on top of steel surface and is put in a vacuum furnace equipped with resistance heating *(Figure 1)*.

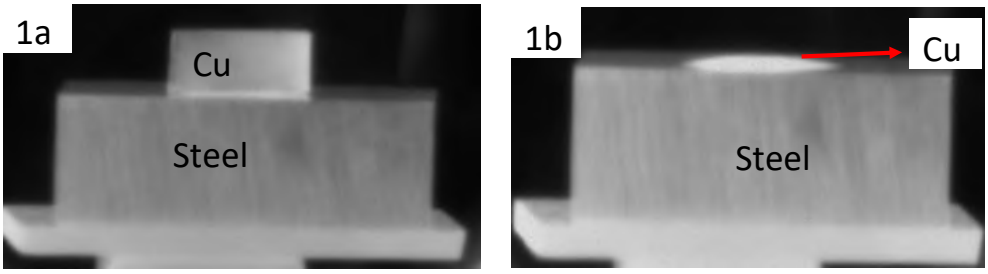

Figure 1

Arrangement of copper foil on steel for sessile drop wetting experiment is shown in Figure 1.a and the spontaneous wetting observed at the melting point of copper is shown in Figure 1.b. It just took 3 seconds for the copper foil on the left picture to achieve the perfect wetting seen in the right picture

The wetting experiment was conducted under vacuum with a residual pressure of 10^{-8} bar. The furnace is heated from room temperature to a temperature of 1,100 °C, which is sufficiently just above the melting point of copper (1,083 °C) in steps at a heating rate of 20 °C/min. The sample was kept at this temperature for 5 minutes before cooling down. Cooling is done via furnace cooling; no external cooling sources were used. The sample was left in the furnace to cool.

Post experimentation, the samples are removed from the furnace and are mounted in Bakelite resin and later analyzed by Scanning Electron Microscopy (SEM – EDS). The equipment used for this purpose is Carl Zeiss EVO MA10 equipment. All the images were taken in BSD mode with an accelerated voltage of 20 KV.

2. RESULTS AND OBSERVATIONS

First observation we make during the experiment is that as the melting point of copper is reached, the copper foil melts on the surface of steel spontaneously. *Figure 1.b* shows this spontaneous melting of copper on the steel. This spontaneous wetting is followed by dissolution of Fe from the steel grain boundary. Grains of Fe are visible in the middle of copper droplet, which can be observed in *Figure 2*. These grains are solidified in the drop as the substrate is cooled down from experimental temperature to room temperature. Hence, it is safe to assume these precipitates would be ferritic in structure (at least theoretically at room temperature).

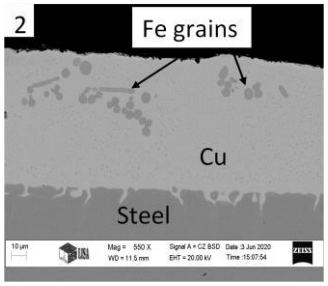

Figure 2
Fe grains dissolved in copper during the wetting experiment. Grain boundary wetting of steels is also observed at the steel/Cu interface

Second observation is the grain boundary penetration of the steel by the molten copper. *Figure 3* shows the observed grain boundary penetration of steels.

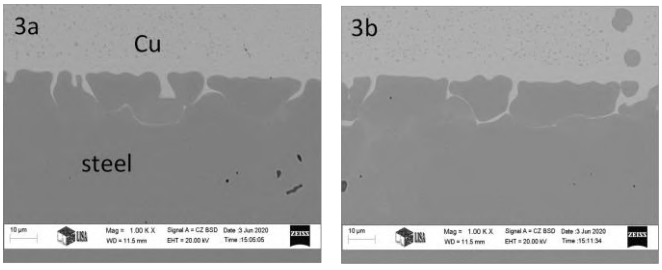

Figure 3. *Grain Boundary penetration of 42CrMo4 steel by molten copper can be observed. Small precipitates of Fe are dissolved in molten copper, seen in small dark grey spots throughout the copper*

3. DISCUSSION

Wetting is the spread of liquid on a solid surface. Generally metal/metal systems have good wetting owing to the formation of metallic bonds. The wetting angle is defined in terms of interfacial energies [19] as given in *Equation 1*.

$$cos\theta = \frac{\sigma_{sv}-\sigma_{sl}}{\sigma_{lv}} \quad (1)$$

Where, σSV, σSL and σLV are the interface energies (J/m^2) of between solid-vapor, solid-liquid and liquid-vapor phases, θ is the contact angle. This famous equation was devised by Thomas Young in nineteenth century. Dupree extended the equation to accommodate adhesion given in *Equation 2*.

$$W_a = \sigma_{sv} + \sigma_{lv} - \sigma_{sl} \quad (2)$$

Where, W_a is the adhesion energy (J); all other quantities are as previously defined.

From above, we can see that wetting is mostly attributed to imbalance of interfacial energies as explained by [20]. Excellent wetting was already observed as seen in *Figures 3.a–b*. The wetting observed is a consequence of *Equation 1*. Logic dictates this can be proven by finding the contact angle theoretically from calculations. *Figure 4* shows the contact angle, 3.2°, of Cu sessile drop on surface of the steel measured from the image analysis provided within the SEM software. This is in accordance with the angle measured using the KSV contact angle measurement software embedded with Young–Laplace programming. The contact angle calculated by the software is 3.79°, which is considered as near perfect wetting.

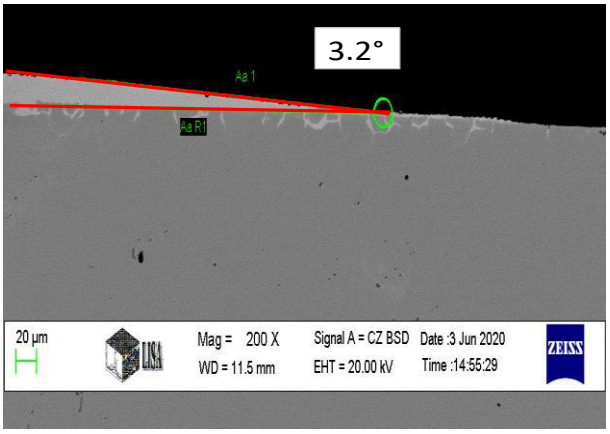

Figure 4
Wetting contact angle of Cu on 42CrMo4 steel as observed and measured from image analysis software from SEM. The angle of 3.2° is observed which is almost perfect wetting angle

The copper spreading on the surface of steel was instantaneous. The drive for the spread and wetting can be calculated from *Equation 1*. The three quantities, σ_{SL}, σ_{SG},

$\sigma_{LG.}$ are previously defined in the manuscript. Well defined equations are defined and formulated by G. Kaptay for finding the interfacial energies [21–22]. The equations are given below, *Equations (3–6)*.

$$\sigma_{S/g} \cong \frac{\alpha_s.\left[q.R.T_{m,s} + \Delta_m H_s + \int_T^{T_{m,S}} C_{P,s} dT\right] - 2.T}{f_S.{V_{m,s}}^{2/3}.{N_{Av}}^{1/3}} \quad (3)$$

$$\sigma_{l/g} \cong \frac{0.182.\left[q.R.T_m - C_{P,l}.(T - T_m)\right] - 2.T}{1.06.{V_{m,l}}^{2/3}.{N_{Av}}^{1/3}} \quad (4)$$

$$\sigma_{s/l} \cong \frac{0.310.{f_b}^{1/3}.\Delta_m H_s + 0.343.\Omega_{s-l} + 3.3T}{{V_{m,s}}^{1/3}.{V_{m,l}}^{1/3}.{N_{Av}}^{1/3}} \quad (5)$$

Where, σ_{Sg}, σ_{lg}, σ_{sl} are the interfacial energies of solid-gas, liquid-gas and solid-liquid phases. α_s and f_s are the solid crystal parameters which are considered as average constants of 0.20 and 1.1 respectively. q is correlation parameter of value 25.4, R is universal gas constant, 8.3145 J/mol K, $\Delta_m H_s$ is the melting enthalpy of the solid (KJ/mol), $C_{P,s}$ and $C_{P,l}$ are the heat capacities of the solid and liquid at temperature T (J/Kmol), T is required temperature (K), $V_{m,s}$ and $V_{m,l}$ are the molar volumes (m^3/mol) of solid and liquid metals in study (Here Fe and Cu respectively), N_{Av} is Avogadro constant ($6.023*10^{23}$ /mol), Ω_{sl} is the solid-liquid interaction energy J/mol. However, for metals with eutectic composition like Sn-Cu, Fe-Cu, the interaction energy is defined from *Equation 6*, [22] given below:

$$\Omega_{sl} \cong \frac{{G^0}_{M,s} - {G^0}_{M,l} - R.T_{eu}.lnx}{(1-x)^2} \quad (6)$$

Where, $G^0_{M,s}$ and $G^0_{M,l}$ (J/mol) are the standard Gibbs energies of solid higher melting point metal and liquid higher melting point metal respectively, T_{eu} (K), is the eutectic temperature of the alloy, R (J/mol K) is the universal gas constant, x is the mole fraction of the higher melting point component in the eutectic composition.

The data required was taken from [23–25] and calculated accordingly to obtain the following interfacial energy values, *Table 2*.

Table 2
Interfacial energies calculated for Fe/Cu system following Equations 3–6

σ_{sg}	2.12 J/m^2
σ_{lg}	1.384 J/m^2
σ_{sl}	0.6431 J/m^2

$$Cos\theta = \frac{2.12 - 0.6431}{1.384} = 1.07 \pm 0.1 \text{ J/m}^2 \quad (7)$$

Once contact has been established between the solid/liquid phases, the adhesion energy comes into play which is essential in maintaining the bond between atoms of dissimilar composition in our case atoms of steel and copper. The adhesion energy can be expressed in terms of surface tension and contact angle by the following relation, colloquially known as Young–Dupree equation [19].

$$\frac{W_a}{\sigma_{lg}} = 1 + Cos\theta \tag{8}$$

Substituting the values form *Table 2* and *Equation 7* into *Equation 8* gives us adhesion energy of 2.86 ± 0.1 J/m^2. This, when compared to the surface tension value of 1.384 J/m^2 is higher and the difference between these two energies provide the driving force for the spread of copper on the surface of steel and ensures perfect wetting between the steel/Cu system.

Grain boundary penetration is an essential part of wetting and follows from thermal grooving at the interface [26]. Copper penetration observed at the steel/Cu interface follows from the formation of grooves at the grain boundary of steel. General condition for penetration is given in *Equation 9* [27–29].

$$\sigma_{GB} \geq 2\,\sigma_{SL} \tag{9}$$

where σ_{GB} (J/m^2) is the grain boundary energy, σ_{SL} (J/m^2) is the solid/liquid interface energy. The grooves observed at the steel grain boundary/Cu interface further enhance the probability of penetration of liquid copper by formation of channels as explained by [8]. Furthermore, precondition for penetration is understood from the relation between dihedral angle (ϕ), σ_{SL} and σ_{GB} [30] given in *Equation 10*.

$$cos\left(\frac{\varphi}{2}\right) = \frac{\sigma_{GB}}{2.\sigma_{SL}} \tag{10}$$

The dihedral angle ϕ is defined as the angle made by the liquid upon intersecting with the solid grain boundary and is a measure of penetration of the liquid into the solid and for penetrating case like ours the ϕ is 0°. Therefore, complete wetting and hence grain boundary penetration is observed.

CONCLUSIONS

1. Wetting and grain boundary penetration of a low alloyed 42CrMo4 steel was observed by molten copper under vacuum.
2. Near perfect wetting was observed of the steel by copper where the spread of copper on the surface of steel was almost instantaneous upon melting. The Young-Dupree model was used to show the drive for the spreading and wetting which is in accordance with the observations.
3. Grain boundary penetration by copper was also observed in the steel, the observations of which are supported by the theory.

ACKNOWLEDGMENTS

Our research was carried out as part of the GINOP-2.3.2-15-2016- 00027 *Sustainable operation of the workshop of excellence for the research and development of crystalline and amorphous nanostructured materials* project implemented in the framework of the Szechenyi 2020 program. The realization of this project is supported by the European Union.

The authors are also thankful to dr. Daniel Koncz-Horvath and dr. Anna Sycheva for SEM measurements. A special thanks to Mrs. Aniko Markus and Mrs. Napsugar Bodnar for their help in sample preparation.

REFERENCES

[1] Cadden, C. H. (2006). Brazing. *Ency. Mater: Sci & Tech*, pp. 1–7.

[2] Janczak-Rusch, J., Kaptay, G., Jeurgens, L. P. H. (2014). Interfacial design for joining technologies: an historical perspective. *Journal of Materials Engineering and Performance*, 23 (5), pp. 1608–1613.

[3] Mullins, W. W. (1957). Theory of Thermal Grooving. *J. Appl. Phy.*, Vol. 28, No. 3, pp. 334–339.

[4] Yoshida, T. (1980). Dissolution and Deposit of Base Metal in Dissimilar Carbon Steel Brazing. *Welding Journal*, Vol. 59 (10), pp. 278–282.

[5] Young, G. F. (1973). On the grian boundary theory of Fisher and Whipple. *J. Appl. Phy.*, Vol. 44, pp. 5151–5154.

[6] Ishida, T. (1986). The Interaction of Molten Copper with Solid Iron. *J. Mater. Sci.*, Vol. 21, pp. 1171–1179.

[7] Huppmann, W. J., Petzow, G. (1978). The role of grain and phase boundaries in liquid phase sintering. *Berichte der Bunsengesellschaft für physikalische Chemie*, Vol. 82, No. 3, pp. 308–312.

[8] Fredriksson, H., Hansson, K., Olsson, A. (2001). On the Mechanism of Liquid Copper Penetration into Iron Grain Boundaries. *Scandanavian Journal of Metallurgy*, Vol. 30, pp. 41–50.

[9] Varanasi, D., Baumli, P. (2018). Grain boundary behavior of copper with C45 meidum carbon steel. *Resolution and Discovery*, 3 (2), pp. 1–5.

[10] Varanasi, D., Szabo, J. T., Baumli, P. (2019). Investigation of the Copper Penetration and Joint Microstructure Observed in Low Alloyed Steels. *NanoWorld J.*, Vol. 5, No. 3, pp. 36–40.

[11] Straumal, B. B., Kogtenkova, O. A., Murashkin, M. Y., Bulatov, M. F., Czeppe, T., Zięba, P. (2017). Grain boundary wetting transition in Al–Mg alloys. *Materials Letters*, 186, pp. 82–85.

[12] Protasova, S. G., Kogtenkova, O. A., Straumal, B. B., Zięba, P., Baretzky, B. (2011). Inversed solid-phase grain boundary wetting in the Al–Zn system. *Journal of Materials Science*, 46 (12), pp. 4349–4353.

[13] Eustathopoulos, N. (1998). Dynamics of wetting in reactive metal/ceramic systems. *Acta Materialia*, 46 (7), pp. 2319–2327.

[14] Landry, K., Eustathopoulos, N. (1996). Dynamics of wetting in reactive metal/ceramic systems: linear spreading. *Acta Materialia*, 44 (10), pp. 3923–3932.

[15] Kumar, G., Prabhu, K. N. (2007). Review of non-reactive and reactive wetting of liquids on surfaces. *Advances in Colloid and Interface Science*, 133 (2), pp. 61–89.

[16] Redon, C., Brochard-Wyart, F., Rondelez, F. (1991). Dynamics of dewetting. *Physical Review Letters*, 66 (6), p. 715.

[17] Liu, C. Y., Kim, H. K., Tu, K. N., Totta, P. A. (1996). Dewetting of molten Sn on Au/Cu/Cr thin-film metallization. *Applied Physics Letters*, 69 (26), pp. 4014-4016.

[18] Xu, L., Bandyopadhyay, D., Shi, T., An, L., Sharma, A., Joo, S. W. (2011). Dewetting kinetics of thin polymer bilayers: Role of under layer. *Polymer*, 52 (19), pp. 4345–4354.

[19] Kaptay, G. (2018). The chemical (not mechanical) paradigm of thermodynamics of colloid and interface science. *Advances in Colloid and Interface Science*, 256, pp. 163–192.

[20] Yost, F. G., Romig, A. D. (1987). Thermodynamics of wetting by liquid metals. *MRS Online Proceedings Library Archive*, 108.

[21] Kaptay, G. (2005). Modelling interfacial energies in metallic systems. *Materials Science Forum*, Vol. 473, pp. 1–10.

[22] Kaptay, G. (2019). Thermodynamic stability of nano-grained alloys against grain coarsening and precipitation of macroscopic phases. *Metallurgical and Materials Transactions A*, 50 (10), pp. 4931–4947.

[23] Kaptay, G. (2008). A unified model for the cohesive enthalpy, critical temperature, surface tension and volume thermal expansion coefficient of liquid metals of bcc, fcc and hcp crystals. *Materials Science and Engineering A*, 495 (1–2), pp. 19–26.

[24] Barin, I. (1989). *Thermochemical data of pure substances*. Weinheim, VCH.

[25] Dinsdale, A. (1989). *SGTE data for pure elements*. Teddington, United Kingdom, National Physical Laboratory, p. 195.

[26] Mullins, W. W. (1957). Theory of thermal grooving. *Journal of Applied Physics*, 28 (3), pp. 333–339.

[27] Straumal, B. B., Kogtenkova, O., Zięba, P. (2008). Wetting transition of grain-boundary triple junctions. *Acta Mater.*, 56 (5), pp. 925–933.

[28] Kaptay, G. (2018). On the solid/liquid interfacial energies of metals and alloys. *Journal of Materials Science*, 53 (5), pp. 3767–3784.

[29] Kaptay, G. (2016). Modelling equilibrium grain boundary segregation, grain boundary energy and grain boundary segregation transition by the extended Butler equation. *Journal of Materials Science*, 51 (4), pp. 1738–1755.

[30] Schmatz, D. J. (1983). Grain boundary penetration during brazing of aluminum. *Welding Journal*, 62 (10), pp. 267–271.

Responsible for the Publication: Prof. dr. Zita Horváth
Published by the Miskolc University Press under leadership of Attila Szendi
Responsible for duplication: Works manager: Erzsébet Pásztor
Technical editor: Csilla Gramantik
Proofreader: Zoltán Juhász
Number of copies printed:
Put the Press in 2020
Number of permission: TNRT–2020– 224 –ME